NASA Contractor Report 189223

IN-07
120879
P-312

LIFE PREDICTION AND CONSTITUTIVE MODELS FOR ENGINE HOT SECTION ANISOTROPIC MATERIALS PROGRAM

Final Report

D. M. Nissley and T. G. Meyer
UNITED TECHNOLOGIES CORPORATION

and

Dr. K. P. Walker
ENGINEERING SCIENCE SOFTWARE, INC.

September 1992

NASA

TABLE OF CONTENTS

TABLE OF CONTENTS (Continued)

LIST OF TABLES

LIST OF TABLES (Continued)

LIST OF FIGURES

LIST OF FIGURES (Continued)

ACKNOWLEDGEMENTS

SECTION 1. SUMMARY

BASE PROGRAM

Thermal mechanical fatigue (TMF) crack initiation mechanisms and methods for life prediction of coated single crystal PWA 1480 were investigated. Isothermal and TMF tests were conducted on over 200 smooth coated specimens. Test conditions were designed to capture material characteristics at relevant turbine blade strains and temperatures. Specimens were fabricated from cast bars which had primary crystallographic orientations of <001>, <011>, <111>, and <213> and coated with one of two generic coating types: a plasma sprayed overlay, designated PWA 286, and an aluminide diffusion, designated PWA 273. To account for the observed cracking trends, the selected life approach considered cyclic life as the sum of coating cracking life, single crystal crack initiation life, and single crystal crack propagation life.

Constitutive models were developed for the overlay coating and single crystal PWA 1480 to provide descriptions of the local coating/substrate stress–strain history. The coating constitutive model was based on Dr. Walker's isotropic viscoplastic model developed for Hastelloy X. The PWA 1480 constitutive model used a micromechanical approach. In this approach, the applied global stresses and strains are resolved into the single crystal cube and octahedral slip systems. Inelastic calculations are performed for each slip system, and then the stresses and strains are resolved back into the global system.

Life models were developed to predict the overlay coating and single crystal TMF crack initiation events. The coating cracking model was based on integrated tensile hysteretic energy. Because coatings exhibit highly nonlinear behavior and because thermal expansion mismatch introduces biaxial loads into the coating during the thermal cycling, inelastic finite element analysis of the coating/single crystal composite was performed to obtain the coating hysteretic response. The PWA 1480 TMF crack initiation life model was based on the maximum mode I stress intensity factor, Kmax. In this model, coating cracks were treated as initial flaws which propagated into the single crystal. Increased crack propagation rate due to bulk cyclic inelasticity was assumed to be insignificant based on the elastic hysteresis observed in the TMF specimens. Both coating and single crystal models include temperature– and time–dependent terms to account for thermal exposure effects.

The constitutive and life models were subsequently incorporated into a computer program called LAYER. LAYER was developed to perform nonlinear finite element and life prediction analyses of multi–layered composites at critical component locations. Input to the LAYER system is obtained from previously conducted component analysis.

OPTION 1 PROGRAM

The Option 1 portion of the contract developed constitutive and fatigue life prediction models applicable to the attachment regions of single crystal turbine blades and vanes. Constitutive and Low Cycle Fatigue (LCF) tests were conducted on smooth and notched single crystal PWA 1480 specimens having several different crystallographic orientations. Specimens were machined from castings having growth directions within 10 degrees of <001>, <011>, <213> or <111>. In all cases, the casting direction corresponded to the loading direction. Notched specimens were carefully machined to control a second geometric axis relative to the crystal axes. A single heat of PWA 1480 was used for all specimens. The bulk of the fatigue testing in the program was conducted at 650°C (1200°F) although some tests were conducted at 760°C (1400°F) and 870°C (1600°F). All of the fatigue data is reported here, but only the 650°C (1200°F) data was used to develop a fatigue model. The fatigue model was developed for notched features typical of the attachment region of single crystal turbine blades. The form of the model was derived from smooth specimen tests for which stresses and strains were well known. The notched fatigue data itself was used to obtain model constants for the notched model. Notch stresses were calculated using a Neuber approach after having been evaluated using nonlinear finite element analyses (FEA) incorporating the Base Program anisotropic PWA 1480 material model. A verification test was conducted using a specimen having a geometry closely matching an actual turbine blade attachment. Finally, a small amount of fatigue data was generated for Hot Isostatically Pressed material.

SECTION 2. INTRODUCTION

One of the more important developments in gas turbine blade materials has been the introduction of directionally solidified and single crystal castings. Among the advantages of these materials are:

- Substantially increased high temperature creep and stress rupture strengths and enhanced oxidation/corrosion resistance due to the elimination of grain boundaries.

- Increased low cycle fatigue life due to a thermal stress reduction incurred as a result of lower elastic modulus along the solidification direction.

- Higher melting temperature and greater heat treatment flexibility resulting from the elimination of grain boundary strengthening elements.

This casting process has matured to the level where it is now routinely used in the production of commercial and military aircraft jet engine turbine blades. Unfortunately, metallurgical and processing advances have not been matched by corresponding advancements in the knowledge and understanding of the mechanics of these materials, their failure mechanisms, and methods for life prediction. In order to realize the full potential of these materials, it is necessary to determine the dominant life limiting parameters. Anisotropy introduces many life prediction questions, especially for stresses which are not parallel to the direction of solidification. Oxidation resistant coatings further complicate the questions. All of these issues were addressed in this NASA sponsored program.

The program consisted of a Base Program and an optional program (Option 1). The Base Program addressed coated single crystal material subjected to relevant turbine airfoil temperatures and load histories. Option 1 addressed uncoated single crystal material operating at root attachment temperatures and notched conditions.

In the Base and Option 1 programs, candidate constitutive and life prediction models were developed concurrently. Laboratory specimens, tested using a variety of mechanical and thermal load histories, provided data for the final model selections. The selected Base Program models were incorporated into computer code.

The first year effort of the program involved materials selection, specimen fabrication, basic material tests, literature searches of appropriate constitutive and life prediction models, initial formulation of constitutive models, and initial constitutive and fatigue life tests. The results of the first year effort were reported in NASA CR-174952 (Reference 1).

The second year effort of the program involved constitutive testing of the selected overlay coating and primary single crystal (PWA 1480) materials, Level I fatigue life testing, development of "microscopic" and "macroscopic" single crystal constitutive models, selection of two coating constitutive models for further development, and initial coating and single crystal life model evaluations. The results of the second year effort were reported in NASA CR-179594 (Reference 2).

The third through fifth years of the program involved selection of coating and PWA 1480 constitutive models, selection of the final overlay coating life model, completion of coated PWA 1480 fatigue life tests, evaluation of candidate TMF life models for coated PWA 1480, completion of elastic finite element stress analysis for notched specimens, and results from initial smooth and notched fatigue tests of uncoated PWA 1480 at root attachment temperature levels. The results of these years were reported in NASA CR-189222 (Reference 3).

This report summarizes the work reported in References 1 to 3 and covers the work period from January, 1989 to May, 1990. During this period the remaining Base Program final model selections were made and incorporated into a computer program called LAYER. The LAYER program was delivered to NASA and a User manual for LAYER was reported in NASA CR-187038 (Reference 4). Finally, the Option 1 life model for uncoated PWA 1480 at root attachment temperatures and notched conditions was completed.

2

SECTION 3. TASK I – MATERIAL/COATING SELECTION AND ACQUISITION

PWA 1480 and Alloy 185 were selected as the primary and secondary single crystal materials, respectively, to be evaluated in this program (Reference 1).

PWA 1480 was the first superalloy specifically designed for use in single crystal form and was developed with the goal of achieving an optimum balance of creep strength, thermal fatigue strength, and oxidation and hot corrosion resistance. PWA 1480 was certified for commercial use in the JT9D-7R4D/E engine in late 1981 and has since been certified for use in the JT9D-7R4G/H, PW2000, PW4000, and V2500 engines.

Two heats of PWA 1480 were procured for this program from the Howmet Turbine Components Corporation, Alloy Division, Dover, New Jersey. The primary heat, identified by Howmet as 2000A14824, was designated P9866. The secondary heat, identified by Howmet as 200B14773, was designated P9867.

Alloy 185 exhibits greater creep anisotropy than PWA 1480 as a result of its higher hardener content compared to PWA 1480 and different structure. Consequently, its selection as the secondary single crystal material made it possible to test the range of applicability of the constitutive and life models developed in the program (Reference 1).

A single heat of Alloy 185 was procured for this program from the Howmet Corporation, Alloy Division. This heat, designated by Howmet as 242A15847, was designated P9921.

Nominal compositions for PWA 1480 and Alloy 185 along with actual compositions of the procured heats are listed in Table 1. The typical solution heat treated microstructures are presented in Figure 1.

The directional solidification casting process was employed to cast cylindrical single crystal bars of both selected alloys with nominal 15.2 cm (6.0 in.) length and 2.54 cm (1.0 in.) and 1.59 cm (0.625 in.) diameters. The primary growth direction was controlled to produce <001>, <111>, <011>, and <213> oriented bars. The castings were solution heat treated, followed by a rigorous evaluation to ensure that only quality castings were used for specimen fabrication (Reference 1).

Two coatings were selected for this program to be representative of those employed on actual turbine airfoils operating in gas turbine engines: PWA 286 overlay coating and PWA 273 outward diffusion aluminide (Reference 1). The general coating compositions and application processes are summarized in Table 2. Typical coating microstructures are presented in Figure 2.

3.1 PRIMARY ALLOY (PWA 1480) AND COATING SPECIMEN FABRICATION

3.1.1 Coating Constitutive Specimens

Overlay Coating

Figure 3 illustrates the specimen geometries employed for testing the mechanical properties of bulk PWA 286 overlay coating material. The specimen diagrammed in Figure 3A was machined from PWA 286 ingots of hot isostatically pressed (HIP) powder. Figure 3B illustrates specimens fabricated from thick sheets of plasma sprayed PWA 286. The thick sheets were produced by plasma spraying thick layers of PWA 286 onto substrates. The substrates were subsequently removed by machining.

Photomicrographs of the overlay coating structure in both types of specimens are presented in Figure 4. It should be noted that the different porosity levels obtained in the two specimens bracket the porosity of overlay coatings on actual airfoils (Figure 2): the HIP specimen contained virtually no porosity, while the unpeened thick plasma spray specimen contained a high level of porosity.

Aluminide Coating

The structure of diffusion coatings is much more complex than that of overlay coatings. The diffusion coating chemistry and microstructure vary from the coating surface to the substrate because of

3

interdiffusion between the coating material and the substrate during the coating process. As a result, aluminide coating mechanical properties can not be effectively determined from homogeneous bulk specimens. To obtain diffusion coating behavior, the approach taken in this program was to coat two thicknesses of thin PWA 1480 substrates and test the resulting composite structure. Theoretically, the effective coating properties could then be obtained by comparing the thicker specimen response to that of the thinner specimen.

Flat specimens for PWA 273 coating constitutive tests were fabricated by forming coating on both sides of the PWA 1480 substrate. PWA 1480 <100> substrates were fabricated from 2.54 cm (1.0 in.) diameter bars of heat P9867 material. The specimens were oriented such that the transverse direction was parallel to a secondary <010> direction. The nominal, before coating, substrate gage section thicknesses were: 0.25 mm (0.01 in.) and 0.13 mm (0.005 in.) as shown in Figure 5. Due to the fragile nature of these specimens, fixtures were constructed to hold the specimens during the coating process and subsequent diffusion heat treatment at 1079°C (1975°F) and aging at 871°C (1600°F).

The microphotographs in Figure 6 show the structure of the completed flat specimens. The 0.25 mm (0.010 in.) initial substrate thickness reduced to about 0.14 mm (0.0055 in.) after coating, while the 0.13 mm (0.005 in.) initial thickness reduced to about 0.02 mm (0.0008 in.) remaining substrate.

3.1.2 PWA 1480 Material Specimens

Figures 7A and 7B illustrate the specimen geometries employed for coated and uncoated tensile and creep testing and uncoated cyclic constitutive testing.

Fatigue test specimen geometries used for coated and uncoated PWA 1480 were chosen to allow test conditions comparable to those found in actual turbine airfoils. Figure 8 schematically illustrates the geometries for the hollow tube LCF/TMF (low cycle fatigue/thermomechanical fatigue) specimens. To take full advantage of external extensometry, a ridgeless specimen (Figure 8B) was developed early in the program to replace the internally ridged specimen (Figure 8A). A comparison study of internal and external extensometers was reported in Reference 2.

3.2 ALTERNATE SINGLE CRYSTAL MATERIAL (ALLOY 185) SPECIMEN FABRICATION

Alloy 185 bars were cast using the single crystal directional solidification process. Bar sizes were consistent with the PWA 1480 bars (Reference 1). The bars were heat treated at 1316°C (2400°F) followed by a forced gas cool to refine and homogenize the gamma prime hardener without the onset of incipient melting. The same inspection procedure used for the PWA 1480 cast bars was employed to ensure the quality of the Alloy 185 castings.

3.3 PHYSICAL, THERMAL AND MONOTONIC MECHANICAL PROPERTIES

3.3.1 Thermal-Physical Properties

The thermal-physical properties of PWA 1480 single crystal material, unlike mechanical properties, are isotropic. Therefore, measurements are required only for a single orientation.

Thermal-physical property tests for <001> oriented PWA 1480 and PWA 273 and PWA 286 coatings were conducted at Southern Research Institute. Thermal conductivity, thermal expansion, specific heat and density property data were obtained and were included in Appendices A and B of Reference 1. Property curves based on the data are presented in Figures 9 through 11, respectively.

3.3.2 Elastic Constants

Elastic constants for PWA 1480 were obtained by ultrasonic wave velocity measurements (Reference 3) over the entire range of temperatures applicable to turbine airfoils. The resulting "dynamic" stiffnesses are shown in Figure 12. Table 3 contains the dynamic stiffnesses, C_{ij}, and the dynamic

compliances, Sij, which are related by the following equations.

$$S11 = \left[\frac{C11 + C12}{(C11 - C12) \ (C11 + 2C12)} \right] \tag{1}$$

$$S12 = \left[\frac{- C12}{(C11 - C12) \ (C11 + 2C12)} \right] \tag{2}$$

$$S44 = \frac{1}{C44} \tag{3}$$

Also included in Table 3 is the "apparent modulus" that would be obtained from a simple tensile test of a single crystal bar oriented in each of the four primary orientations used in this program. The apparent modulus is obtained through the following equation.

$$''E'' = \{S11 - [2(S11 - S12) - S44] \ F\}^{-1} \tag{4}$$

$$\text{where } F = \sin^2 \alpha \ \cos^2 \alpha \ + \ \frac{\sin^4 \alpha \ \sin^2 2 \beta}{4} \tag{5}$$

The angles α and β define the tensile direction as shown in Figure 13.

Figures 14 through 17 compare the apparent modulus obtained from "static" tensile testing to the apparent modulus from the dynamic constants. At higher temperatures and for certain orientations the "static" modulus is lower than the "dynamic" modulus. The orientation dependence appears to have at least some degree of correlation with the cube slip system shear stresses. The maximum resolved shear stresses and the number of slip systems with shear stresses within 10 percent of the maximum are given below.

Resolved Shear Stress (% of Applied Stress)

Tensile Direction	Octahedral Systems		Cube Systems	
	Maximum	# within 10%	Maximum	# within 10%
<001>	41%	8	0%	0
<213>	47%	1	46%	2
<011>	41%	4	35%	4
<111>	27%	6	47%	3

The dynamic elastic constants were used in the PWA 1480 single crystal constitutive modeling effort.

3.3.3 Tensile Properties

A total of 40 monotonic tensile tests were conducted on PWA 1480 single crystal specimens with orientations of <100>, <110>, <111> and <213>. All tests were run at the American Society for Testing Materials (ASTM) standard strain rate of 0.005 min^{-1}. Tests included uncoated and

aluminide and overlay coated < 100 > and < 111 > oriented specimens. A summary of test conditions and observed material properties is presented in Table 4. Additional tensile tests were conducted in the Option 1 program (see Section 11.2).

Some of the tensile test results can be understood by examining the fracture surfaces (Figure 18). Note that the faceting is quite pronounced at 760°C (1400°F), but as the temperature is increased to 1093°C (2000°F), the number of faceting planes increases dramatically and the fracture surface appears more normal to the tensile load. Also note that necking and the ductility of the specimens increase with temperature. All of these trends can be explained by the increase in the number of active slip systems with temperature.

3.3.4 Creep Properties

PWA 1480 Single Crystal

A total of 40 monotonic creep tests were conducted on PWA 1480 single crystal specimens with orientations of < 100 >, < 110 >, < 111 > and < 213 >. Tests were run at constant temperature and load conditions, and included uncoated and aluminide and overlay coated specimens. The test results were summarized in Table 5 and a discussion of the results was presented in Reference 2.

PWA 286 Overlay Coating

A summary of the test conditions and observed material properties is presented in Table 6. No previous creep experience was available with this material. The creep test conditions were set based on the limited stress relaxation tests conducted for the constitutive modeling effort. As a result, most tests required uploading or were discontinued before rupture.

SECTION 4.   TASK II – SELECTION OF CANDIDATE LIFE PREDICTION AND CONSTITUTIVE MODELS

4.1 SELECTION OF CONSTITUTIVE MODELS FOR COATINGS AND SINGLE CRYSTAL MATERIALS

Basic to life prediction for any structural component is the description of local stress–strain history. This necessitates availability of good constitutive models. As a gas turbine part is cycled through a wide range of stresses, strains, and temperatures, deformation and damage accumulate by a variety of mechanisms both in the single crystal alloy base material and the coating, all of which play a role in the component's ultimate failure. It is the goal of constitutive modeling to predict this stress–strain history so that the conditions at fatigue crack initiation are accurately known.

During the first year of this program, candidate constitutive models for the coatings and single crystal material were selected for evaluation (Reference 1). The selected models included:

1. Coatings

    a. Classical model   (uncoupled plasticity and creep, e.g. Reference 5)

    b. Walker's model   (unified viscoplastic, References 6 and 7)

    c. Simplified Walker's model   (no equilibrium stress term, Reference 1)

    d. Moreno's Simplified Approach   (hybrid model for Hastelloy X, Reference 8)

    e. Stowell equation   (based on self–diffusion mechanism, References 9–11)

2. Single Crystal Material

    a. Classical Hill model   (based on Von Mises yield function, Reference 12)

    b. Lee and Zaverl model   (macroscopic viscoplastic model, References 6 & 13)

    c. Micromechanical Viscoplastic Formulation   (extension of Walker's model to crystallographic deformation, References 6 and 14)

Detailed descriptions of these models and discussion of their selection were presented in Reference 1.

4.2 SELECTION OF LIFE PREDICTION MODELS

4.2.1 Literature Survey

In order to identify life prediction models which were applicable to coated anisotropic materials of gas turbine airfoils, a literature survey was conducted as part of the work reported in Reference 1. The survey resulted in an extensive listing of model concepts that have been used to match available data and meet specific needs of individual investigators.

Three broad classes of life models were available: phenomenological, cumulative damage, and crack growth.

A detailed discussion of individual model descriptions was presented in Appendix C of Reference 1.

4.2.2 Life Prediction Model Approach

Based on the literature survey (see e.g., References 15 to 20), previous Pratt & Whitney experience, and specimen tests conducted under this program, it was concluded that coatings have a role equally

important with that of the base material in determining turbine airfoil crack initiation life. Coatings, applied to the airfoil surfaces to provide oxidation protection, were found to serve as primary crack initiation sites at relevant turbine operating conditions. Thus, coatings were a major determinant of cracking location and life. Base material cracks subsequently develop from coating cracks and propagate to failure.

Base material cracking underneath the coating was also observed on coated single crystal specimens. Base alloy initiated cracks typically occurred when the base alloy was subjected to high stress levels and low strain levels such as under high temperature isothermal conditions for single crystal primary orientations which significantly deviate from <001>. Such orientations had high elastic modulus relative to <001> so that smaller strains introduced higher stresses. In some instances, coating cracks were observed along with base alloy initiated cracks, but they did not influence the specimen's fatigue life.

The large variety of cracking modes that were observed on anisotropic material test specimens indicated that a complex life prediction approach was required to determine when such materials will fail due to fatigue. For coated surfaces, the approach must include the capability to account for coating cracking, coating affected cracking of the base alloy and crack propagation in the base alloy. Base material crack initiation was a competing failure mode to coating cracking and required additional predictive capabilities. These included predicting crack initiation from three sources: macroscopic inelasticity, uncoated surface interaction with the environment, and microscopic defects (e.g., porosity).

The following overall life prediction approach was selected:

$$Nf = Nc + Nsc + Nsp \qquad (6)$$

$$\text{or} \qquad Nf = Nsi + Nsp, \text{ whichever is smaller,} \qquad (7)$$

where   Nf   =   Total cycles to failure.

          Nc   =   Cycles to initiate a crack through the coating.

          Nsc   =   Cycles for a coating crack to penetrate a small distance into the substrate (base alloy).

          Nsi   =   Cycles to initiate a substrate (base alloy) crack.

          Nsp   =   Cycles to propagate a substrate (base alloy) crack to failure.

In this program, crack initiation of coated nickel–based single crystal materials operating at relevant gas turbine airfoil conditions was addressed. As such, only the prediction of the cyclic life given by Nc and Nsc was considered.

4.2.3 Candidate Life Prediction Models

Coating Life (Nc):

Coatings undergo substantial inelastic deformation during typical gas turbine engine operation and coating cracking appears strongly related to such deformation.

Two candidate models for coating cracking life prediction were selected for evaluation. These were the Coffin–Manson model which relates life to inelastic strain and Ostergren's hysteretic energy model. An important ingredient for these models was that terms may be added to account for environmental degradation of the coatings.

Coffin–Manson (Reference 21):

$$\epsilon_{inel} \cdot N^{B1} = C1 \qquad (8)$$

Ostergren (Reference 22):

$$W_t \cdot N^{B2} = C2 \qquad (9)$$

where ϵ_{inel} = inelastic strain range

W_t = tensile inelastic hysteretic energy

N = cracking life, including cycle frequency correction for environmental exposure

B1, B2, C1, C2 = material constants

Phenomenological models were particularly appropriate for coating life prediction because structural modeling and experimental capabilities for coatings significantly lag those for structural materials. Coating microstructure and composition change with time as the coating is exposed to the severe turbine operating environment. As a result, the coating properties which affect coating fatigue life, such as thermal expansion, ductility, and creep resistance, are altered. To accommodate such behavior, complex life prediction models typically require material property information documenting the change in each coating property. Obtaining such information was beyond the available capabilities of specimen fabrication and experimentation for coatings. Thus, simple models which were able to include environmental effects were chosen in this program.

<u>Single Crystal Life (Nsc)</u>:

In order to extend isotropic material life prediction models to anisotropic materials such as single crystals, a method to account for material orientation effects was required. Similar to the methods for single crystal constitutive modeling, both macroscopic and micromechanical approaches were possible. The macroscopic approach describes anisotropy effects in terms of bulk material properties and observed loading response. The use of this approach generally assumes that the initiating crack orientation is known, usually normal to the applied load direction. The micromechanical approach utilizes material deformations at the slip level. Applied strains are resolved into components along the individual slip directions which depend on the material orientation. Fatigue life may then be related to the resulting slip plane stresses and strains.

Based on previous Pratt & Whitney experience and the fatigue data generated in this program, coated single crystal material initiates cracks normal to the loading direction. Crystallographic fatigue crack initiation, which would necessitate a micromechanical based model, was not observed for relevant gas turbine cyclic loading conditions. As a result, macroscopic based models were considered a good starting point from which to develop a single crystal life model.

At least one representative model from each class (phenomenological, cumulative damage, and crack growth) was selected for evaluation.

1. Coffin–Manson (Reference 21)

2. Modified Strain Model

3. Hysteretic Energy Approach (References 15 and 23)

4. Cyclic Damage Accumulation (CDA) (References 24 and 25)

5. Crack Tip Opening displacement (CTOD) (Reference 25)

Detailed descriptions of these models and discussion of their selection were presented in Reference 3.

SECTION 5. TASK III – LEVEL I EXPERIMENTS

5.1 COATING CONSTITUTIVE TESTS

Cyclic stress relaxation tests were conducted to determine the constitutive behavior for the coating systems selected in this program. A typical test cycle is presented in Figure 19.

In order to obtain data from coating specimens, significant development of testing techniques was required, including rig control improvements and extensometry development. Manual specimen loading was not adequate for maintaining constant strain rates. Also, maintaining constant strain hold periods during stress relaxation was difficult. For these reasons, computer controls were installed, making use of a test software package developed in a separate Pratt & Whitney program. Another concern was the method for obtaining deflection measurements from the PWA 273 specimens. Such a thin specimen could not support the extensometer hardware. Two externally supported extensometry setups were subsequently developed in another Pratt & Whitney program. The first extensometer concentrated on minimizing the extensometer loads on the specimen and resulted in the counter–balanced lever type extensometer shown in Figure 20. This extensometer was successfully used to gather data on the 0.25 mm (0.010 in.) thick specimens up to 982°C (1800°F). Unfortunately, at higher temperatures (or low loads), this extensometer tended to produce an irregular response due to motion at the pivot points. In the second extensometer setup, the pivot points were eliminated and the deflections were measured directly using an MTS extensometer (Figure 21). Specially designed double quartz rods were used to balance side forces on the specimen normally caused by the spring loaded extensometer rods. The results of the coating constitutive tests are presented in Appendices A, B and C.

5.2 SINGLE CRYSTAL CONSTITUTIVE TESTS

Cyclic tests were conducted to determine the constitutive behavior of PWA 1480. A typical specimen test consisted of fully reversed cycling over several strain ranges and, for the high temperature tests, several orders of magnitude in strain rate.

The test matrix is presented in Table 7. Test results are too voluminous for this report, but they are available from NASA Lewis in the form of raw load–deflection plots. Stress and strain conversion factors are noted on the cover sheet of each specimen test.

5.3 SINGLE CRYSTAL FATIGUE TESTS

5.3.1 Test Facility

The test facility used for isothermal and thermomechanical fatigue (TMF) tests consisted of a servo–controlled, closed loop hydraulic testing machine with MTS controllers, a low frequency (10 kHz) 20 kW TOCCO induction heater, and an Ircon model 7000 radiation pyrometer, calibrated over a temperature range of 260°C to 1371°C (500°F to 2500°F), for temperature measurement. Induction heating was selected to accommodate MTS external extensometry and to provide adequate heating rates. The quartz rods of the MTS extensometer, which define a 2.54 cm (1.0 in.) gage section, are spring loaded against the specimen and did not show signs of slippage during testing. A typical test setup is illustrated in Figures 22 and 23.

The internal and external extensometer setup shown in Figure 22 was used during initial fatigue tests to compare the two extensometers and gain experience with the external extensometer. The external extensometer was proven to provide better deflection measurements and was chosen as the sole deflection measurement device. A summary of the internal and external extensometer comparison study was given in Reference 2.

5.3.2 Fatigue Tests

Isothermal fatigue and TMF tests were conducted to define crack initiation life of coated PWA 1480 single crystal material and to provide data for initial life prediction model evaluations. All fatigue tests used the specimen geometry shown in Figures 8A or 8B. The latter design (denoted as 73C) relied

on an MTS extensometer for deflection measurement. Where necessary, the recorded deflections obtained from the internal extensometer in the 44C design were corrected by 2-D finite element analysis to be consistent with the MTS extensometry.

Level I tests were limited to key variables considered relevant to creep-fatigue and TMF life prediction. The variables included crystallographic orientation, coating, strain range, mean strain, strain rate, strain hold periods, and temperature. Tests were conducted using strain controlled conditions. A summary of Level I fatigue lives and specimen responses is presented in Appendices D and E.

The onset of coating cracking and crack propagation was monitored during each test by taking a series of acetate film surface replicas. Metallographic inspection of the tested specimens was performed at the conclusion of each test in order to interpret the replica data, characterize cracking patterns, and identify crack initiation sites. Specimen load, strain, and temperature histories were monitored during the course of testing to provide information useful for the modeling efforts. Typical isothermal and TMF specimen hysteresis loops and representative dislocation networks produced during TMF were presented in Reference 2.

In general, both PWA 286 overlay and PWA 273 diffusion aluminide coated specimens were found to develop coating cracks substantially before specimen failure. Subsequent metallographic inspection of failed specimens indicated that, in many specimens, the coating cracks had progressed into the PWA 1480 substrate and directly caused failure. However, in other specimens, the coating cracks did not extend into the PWA 1480 substrate, and the failure resulted from a competing crack which had initiated near to, or at, the uncoated ID of the specimen. In all cases, PWA 273 aluminide coating initiated cracks propagated into the PWA 1480 substrate. PWA 286 overlay coated specimens, however, did not propagate coating cracks into the PWA 1480 when the specimen was subjected to tensile stresses at high temperatures (1038°C isothermal or in-phase TMF). In such instances, ID cracks caused specimen failure, even though the overlay coating cracks developed early in the isothermal tests. Overlay coating cracks propagated into the PWA 1480 during low temperature isothermal LCF or out-of-phase TMF tests. Representative coating crack microphotographs are presented in Figure 24. In some other coated specimens, principly the <111> PWA 1480 coated specimens, subsurface crack initiation was observed.

To bookkeep all the observed crack initiation modes, the following nomenclature was adopted for identifying where the crack which led to specimen failure had initiated:

    c   = Coating

    cs   = Coating diffusion zone

    sc   = Coating-substrate interfacial region

    s   = Substrate (subsurface)

    ID   = Uncoated ID surface of the specimen

    IDc = Uncoated ID surface of the specimen; coating cracks observed along the OD surface

    IDs = Substrate (subsurface) initiation near the uncoated ID surface

    d   = Test discontinued with no observed cracks

    dc   = Test discontinued with coating cracks observed along the OD surface

    dcs = Test discontinued with cracks along the OD surface which initiated at the coating
            diffusion zone

    dsc = Test discontinued with cracks along the OD surface which initiated at the coating-
            substrate interfacial region

11

Examples of c, cs, sc, and s failure modes are presented in Figures 25 to 28.

Level I tests indicated that creep-fatigue and TMF life is dependent on several factors: 1) the presence of a coating, 2) the coating composition and microstructure, 3) single crystal orientation, and 4) the cyclic strain-temperature-time relationship (i.e., the cyclic loading history). And, of those variables encompassed by cyclic loading history, mean strain appeared to be the least significant. Observations made during the Level I experiments reinforced the need for constitutive and life models for coating materials and verified the chosen life approach (Section 4.2.2). Discussions of critical experiments conducted to define important fatigue attributes were presented in References 1 to 3.

SECTION 6. TASK IV – CORRELATION OF MODELS WITH LEVEL I EXPERIMENTS

6.1 OVERLAY COATING CONSTITUTIVE MODEL

Evaluation results of the five candidate coating constitutive models (see Section 4.1) were presented in References 2 and 3. Discussion of the final overlay coating constitutive model is presented in Section 8.1.

6.2 SINGLE CRYSTAL CONSTITUTIVE MODEL

Evaluation results of the three candidate single crystal constitutive models (see Section 4.1) using PWA 1480 isothermal data were presented in Reference 2. Discussion of the final single crystal constitutive model is presented in Section 8.2.

6.3 COATED SINGLE CRYSTAL LIFE PREDICTION MODELING

Fatigue life for coated single crystal materials was defined as follows (see Section 4.2.2):

$$Nf = Nc + Nsc + Nsp \tag{10}$$

$$\text{or} \quad Nf = Nsi + Nsp, \text{ whichever is smaller,} \tag{11}$$

where Nf = Total cycles to failure.

Nc = Cycles to initiate a crack through the coating.

Nsc = Cycles for a coating crack to penetrate a small distance into the substrate (base alloy).

Nsi = Cycles to initiate a substrate (base alloy) crack.

Nsp = Cycles to propagate a substrate (base alloy) crack to failure.

The choice of coating crack initiation (Nc) was based on experimental observations and the practical limitation of the acetate film inspection technique. Acetate replicas of surface cracks during TMF tests and the post–test crack morphology exams together indicated that coating cracks rapidly penetrate through the coating. Also, crack depths less than ½ to 1 coating thickness (about 0.08 mm (0.003")) were difficult to replicate and were considered at the limit of acetate film replica resolution.

Substrate cracking (Nsc or Nsi) included short crack behavior. For engineering purposes, a crack size which is easily inspected in a component is desirable. This translated to a surface crack size of about 0.76 mm (0.031 in.). Thus, the depth of penetration into the substrate was selected to be 0.254 mm (0.010 in.) so that the overall surface crack length would approximate 0.76 mm (0.031 in.) for a 2.0 aspect ratio thumbnail crack in a specimen with a 0.127 mm (0.005 in.) coating.

Modeling of substrate crack initiation life (Nsi) or substrate crack propagation life (Nsp) was not addressed in this program.

6.3.1 Overlay Coating Life Model

Evaluation results of the two candidate coating life models (see Section 4.2.3) were presented in Reference 3. Discussion of the final overlay coating life model is presented in Section 8.3.1.

6.3.2 Single Crystal Life Models (Coated)

Five life models were applied to an isothermal data base consisting of PWA 273 coated PWA 1480 crack initiation lives at 927°C (1700°F).

13

1) Coffin–Manson $$N = A\Delta\epsilon_{in}^B \tag{12}$$

2) Crack Tip Opening Displacement (CTOD): $$N = A(\sigma_t^2/E\sigma_y)^B \tag{13}$$

3) Modified Strain: $$N = A(\Delta\epsilon\ E/2)^B \tag{14}$$

4) Ostergren: $$N = A(\sigma_t\ \Delta\epsilon_{in})^B \tag{15}$$

5) Hysteretic Energy Approach : $$N = A\left[\sigma_t\ \Delta\epsilon_{in}\ \frac{\Delta\sigma_{[111]}}{E} \right]^B \tag{16}$$

where:

σ_t	=	Specimen tensile stress
σ_y	=	0.2% PWA 1480 yield stress
$\Delta\epsilon_{in}$	=	Specimen inelastic strain range
E	=	PWA 1480 elastic modulus parallel to specimen loading direction
$\Delta\epsilon$	=	Specimen total (mechanical) strain range
$\Delta\sigma_{[111]}$	=	PWA 1480 resolved maximum octahedral normal stress range

The model correlations were presented in Reference 3.

Of the five models considered, the Hysteretic Energy Approach, Ostergren, and Coffin–Manson models were the most promising for correlating isothermal fatigue life data when measureable inelastic strains were present.

This program, however, emphasized life prediction of TMF cycles. As such, selection of life prediction models for PWA 1480 was deferred until sufficient TMF life data from all four orientations was available from the Level II experiments. The remainder of the PWA 1480 life model development effort in this task was devoted to developing a process by which accurate PWA 1480 life data may be obtained from the tested specimens.

PWA 1480 Single Crystal Life Determination

Specimen failures caused by cracking were observed at several locations depending on the test temperatures and loads and specimen orientation. A description of each failure location is presented below:

gag	=	Specimen failed inside the 2.54 cm (1.0 in.) extensometer monitored gage section.
but	=	Specimen failed at the specimen buttonhead grip fillet.

ext	=	Specimen failed from crack which initiated underneath the MTS extensometer quartz rods.
IDr	=	Specimen failed from the ID surface near the ID ridge region (44C specimen design only).
gagr	=	Specimen failed inside the monitored gage section near the ID ridge region (44C specimen design only).
ogag	=	Specimen failed outside the monitored gage section, but within the constant cross-section portion of the specimen.

"IDr" and "gagr" type of failures were limited to certain 44C specimen tests conducted in the Level I experiments. Only cracks which initiated along the OD surface, away from the extensometer rods, and inside the constant cross-section portion of the specimen were considered useful for life prediction modeling of Nc and Nsc. Other cracks which appeared outside this restriction were not evaluated.

Several methods were identified and used to obtain PWA 1480 crack initiation life, Nsc or Nsi, from the coated specimens. A particular method was chosen for each specimen based on its observed cracking behavior. A synopsis of when and how each method was applied is presented below. Slight modifications to these basic methods were considered when specimen information was limited.

Case 1 – "Classical" Cracking

In this case, crack geometry was typically thumbnail in nature and OD surface replicas were used to establish PWA 1480 crack initiation life. This type of crack geometry is shown in Figure 29A.

Method 1 : Obtain crack aspect ratio (length/depth) from fractographic analysis.

- Enter surface crack length versus cycle number curve at crack length of: (crack aspect ratio)*(crack depth); Crack depth = coating thickness + 0.254 mm (0.010 in.).

- Replica data may be prudently extrapolated.

- See Figure 30.

Case 2 – "Non-Classical" Cracking

Coating cracks grew along the specimen circumference and minimally penetrated into the substrate or appearred as "ring" cracks. These types of cracks are shown in Figure 29B. Long OD surface cracks observed on replicas were, therefore, not indicative of substrate cracking. As such, it was considered reasonable to determine lower and upper bounds on life (Nmin and Nmax) between which the actual life lies.

Nmin	=	Lower life bound = Nc + Nsc (lower bound)
Nmax	=	Upper life bound = Nc + Nsc (upper bound)
Nc	=	Coating life

Method 2 : For a primary gage section crack that penetrates less than 0.254 mm (0.010 in.) into the substrate.

- Set Nmin = cycle number which generated the small crack.

- Obtain estimate of substrate crack aspect ratio from fractographic analysis.

- Draw a straight line from the replica data curve at the point where Nc occurs through the known crack length (crack aspect ratio * known crack depth), Nmin point.

- Extrapolate the straight line to the desired crack length and pick off Nmax.

- See Figure 31.

Method 3 : For a primary gage section crack that penetrates more than 0.254 mm (0.010 in.) into the substrate.

- Determine number of cycles (typically Nf) to a known crack depth and crack aspect ratio by using fracture photos.

- Plot the known crack surface length (crack aspect ratio * known crack depth), cycle number point together with the specimen replica data.

- Extrapolate replica data curve beyond the last replica data point. Note: This extrapolated curve will rarely pass through the known crack size, cycle point.

- Draw a straight line from the replica data curve at the point where Nc occurs to the known crack size, cycle point.

- Pick Nmin off the straight line at a surface crack length equal to the (crack aspect ratio)*(desired crack depth).

- If Nmin is less than would be obtained by using the extrapolated replica data curve, redetermine Nmin from the extrapolated replica data curve.

- Translate extrapolated replica data curve so that it passes through the known crack size, cycle point.

- Pick Nmax off the translated replica data curve in the same manner as Nmin was picked.

- See Figures 32 and 33.

Method 4 : Check of Nmax obtained by Methods 2 and 3.

- Using plot of specimen stress range versus cycle number, determine cycle number at which load range drop initiates (Nld), see Reference 26.

- If Nld < Nmax ; Nmax = Nld.

- See Figure 34.

SECTION 7. TASK V – LEVEL II SINGLE CRYSTAL EXPERIMENTS

Isothermal fatigue and TMF tests were conducted to define the crack initiation life of coated PWA 1480 single crystal material in order to verify Level I data trends and increase the database for life model selection and development.

All fatigue tests used the specimen geometry shown in Figure 8B.

The test facility used for Level II experiments was identical to that used in the Level I experiments (see Section 5.3).

The specimen and fatigue test variables considered for Level II experiments included thermal exposure in addition to those variables considered in the Level I tests (see Section 5.3).

The onset of coating cracking and crack propagation was monitored during each test by taking a series of acetate film surface replicas. Metallographic inspection of the tested specimens was performed at the conclusion of each test in order to interpret the replica data, characterize cracking patterns, and identify crack initiation sites. Specimen load, strain, and temperature histories were monitored during the course of testing to provide information useful for the modeling efforts.

7.1 UNIAXIAL FATIGUE TESTS

A summary of Level II uniaxial fatigue lives and specimen responses is presented in Appendices D and E.

Level II tests confirmed that coated PWA 1480 single crystal creep–fatigue and TMF life is dependent on several factors: 1) the presence of a coating, 2) the coating composition and microstructure, 3) single crystal orientation, and 4) the cyclic strain–temperature–time relationship (i.e., the cyclic loading history). In addition, thermal exposure effects were shown to be important.

The effect of cyclic history on coated TMF life was confirmed during Level II experiments and was consistent with the results of the Reference 23 program. PWA 286 overlay coated <111> PWA 1480 specimens LB–32 and LB–29 were TMF tested using the "baseball" cycle shown in Figure 35 to verify the data trend observed from aluminide coated specimens LB–21 and LB–156. Specimen LB–32 was cycled in a counter–clockwise (ccw) direction and LB–29 was cycled in a clockwise (cw) direction. Stabilized hysteresis loops for LB–29 and LB–32 were practically identical to those presented in Figures 36 and 37 for specimens LB–156 and LB–21, respectively. Specimen LB–29 (cw cycle) crack initiation and failure lives were 2600–3200 and 3773 cycles while the crack initiation life for specimen LB–32 was >11852 cycles. At 11852 cycles no cracks were observed on LB–32 and the test was discontinued.

PWA 286 overlay coated <111> PWA 1480 specimens LB–26 and LB–30 confirmed the importance coatings play in fatigue crack initiation. Specimen LB–30 was isothermally fatigued at 427°C (800°F), ±0.25% strain at 10 cpm. Specimen LB–26 was TMF tested at ±0.25% strain using the "T–cycle" strain–temperature cycle shown on the first page of Appendix D. The associated crack initiation and failure lives of these two specimens were >7130 and 7130 for LB–30 and >3260 and 3532 for LB–26. Specimen LB–30 failed at the specimen buttonhead grip fillet at 7130 cycles and no cracks were observed in the gage section. Specimen LB–26 failed from a crack underneath the extensometer quartz rods and small cracks were observed in the gage section which penetrated the coating at 2560 cycles and minimally penetrated into the PWA 1480 substrate. Further discussion of the "T–cycle" was presented in Reference 3.

A coating spalling failure mode in which the coating is liberated from the substrate may occur when the coating undergoes severe compressive deformation. Specimen JB–102 was TMF tested using a counter–clockwise baseball cycle at 427–1038°C (800–1900°F), ±0.4%, 1 cpm. Note that this specimen previously ran roughly 41000 cycles at 800°F, ±0.3%, 8 cpm. Although JB–102 failed from a crack which initiated at the uncoated ID surface, the coating surface was littered with cracks which were inclined roughly 45° to the loading axis. A transverse coating micrograph is presented in Figure

17

38. Acute coating rumpling and cracks tending to propagate parallel to the interface were the dominant features. The coating cracks were apparently due to shear, not tensile forces. Severe compressive nonlinear coating behavior was predicted by the PWA 286 overlay coating constitutive model, thus activating the shear failure mode. In addition, the predicted level of coating compressive stress introduces a significant tensile radial stress component in the tube specimen at the coating–substrate interface. It is believed that this radial stress influenced the crack trajectory, forcing it to turn along the interface. Coating spalling was observed for aluminide coated PWA 1480 specimens undergoing similar test conditions in the Reference 23 program. Final fracture was crystallographic in nature indicating that the PWA 1480 load levels were not generally relevant to gas turbine airfoils. However, the interesting failure of JB–102 indicates that multiple failure modes are possible in coatings. This places limits on the realistic extrapolation capability of the coating life models developed for cracks normal to the loading direction (i.e., typical Mode I cracks).

Numerous coated non-<001> oriented PWA 1480 specimens tested under isothermal conditions failed from PWA 1480 porosity adjacent to the coating or uncoated ID surface. Examples of crack initiation sites from such specimens are presented in Figures 39 to 41. Contrary to that experience, out–of–phase TMF tests produced failures which originated from coating cracks in a manner consistent with Pratt & Whitney's experience with coated single crystal airfoils. Typical TMF failures are presented in Figures 42 to 44.

7.2 EFFECT OF THERMAL EXPOSURE ON FATIGUE LIFE

A total of 12 coated PWA 1480 specimens were pre–exposed 100 hours at 1093°C (2000°F) before testing to determine the significance of thermal exposure on coated fatigue life. A summary of these test results are included in Appendices D and E.

7.2.1 Coating Materials

TMF coating lives for the pre–exposed specimens is presented in Figures 45 and 46. PWA 286 overlay coating out–of–phase TMF life was not significantly affected by the pre–exposure. Baseline PWA 273 aluminide TMF data is limited. However, the life trend suggests that pre–exposure was detrimental.

Insufficient information exists from which to conclude what specific physical mechanism causes the observed life trends. It is speculated, however, that the composition and microstructure evolution which occurs as a result of high temperature exposure is the main cause.

Coatings, by their very nature, are not stable alloys. High temperature exposure causes diffusion of aluminum towards the surface for oxidation protection and into the substrate. Depletion of aluminum precipitates formation of gamma prime and/or gamma matrix in the coating, principly at coating grain boundaries. Coating micrographs from pre–exposed specimens JB–133 and JB–154 are compared to non–pre–exposed micros from specimens JB–147 and JB–98 in Figures 47 and 48. As a result of these coating compositional and microstructural changes which occur during exposure, coating constitutive behavior and properties such as ductility and coefficient of thermal expansion are different than those obtained from virgin specimens.

One factor which may play a significant role is thermal expansion (see Figure 49). A NiCoCrAlY overlay coating is composed of aluminum rich beta (NiAl) and the heavier elemental gamma phases. This is a much more stable composition and microstructure than in an aluminide which is initially composed of the beta phase. As diffusion occurs, more gamma phase is formed in both coatings, but the potential gradient for diffusion is higher in the aluminide than the overlay. Since gamma phase is generated, it is anticipated that the coefficient of thermal expansion increases for both coatings, but more rapidly in the aluminide. This suggests that the life of an aluminide is more sensitive to exposure than that of an overlay for certain TMF cycle types.

An increase in coating coefficient of thermal expansion is detrimental to coating life in cases when tensile straining is occurring during cooling (i.e., out–of–phase TMF). In such cases, higher tensile strains (or stresses) are produced. Aluminides, which have limited ductility at low temperatures, would be sensitive to such cases. For discussion purposes, hysteretic energies for the aluminide

coating were generated using the PWA 286 overlay coating constitutive model with the aluminide coefficient of thermal expansion (i.e., unexposed coating coefficient of thermal expansion). The resulting life relationship for 427-1038°C (800-1900°F) out-of-phase TMF is presented in Figure 50. As shown in this figure, arbitrarily increasing the coefficient of thermal expansion by 10% produces a significant increase in hysteretic energy and nearly a 7X life reduction.

7.2.2   PWA 1480 Single Crystal Material

The crack initiation (N_{sc}) and propagation (N_{sp}) lives for the pre-exposed specimens subjected to TMF are compared to TMF tested non-pre-exposed specimens in Figures 51 and 52, respectively. In general, the pre-exposure was found to be somewhat more detrimental to the propagation life than the crack initiation life. This observation suggests that the crack propagation rate of PWA 1480 (associated with N_{sp}) is more sensitive to thermal exposure than PWA 1480 crack initiation. However, the shorter pre-exposed specimen propagation lives were generally associated with crack geometries which generate high values of stress intensities. Thus, it is felt that the pre-exposure had little overall effect on PWA 1480 TMF life.

SECTION 8. TASK VI – FINAL SELECTION OF LIFE PREDICTION AND CONSTITUTIVE MODELS

8.1 OVERLAY COATING CONSTITUTIVE MODEL

8.1.1 Final Model Formulation

Based on overall correlation and prediction capabilities as well as ease of incorporation into a finite element code, the Walker model was selected as the final overlay coating constitutive model (References 2 and 3).

Final coating constitutive model selection was based on the second series of overlay coating stress relaxation experiments conducted at the United Technologies Research Center (UTRC) and shown in Appendix B. The results of these experiments were considered superior to the first series of tests which are shown in Appendix A. However, the data used at 427°C (800°F) was from the first series of experiments, not the second, because the second series specimen at 427°C (800°F) broke at the specimen grip before any inelastic activity was observed. This test is included as part of Appendix B.

The Walker model utilized, presented in one–dimensional form below, was the differential form of the Hastelloy X model discussed in Reference 6.

$$\epsilon = \frac{\sigma}{E} + \epsilon_{in} \tag{17}$$

$$\dot{\epsilon}_{in} = \left(\frac{\sigma - \Omega}{K} \right)^n \tag{18}$$

$$K = K_1 - K_2 \exp\left(-n_7 R\right) \tag{19}$$

$$\dot{\Omega} = (n_1 + n_2)\, \dot{\epsilon}_{in} + \epsilon_{in} \frac{\partial n_1}{\partial T}\, \dot{T} - (\Omega - \Omega_0 - n_1 \epsilon_{in}) \left(\dot{G} - \frac{1 \partial n_2}{n_2 \partial T}\, \dot{T} \right) \tag{20}$$

$$\dot{G} = (n_3 + n_4 \exp(-n_5 R))\, \dot{R} + n_6 (\Omega - \Omega_0 - n_1 \epsilon_{in})^{m-1} \tag{21}$$

$$\dot{R} = |\dot{\epsilon}_{in}| \tag{22}$$

Material constants: E, Ω_0, n, m, n1, n2, n3, n4, n5, n6, n7, K1, K2, depend on temperature, T.

Interpolation and extrapolation of model constants was performed to produce consistent tensile behavior throughout a 427–1204°C (800–2200°F) temperature range. A summary of regressed Walker model constants for unexposed, bulk HIP PWA 286 overlay coating is presented in Table 8.

Poisson's ratio for PWA 286 was assumed equivalent to Hastelloy X. Based on the observed inelastic flow similarity between PWA 286 and Hastelloy X, Poisson's ratio for PWA 286 was obtained from Reference 6.

Correlation of the 649°C (1200°F) stress relaxation test from the second test series by the Walker model is presented in Figure 53. Overall, the Walker model correlates this data set reasonably well and is able to fit the positive stress relaxation trend.

Walker model prediction of the response of an unexposed, bulk HIP PWA 286 coating specimen tested using an out–of–phase TMF waveform is presented in Figure 54. Again, the Walker model is reasonably able to duplicate the observed behavior. The Walker model does overpredict the maximum tensile stress, however, it is able to predict the graceful tensile yielding trend. Note that the second cycle maximum compressive stress is also overpredicted. This was not expected since the model fit the baseline relaxation rates well.

A summary of predicted secondary creep rates versus data is presented in Table 9. The secondary creep rates were generally overpredicted. Coatings do not elongate in gas turbine applications because the substrate material constrains the coating creep extension. As such, the inability to predict long term creep rates should not restrict the model. Walker model predicted creep strain versus creep data is presented in Figure 55. Note that the primary creep regime (i.e., for times less than 15 minutes) was fairly well duplicated by the Walker model. Times up to 15 minutes are consistent with the maximum strain hold time present in the baseline stress relaxation experiments.

8.1.2 Computer Software Development

Checkout of the MARC (Reference 27) user subroutine HYPELA was completed for isothermal cases and MARC element types 7 and 21 (3D "brick" elements). As part of the checkout process, a study of the "reference" stiffness matrix concept (Reference 28) was conducted. A detailed description of the "reference" stiffness matrix concept is presented in Section 8.2. Results indicated that reassembly of the stiffness matrix is necessary for this material. In fact, cases in which the temperature was not equivalent to the reference temperature (temperature at which the reference stiffness matrix was formed) failed to converge.

Every convergence strategy available in the MARC version K.1 was considered, but none was successful. Evidently, this material's stiffness variation across the relevant temperature range is too great to use the reference stiffness matrix concept. Presumably, after a few attempts, an adequately small MARC increment size could be chosen to obtain convergence. However, the associated cost of conducting coated component analyses in such a manner is probably higher than the cost to reassemble the stiffness matrix.

A check on the effective inelastic strain increment size was included in the PWA 286 MARC HYPELA routine to prevent non–convergence during stress relaxation. Previously, PWA 286 HYPELA subincrement step size determination was based solely on mechanical strain, temperature, or time MARC increments only. During isothermal stress relaxation, however, strain and temperature increments are zero and the number of subincrements obtained from the time increment criterion is too small. This results in MARC convergence failure. Currently, when the effective inelastic strain increment size limit is exceeded, the number of subincrements is recalculated and the MARC increment is recycled through the subincrement loop. The effective inelastic strain increment size limit and the maximum number of subincrements allowed are user defined variables.

8.2 SINGLE CRYSTAL CONSTITUTIVE MODEL

The micromechanical model was selected as the final single crystal constitutive model. A discussion of candidate model formulations and correlations of PWA 1480 isothermal hysteresis loop data was reported in Reference 2.

8.2.1 Metallurgical Background for Micromechanical Model

The cast single crystal nickel–base superalloy PWA 1480 has been under development at Pratt & Whitney for nearly 15 years and has been successfully tested as a blade alloy in both commercial and military engines. Other single crystal alloys such as the General Electric alloy Rene–N4 and the Canon–Muskegon alloy CMSX–2 are also being used in gas turbine engines. These alloys were developed in order to eliminate the grain boundaries which are present in conventionally cast equiaxed polycrystalline superalloys, and which are susceptible to grain boundary corrosion, cracking, and creep deformation. In alloy PWA 1480 the normal grain boundary strengthening elements (hafnium, carbon, boron, and zirconium) have been deleted. These elements are also melting point depressants and without them the single crystal alloy PWA 1480 has an incipient melt temperature above 1300°C (2372°F). This allows nearly complete γ' solutioning during heat treatment and a reduction in dendritic segregation. The absence of grain boundaries, the opportunity for full solution heat treatment, and the reduced dendritic segregation after heat treatment have resulted in single crystal alloys with significantly improved properties over conventionally cast blade materials.

Single crystal nickel–base superalloys are essentially two–phase composite materials (Reference 29) consisting of a large volume fraction ($\sim$60% to 65%) of intermetallic γ' precipitates having the $L1_2$ crystal structure (Reference 30) interspersed in a coherent face–centered cubic γ solid solution nickel matrix. In the heat treated condition the γ' precipitates to form periodic three–dimensional arrays of cuboidal particles immersed in the γ matrix of face–centered nickel material, with the cuboid edges aligned along the (001) directions of the γ and γ' phases.

Recent evidence suggests that the deformation behavior of the γ–γ' composite single crystal alloy is governed largely by the behavior of the $L1_2$ ordered γ' phase. A summary of the constitutive behavior of pure γ' Ni_3Al material which has the $L1_2$ crystal structure has been presented in the review paper by Pope and Ezz in Reference 30. They state that little is known regarding its creep behavior, but a fairly complete concensus of opinion about its flow stress behavior has been compiled. They also point out that Ni_3Al γ' material exhibits an anomalous increase of flow stress with increasing temperature up to about 760°C (1400°F) after which the flow stress rapidly decreases with further temperature increases. In two–phase γ–γ' alloys this behavior is rationalized on the basis of cross–slip of screw dislocations from the octahedral crystallographic slip planes to the cube slip planes when dislocation pairs enter and shear the γ' precipitates. Shearing of the γ' precipitates, rather than dislocation bowing around the γ' precipitates, occurs due to the high volume fraction (65%) of precipitate particles. Dislocations travel in pairs because single dislocations on the octahedral planes create an Antiphase Boundary (APB) trail where atoms of the structure are out–of–phase with each other. The energy associated with this APB is removed by the passage of another dislocation, which leaves a trail in which the atoms in the structure are in–phase with each other. Dislocations are therefore attracted to each other in pairs, in which there is an APB between each dislocation pair. The APB energy is anisotropic, being smaller on the cube planes than on the octahedral planes. Screw dislocations thus tend to cross–slip from the octahedral planes where the APB energy is high to the cube planes where it is low. As the octahedral dislocations enter the γ' particles they cross–slip onto the cube planes and are prevented from further motion by a pinning process (Reference 30). This pinning of the screw dislocations on the cube planes impedes the motion of the primary octahedral screw dislocations and raises the flow stress in the octahedral system. The octahedral flow stress thus increases with temperature since the rate at which the screw dislocations cross–slip and become pinned is governed by a diffusive process which increases with temperature.

Takeuchi and Kuramoto (Reference 31) proposed a theory for the anomalous increase of flow stress with temperature based on this diffusive cross–slip behavior, and the theory was refined by Lall, Chin and Pope (Reference 32). In the latter theory the octahedral $(a/2)[\bar{1}01]$ dislocation is an extended dislocation (Reference 33) consisting of two Shockley partial dislocation pairs, $(a/6)[\bar{2}11] + (a/6)[\bar{1}\bar{1}2]$, separated by a stacking fault. In order to slip the pair must constrict into a single $(a/2)[\bar{1}01]$ dislocation. The constriction is aided by a shear stress on the (111) plane in the $[1\bar{2}1]$ direction, whereas a shear stress in the opposite direction extends the dislocation pair and tends to inhibit cross–slip. This "core–width effect" gives rise to the tension–compression asymmetry observed in $L1_2$

crystal alloys. In recent work Paidar, Pope, Vitek and Umakoshi (References 34 and 35) have noted that the tension–compression asymmetry disappears, according to the theory of Lall, Chin and Pope, on the $[012]-[\bar{1}13]$ great circle in the standard $[001]-[011]-[\bar{1}11]$ stereographic triangle. However, experimental work shows that the tension–compression asymmetry disappears to the left of the $[012]-[\bar{1}13]$ great circle in the standard stereographic projection, and Paidar, Pope and Vitek (Reference 34) have modified the Lall, Chin and Pope approach (Reference 32) to account for this effect by incorporating work originally due to Escaig (Reference 36) in their flow stress model. Below a temperature of 760°C (1400°F) the flow stress of pure Ni_3Al γ' material increases with increasing temperature due to the pinning of screw dislocations on the cube planes, but the overall macroscopic deformation is due to octahedral slip. No macroscopic cube slip is evident. However, above the peak temperature of 760°C (1400°F) the flow stress rapidly decreases with increasing temperature when large amounts of macroscopic cube slip occur in the γ' material. For [001] orientated specimens no cube slip can occur and it is probable that the flow stress decreases with increasing temperature when the screw dislocations which have become pinned on the $\{100\}$ cube planes by cross–slip from the $\{111\}$ octahedral planes become unpinned (References 34 and 37 to 39) as soon as they are formed and cross–slip back to the $\{111\}$ octahedral planes.

8.2.2 Single Crystal Micromechanical Model Formulation

Constitutive modelling of nickel–base single crystal superalloys began with the work of Paslay, Wells and Leverant (Reference 39) in 1970. They proposed a theoretical formulation of steady state creep deformation based on crystallographic slip theory of face–centered cubic materials. In 1971 the theory was applied by Paslay, Wells, Leverant and Burck (Reference 40) to describe the creep behavior of single crystal nickel–base superalloy tubes under biaxial tension. Steady state creep formulations suitable for the analysis of single crystals were used by Brown (Reference 41) in 1970 and by Hutchinson (Reference 42) in 1976 to predict the behavior of polycrystalline materials whose aggregate consists of randomly orientated single crystal grains. Recently, Weng (Reference 43) has developed a single crystal creep formulation which accounts for transient (primary) as well as steady state (secondary) creep. However, in order to describe the combined plastic and creep behavior of polycrystalline materials, Weng combines the rate–independent plastic and rate–dependent creep components in such a way that each component is governed by a separate constitutive relation; that is, plasticity and creep are assumed to be uncoupled phenomena.

In the decade of the seventies the creep and plastic responses of materials were combined into unified viscoplastic formulations (References 6, 7 and 44 to 48). These formulations differ from steady state creep theories by introducing history dependent state variables to account for primary creep and plasticity, A single crystal formulation which accounts for the time–dependent viscoplastic behavior of materials at elevated temperature can therefore be constructed by incorporating the steady state crystallographic creep model presented by Paslay, Wells, and Leverant (Reference 39) into a unified viscoplastic formulation. The Takeuchi–Kuramoto cube cross–slip mechanism (Reference 31) and the Lall, Chin, and Pope (References 32, 34, 35 and 37) Shockley partial tension–compression flow stress asymmetry mechanism may then be incorporated into the drag stress state variable of the unified viscoplastic constitutive formulation.

In order to model the constitutive behavior of single crystal superalloys it is necessary to include both octahedral and cube crystallographic slip systems in the viscoplastic formulation. In the unit cell of the face–centered cubic crystal we denote by $\bar{m}_r^0$ a unit vector in the rth slip direction (of type (110)), whilst $\bar{n}_r^0$ is a unit vector in the normal direction to the slip plane (of type $\{111\}$) of which $\bar{m}_r^0$ constitutes a slip direction. The four octahedral $\{111\}$ planes and the twelve corresponding (110) slip directions (three on each plane) are shown in Figure 56. To each of the unit vectors $\bar{m}_r^0$ and $\bar{n}_r^0$ in the rth slip system there correspond perpendicular unit vectors, $\bar{z}_r^0$, given by $\bar{z}_r^0 = \bar{m}_r^0 \times \bar{n}_r^0$. The vector $\bar{z}_r^0$ corresponds to the octahedral (112) type slip directions and lies in the slip plane containing the vector $\bar{m}_r^0$, and the vectors $\bar{m}_r^0, \bar{n}_r^0, \bar{z}_r^0$ form an orthogonal triad of unit vectors for the rth octahedral slip system. The corresponding unit vectors for the cube slip planes are denoted by $\bar{m}_r^c$ and $\bar{n}_r^c$, where

the three cube {100} planes and the six corresponding (110) slip directions (two on each plane) are shown in Figure 57.

From the crystal geometry in Figure 56 the twelve unit vectors for the octahedral slip system are given by

$$\bar{m}_1^0 = (\bar{i} - \bar{k})/\sqrt{2}, \quad \bar{m}_2^0 = (-\bar{i} + \bar{j})/\sqrt{2}, \quad \bar{m}_3^0 = (-\bar{j} + \bar{k})/\sqrt{2}, \quad \bar{m}_4^0 = (\bar{j} - \bar{k})/\sqrt{2},$$

$$\bar{m}_5^0 = (-\bar{i} - \bar{j})/\sqrt{2}, \quad \bar{m}_6^0 = (\bar{i} + \bar{k})/\sqrt{2}, \quad \bar{m}_7^0 = (-\bar{i} - \bar{k})/\sqrt{2}, \quad \bar{m}_8^0 = (\bar{i} - \bar{j})/\sqrt{2}, \tag{23}$$

$$\bar{m}_9^0 = (\bar{j} + \bar{k})/\sqrt{2}, \quad \bar{m}_{10}^0 = (-\bar{j} - \bar{k})/\sqrt{2}, \quad \bar{m}_{11}^0 = (\bar{i} + \bar{j})/\sqrt{2}, \quad \bar{m}_{12}^0 = (-\bar{i} + \bar{k})/\sqrt{2},$$

with unit normals

$$\bar{n}_1^0 = \bar{n}_2^0 = \bar{n}_3^0 = (\bar{i} + \bar{j} + \bar{k})/\sqrt{3}, \qquad \bar{n}_4^0 = \bar{n}_5^0 = \bar{n}_6^0 = (-\bar{i} + \bar{j} + \bar{k})/\sqrt{3},$$

$$\tag{24}$$

$$\bar{n}_7^0 = \bar{n}_8^0 = \bar{n}_9^0 = (-\bar{i} - \bar{j} + \bar{k})/\sqrt{3}, \qquad \bar{n}_{10}^0 = \bar{n}_{11}^0 = \bar{n}_{12}^0 = (\bar{i} - \bar{j} + \bar{k})/\sqrt{3},$$

and corresponding perpendicular vectors

$$\bar{z}_1^0 = (\bar{i} - 2\bar{j} + \bar{k})/\sqrt{6}, \quad \bar{z}_2^0 = (\bar{i} + \bar{j} - 2\bar{k})/\sqrt{6}, \quad \bar{z}_3^0 = (-2\bar{i} + \bar{j} + \bar{k})/\sqrt{6},$$

$$\bar{z}_4^0 = (2\bar{i} + \bar{j} + \bar{k})/\sqrt{6}, \quad \bar{z}_5^0 = (-\bar{i} + \bar{j} - 2\bar{k})/\sqrt{6}, \quad \bar{z}_6^0 = (-\bar{i} - 2\bar{j} + \bar{k})/\sqrt{6},$$

$$\tag{25}$$

$$\bar{z}_7^0 = (-\bar{i} + 2\bar{j} + \bar{k})/\sqrt{6}, \quad \bar{z}_8^0 = (-\bar{i} - \bar{j} - 2\bar{k})/\sqrt{6}, \quad \bar{z}_9^0 = (2\bar{i} - \bar{j} + \bar{k})/\sqrt{6},$$

$$\bar{z}_{10}^0 = (-2\bar{i} - \bar{j} + \bar{k})/\sqrt{6}, \quad \bar{z}_{11}^0 = (\bar{i} + \bar{j} - 2\bar{k})/\sqrt{6}, \quad \bar{z}_{12}^0 = (\bar{i} + 2\bar{j} + \bar{k})/\sqrt{6},$$

where $\bar{i}, \bar{j}, \bar{k}$, are unit vectors along the x, y, z, crystallographic axes. The six corresponding unit vectors for the cube slip system are given by

$$\bar{m}_1^\varsigma = (\bar{i} + \bar{j})/\sqrt{2}, \quad \bar{m}_2^\varsigma = (-\bar{i} + \bar{j})/\sqrt{2}, \quad \bar{m}_3^\varsigma = (\bar{i} + \bar{k})/\sqrt{2},$$

$$\tag{26}$$

$$\bar{m}_4^\varsigma = (-\bar{i} + \bar{k})/\sqrt{2}, \quad \bar{m}_5^\varsigma = (\bar{j} + \bar{k})/\sqrt{2}, \quad \bar{m}_6^\varsigma = (-\bar{j} + \bar{k})/\sqrt{2},$$

with unit normals

$$\bar{n}_1^c = \bar{n}_2^c = \bar{k}, \quad \bar{n}_3^c = \bar{n}_4^c = \bar{j}, \quad \bar{n}_5^c = \bar{n}_6^c = \bar{i}. \tag{27}$$

Figure 58 shows a single crystal bar specimen whose global axes are denoted by x^*, y^*, z^* and whose crystallographic axes are denoted by x, y, z. If Q_{ij} denotes the orthogonal tensor which rotates the crystallographic (unstarred) axes into the global (starred) axes, viz., $x_i^* = Q_{ij}x_j$, then the stress tensor σ_{ij} and the strain rate tensor $\dot{\epsilon}_{ij}$ in the crystallographic axes may be obtained from the stress tensor σ_{ij}^* and the strain rate tensor $\dot{\epsilon}_{ij}^*$ in the global system from the usual transformation relations,

$$\sigma_{ij} = Q_{ik}\sigma_{kl}^* Q_{jl} \quad \text{and} \quad \dot{\epsilon}_{ij} = Q_{ik}\dot{\epsilon}_{kl}^* Q_{jl}, \tag{28}$$

where, for the bar specimen shown in Figure 58,

$$[\bar{Q}] = \begin{bmatrix} \cos\psi & 0 & -\sin\psi \\ \sin\vartheta\sin\psi & \cos\vartheta & \sin\vartheta\cos\psi \\ \cos\vartheta\sin\psi & -\sin\vartheta & \cos\vartheta\cos\psi \end{bmatrix}. \tag{29}$$

The assumption is now made that any of the unified viscoplastic models discussed in References 6, 7 and 44 to 47, when specialized to the case of shear deformation, is a valid constitutive relation in each of the twelve octahedral and six crystallographic slip directions. In the rth octahedral slip direction the Schmid resolved shear stress, π_{mn}^r, is obtained from the relation

$$\pi_{mn}^r = \bar{m}_r \cdot \bar{\sigma} \cdot \bar{n}_r \qquad (r = 1, 2, ..., 12), \tag{30}$$

where no sum over r is implied in equation (30) or in the equations which follow. When referred to the orthogonal system $\bar{m}_r^0$, $\bar{n}_r^0$, $\bar{z}_r^0$, the remaining components of the octahedral stress tensor can be written in the form:

$$\pi_{mm}^r = \bar{m}_r^0 \cdot \bar{\sigma} \cdot \bar{m}_r^0 , \quad \pi_{nn}^r = \bar{n}_r^0 \cdot \bar{\sigma} \cdot \bar{n}_r^0 , \quad \pi_{zz}^r = \bar{z}_r^0 \cdot \bar{\sigma} \cdot \bar{z}_r^0 ,$$

$$\pi_{zm}^r = \pi_{mz}^r = \bar{m}_r^0 \cdot \bar{\sigma} \cdot \bar{z}_r^0 , \quad \pi_{zn}^r = \pi_{nz}^r = \bar{n}_r^0 \cdot \bar{\sigma} \cdot \bar{z}_r^0 \qquad (r = 1, 2, ..., 12), \tag{31}$$

The Schmid resolved shear stress in the rth cube slip direction, τ_r, is obtained from the corresponding relation,

$$\tau_r = \tau'_{mn} = \bar{m}_r^c \cdot \bar{\sigma} \cdot \bar{n}_r^c \qquad (r = 1, 2, ..., 6). \tag{32}$$

It is further assumed, in a manner analogous to the unified isotropic viscoplastic models, that the applicable relation governing the inelastic shear strain rate in the rth octahedral slip direction is

$$\dot{\gamma}_r = K_r^{-p}(\pi_r - \omega_r)|\pi_r - \omega_r|^{p-1} \qquad (r = 1, 2, ..., 12), \tag{33}$$

where K_r and ω_r denote the total drag stress and the equilibrium (rest or back) stress in the rth octahedral slip direction. The stress component π_r is defined by the relation

$$\pi_r = \pi'_{mn} + a_{mm}\pi'_{mm} + a_{nn}\pi'_{nn} + a_{zz}\pi'_{zz} + 2a_{mz}\pi'_{mz} + 2a_{nz}\pi'_{nz} \quad (r = 1, 2, ..., 12), \tag{34}$$

in which the tensor α_{pq} represents the effect of the non-Schmid factors (Reference 49) upon the inelastic strain rate in the rth octahedral slip direction. For example, the term containing α_{nn} represents the effect of the resolved stress, normal to the slip plane containing the rth octahedral slip direction, on the inelastic strain rate in the rth octahedral slip direction. Such terms can represent the effect of a pressure dependent inelastic strain rate. The dominant term in equation (34) is the Schmid type term containing the stress component π'_{mn}; estimates of the magnitude of the non-Schmid type terms containing the tensor α_{pq} have been given by Asaro and Rice (Reference 49).

A power law expression is used in equation (33), but hyperbolic sine and exponential functional forms may also be used, as deemed appropriate for the material in question.

To complete the octahedral constitutive formulation it is necessary to specify the growth relations for the equilibrium and drag stress state variables. The equilibrium stress in the rth octahedral slip system may be assumed to evolve according to the evolution equation

$$\dot{\omega}_r = \varrho_1\dot{\gamma}_r - \varrho_2|\dot{\gamma}_r|\omega_r - \varrho_3|\omega_r|^{m-1}\omega_r \qquad (r = 1, 2, ..., 12). \tag{35}$$

The integral form of equation (35) is

$$\omega_r(t) = \varrho_1(t) \int\limits_{\zeta=0}^{t} (\partial\gamma_r/\partial\xi) \exp\left[- \int\limits_{\zeta=\xi}^{t} \left\{ \varrho_2(t)|\partial\gamma_r/\partial\zeta| + \varrho_3(t)|\omega_r(\zeta)|^{m(t)-1} \right\} d\zeta \right] d\xi, \tag{36}$$

with $\rho_1(t) = \rho_1[T(t)]$ etc. in contemplation of the fact that the material constants ρ_1, ρ_2 ρ_3, and m may change with temperature T during a thermomechanical loading history. The integral of equation

26

(35) should strictly be written in the form of equation (36) in which the material constant $\rho_1(t)$ occurs inside the integral over ξ in the form $\rho_1(\xi)$, and the material constants $\rho_2(t)$, $\rho_3(t)$ and $m(t)$ occur inside the integral over ζ in the forms $\rho_2(\zeta)$, $\rho_3(\zeta)$ and $m(\zeta)$. However, the integral form in equation (35) is preferred, since this form allows $\omega_r(t)$ to change instantaneously with temperature in the absence of inelastic deformation.

Upon differentiation with respect to time, equation (36) yields the relation

$$\dot{\omega}_r = \varrho_1\dot{\gamma}_r - \varrho_2|\dot{\gamma}_r|\omega_r - \varrho_3|\omega_r|^{m-1}\omega_r + \chi_r \qquad (r = 1, 2, \dots, 12), \qquad (37)$$

where

$$\chi_r(t) = [\dot{\varrho}_1(t)/\varrho_1(t)]\omega_r(t) - \varrho_1(t)\int_{\xi=0}^{t}(\partial\dot{\gamma}_r/\partial\xi)\left[\exp\left[-\int_{\zeta=\xi}^{t}\left\{\varrho_2(t)|\partial\dot{\gamma}_r/\partial\zeta| + \varrho_3(t)|\omega_r(\zeta)|^{m(t)-1}\right\}d\zeta\right]\right]$$

$$\times \left[\int_{\chi=\xi}^{t}\left\{\dot{\varrho}_2(t)|\partial\dot{\gamma}_r/\partial\chi| + \dot{\varrho}_3(t)|\omega_r(\chi)|^{m(t)-1} + \dot{m}(t)\varrho_3(t)|\omega_r(\chi)|^{m(t)-1}\log|\omega_r(\chi)|\right\}d\chi\right]d\xi \qquad (38)$$

Without the term χ_r, the differential form of equation (36) shows that in the absence of inelastic deformation (i.e. when $\dot{\gamma}_r$ is very small) the equilibrium stress ω_r changes only by thermal recovery. With χ_r included in the differential equation the equilibrium stress ω_r can change with temperature in the absence of inelastic deformation.

The drag stress for the rth octahedral slip system may be assumed to grow according to the evolution equation

$$\dot{K}_r = \left\{\sum_{\kappa=1}^{12}[\beta_1[q + (1-q)\delta_{rk}] - \eta_1(K_{rt} - K_{ro})]|\dot{\gamma}_k|\right\} - h_1(K_{rt} - K_{ro})^s \quad (r = 1, 2, \dots, 12) \qquad (39)$$

On each octahedral slip system the drag stress is assumed to harden according to the hardening modulus $h_{rk} = \beta_1[q + (1-q)\delta_{rk}]$, which accounts for the latent hardening effects observed in single crystal materials. Numerous forms of the hardening moduli h_{rk} have been proposed in the literature and a review of single crystal hardening moduli may be found in the article by Asaro (Reference 50). The particular form for h_{rk} adopted in equation (39) is due to Hutchinson (Reference 51); similar forms, which include the effects of finite deformation, were used by Asaro (Reference 52), and Peirce, Asaro and Needleman (Reference 53), in finite element computations of finite deformation slip behavior in single crystal materials. Further reviews concerning the hardening moduli can be found in the paper by Havner (Reference 54), which refers to previous work by Havner and his colleagues. Taylor hardening, in which each slip system hardens at equal rates, can be simulated with the Hutchinson modulus, h_{rk}, by setting $q = 1$.

The initial value of the drag stress in the rth octahedral slip system, K_{ro}, is defined by the relation

$$K_{ro} = K_1 + \quad \rho_4 \pi^r_{nz} + \rho_s |\Psi_r| \quad (r = 1, 2, ..., 12) \tag{40}$$

accounts for the tension–compression asymmetry of the flow stress observed in single crystal nickel–base superalloys. The shear stress component Ψ_r is the resolved shear stress on the cube crystallographic slip planes in the direction of the octahedral slip vector m^0_r. According to the Takeuchi–Kuramoto cross–slip model this stress component is the driving force which causes the primary dislocations on the {111} octahedral planes to cross–slip onto the {100} cube planes where they form sessile segments. The interaction between the primary octahedral dislocations and the pinned sessile segments increases the flow stress in the octahedral system. An increase in temperature enhances the cross–slip process and is therefore responsible for the increase in flow or yield stress with temperature in the octahedral slip system. In a unified viscoplastic formulation the yield or flow stress is analogous to the drag stress state variable and the constants ρ_4, ρ_5 therefore increase with temperature T (in Takeuchi and Kuramoto's model according to the relation exp[-H/kT]). This provides the anomalous increase of flow stress with increasing temperature found in superalloy crystals which have γ' precipitate particles possessing the $L1_2$ superlattice crystal structure. Since the magnitude of the stress component Ψ_r occurs in equation (40), the increase in yield (flow) stress due to the cube cross–slip process is the same for both tension and compression testing of a single crystal bar specimen.

The effect of the Shockley partial dislocations on yield stress asymmetry is recognized explicitly in the "core–width" term containing the stress component π^r_{nz} in the initial drag stress term in equation 40. This shear stress component in the octahedral (112) type directions can extend or constrict the Shockley partial dislocations and changes sign when the applied stress state changes from tension to compression in a single crystal bar specimen, as proposed by Lall, Chin and Pope (References 30 and 32). The expression for π^r_{nz} is given in equation 31, whilst the cube cross–slip component Ψ_r is obtained from the following relations:

$$\Psi_1 = \bar{m}^0_1 \cdot \bar{\sigma} \cdot \bar{j}, \quad \Psi_2 = \bar{m}^0_2 \cdot \bar{\sigma} \cdot \bar{k}, \quad \Psi_3 = \bar{m}^0_3 \cdot \bar{\sigma} \cdot \bar{i}, \quad \Psi_4 = \bar{m}^0_4 \cdot \bar{\sigma} \cdot \bar{i},$$

$$\Psi_5 = \bar{m}^0_5 \cdot \bar{\sigma} \cdot \bar{k}, \quad \Psi_6 = \bar{m}^0_6 \cdot \bar{\sigma} \cdot \bar{j}, \quad \Psi_7 = \bar{m}^0_7 \cdot \bar{\sigma} \cdot \bar{j}, \quad \Psi_8 = \bar{m}^0_8 \cdot \bar{\sigma} \cdot \bar{k}, \tag{41}$$

$$\Psi_9 = \bar{m}^0_9 \cdot \bar{\sigma} \cdot \bar{i}, \quad \Psi_{10} = \bar{m}^0_{10} \cdot \bar{\sigma} \cdot \bar{i}, \quad \Psi_{11} = \bar{m}^0_{11} \cdot \bar{\sigma} \cdot \bar{k}, \quad \Psi_{12} = \bar{m}^0_{12} \cdot \bar{\sigma} \cdot \bar{j},$$

The expressions containing the material constants η_1 and h_1 in equation (39) represent the dynamic and thermal recovery terms of the drag stress evolution equations in which the recovery is assumed to take place towards the initial value of the drag stress, K_{ro}.

The integral forms of the equilibrium stress and drag stress components listed in equation (36) change instantaneously with temperature, since the material constants which occur in the integral forms are evaluated at the current temperature. The differential form of the integral in equation (36) will involve terms such as X_r, containing the derivatives of the material constants with temperature, in addition to the terms already present in equations (35) and (39). These extra terms allow the state variables to change with temperature in the absence of inelastic deformation. In a yield surface plasticity theory a change in the equilibrium (rest or back) stress corresponds to a kinematic shift of the center of the yield surface, while a change in the drag stress corresponds to an isotropic change in the radius of the yield surface. In the absence of inelastic deformation both the yield surface center and its radius can change instantaneously with temperature, and the integral forms of the state variables in equation (36) is the corresponding analogue in the unified constitutive formulation.

A similar set of constitutive equations is assumed to hold for the case of crystallographic cube slip. The inelastic shear strain rate in the rth cube slip direction is assumed to have the form

$$\dot{a}_r = L_{rt}^{-d}(\tau_r - \Omega_r)|\tau_r - \Omega_r|^{d-1} \qquad (r = 1, 2, ..., 6) \tag{42}$$

where L_{rt} and Ω_r denote the total drag stress and the equilibrium (rest or back) stress in the rth cube slip direction. These state variables are assumed to evolve according to the evolution equations

$$\dot{\Omega}_r = \varrho_6 \dot{a}_r - \varrho_7 |\dot{a}_r| \Omega_r - \varrho_8 |\Omega_r|^{n-1} \Omega_r \qquad (r = 1, 2, ..., 6) \tag{43}$$

and

$$\dot{L}_r = \left\{ \sum_{k=1}^{6} [\beta_2[q_2 + (1 - q_2)\delta_{rk}] - \eta_2(L_{rt} - L_{ro})]|\dot{a}_r| \right\} - h_2(L_{rt} - L_{ro})^{\mu} \qquad (r = 1, 2, ..., 6) \tag{44}$$

where $L_{ro} = L_1$ is the initial constant value of the drag stress component on the rth cube slip system.

The shear slip strain rates may now be resolved into the crystallographic system and summed for each slip system to obtain the inelastic strain rate tensor, $\dot{c}_{ij}$, with respect to the crystal axes in the form

$$\dot{c}_{ij} = \sum_{r=1}^{12} a_{ij}^r \dot{\gamma}_r + \sum_{r=1}^{6} b_{ij}^r \dot{a}_r \tag{45}$$

where

$$a_{ij}^r = \tfrac{1}{2}\left[(\bar{i} \cdot \bar{n}_r^0)(\bar{m}_r^0 \cdot \bar{j}) + (\bar{i} \cdot \bar{m}_r^0)(\bar{n}_r^0 \cdot \bar{j})\right] \text{ and } b_{ij}^r = \tfrac{1}{2}\left[(\bar{i} \cdot \bar{n}_r^c)(\bar{m}_r^c \cdot \bar{j}) + (\bar{i} \cdot \bar{m}_r^c)(\bar{n}_r^c \cdot \bar{j})\right] \tag{46}$$

29

Finally, the stress rate tensor with respect to the crystallographic axes is determined from the relation

$$\dot{\sigma}_{ij} = D^c_{ijkl}(\dot{\epsilon}_{kl} - \dot{c}_{kl}) + \dot{D}^c_{ijkl}(\dot{\epsilon}_{kl} - c_{kl}), \tag{47}$$

where D^c_{ijkl} is the anisotropic elasticity tensor for the face–centered cubic crystal referred to the crystallographic axes. The variables can now be updated in the Euler forward difference form:

$$\sigma_{ij}(\tau + \Delta\tau) = \sigma_{ij}(\tau) + \dot{\sigma}_{ij}(\tau)\Delta\tau, \quad \epsilon_{ij}(\tau + \Delta\tau) = \epsilon_{ij}(\tau) + \dot{\epsilon}_{ij}(\tau)\Delta\tau, \quad c_{ij}(\tau + \Delta\tau) = \dot{c}_{ij}(\tau)\Delta\tau,$$

$$\omega_r(\tau + \Delta\tau) = \omega_r(\tau) + \dot{\omega}_r(\tau)\Delta\tau, \quad \Omega_r(\tau + \Delta\tau) = \Omega_r(\tau) + \dot{\Omega}_r(\tau)\Delta\tau, \quad K_r(\tau + \Delta\tau) = K_r(\tau) + K_r(\tau)\Delta\tau,$$

$$\tag{48}$$

$$L_r(\tau + \Delta\tau) = L_r(\tau) + \dot{L}_r(\tau)\Delta\tau \,, \gamma_r(\tau + \Delta\tau) = \gamma_r(\tau) + \dot{\gamma}_r(\tau)\Delta\tau, \quad a_r(\tau + \Delta\tau) = a_r(\tau) + \dot{a}_r(\tau)\Delta\tau,$$

$$\sigma_{ij}(\tau + \Delta\tau)^* = Q_{ki}\sigma_{ki}(\tau + \Delta\tau)Q_{ij}, \quad \epsilon_{ij}(\tau + \Delta\tau) = Q_{ki}\epsilon_{ki}(t + \Delta t)Q_{ij}.$$

A summary of the slip system viscoplastic equations is presented in Figures 59 and 60.

Many of the temperature dependent constants are effectively zero for PWA 1480. Thus, the PWA 1480 constitutive model was simplified to that shown in Figure 61. PWA 1480 constants are presented in Figures 62 to 69 for both the Base and Option 1 programs. Typical high temperature isothermal results from the PWA 1480 constitutive model are compared to data in Figure 70. Low temperature results (Set B constants) are discussed in Section 14.

8.2.3 Computer Software Development

Effort concentrated on incorporating the slip system based constitutive model into the MARC finite element program with particular emphasis on non–isothermal loading.

<u>Reference Stiffness Matix</u>

Generally, if the temperature at any part of a structure experiences a temperature change from one increment to the next, the structural stiffness matrix is reformulated with the elastic constants at the new temperature. This is a time consuming task which is circumvented by measures introduced in

30

previous NASA sponsored constitutive modeling contracts (Reference 28). In brief, these measures set flags in appropriate MARC subroutines so that the structural stiffness matrix is formulated and inverted only once using elastic constants from a "reference temperature". All elastic stress changes due to temperature variations (as well as actual inelastic stress increments) are included in the inelastic stress increment vector, G, supplied by the HYPELA subroutine. A schematic of this method is presented in Figure 71.

Elastic Elements

A provision has been made for elastic behavior of selected elements in a structure. Such a feature was provided in the constitutive model for B1900 + Hf in a previous NASA contract (Reference 55), and it was shown to be very desirable for analysis of large complicated structures that may have regions of confined inelasticity or regions where only "average" stiffnesses contribute to structural loads (e.g., internal pedestals in a turbine blade). For the elastic elements, the inelastic calculations are bypassed so that the contribution to the G vector (the inelastic stress increment) due to material inelasticity is zero. However, the contribution to G due to an elastic modulus change from the reference stiffness temperature will be included.

Rate Independent Material Model

To improve low temperature model predictions, the low temperature model response was reformulated based on the observed rate independent material behavior. As temperature decreases below approximately 760°C (1400°F), PWA 1480 material becomes increasingly rate independent. This poses a fundamental difficulty for viscoplastic models which are formulated to be rate dependent. In the present model, the low temperature rate independence effectively imposes a severe constraint on the model constants, causing, for example, the exponent of the overstress to be very high for the octahedral systems. To overcome these concerns, the applied strain rates are "transformed" to effective strain rates before being used with the same set of evolutionary equations. The transformation is such that applied strain rates are preserved at high temperatures, while a constant (reference) strain rate is achieved at low temperatures. In a transition temperature regime (approximately 704°C (1300°F) to 816°C (1500°F)), the effective strain rate transitions between the two limits. Symbolically, the transformation is:

$$\text{E eff} \quad = \quad \text{A x E actual + B} \tag{49}$$

where
E eff   = the effective strain rate
E actual = the applied strain rate

and the limits on the constants A and B are as follows:

Low Temperature Limit	Constant	High Temperature Limit
0	A	1
E ref	B	0

A routine was subsequently added to the HYPELA code that produces rate independent behavior at low temperatures. The model constants were fit to isothermal cyclic stress–strain data at temperatures of 760°C (1400°F) and above. At 649°C (1200°F) and below, the model constants were fit to monotonic tensile data. Because the thermal mechanical fatigue cycles of interest in this contract are nominally elastic below 649°C (1200°F) it was judged that this assumption would not severely affect the use of the model in the Base Program. A schematic of the rate independent correction is presented in Figure 72.

Software Verification

The micromechanical HYPELA code was checked out using simple one element test cases. An out-of-phase thermal mechanical fatigue cycle, similar to that conducted on specimen LB–34, was

used as one of the test cases. Figure 73 compares the test case strain-temperature cycle to that imposed on specimen LB-34. In each cycle the strain-time variation is sinusoidal over a period of 60 seconds. The MARC test case results and the experimental results from LB-34 are shown in Figure 74.

No obvious incompatabilities with the MARC code were observed in the test cases. In spite of the relatively large load steps in some portions of the TMF cycle, convergence was achieved without recycling. The load increments are shown in Figures 73 and 74. Additional test cases, using even larger load increments and a strain hold period at the high temperature end of the cycle also executed well. The test case load increments are expected to be larger than those that would be employed in a transient analysis of a turbine airfoil. For example, in a previous NASA HOST contract (Reference 55), the load increments corresponded to 10°C (50°F) temperature increments.

Back Stress Evolution Formulation for Non-Isothermal Cycles

Based on the low temperature model prediction shown in Figure 74, the back stress formulation was revised to include the effect of temperature rate. This feature is schematically presented in Figure 75 for the non-isothermal cycle of LB-34. Allowing the back stress to evolve during the elastic (tensile-going) loading portion of the cycle effectively reduces the overstress ($\sigma-\omega$), thereby increasing the predicted yield point.

Prediction of LB-34 incorporating this feature is presented in Figure 76.

Another feature was added to the model to effect a controlled cycle-by-cycle relaxation of non-isothermal loops. It is a characteristic of viscoplastic models containing a back stress that over many cycles of loading the entire hysteresis loop will relax in stress until the back stress is approximately symmetric about zero global stress. The rate of relaxation of the loop is usually uncontrolled in that it is not explicitly modeled in the evolutionary equations for the state variables. Such is the case with the model developed in this program. That is, the model was formulated and the constants were fit to reproduce the stress-strain loop shape; long term cyclic evolution was not modeled.

In general, comparisons between predicted and experimental non-isothermal hysteresis loops indicated that the predicted stress range was accurately represented, but the hysteresis loop stress relaxed much too rapidly and provided a poor mean stress evolution with continued cycling. As a means to control the rate of stress relaxation, additional temperature rate terms were added to the evolutionary equations for octahedral and cube equilibrium (back) stresses (compare Figures 61 and 75).

The constants which drive the temperature rate terms were set by an iterative technique using <001> TMF data to set the octahedral term and <111> TMF data to set the cube term. Although acceptable stress relaxation behavior was obtained for the data used to set the temperature rate constants, prediction of other TMF cyclic conditions was adversely affected. For example, Figure 77 shows the predicted TMF behavior for <001> PWA 1480 without the temperature rate terms. Note the seemingly constant stress relaxation rate per cycle for the three different mean strains. Also, the prediction of the V = 1 test shows continued ratchetting of the minimum stress into tension. Such a trend was not observed in any TMF test. The predictions were repeated, but this time, the temperature rate term for the octahedral equilibrium stress was activated. These predictions are presented in Figure 78. Although the V = 0 mean strain condition reasonably matched the TMF test data, the predicted relaxation response of the other mean strain conditions was generally worse than before. The V = -1 test data indicates a very rapid initial relaxation should occur, but the predicted loop stabilized after the first quarter cycle. Overall, the incorporation of the temperature rate terms did not improve the predictions of non-isothermal hysteresis loops for turbine blade relevant conditions. As a result, the temperature-rate terms were inactivated (see note at bottom of Figures 59, 60 and 61).

Because the prediction of PWA 1480 TMF life requires an accurate definition of tensile stress and the PWA 1480 constitutive model was unable to reasonably predict tensile stress, the current form of the PWA 1480 constitutive model, by itself, was judged inadequate for TMF life prediction.

32

An alternative "stress envelope" approach was developed to predict tensile stress during TMF. This approach was based on the assumption that out-of-phase TMF loops of <001> PWA 1480 at maximum temperatures above roughly 927°C (1700°F) tend to stabilize according to conventional yield surface criteria. And, since the cyclic TMF hysteresis loops of interest are nominally elastic in nature, the yield surface envelope was taken to be defined by the proportional limit of a tensile test (i.e., the stress at which the tensile curve deviates from a linear response). Then, knowing the stress range of a particular TMF cycle (remember that the constitutive model predicted TMF stress ranges well), the "effective" tensile stress can be calculated using the following simple formula:

$$S_t = S_{ten} * (DS / (S_{ten} + S_{comp})) \tag{50}$$

where: S_t =   "Effective" tensile stress

DS =   Predicted stress range.

S_{ten} =   Proportional limit stress at the temperature associated with the maximum predicted stress.

S_{comp} =   Proportional limit stress at the temperature associated with the minimum predicted stress.

Further information on this method and its application was presented in Reference 4.

8.2.4   Model Limitations and Future Work

While the constitutive model for PWA 1480 was successful in modeling the high temperature orientation and rate dependence, there are some aspects of PWA 1480 material behavior that are not accurately modeled. This discussion is intended to highlight those areas so that the analyst can intelligently decide whether to pursue nonlinear analyses using the model and to make informed judgements about analytical results obtained with the model.

The model was formulated to reproduce the stabilized stress-strain behavior during cyclic loading. The data used to obtain the material constants was from completely reversed strain controlled isothermal tests. The correlation with test data above (760°C) (1400°F) is quite good. Below 760°C (1400°F), the material becomes rate independent, and the uniaxial tests were judged to be unreliable for obtaining cyclic material behavior due to the onset of sudden, localized slip. So the material constants used in the current version of the model for temperatures below 760°C (1400°F) attempt to reproduce the monotonic tensile properties. The subject of low temperature behavior is discussed in Section 14.

In general, the single crystal constitutive model suffers from "traditional" viscoplastic model deficiencies such as:

- Unstable mean stress at low temperature

- Predicts cyclic or monotonic data, but not both

- Uses homogeneous slip formulation to model discrete slip phenomena – need two deformation modes for this class of alloys

- Long term cycle to cycle ratchetting during TMF is not captured, and would be too costly to model by full integration over thousands of cycles.

Nonetheless, the PWA 1480 micromechanical model is regarded as a valuable research tool and as a good starting point for further development.

8.3 COATED SINGLE CRYSTAL LIFE PREDICTION MODELING

The fatigue life approach for coated single crystal materials was defined in Section 6.3.

8.3.1 Overlay Coating TMF Life Model

The final PWA 286 TMF life model formulation was based on Ostergren's hysteretic energy approach (Reference 22). In this case, however, Ostergrens' time dependent damage term, v, was extended to include temperature effects by introducing a temperature dependent damage rate which, in combination with the time, describes damage. The damage rate was formulated by an equation usually applied to thermally activated processes, such as oxidation and diffusion. Since v was defined as a correction for temperature- and time-dependent damage, $v \leq 1.0$ by definition. A change from Ostergrens' model was that compressive hold time contributes to damage. Dwell periods, which frequently occur within a gas turbine duty cycle, were explicitly treated in the temperature- and time-dependent damage term. The formulation is presented below:

$$Nc = 28050 W_t^{-0.81} v^{0.5} \tag{51}$$

$$W_t = \int\limits^{cycle} \sigma \Delta \epsilon_{in} \; ; \; \sigma \geq 0 \tag{52}$$

$$v = \cfrac{1.0}{\int\limits^{cycle} \exp\left[Q_o\left(\frac{1}{T_o} - \frac{1}{T}\right)\right] Fac \; \Delta t} \; ; \; v \leq 1.0 \tag{53}$$

$$Fac = 1.0 + [c_1 - c_2 \tanh(\sigma - \Omega) - 1.0] \exp(-10000 | \dot{\epsilon}_{mech} |) \tag{54}$$

$$c_1 = \frac{Chf + Thf}{2} \tag{55}$$

$$c_2 = \frac{Chf - Thf}{2} \tag{56}$$

where:

W_t = Integrated tensile hysteretic energy (psi)

v = Effective cycle frequency (Hz)

T_{eff} = 1.0/n = Effective time (sec)

σ = Stress (psi)

Ω =   Equilibrium stress (psi)

$\Delta\epsilon_{in}$ =   Inelastic strain increment (in/in)

Q_o =   Normalized effective activation energy = $50000°R$

T_0 =   Reference temperature = $2660°R$

Fac   =   Hold time correction factor

$\dot{\epsilon}_{mech}$ =   Mechanical strain rate (sec^{-1}) associated with the stress s

Δt =   Time increment (sec)

Chf   =   Compression hold factor = 0.19

Thf   =   Tension hold factor = 0.38.

Application of the PWA 286 overlay coating life model included consideration of multiaxial loadings. It is well known that biaxial loads are introduced into the coating during thermal cycling due to coating/substrate thermal growth mismatch. This biaxial loading contribution to coating damage was not ignored. For example, MARC finite element analysis of a simple two element structure was performed to obtain the coating hysteretic response to a uniaxial, out–of–phase TMF test conducted at 427–1038°C (800–1900°F), ±0.15 percent, and 1 cpm. The predicted hysteresis loop from the finite element analysis is compared to the predicted loop from a one–dimensional analysis in Figure 79.

In an effort to reduce application inconsistencies, the expression Fac was formulated which describes a hold time as a cyclic condition where mechanical strain rate is negligible. The function, Fac, is presented in Figure 80.

Model constants were obtained by regression analysis from predicted hysteresis loops and out–of–phase TMF test life data. The resulting correlation is presented in Figure 81 and summarized in Table 10. All data in this set is correlated well within ±2X which is considered excellent.

The predictive capability of the model was judged based on the predictions of all the remaining PWA 286 overlay coating TMF life data obtained in this program. The resulting predictions are shown in Figure 82 and summarized in Table 11. All predictions of the known life points were made within a ±2.5X life band and the majority lie within a ±2X life band. Also, the predicted versus actual life of the TMF test designed to simulate an airfoil leading edge loading condition was within the ±2X life band. The "runout" tests were generally underpredicted.

8.3.2 Coated PWA 1480 TMF Life Model

The final life model formulation for PWA 1480 single crystal was based on maximum stress intensity factor, Kmax, modified to account for the effects of threshold stress intensity, crystallographic orientation and temperature– and time–dependent damage. Selection of the Kmax based model was discussed in Reference 3.

a) Base

$$N_{sc} = \frac{1}{A}\left(\beta \ \sigma_t \ \sqrt{\pi}\right)^{-2} \ln\left(\frac{t_c + ds}{t_c}\right) \qquad (57)$$

where: σ_t =   Maximum tensile stress (ksi)

         β =   Crack boundary correction factor

$$t_c \quad = \text{ Coating thickness (in)}$$

$$ds \quad = \text{ Maximum crack depth in the substrate (in); ds } = 0.01 \text{ in this program.}$$

b) Base + Threshold Effects

Based on observations from both high temperature isothermal fatigue and in–phase TMF data, coating cracks do not always propagate into the substrate. This phenomenon indicated that a threshold stress intensity exists for uniaxial TMF of PWA 1480.

$$N_{sc} = \frac{2}{A} \left(\beta \sigma_t \sqrt{\pi} \right)^{-2} \left[\ln \ (K_m - K_{th}) \ - \ \frac{K_{th}}{K_m - K_{th}} \right]_{K_m^{initial}}^{K_m^{final}} \tag{58}$$

where: $\quad K_m = \beta \sigma_t \sqrt{\pi a}$ \hfill (59)

$$K_m^{initial} = \beta \sigma_t \sqrt{\pi t_c} \tag{60}$$

$$K_m^{final} = \beta \sigma_t \sqrt{\pi (t_c + ds)} \tag{61}$$

$K_{th} = \textit{Threshold stress intensity } (ksi \sqrt{in})$

c) Base + Threshold + Crystallographic Effects

A comparison of median predicted lives obtained from model b) above indicated that crystallographic orientation was also important for prediction of uniaxial TMF. Initially, the damage factor reported in Reference 15 was investigated; however, that particular factor produced unsatisfactory predicted life trends. To better capture the observed crystallographic effects, another crystallographic factor was derived from the following assumptions:

- All crack growth occurs along the maximum normal stressed octahedral slip plane.

- The energy required to grow a crack is a function of the crystallographic orientation relative to the loading direction.

- The ratio of elastic modulus, E, to the spring constant, K, is a constant for all orientations.

Combining the first two assumptions yields:

$$W_{<111>}^{<001>} \neq W_{<111>}^{<111>} \tag{62}$$

where: $\quad W_{<111>} \quad = \text{ Energy portion due to the maximum normal octahedral slip plane force and associated deflection and the superscripts refer to the crystalline orientation along which the load is applied.}$

For life modeling purposes, it was not necessary to determine the absolute level of $W_{<111>}$, but rather its relative ranking among the orientations. Since, in a <111> oriented uniaxial tensile specimen, an octahedral slip plane is situated normal to the applied load, the <111> orientation was chosen as the baseline or reference orientation against which all orientations were compared.

$$\frac{W_{<111>}^{<111>}}{W_{<111>}^{<111>}} = 1.0 \quad \text{by definition} \tag{63}$$

$$\frac{W_{<111>}}{W_{<111>}^{<111>}} = \frac{(F*\delta)_{<111>}}{(F*\delta)_{<111>}^{<111>}} \quad \text{and} \quad \delta = \frac{F}{K} = \frac{Force}{Spring\ Constant} \tag{64}$$

$$= \frac{(F^2/K)_{<111>}}{(F^2/K)_{<111>}^{<111>}} = \frac{F^2_{<111>}/K_{<111>}}{F_{<111>}^{<111>2}/K_{<111>}^{<111>}} \tag{65}$$

Now, $F_{<111>} = F \cos \theta = F\sqrt{f_{<111>}}$ where $f_{<111>}$ is the factor which resolves the applied stress into the maximum normal octahedral slip plane stress. $f_{<111>}$ is given below for the crystalline orientations used in this program.

Orientation	$f_{<111>}$
<001>	1/3
<111>	1
<011>	2/3
<213>	0.857

Also, from assumption 3,

$$\frac{K_{<111>}}{E_{<111>}} = \frac{K_{<111>}^{<111>}}{E_{<111>}^{<111>}} \tag{66}$$

$$\text{or} \quad K_{<111>} = \frac{K_{<111>}^{<111>}E_{<111>}}{E_{<111>}^{<111>}} \tag{67}$$

Substituting the expressions for $F_{<111>}$ and $K_{<111>}$ into the energy ratio equation yields:

$$\frac{W_{<111>}}{W_{<111>}^{<111>}} = \frac{f_{<111>}\ F^2/(K_{<111>}^{<111>}E_{<111>}/E_{<111>}^{<111>})}{f_{<111>}^{<111>}\ F^2/K_{<111>}^{<111>}} \tag{68}$$

which reduces to:

$$\frac{W_{<111>}}{W_{<111>}^{<111>}} = \frac{f_{<111>}\ E_{<111>}^{<111>}}{E_{<111>}} \tag{69}$$

since $f_{<111>}^{<111>} = 1.0$.

For example, the energy ratio for the <001> orientation is given by:

$$\frac{W_{<111>}^{<001>}}{W_{<111>}^{<111>}} = \frac{E^{<111>}}{3\ E^{<001>}} = \frac{41.85}{3\ (16.15)} \quad at \quad 800°F = 0.864 \tag{70}$$

This was interpreted to mean that the <001> orientation requires 86.4 percent of the energy required by the <111> orientation to extend a crack at 800°F. Therefore, the associated <001> damage factor relative to <111> is 1.0 / 0.864 which equals 1.157 and the appropriate damage factor is:

$$Damage \ factor = \frac{E}{f_{<111>} \ E^{<111>}} \qquad (71)$$

where the <111> subscripts associated with the moduli have been deleted.

Substituting the above expression into model b) yields:

$$N_{sc} = \frac{2}{A} \left(\frac{E}{f}\right) \left(\beta\sigma_t\sqrt{\pi}\right)^{-2} \left[\ln \ (K_m - K_{th}) - \frac{K_{th}}{K_m - K_{th}}\right]_{K_m^{initial}}^{K_m^{final}} \qquad (72)$$

where:
$$f = \frac{1}{f_{<111>}} \left(\frac{E}{E^{<111>}}\right)^2 \qquad (73)$$

Note that the factor f includes an extra $1/E^{<111>}$ in its formulation. This was done so that the crack growth equation was consistent with an elastic strain energy density.

$$K_m^2 \propto J_m * E * \frac{E^{<111>}}{E} \qquad (74)$$

where J_m = elastic strain energy density based on K_m. The elastic modulus proportionality factor, $E^{<111>}$, was effectively nullified by a change in the regression constant 1/A.

d) Base + Threshold + Crystallographic + Temperature- and Time-Dependent Effects

A comparison of median predicted lives obtained from model c) for 1038°C (1900°F) maximum temperature (Tmax) TMF tests without hold times, 1038°C (1900°F) Tmax TMF tests with hold times and 1149°C (2100°F) Tmax TMF tests indicated that the median lives of the latter two data sets were overpredicted. Model c) was subsequently modified to include the temperature- and time-dependent damage term developed for coatings.

$$N_{sc} = 330 \left(\frac{E}{f}\right) \left(\beta\sigma_t\sqrt{\pi}\right)^{-2} \left[\ln \ (K_m - K_{th}) - \frac{K_{th}}{K_m - K_{th}}\right]_{K_m^{initial}}^{K_m^{final}} * v^{0.15} \qquad (75)$$

$$v = \frac{1.0}{\int\limits^{cycle} \exp\left[Q_o\left(\frac{1}{T_o} - \frac{1}{T}\right)\right] \ Fac \ \Delta t} \qquad (76)$$

$$Fac = 1.0 + \left[c_1 - c_2 \tanh (\sigma - \Omega) - 1.0\right]\exp(-250000|\dot{\epsilon}_{mech}|) \qquad (77)$$

$$c_1 = \frac{Chf + Thf}{2} \qquad (78)$$

$$c_2 = \frac{Chf - Thf}{2} \qquad (79)$$

where:

K_{th}	=	Threshold stress intensity factor 1.30 ksi $\sqrt{in}$	
ν	=	Effective cycle frequency (Hz)	
T_{eff}	=	1.0/n = Effective time (sec)	
σ	=	Stress (psi)	
Ω	=	Equilibrium stress (psi)	
Q_0	=	Normalized effective activation energy = 33500°R	
T_o	=	Reference temperature = 2860°R	
Fac	=	Hold time correction factor	
$\dot{\epsilon}_{mech}$	=	Mechanical strain rate (sec^{-1}) associated with the stress s	
Δt	=	Time increment (sec)	
Chf	=	Compression hold factor = 0.05	
Thf	=	Tension hold factor = 0.05	

The final model was selected from models a) through d) by applying the Quality Loss Function (QLF) described in Reference 56 to the ratio of predicted to actual life (Np/Na). For a perfect prediction Np/Na = 1.0. As Np/Na deviates from 1.0, significant cost implications arise. If Np/Na < 1.0, the model is conservative and components may be retired prematurely. If Np/Na > 1.0, the model is anticonservative and components may crack unexpectedly. In this application, the QLF was used to quantify the relative cost associated with using a particular life model. Lower values of the QLF translate into lower customer life cycle costs. Calculated QLF values are presented in Table 12.

Based on the QLF, model d) was the model which best minimized the customer life cycle cost. Model d) was thus selected as the final coated PWA 1480 uniaxial TMF life model.

Model constants were obtained by regression analysis of out-of-phase TMF test data. The resulting correlation is presented in Figure 83 and summarized in Table 13. All data in this set is correlated within about ±2X which is considered good.

The predictive capability of the model was judged based on the predictions of all the remaining coated PWA 1480 TMF life data obtained in this program. The resulting predictions are shown in Figure 84 and summarized in Table 14. The predictions were made within about a ±2.5X life band and the majority lie within a ±2X life band. Also, the predicted versus actual life of the TMF test designed to simulate an airfoil leading edge loading condition fell within the ±2X life band.

39

The PWA 1480 TMF crack growth data obtained in the Reference 57 program was reduced using the maximum mode I stress intensity, Kmax. The Paris Law exponent from the TMF crack growth data was then compared to that obtained from the Kmax correlation of initiation data (Nsc) obtained in this program. The two exponents differed by roughly 50% with the exponent from the initiation data being smaller than that of the crack growth data. In addition, the crack growth data indicated that Kmax did not collapse data of different maximum temperatures which appears contrary to the experience with the initiation data.

The inability of crack growth data to replicate the crack initiation data is unfortunate but not unexpected. The crack growth data was obtained from a similar TMF specimen geometry as the initiation data but used a through–wall crack started out of a small (0.010") machined slot. In some instances, the initiation data Kmax was below the initial Kmax induced by the machined slot. Another important consideration is the fact that the initiation data lives used to deduce the exponent on Kmax were based on the largest observed crack and did not include the effects of multiple cracks which were typically adjacent to, and often linked–up with, the largest crack.

8.3.3 Life Model Limitations

The life models developed in this NASA sponsored effort do not cover the entire range of potential application and have not been calibrated with gas turbine engine thermomechanical fatigue cracking experience. TMF specimen tests were limited to two maximum metal temperatures ($1038\,^\circ$C ($1900\,^\circ$F) and $1149\,^\circ$C ($2100\,^\circ$F)). Extrapolation of TMF life outside these temperature limits should be viewed with some skepticism.

8.3.4 Life Model Constant Determination

Model constant determination from TMF cycles is complicated and cannot be effectively accomplished by hand analysis. Application of a nonlinear least squares regression computer code is probably the best means to obtain the model constants. This is not considered an impractical approach since such regression capability is generally required to obtain constitutive material model constants. The following procedure was used:

A) Coating

1) Predict the coating hysteresis loop for each TMF specimen by executing the LAYER program (Reference 4). Note: Both coating and substrate material models (HYPELA) must be compiled using the AUTODBL option to create executable files with double precision (Real*8). Also, check to make sure that HYPELA is set to generate a nonlinear analysis (i.e., set NELAS = 1) for both materials.

    a) Generate stress analysis input file (GENERATE)

        – Two elements are used, one coating and one substrate

        – To properly predict the load share, the thickness of the substrate is set to 1.0 in. and the thickness of the coating is set to the ratio of coating to substrate cross-sectional areas (Ac / As). This is done to ensure convergence of the STRESS program. The STRESS program converges using an energy term which tends toward zero for small thicknesses.

    b) Execute stress analysis (STRESS)

    c) Post-process stress analysis output (POST)

    d) Obtain integrated tensile hysteretic energy, Wt (LIFE)

        Note: If the substrate life model is to be regressed at a later date, record the coating stress which occurs at the maximum substrate stress. This coating stress is needed to adjust the observed coated specimen loads to account for coating load share.

40

2) Create a file to store the predicted coating responses from each TMF specimen analyzed. The coating response is contained in the file Post Output which is created by the POST program.

Note: If the substrate life model is to be regressed at a later date, store the substrate stress response in a separate file. This will eliminate the necessity to rerun the TMF specimen analyses.

Note: Put all the TMF cycles of the correlation data set in one file and the TMF cycles of the verification (or prediction) data set in another file. The correlation data set for the coating many not be identical to that of the substrate.

3) At this point, the following are available for model constant regression:

a) Actual coating life, Nc-act (cycles)

b) Integrated tensile hysteretic energy, Wt (psi)

c) Coating response for each TMF specimen test stored in a file (i.e., the correlation data set file).

The procedure from this point is largely up to the individual user. There are perhaps many different approaches one may take to perform the actual constant regression. The challenge is to develop a regression technique which can integrate the temperature- and time-dependent damage term each time a particular TMF specimen life is calculated. The regression routine used to obtain model constants in this program has the capability to read the coating behavior of a particular specimen from the correlation data set file each time that specimen life is calculated. The temperature- and time-dependent damage term is then integrated and combined with the corresponding Wt and the life is calculated using the current values of the model constants. The Wt parameter was previously integrated to save computer cost because non-linear regression techniques are computer intensive. The regression routine also has the capability to constrain constants to a fixed value. This helps the user apply the regression routine. For example, the exponent, b, on Wt can be found by using specimen tests without significant temperature- and time-dependent damage (i.e., fast cyclic rates or low temperatures). Once b is determined, it is constrained for the balance of the regression. Of course, it helps to have a good starting point for each of the constants. To that end, the following suggestions may help in choosing initial guesses for coating constants:

Constant	Final Value	Initial Guess
A	28050.	Between 10000 and 100000, based on experience.
b	-0.81	Between -0.8 and -1.0, based on experience.
c	0.50	0.5, based on the notion that coating damage at high temperatures and/or times is controlled by inelastic deformation which gives an exponent, n, of roughly 2.0 on the inelastic strain flow rule and $c = 1 / n$. An exponent of 0.5 is also consistent with parabolic oxidation kinetics.
Q_o	50000.	Between 30000 and 70000 depending on how rapidly the coating life drops with increasing temperature. Higher life reductions generally require higher values of Q_o.
T_o	2660.	Roughly equivalent to the incipient melting point temperature.
Chf	0.19	Determined from tests with and without hold times at a maximum temperature which occurs in compression (out-of-phase TMF).
Thf	0.38	Determined from tests with and without hold times at a maximum temperature which occurs in tension (in-phase TMF).
Ψ	10000.	Arbitrarily determined, suggested value = 10000 for coatings.

B) Substrate

1) Obtain the substrate maximum stress from each TMF specimen by correcting the observed specimen maximum stress for the coating load share. This is accomplished by subtracting the product of coating stress (which occurs at the observed maximum specimen stress) and coating area from the observed specimen load and dividing the result by the substrate area. Coating stress is predicted by the STRESS program.

$$\sigma_s = (P_o - \sigma_c A_c)/A_s \tag{80}$$

2) Obtain the crack boundary correction factor by executing the LIFE program portion of the LAYER program using the correct specimen and crack geometries. Dummy values for stresses are used.

3) Create a file to store the predicted substrate responses from each TMF specimen analyzed by the LAYER program. This file should be available from the analyses performed for the coating life model.

4) At this point, the following are available for model constant regression:

   a) Actual substrate life, Nsc–act (cycles)

   b) Maximum substrate tensile stress, σ_t (ksi)

   c) Coating thickness, tc (in)

   d) Crack boundary correction factor, β

   e) Elastic modulus of the substrate, E (ksi)

   f) Elastic modulus of a <111> oriented bar, $E^{<111>}$ (ksi)

   g) Factor which resolves the applied stress into the maximum normal octahedral slip plane stress, $f_{<111>}$

   h) Substrate response for each TMF specimen test stored in a file (i.e., the correlation data set file).

The procedure from this point is largely up to the individual user. There are perhaps many different approaches one may take to perform the actual constant regression. The challenge is to develop a regression technique which can integrate the temperature– and time–dependent damage term each time a particular TMF specimen life is calculated. The regression routine used to obtain model constants in this program has the capability to read the substrate behavior of a particular specimen from the correlation data set file each time that specimen life is calculated. The temperature– and time–dependent damage term is then integrated and combined with the corresponding integrated crack growth life using the current values of the model constants to obtain the calculated life.

Constant	Final Value	Initial Guess
1/A	165.	Between 50 and 500, based on experience.
b	–1.00	Between –0.8 and –2.0, based on experience.
K_{th}	1.30	Less than 1.7 based on the results of specimen JB–29.
c	0.15	Based on the notion that substrate damage at high temperatures and/or times is controlled by creep type inelastic deformation. In keeping with the notion that all crack growth occurs along the maximum normal stressed octahedral (<111>) plane, the exponent, n, was determined from a power law relationship of <111> specimen secondary creep rate vs. stress. The constant c = 1/n.

Q_o	33500.	Between 20000 and 50000 depending on how rapidly the substrate life drops with increasing temperature. Higher life reductions generally require higher values of Q_o.
T_o	2860.	Roughly equivalent to the incipient melting point temperature.
Chf	0.05	Determined from tests with and without hold times at a temperature which occurs in compression (out–of–phase TMF).
Thf	0.05	Determined from tests with and without hold times at a temperature which occurs in tension (in–phase TMF).
Ψ	250000.	Arbitrarily determined.

8.4 COMPUTER SOFTWARE DEVELOPMENT

Conducting an analysis of a coated airfoil was considered impractical for general design applications due to the increased model complexity and the small increments needed to converge the coating constitutive model (i.e., overwhelming engineering and computer costs). Instead, an alternative method was developed. One which used a simplified structural analysis to simulate airfoil critical locations and drive the life prediction models. This simplified structural model has the capability to model the general multiaxial loading conditions of a smooth flat surface. Boundary conditions for the simplified structural model could be obtained from an uncoated airfoil elastic or inelastic analysis.

Integration of all constitutive and life models with the simplified structural analysis technique is detailed in Reference 4, "LAYER User and Programmer Manual." The software flowchart is shown in Figure 85. All the LAYER program software is modular to permit future model additions or alterations.

SECTION 9.   TASK VII – SUBCOMPONENT VERIFICATION FOR PRIMARY SC MATERIAL

9.1   TEST SPECIMEN AND CYCLE

The specimen geometry selected for the verification test is shown in Figure 8B. Specimen orientation and coating chosen were <001> and PWA 286 overlay (specimen JB-135). The test envelope chosen was 427-1038°C (800-1900°F) with a strain range of 0.45% and strain ratio (V-ratio) of -1.

The verification test TMF cycle was defined based on the nonlinear airfoil analysis conducted by T. Meyer in support of NASA Contract NAS3-23925 (Reference 55). Specifically, the predicted airfoil leading edge strain-temperature history presented by Meyer for an entire transient flight cycle was normalized and used to calculate test parameters. Maximum and minimum temperatures and strain range were selected to approximate the airfoil loading history. The predicted airfoil versus test strain-temperature histories are compared in Figure 86 and a description of the airfoil transient flight cycle is presented in Table 15. Constant loading conditions which occur in the airfoil during climb and cruise were modeled by holding constant strain. Test strain versus time and temperature versus time cycles are presented in Figures 87 and 88, respectively.

9.2   VERIFICATION TEST RESULTS

The results from specimen JB-135 are included in Appendices D and E and the strain-temperature and initial hysteresis loops are presented in Figures 89 and 90. Cracking was typical of an overlay coated PWA 1480 specimen. Coating cracks initiated at multiple sites throughout the specimen gage section. Failure was caused by linkup of multiple, coating generated, cracks which had initiated at slightly different gage section levels along the specimen OD. The general appearance of the fracture surface of JB -135 is presented in Figure 91.

9.3   LIFE MODEL PREDICTION OF VERIFICATION TEST

The predicted sum of coating and substrate crack initiation life (Nc + Nsc) for the TMF verification test is 1994 + 1013 = 3007 cycles relative to the observed life of 1280 + 790 = 2070 cycles which is well within a factor of 2X.

The substrate life (Nsc) was predicted using the calculated substrate stress level from the specimen response and the associated specimen coating and substrate thicknesses and crack geometry. Using predicted stresses obtained by the stress envelope method (Section 8.2.3) gives Nsc = 1324 to 1757 cycles. Using an average crack geometry and nominal coating and substrate thicknesses along with the predicted stresses gives Nsc = 1429 to 1901 cycles. The true predicted life is then 1994 + 1429 (or 1901) = 3423 to 3895 cycles which is just within 2X of the actual life. From these analyses, it was concluded that the Nsc life prediction can be improved by developing a better method for predicting the substrate tensile stress.

SECTION 10. TASK VIII – ALTERNATE SC MATERIAL CHARACTERIZATION FOR AIRFOILS

10.1 TEST SPECIMEN FABRICATION

Eighteen (18) solid bar and ten (10) cylindrical tube specimens were fabricated to support Task VIII testing. A summary of the fabricated specimens is presented in Table 16 and specimen geometries are shown in Figure 92 (solid) and 8B (tube).

10.2 MONOTONIC TESTS

10.2.1 Alloy 185 Tensile Tests

A summary of Alloy 185 tensile test results is presented in Table 17.

10.2.2 Alloy 185 Creep Tests

A summary of Alloy 185 creep test results is presented in Table 18.

10.3 FATIGUE TESTS

Baseline PWA 286 overlay coated Alloy 185 TMF experiments were conducted. The results from optical fracture surface inspection are given below:

1) <001> HJB-4 427-1038°C (800-1900°F), ±0.15%, 1 cpm, Out-of-phase
Coating initiated cracking. Multiple sites observed along fracture surface. Coating cracks appeared early during the test and grew along the specimen circumference with little growth into the substrate. This resulted in substrate cracks which were long and shallow.

2) <001> HJB-1 427-1038°C (800-1900°F), ±0.25%, 1 cpm, Out-of-phase
Mixed mode (ID and OD surface initiation) cracking was observed. The predominant mode was OD coating initiated cracking. Multiple coating cracks were observed along the fracture surface.

3) <001> HJB-8 427-1038°C (800-1900°F), ±0.35%, 1 cpm, Out-of-phase
Coating initiated cracking. Some small ID surface cracks were also observed. Coating cracks appeared early and formed long, shallow substrate cracks similar in nature to specimen HJB-4.

Life and stress history for the Alloy 185 tests are presented in Appendix F.

In general, out-of-phase TMF cracking of overlay coated <001> Alloy 185 was similar in nature to that of overlay coated PWA 1480 (i.e., multiple coating initiated substrate cracks). Typical fracture surface appearance is presented in Figure 93. Initiation life (Nsc) of coated Alloy 185 is compared to coated PWA 1480 in Figure 94. As expected, PWA 1480 is the superior alloy.

45

SECTION 11.   TASK XII – SPECIMEN PREPARATION

11.1 SPECIMEN DESIGN AND PREPARATION

The initial smooth section strain controlled fatigue tests showed a propensity to fail in the threaded section outside the monitored gage section. The smooth specimen geometry was subsequently redesigned. The new design had a smaller gage section diameter (0.63 cm versus 0.76 cm, 0.25 in. versus 0.30 in.) and finer threads. As a part of the new design, slight sockets were placed in the gage section to receive the ends of the extensometer to prohibit extensometer slipping. These sockets did not cause premature fatigue crack initiation. The original and new smooth specimen geometries are shown in Figure 95.

Specimen designs for the rectangular section, notched specimens are presented in Figures 96 through 98.

To facilitate SEM (Scanning Electron Microscope) inspection of the notch slip behavior, selected notched specimens were polished to about 4 rms surface finish.

Criteria used in designing the notched specimens and selecting their primary $(\bar{P})$ and secondary $(\bar{S})$ orientations included testability, parametric variation of possible deformation and fatigue life variables, and applicability of two dimensional analyses. A discussion of these specimen design considerations was presented in Reference 3.

11.2 PHYSICAL, THERMAL, AND MONOTONIC MECHANICAL PROPERTIES

Thirteen (13) monotonic tensile tests were conducted to supplement the tensile tests conducted in the Base Program.

Table 19 summarizes the results of these tests along with previously generated uncoated monotonic data. The reduction in area was not reported because many of the final cross sections at the lower temperatures were either highly elliptical due to coarse slip on octahedral planes or were multi–planar (also on the octahedral slip planes). Figure 99 is a plot of the 0.2% offset yield strength. A summary of tensile specimen ovalization was presented in Reference 3.

46

SECTION 12. TASK XIII – SELECTION OF CANDIDATE CONSTITUTIVE AND LIFE PREDICTION MODELS

12.1 SPECIMEN STRUCTURAL ANALYSIS

Three dimensional elastic structural analyses of the Option 1 specimen designs were conducted for use in the life prediction models. MARC finite element and BEST3D boundary element (which was developed under NASA contract NAS3–23697) codes were used in this effort.

Figure 100 shows the typical BEST3D mesh used in the analyses and Table 20 summarizes the results. Stress values were normalized by the net section stress to give a stress concentration factor. Figures 101 through 103 show the variation of the principal stress on the surface of the notch and the maximum octahedral slip system shear stress for <001> <100> oriented specimens with a net section stress of 689 MPa (100 Ksi). A curve was fit through the BEST3D nodal points based on a more refined two dimensional boundary element analysis. These plots show that the location of maximum principal stress is not at the minimum section (theta = 0) as would be expected for an isotropic material. Table 20 also includes the results for an isotropic material using the same BEST3D mesh.

The finite element analyses were conducted using the K.3 version of the MARC program. This version of the MARC program calculates stresses at nodal points and they have been found to agree well with BEST3D boundary element results. The MARC analysis was chosen for all future analysis in the program because of its widespread use in industry and its nonlinear material capability. Figure 104 shows the finite element meshes used for each of the specimens. Prior to the anisotropic analyses, an isotropic material analysis was conducted to evaluate the accuracy that could be expected from the mesh being used. Results were within 3% of handbook solutions for the geometries. Figure 105 shows the results of the anisotropic stress analyses. The stresses shown are normalized to net section stress and correspond to the maximum values whether they are mid–plane or locations near the lateral surface of the specimen. It is only in the <213> and the <111> primary orientations that restrained out–of–plane warping leads to peak stresses near the lateral surface. In all other orientations, the peak stresses occur at the mid–plane. (It is interesting to note that fatigue initiation sites in the <111> primary oriented specimens did not appear to be at the lateral surface, indicating that the actual restraints during testing may not be as severe as those modeled by restrained lateral motion.) The principle stresses shown in Figure 105 are parallel to the contour of the notch at the angular location indicated. The slip system shear stress shown (also normalized to net section stress) is that corresponding to the octahedral slip system having the highest shear stress. All six components of global stress were used in determining the slip system shear stress.

12.2 CANDIDATE CONSTITUTIVE MODELS

The slip system based constitutive model developed in the Base Program was selected for the low temperature notched regions. A major difficulty with this model and all "unified" material models is that the basic mathematical formulation is strain rate dependent and so has difficulty in reproducing rate independent behavior at low temperatures. This difficulty has been overcome by incorporating a subroutine in the model which changes the applied time increment to one which will result in a constant reference strain rate for low temperatures. The transition between rate dependence and rate independence occurs gradually between 816°C (1500°F) and 704°C (1300°F) (see Section 8.2.3).

The fatigue data obtained indicates that the total stress excursions in the notches are less than twice the 0.2% yield strength for low cycle fatigue lives greater than approximately 1000 cycles. See Figures 99 and 106. This conclusion is based on elastic finite element analyses of the specimens which should produce an upper bound on the stress range. This indicates that large cyclic inelastic strains are not likely to be encountered in the notches. In addition, only small cyclic inelastic strains were observed in strain controlled fatigue tests whose lives were greater than approximately 1000 cycles. In contrast, significant inelasticity is expected during the initial loading portion of the fatigue cycle. So the efforts in the constitutive model development focused on the monotonic response of the material. This was important for determining the mean stress in the notches.

12.3 CANDIDATE LIFE PREDICTION MODELS

Four candidate life prediction models were identified for evaluation:

1) Hysteretic energy (Reference 15)

2) Maximum principle stress

3) Octahedral slip system shear stress

4) Stress range, mean stress (Reference 58)

SECTION 13.   TASK XIV – CYCLIC LIFE AND CONSTITUTIVE BEHAVIOR

The intent of this program was to develop constitutive and life models applicable to relatively low temperature (i.e. below the creep regime) notched regions typical of attachment regions of single crystal components. The dominant loading in the attachment region of a turbine blade is centrifugal loading which may lead to localized tensile yielding in notched details at maximum rotor speed. Reverse yielding is not expected when rotor speed is decreased. Therefore, the relevant fatigue cycle can be idealized as a strain controlled, one way fatigue cycle which may produce localized plasticity. The test conditions employed in this program have been selected to simulate these conditions.

13.1 TEST FACILITY

The tests for Option 1 were conducted on two MTS servohydraulic test machines available at United Technologies Research Center. Strain controlled tests employed standard MTS extensometry and were controlled by a DEC computer running MTS BASIC. Special purpose control and data acquisition programs provided control for the constitutive and strain controlled fatigue tests. Load controlled fatigue tests were controlled by the standard function generators supplied with each system. Specimens were heated with standard resistance furnaces.

13.2 CYCLIC LIFE TESTS

13.2.1 Specimen Inspection Technique

A sensitive die penetrant had been used to inspect for cracks but without success in spite of frequent inspections. That inspection technique is capable of detecting cracks as small as 0.25 mm (0.010 in.). Inspection intervals were as frequent as 2000 cycles. More frequent inspections were impractical due to the large number of tests conducted and the life regime being tested (5000 to 100000 cycles).

All efforts to find developing fatigue cracks failed. Scanning Electron Microscopy has shown that the steady fatigue crack zone was confined to a very small surface crack length which in many cases was near the detection limits of standard wink zyglo techniques. Consequently, inspections for crack initiation were suspended and specimens were cycled to failure.

13.2.2 Fatigue Tests

Smooth Fatigue

Strain controlled fatigue tests were conducted on 6.35 mm (0.25 inch) diameter bars having a gage length of 25.4 mm (1.0 inch). All tests were conducted at a strain rate of 0.1% per minute. All specimens were loaded in tension first to the maximum strain limit. The minimum strain limit for the majority of the tests was zero although some non–zero R ratio (minimum strain/maximum strain) tests were included in the data set. Tests conditions and resulting stresses and lives for all tests are shown in Appendix G. The majority of the tests were conducted at 649°C (1200°F).

Fatigue cracks were observed to initiate from micropores located at the surface or very near the surface of the specimens. No cracks were observed to start from surface features such as machining marks or crystallographic slip steps. Typically the fatigue cracks were observed to originate at micropores and progress along a plane perpendicular to the loading direction. Final fracture occurred along <111> type crystallographic planes.

Notched Fatigue

Notched fatigue tests were conducted in load control at a constant temperature. Test conditions and results for all tests are given in Appendix H.

The locations of the maximum principal stress and the maximum principal strain do not coincide in the <001> <100> oriented specimens. Typically, the fatigue crack initiation sites are at the maximum principal stress location as illustrated in Figure 107. As with the smooth specimens, fatigue cracks were observed to initiate from micropores at the specimen surface or very near the surface. The majority of the initiation sites also occurred at the mid–plane of the specimen.

49

Secondary Orientation Effect

X-ray analyses were conducted on several <001> oriented smooth specimens to determine the secondary orientation of the fatigue crack initiation sites. The results of these analyses are shown in Table 21. At 649° (1200°F), three of the four specimens examined had initiating pores at a circumferential location corresponding to the point where the <010> crystal axes coincides with the surface normal. This trend does not appear to hold at higher temperatures or for HIP'd material as indicated in Table 21. Secondary orientation of initiation sites in smooth <111> fatigue samples were identified to determine if there was a similar trend. The results are shown in Table 22.

The initiation sites were measured from either the <011> or the <112> type crystal directions which are 30 degrees from each other and lie in the plane perpendicular to the <111> load axis. Table 22 shows that there is not a strong correlation between the initiation site and these two directions. Taken in combination with the other results for the <001> specimens, it is concluded that there is at most a weak correlation of initiation site with secondary crystal direction. However, a much larger number of samples would be needed to reach a definitive conclusion.

Porosity Effect

Several smooth and notched specimens were examined to quantify pore size at the initiation sites. The initiating pores were always either surface connected or very slightly (approximately one pore diameter) subsurface and could be classified as either very regular shaped micropores or irregular shaped shrinkage pores. Even though quantifying the size of shrinkage pores is very subjective, no correlation could be drawn between pore size or shape and fatigue life.

Hot Isostatically Pressed Material Data

A small amount of fatigue testing was conducted using PWA 1480 material that had been Hot Isostatically Pressed (HIP) to eliminate micropores prior to machining. Micropores were observed to be fatigue crack initiation sites in the testing described above. Individual test conditions for the HIP specimens are included in Appendices G and H.

Substantial life improvements are observed for HIP'd material when compared to un-HIP'd material. The fatigue crack initiation sites of HIP'd specimens correspond to the maximum stress location in the notch. They are neither casting pores (as would be expected since the material is HIP'd to eliminate pores) nor slip bands at the surface. The smooth HIP'd data, although limited, indicates that a life improvement remains at 871°C (1600°F) for <001> bars (although possibly somewhat diminished from that observed at 649°C (1200°F)), but virtually no life improvement remained at 871°C (1600°F) for the HIP'd <111> specimen tested.

13.3 CONSTITUTIVE TESTS

Two room temperature tensile tests were conducted using tube specimens rather than the solid cylindrical specimens used in previous constitutive tests. Unlike the solid specimens, the tube specimens exhibited very fine, evenly distributed slip lines throughout the gage section. The stress-strain response of the tube specimen did not display an unstable strain burst at the onset of yielding. The 0.2% yield strength measured from the tube specimens compared very well to the solid bar data.

Strain gage surveys were conducted on two mild notched specimens to provide an experimental evaluation of the constitutive model. One specimen had a <001> <100> orientation, the other was oriented in the <011> <01-1> direction. Strains were recorded at several different load levels and the residual strains were measured after unloading from several of the peak load levels. Figure 108 is the strain history of one of the strain gages on the <011> <01-1> specimen. This strain gage was located on the lateral surface of the specimen, approximately 0.025 inches from the maximum principal stress location. One very important observation is that there was very little cyclic inelasticity even for peak loads as high as 3500 lbs. This corresponds to an elastic notch stress which is more than 30 percent higher than the peak stress levels in fatigue (> 1000 cycles in life). This implies that very little cyclic inelasticity is occurring in the fatigue life regime of interest.

SECTION 14. TASK XV - FINAL SELECTION OF CONSTITUTIVE AND LIFE PREDICTION MODELS FOR UNCOATED SINGLE CRYSTAL MATERIALS AT ROOT ATTACHMENT TEMPERATURES

14.1 CONSTITUTIVE MODEL

In order to apply the life model of Equation 83 (Section 14.2.1), the stress range, mean stress and inelastic strain range in the notched specimens must be calculated. As discussed previously, little or no cyclic inelasticity is expected so that inelastic strain range can be taken to be zero and the stress range can be obtained from conventional elastic stress analyses. However, a viable nonlinear analysis is needed to determine the mean stress in the notch. Because the notch is expected to yield only during the initial loading portion of the fatigue cycle, only the monotonic tensile response is required. The mean stress is simply the stress achieved during initial loading minus half the (elastic) stress range.

The Base Program single crystal constitutive model (with Set B constants) was used to simulate room temperature strain gage surveys conducted on the mild notched specimen shown in Figure 104. The results are shown in Figures 109a and 109b for the strain gage test of a <011> <01-1> specimen. The overall correlation of the analysis and the data is encouraging especially at load levels that were used in the fatigue program. Figure 110 shows that the nonlinear analysis predicts a stress strain response close to the uniaxial stress strain curve in the appropriate orientation.

Figures 111a and 111b show room temperature monotonic data and simulations. The overall correlation is fairly good. However,it should be noted that the model does not match the observed ordering of the limit stress with orientation. The model predicts that the <011> and <213> curves fall between the <001> and <111> curves. The data shows a different trend. On the other hand, there is not a great deal of variation in the numerical values of limit stress between the orientations tested. Figures 112a and 112b make the same comparisons at 649°C (1200°F). Once again the ordering of the model is not consistent with the data and unlike the room temperature results, there are large numerical differences between the actual limit stresses. From these two comparisons, it can be concluded that use of the model at room temperature should produce reasonable inelastic stress levels, within approximately 20 Ksi (the scatter in the data itself) but may give incorrect orientation trends within the range. But at 649°C (1200°F), there is considerably more orientation dependence as seen in Figure 112, and the constitutive model did not predict the correct ordering of the data. It was therefore concluded that the constitutive model could not be used to determine mean stress at 649°C (1200°F).

However, the need to calculate the yield stress in the notch remains. The procedure introduced by Neuber (Reference 59) has been used to this end since his procedure does not require a sophisticated constitutive model, but can instead use experimental stress strain curves. To apply the Neuber procedure, the product of stress and strain at the maximum stress location is determined from an elastic finite element analysis. The actual stress and strain values are then assumed to lie on the experimental stress strain curve for the relevant orientation.

In an attempt to evaluate this procedure, nonlinear finite element analyses (FEA) were conducted using a "model" anisotropic material and the FEA results were compared to the Neuber results. The constitutive model discussed above was taken to describe the model material. Evaluations were made for the thin mild notched specimens having two crystallographic orientations: <001> in the loading direction with <100> normal to the notch and <111> in the loading direction with <01-1> normal to the notch.

A Neuber parameter at a reference (elastic) loading condition was determined from an initial elastic finite element analysis. The Neuber parameter is simply the product of stress and strain components parallel to the contour of the notch:

$$P_0 = \sigma_0 \, \epsilon_0 ,$$

(81)

where σ_0 = stress at a reference elastic condition,

ϵ_0 = strain at a reference elastic condition.

In this evaluation, stress and strain at the finite element integration point closest to the notch surface are used. It should be noted that in general, all components of stress and strain are present at these integration points since they do not lie on a free surface. However, only the components of stress and strain parallel to the contour of the notch are considered here.

Because both stress and strain can be scaled by the applied load in an elastic analysis, the Neuber parameter at any other nominal stress level, S, is

$$P = P_0 (S/S_0)^2 , \qquad (82)$$

where S_0 = Nominal stress at the reference condition,

P_0 = Neuber parameter at the reference condition.

The Neuber procedure assumes that the value of this parameter is the same whether an elastic or an inelastic analysis is performed. Figure 113 shows the value of this parameter obtained from the nonlinear FEA compared to Equation 82. The reference elastic conditions required in Equations 81 and 82 were taken from the first (elastic) increment of loading in the nonlinear stress analysis. Figure 113 shows good correlation even for nominal stresses that approach net section yielding.

Finite element and Neuber predictions of the individual stresses and strains were compared at several locations in the notches. Figures 114 through 117 show the ratio of the Neuber and the FEA results as a function of the applied nominal stress on the specimen. The ratio of the Neuber parameter derived from Equation 82 and that obtained from the FEA are also shown in these figures. Results are shown for two locations in the notch; at theta = 3.8 and at theta = 22.4 degrees (see Figure 118). Theta = 0 corresponds to the maximum stress location in the <111> <01-1> specimen and theta = 22.4 degrees corresponds to the maximum stress location in the <001> <100> specimen. The model material's stress strain response, which "partitions" the Neuber parameter into individual stresses and strains, was obtained from the constitutive model under uniaxial conditions. Figures 119 through 122 show the corresponding stress–strain responses for these locations. These figures show that there are significant differences between the two analyses. If it is assumed that the finite element analyses give the correct results, then the Neuber procedure must be modified.

A modification of the Neuber procedure certainly must address the multiaxial stress state since it is clear from Figures 119 through 122 that such high stresses can only be achieved in the presence of a substantial multiaxial stress state. The direct components of stress at the last load step of the nonlinear analysis are shown in these figures. Shear stresses are also present but are an order of magnitude smaller than the direct components. A suggested modification would be to perform the Neuber calculations based on deviatoric stress and strain rather than the direct component. Figure 123 shows the product of the deviatoric stress and strain at different applied nominal stresses for the <001> <100> mild notched specimen. This parameter appears to vary in a manner similar to Equations 81 and 82 suggesting that such a parameter could be used in conjunction with an experimental effective stress–strain curve to calculate the value at any desired load level. In order to recover the direct component of stress at any nominal stress level, the degree of multiaxiality would also have to be known. Figure 124 shows that the degree of multiaxiality (measured as the ratio of the hydrostatic stress or strain component to the direct component) changes as yielding proceeds but that the product of these ratios remains approximately equal to that for the elastic case. These two figures suggest an approach for modifying the Neuber procedure for multiaxiality. But to further develop this approach would require a considerable effort which is beyond the scope of this program.

14.2 LIFE PREDICTION MODEL

The majority of the tests were conducted at 649°C (1200°F) and only this data was used to develop fatigue life prediction models.

The correlations reported in Reference 15 and the Base Program (Reference 3) were encouraging, but an inelastic strain based model such as hysteretic energy was considered difficult to apply to the predominantly elastic cyclic loading and conditions found in the relevant life regime.

The octahedral slip system shear stress at the initiation site was evaluated as a correlating parameter. The results are shown in Figures 125 and 126. Figure 125 shows that the smooth and mild notched

data are segregated by this parameter. As shown in Figure 126, the apparent slope difference between thin and thick specimens is no longer apparent. However, it is clear that the parameter does not account for orientation properly since the thick <111> specimens fall well below the rest of the data. While it is possible that different surface finish conditions could account for the segregation of the smooth and the notched data seen in Figure 125, the unexplained orientation dependence seen in Figure 126 was not acceptable. So a slip system based fatigue model was not pursued further.

Correlations were tried using the principal stress range as a correlating parameter. As shown in Figure 127, the smooth specimen and mild notched specimen data were fairly well correlated using this parameter. However, it was noted that this parameter did not fully account for orientation effects. Furthermore, as shown in Figure 128, thick specimens appeared to have a different slope on the S-N diagram than the smooth and mild notched specimens. So a fatigue model based only on maximum principal stress was judged inadequate. The model finally selected is discussed below.

14.2.1 Smooth Fatigue

Figures 129 and 130 show the correlation between separation life and either strain range or stress range. Clearly, stress range more nearly collapses the fatigue data. However, a clear orientation dependence is still apparent in Figure 130. The <001> data and the <111> data fall into two separate groups as indicated by the mean life lines. Figure 131 further illustrates this segregation by plotting actual fatigue life versus the life calculated from a single trend line through all of the data in Figure 130. Nearly all of the <001> specimen lives are overpredicted by the single trend line while nearly all of the <111> specimen lives are underpredicted.

The observed mean stress levels for each of the strain controlled tests are plotted in Figure 132 versus the observed stress range. The <001> specimens have higher mean stress levels than the <111> specimens for a given stress range. This agrees qualitatively with the trend lines shown in Figure 130. That is, the <001> specimens have lower lives than <111> specimens for the same stress range. The difference in mean stress levels is a consequence of the different yield behavior of the two orientations during the first cycle of loading. Referring to the 649°C (1200°F) tensile curves in Figure 112, it can be expected that a <001> specimen would achieve a higher peak stress during the first cycle of loading than would a <111> specimen. Subsequent elastic unloading from these different peak stress levels produces a higher mean stress for <001> specimens than for <111> specimens. Since this material neither cyclicly hardens nor cyclicly softens, the mean stress level is set during the initial loading. Figure 132 shows the possible stress range and mean stress values for fatigue cycles with a minimum strain of zero and an elastic-perfectly plastic idealization of the <001> and <111> tensile behavior. For the sake of illustration in Figure 132, the yield point has been taken to be the actual 0.2% yield strength for the respective orientations.

It should be noted that a two parameter model based on stress range and mean stress has a limitation for strain controlled conditions tested in this program. That is, for monotonic stress strain curves with little or no strain hardening (which is the case for all orientations except <001>), the mean stress approaches zero and the stress range will not increase appreciably beyond twice the yield stress. So a fatigue model based only on stress range and mean stress could not be expected to apply to the very low cycle life regime where cyclic inelastic strains are significant. As discussed above, fatigue cycles with significant cyclic inelasticity would not be expected in the notched regions of turbine blade attachments. However, in order to broaden the data base used in the model development and to provide a more general model, these data points have been included. The following three parameter model was adopted and fit to the smooth specimen data set.

$$N = A \, \Delta\sigma^B \, 10^{C\sigma_m} \, 10^{D\Delta\epsilon_p} \tag{83}$$

where N =   separation life (cycles),
          $\Delta\sigma$ =   stress range (psi),
          σ_m =   mean stress (psi),
          $\Delta\epsilon_p$ =   cyclic inelastic strain (in./in.)

and	A	=	1.291 E43
	B	=	-7.339
	C	=	-8.795 E-6
	D	=	-132.2

Figure 133 and Table 23 show actual lives versus lives calculated using this three parameter model. As expected, the segregation of the data by orientation has been significantly reduced and those specimens with significant cyclic inelastic strain are also reasonably well predicted.

14.2.2 Notched Fatigue

Figure 134 shows the correlation of the thin, mild notched data with stress range alone. The limits of the <001> and <111> specimen data are indicated for clarity along with the mean trend line for the smooth <001> specimens. The single data point that lies outside of the limit lines corresponds to a specimen (JJB105A) tested at a maximum load very near net section yielding. This test condition is outside of the load regime expected in gas turbine blade attachment. Consequently this test was not considered in developing the fatigue model and will not be included in the following data analysis.

A significant orientation dependence is apparent in Figure 134 which is similar to that seen in the smooth specimen data. For the same stress range the <111> specimens have lives that are on the average an order of magnitude longer than the <001> specimen. In addition, Figure 134 shows considerably more scatter in the mild notched data than in the smooth specimen data. The apparent scatter is a factor of 60:1 for the <001> data and a factor of 90:1 for the <111> data. A significant portion of this scatter has been found to be associated with the time period during which different groups of specimens were manufactured. The time at which the raw bars were cast, heat treated and machined to final shape was different for different groups or "lots" of specimens. With the large number of specimens used in the program, it was not possible to coordinate each phase of manufacturing to occur at the same time. Nor was it possible to systematically vary the specimen lots with test conditions and orientations to rank or normalize them. Table 24 shows the combinations of specimen geometries, orientations and lot numbers tested. Within the time constraints and the specimens available, as many duplicate tests as possible were conducted to better define the lot-to-lot variations. Figures 135 and 136 show the variation in fatigue lives at given stress level as a function of lot number. The largest variation between lots was observed in the <111> specimens, with at least a 20:1 life variation between typical lives and 40:1 variation between the extremes. There were insufficient specimens available to conduct a more extensive characterization of the scatter or to isolate the causes.

The fatigue model given in Equation 83 was used to predict the notched data. Predicted lives versus actual lives are shown in Figure 137 for the mild notched data and in Figure 138 for all notched geometries. The orientation dependence noted above has been greatly reduced. Considering only the mild notched data, the average difference between <001> and <111> specimens has been reduced from a factor 10:1 to a factor of 3:1. The scatter in this data set remains approximately the same as seen above.

To calculate the mean stress for Equation 83, a simple correction was made to the Neuber stresses based on the finite element analysis of the thin mild notched specimen using the Base Program single crystal material model. Figure 139 shows the error in the Neuber stress at the maximum stress location as a function of the Neuber parameter. This error curve was assumed to apply for PWA 1480 and all notch configurations tested in this program. The maximum stress for each test condition was calculated by the Neuber procedure using experimental stress strain curves and divided by the Neuber correction given in Figure 139. Table 25 shows the elastic stresses and strains for a unit reference stress that were used in the Neuber calculations (Equations 81 and 82). Table 25 also shows the crystallographic orientation at the maximum stress location and the orientation of the experimental stress strain curve used in the analyses. For the <001> <100> oriented specimens, experimental stress strain curves were not available in the orientation exactly matching the crystal direction at the maximum stress location. For these specimens the <001> experimental curves were used. The corrected maximum stress was then used to calculate mean stress. (Mean stress is the peak stress minus one half the stress range.)

Figure 138 shows that virtually all of the notched specimens have longer lives than predicted. Taken as a whole, the notched data is an order of magnitude longer in life than predicted. Possible inaccuracies in the stress calculations were explored as a source of this difference. The stress range calculation is believed to be quite accurate since it is an elastic calculation and the stress ranges tested are insufficient to cause cyclic plasticity. A small error may be due to the use of integration point values rather than values extrapolated to the surface. Comparison of three dimensional finite element and a plane strain Boundary Element analysis (which is presumed to be more accurate) showed that this error was less than 4 percent, with the FEA results giving somewhat higher stresses. A 4% overprediction of the stress range would lead to a 35% underprediction of life. An error of 35% in the stresses would be required to produce the observed order of magnitude difference in life. The mean stress calculation is likely to be less accurate. Figure 140 shows the stress range – mean stress pairs for smooth and notched specimen test conditions. For the smooth data, the values are measured, whereas the values are calculated for the notched data by the method discussed above. The effect of the notch multiaxiality can be seen in the higher mean stresses for a given stress range. This would lead to lower predicted lives for a given stress range. However, it should be noted that the model constants in Equation 83 would require approximately a 115,000 psi error in mean stress to account for the approximate order of magnitude error in the prediction. Even though the mean stress calculation must be viewed as approximate, such a large error is not likely. By examining Figures 120 and 122, which correspond to the maximum stress locations in mild notch specimens, the error in mean stress cannot be more than approximately 40,000 psi. An error of this magnitude would predict a life 45% too low.

Another possible reason for the discrepancy may be associated with different processing of the smooth and notched specimens. As previously noted, scatter as large as 40:1 can be attributed to different lots of notched specimens. Similar processing variations cannot be ruled out as a source of difference between the smooth and the notched data.

A third possibility is an expected difference in the crack growth portion of the failure lives. No crack growth data was obtained in either the smooth or the notched specimen tests. However, it can be expected that the crack growth portion would be longer in the notched specimens.

Being unable to determine the source of the difference between the smooth and notched data, a practical engineering approach was adopted: the notched data alone was used to develop a fatigue model. The smooth data was used only to provide the functional form of the model. That is, the general form of Equation 83 was assumed to apply and the model constants were determined from the notched data alone. Because no cyclic inelasticity was present, the plastic strain range term was not included in the model. So the resulting notch fatigue model is:

$$N = A\Delta\sigma^B 10^{C\sigma_m} \tag{84}$$

where N = separation life (cycles),

$\Delta\sigma$ = stress range (psi),

σ_m = mean stress (psi),

and A = 1.496 E43

B = –7.181

C = –8.440 E–6

Figure 141 and Table 26 show the lives predicted using Equation 84 versus actual fatigue lives. Considering only the thin, mild notched data, there is still a 3:1 difference between <001> and <111> data. The statistical significance of this difference is questionable in view of the demonstrated lot–to–lot scatter. Considering the entire notched data set, there is no significant difference between the orientations and no clear trends with specimen geometry. It is therefore concluded that, within the scatter of the data, Equation 84 provides a reasonable fatigue model for notched geometries.

14.2.3 Hot Isostatically Pressed Material Data

Figure 142 compares the actual and predicted fatigue lives for these notched data. As seen in Figure 142, there is an average life improvement of approximately an order of magnitude for the HIP material relative to the conventional material. All the HIP data is shown except specimen JJB86A (see Table 26). This specimen was tested at a nominal stress approaching net section yielding which was not in the loading regime of interest. However, this test condition can be compared directly to a non-HIP specimen JJB105A, which is also contained in Table 26. This comparison shows a significant life enhancement due to HIP even for this high stress level.

SECTION 15. TASK XVI – MODEL VERIFICATION ON PRIMARY SC MATERIAL FOR BLADE ROOT ATTACHMENT

A verification fatigue test was conducted on a specimen designed to simulate the load transfer features in a turbine blade attachment. Figure 143 shows the test specimen and its loading fixture. The specimen was machined with the <001> crystal direction in the loading direction and the <100> crystal direction in the plane of the specimen. A plane strain elastic Boundary Element analysis was conducted to determine stress and strain at the maximum stress location. Stress range and mean stress were then calculated by the procedure outlined previously. Details of the verification specimen such as stress levels, test conditions and predicted lives are included in Appendix H for convenience but this test result was not used to develop model constants. This verification test was reasonably well predicted by the notched fatigue model given by Equation 84 (see Figure 141).

SECTION 16. REFERENCES

1. Swanson, G.A., I. Linask, D.M. Nissley, P.P. Norris, T.G. Meyer and K.P. Walker, "Life Prediction and Constitutive Models for Engine Hot Section Anisotropic Materials Program, Annual Status Report, " NASA CR-174952, February, 1986.

2. Swanson, G.A., I. Linask, D.M. Nissley, P.P. Norris, T.G. Meyer and K.P. Walker, "Life Prediction and Constitutive Models for Engine Hot Section Anisotropic Materials Program, Second Annual Status Report," NASA CR-179594, April, 1987.

3. D.M. Nissley and T.G. Meyer, "Life Prediction and Constitutive Models for Engine Hot Section Anisotropic Materials Program, Interim Report," NASA CR-189222, August, 1992.

4. D.M. Nissley, "LAYER User and Programmer Manual," NASA CR-187038, October, 1990.

5. Kraus, H., Creep Analysis, John Wiley & Sons, Inc., New York, Chapter 2, 1980.

6. Walker, K.P., "Research and Development Program for Nonlinear Structural Modeling with Advanced Time-Temperature Dependent Constitutive Relationships," NASA CR-165533, November, 1981.

7. Lindholm, U.S. et al, "Constitutive Modeling for Isotropic Materials (HOST)," NASA CR-174718, May 1984.

8. Moreno, V., "Development of a Simplified Analytical Method for Representing Material Cyclic Response," NASA CR-168100, January, 1983.

9. Stowell, E.Z., et al, "Predicted Behavior of Rapidly Heated Metal in Compression," NASA TR R-59, 1960.

10. Stowell, E.Z., "The Properties of Metals Under Rapid Heating Conditions," J. Aeron. Sci., pp. 922-923, December, 1957.

11, Stowell, E.Z., "A Phenomenological Relation Between Stress, Strain Rate, and Temperature for Metals at Elevated Temperature," NASA TR-R1343, February, 1957.

12. Hill, R., "A Theory of the Yielding and Plastic Flow of Anisotropic Metals," Proc. Royal Society of London, Ser. A, Vol. 193, pp. 281-297, 1948.

13. Lee, D., Zaverl, F., Shih, C.F. and German, M.D., "Plasticity Theories and Structural Analysis of Anisotropic Metals," Report No. 77CRD285, General Electric Corporate Research and Development Center, Schenedtady, New York, 1977.

14. Walker, K.P. and Jordan, E., "First-Annual Report on NASA Grant NAG-512," 1985.

15. DeLuca, D.P. and B.A. Cowles, "Fatigue and Fracture of Advanced Blade Materials, Final Report," AFWAL-TR-84-4167, February, 1985.

16. Linask, I. and J. Dierberger, "A Fracture Mechanics Approach to Turbine Airfoil Design," ASME Gas Turbine Conference and Products Show, March 2-6, 1975.

17. Anton, D.L. and Fine, M.E., "Fatigue Crack Evolution in Overaged Ni-14.4 at Percent Al Alloy with Coherent Precipitates," Materials Science and Engineering, Vol. 58, 1983, pp. 135-142.

18. Leverant, G.R. and Gell, M., "The Elevated Temperature Fatigue of a Nickel-Base Superalloy, Mar-M200," Trans. Metallurgical Society of AIME, Vol. 245, 1969, pp. 1167-1173.

19. Gell, M., Leverante, G.R. and Wells, C.H., "The Fatigue Strength of Nickel–Base Superalloys," Achievement of High Fatigue Resistance in Metals and Alloys, STP 467, ASTM, 1970, pp. 113–153.

20. Barkalow, R.H., "Effect of Cyclic Strain/Temperature Exposure on Fatigue Life of Coated Turbine Alloys," Interim Report to AFWAL/ML, FR–18605, Pratt & Whitney, September, 1984.

21. Manson, S.S., "Behavior of Materials Under Conditions of Thermal Stress," NACA TN–2933, 1953, and Coffin, L.F., "A Study of the Effects of Cyclic Thermal Stress In a Ductile Metal," Trans. ASME, Vol. 76, 1954, p. 931.

22. Ostergren, W.J.: "A Damage Function and Associated Failure Equations for Predicting hold Time and Frequency Effects in Elevated–Temperature Low–Cycle Fatigue," Jl. of Testing and Evaluation, Vol. 4, No. 5, Sept. 1976, pp. 327–339.

23. Heine, J.E., J.R. Warren and B.A. Cowles, "Thermal Mechanical Fatigue of Coated Blade Materials, Final Report," WRDC–TR–89–4027, June 1989.

24. Nelson, R.S., Schoendorf, J.F.,and Lin, L.S.: "Creep Fatigue Life Prediction for Engine Hot Section Materials (Isotropic), Interim Report." NASA CR–179550, December, 1986.

25. Moreno, V., Nissley, D.M., and Lin, L.S.: "Creep Fatigue Life Prediction for Engine Hot Section Materials (Isotropic), Second Annual Report." NASA CR–174844, December, 1984.

26. Leis, B.N. and T.P. Forte, "Nonlinear Damage Analysis: Postulate and Evaluation," Final Report on Contract NAS3–22825 to NASA Lewis Research Center, February, 1983.

27. MARC General Purpose Finite Element Program, MARC Corporation, Palo Alto, CA.

28. Cassenti, B.N.: "Research and Development Program for Nonlinear Structural Modeling with Advanced Time–Temperature Dependent Constitutive Relationships, Vol. I – Theoretical Discussion." NASA CR–168191, July 1983.

29. Sabol, G.P. and Stickler, R. (1969) Microstructure of Nickel–Based Superalloys, Phys. Stat. Sol. 35, p.11.

30. Pope, D.P. and Ezz, S.S. (1984) Mechanical Properties of Ni_3Al and Nickel–Base Alloys with High Volume Fraction of g', Int. Metals Reviews, 29, No. 3, p. 136.

31. Takeuchi, S. and Kuramoto, E. (1973) temperature and Orientation Dependence of the Yield Stress in Ni_3Ga Single Crystals, Acta Met., 21, p. 415.

32. Lall, C., Chin, S. and Pope, D. (1979) The Orientation and Temperature Dependence of the Yield Stress of $Ni_8(Al,Nb)$ Single Crystals, Met. Trans., 10A, p. 1323.

33. Hirth, J.P. and Lothe, J. (1982) Theory of Dislocations, 2nd Edition, p. 314.

34. Paidar, V., Pope, D.P. and Vitek, V. (1984) A Theory of the Anomalous yield Behavior in $L1_2$ Ordered Alloys, Acta Met., 32, p. 435.

35. Umakoshi, Y., Pope, D.P. and Vitek, V. (1984) The Asymmetry of the Flow Stress in $Ni_8(Al,Ta)$ Single Crystals, Acta Met., 32, p. 449.

36. Escaig, B. (1968) J. Phys., 29, p. 225.

37. Shah, D.M. and Duhl, D.N. (1984) The Effect of Orientation, Temperature and Gamma Prime Size on the Yield Strength of a Single Crystal Nickel–Base Superalloy, Proc. 5th Int. Symp. on Superalloys, ASM, Metals Park, Ohio, USA.

38. Greenberg, B.A., Ivanov, M.A., Gornostirev, Yu.N. and Karkina, L.E. (1978) Phenomenological Theory of Plastic Deformation with Several Types of Mobile and Immobile Dislocations, Phys. Stat. Sol. (a), 49, p. 517.

39. Paslay, P.R., Wells, C.H. and Leverant, G.R. (1970) An Analysis of Primary Creep of Nickel–Base Superalloy Single Crystals, ASME J. Appl. Mech., 37, p. 759.

40. Paslay, P.R., Wells, C.H., Leverant, G.R. and Burck, L.H. (1971) Creep of Single Crystal Nickel–Base Superalloy Tubes under Biaxial Tension, ASME J. Appl. Mech., 38, p. 623.

41. Brown, G.M. (1970) A Self–Consistent Polycrystalline Model for Creep under Combined Stress States, J. Mech. Phys. Sol., 18, p. 367.

42. Hutchinson, J.W. (1976) Bounds and Self–Consistent Estimates for Creep of Polycrystalline Materials, Proc. Roy. Soc. London, A348, p. 101.

43. Weng, G.J. (1983) The Influence of Fatigue Stress on the Creep Behavior of Metals, Acta met., 31, p. 207.

44. Lindholm, U.S., Chan, K.S. Bodner, S.R., Weber, R.M., Walker, K.P. and Cassenti, B.M. (1985) Constitutive Modelling for Isotropic Materials (HOST), NASA CR 174980.

45. Walker, K.P. and Wilson, D.A. (1983) Constitutive Modelling of Engine Materials, Wright Patterson Air Force Base Report FR 17911.

46. Kaufman, A, Laflen, J.H. and Lindholm, U.S. (1985) Unified Constitutive Models for Nonlinear Finite Element Structural Analysis, NASA Technical Memorandum 86985, presented at the 21st Joint Propulsion Conference, Monterey, California, USA, July 8–10, 1985.

47. Ramaswamy, V.G., Van Stone, R.H., Dame, L.T. and Laflen, J.H. (1984) Constitutive Modelling for Isotropic Materials (HOST), NASA CR 17485.

48. References [6 and 39 to 43] make extensive reference to the unified viscoplastic constitutive models of Sol Bodner, Jean Louis Chaboche, Ed Hart, Erhard Krempl, Paul Cernocky, Ray Krieg, Jack Swearengen, Jim Laflen, David Lee, Don Stouffer, Alan Miller, Dave Robinson, Kirk Valanis and Kevin Walker.

49. Asaro, R.J. and Rice, J.R. (1977) Strain Localization in Ductile Single Crystals, J. Mech. Phys. Sol, 25, p. 309.

50. Asaro, R.J. (1983) Micromechanics of Crystals and Polycrystals, Advances in Applied Mechanics, p. 1., Academic Press.

51. Hutchinson, J.W. (1970) Elastic–Plastic Behavior of Polycrystalline Metals and Composites, Proc. Roy. Soc. London, A319, p. 247.

52. Asaro, R.J. (1970) Geometrical Effects in the Inhomogeneous Deformation of Ductile Single Crystals, Acta Met., 27, p. 445.

53. Peirce, D., Asaro, R.J. and Needleman, A. (1982) An Analysis of Nonuniform and Localized Deformation in Ductile Single Crystals, Acta Met., 30, p. 1087.

54. Havner, K.S. (1981) Aspects of the Simple Theory of Rotation-Dependent Crystal Anisotropy, in Plasticity of Metals at Finite Strain: Theory, Experiment and Computation, pp. 318, Proceedings of Research Workshop held at Stanford University, June 29–July 1, 1981.

55. Hill, J.T.; Weber, R.M.; and Meyer, T.G.: "Constitutive Modeling for Isotropic Materials," Addendum to Second Annual Status Report, NASA CR–174980, 1985.

56. Ross, Phillip J.: Taguchi Techniques for Quality Engineering, McGraw-Hill Book Company, 1988, pp. 18–20.

57. NADC Contract N62269-83-C-0329: Thermal Fatigue Crack Propagation in Single Crystal Nickel-Base Superalloys.

58. Meyer, T.G. and Cruse, T.A., "Low Cycle Fatigue Life Model for Gas Turbine Engine Disks," Journal of Eng. Materials and Tech., Jan. 1980, Vol. 102, pp. 45–49.

59. Neuber, H., "Theory of Stress Concentration for Shear-Strained Prismatic Bodies With Arbitrary Nonlinear Stress-Strain Law," J. Appl. Mech. 28, 544–551, 1969.

APPENDIX A

PWA 286 CONSTITUTIVE DATA

SERIES 1

1000°F PWA 286 BULK (HIP); UNEXPOSED

STRAIN
(in/in)

STRESS
(psi)

x10⁵
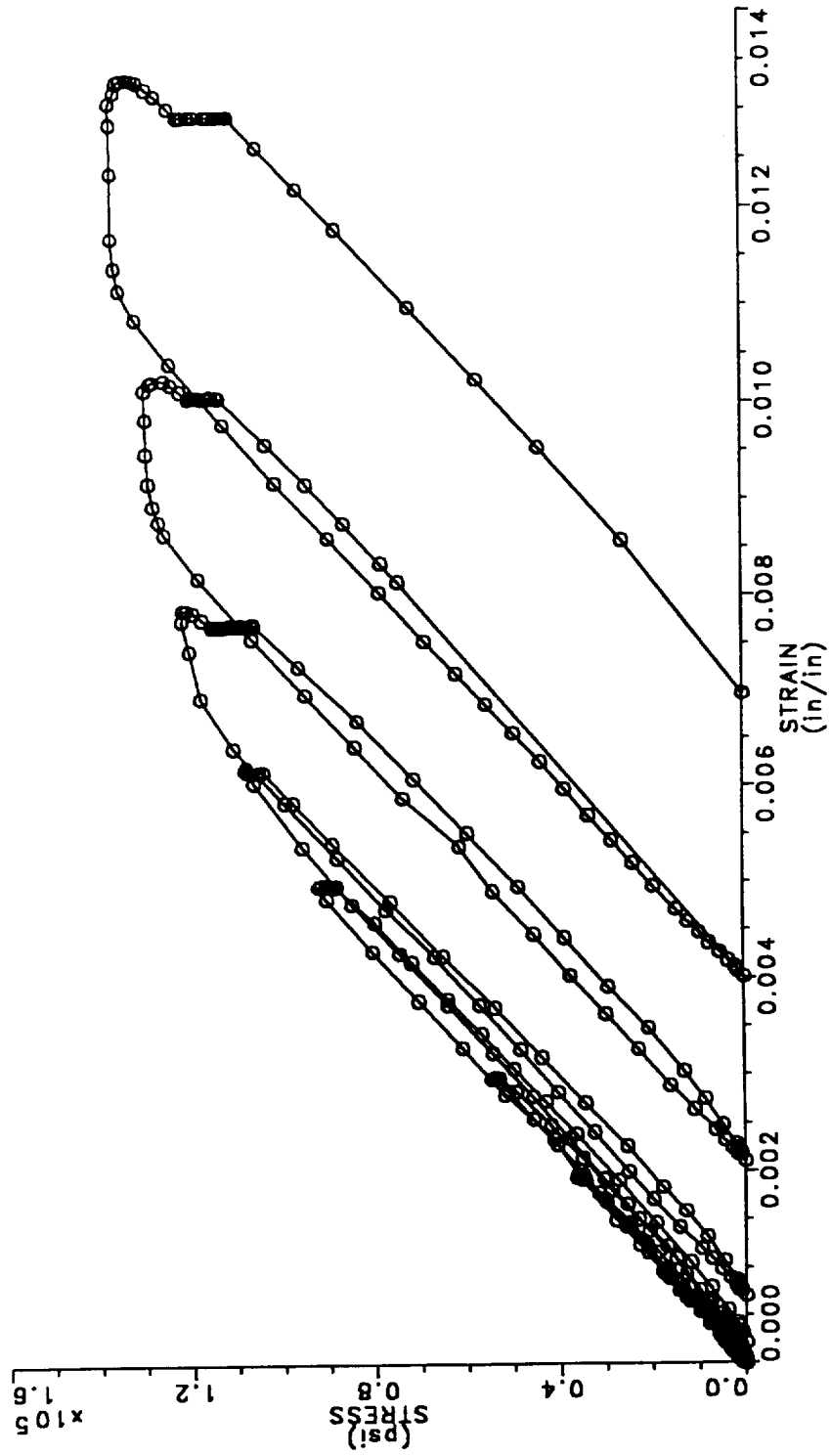
1200° PWA 286 BULK (HIP); UNEXPOSED

1400°F PWA 286 BULK (HIP); UNEXPOSED

1400°F PWA 286 BULK (HIP); EXPOSED 100 HRS AT 2000°F

66
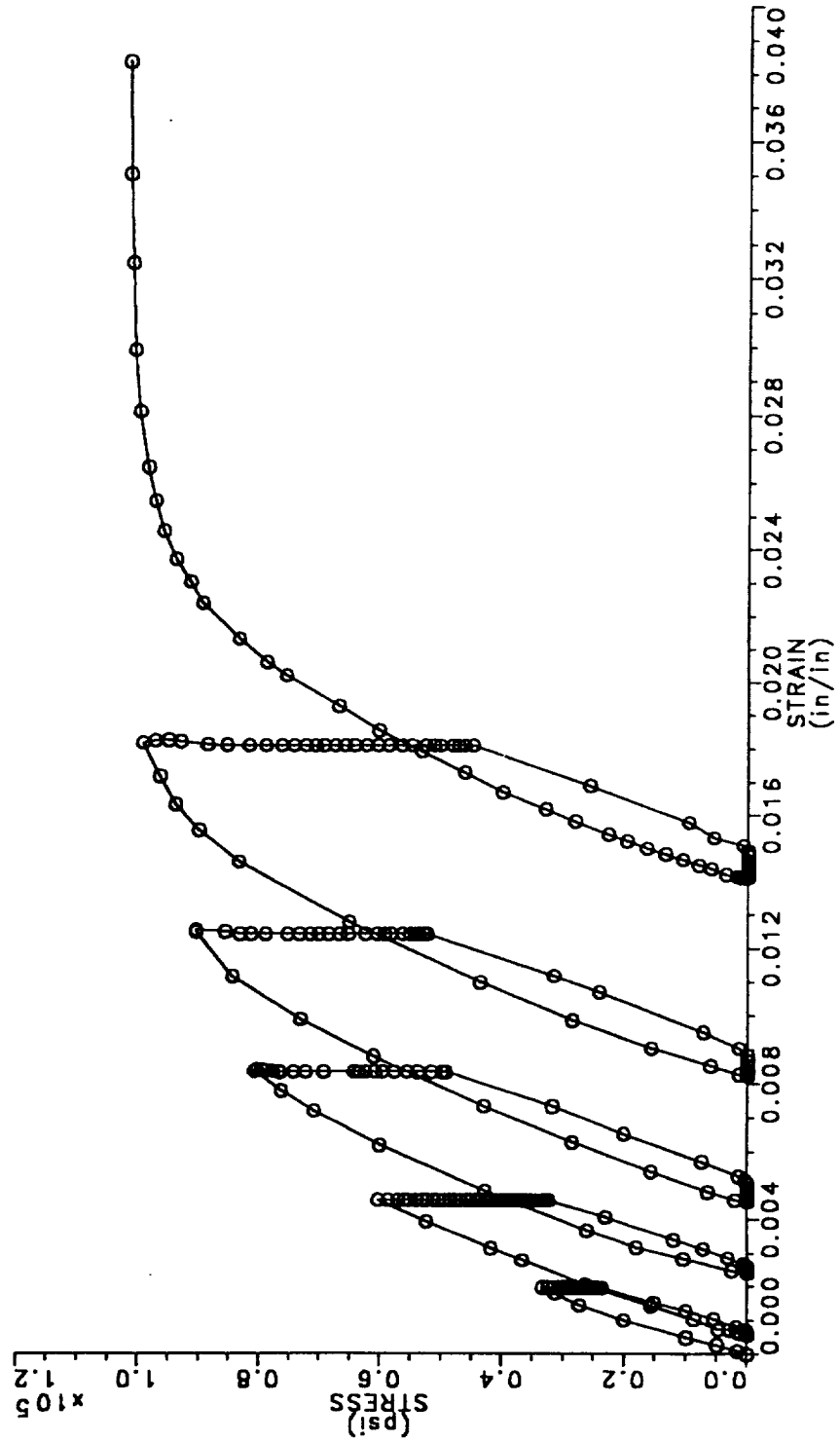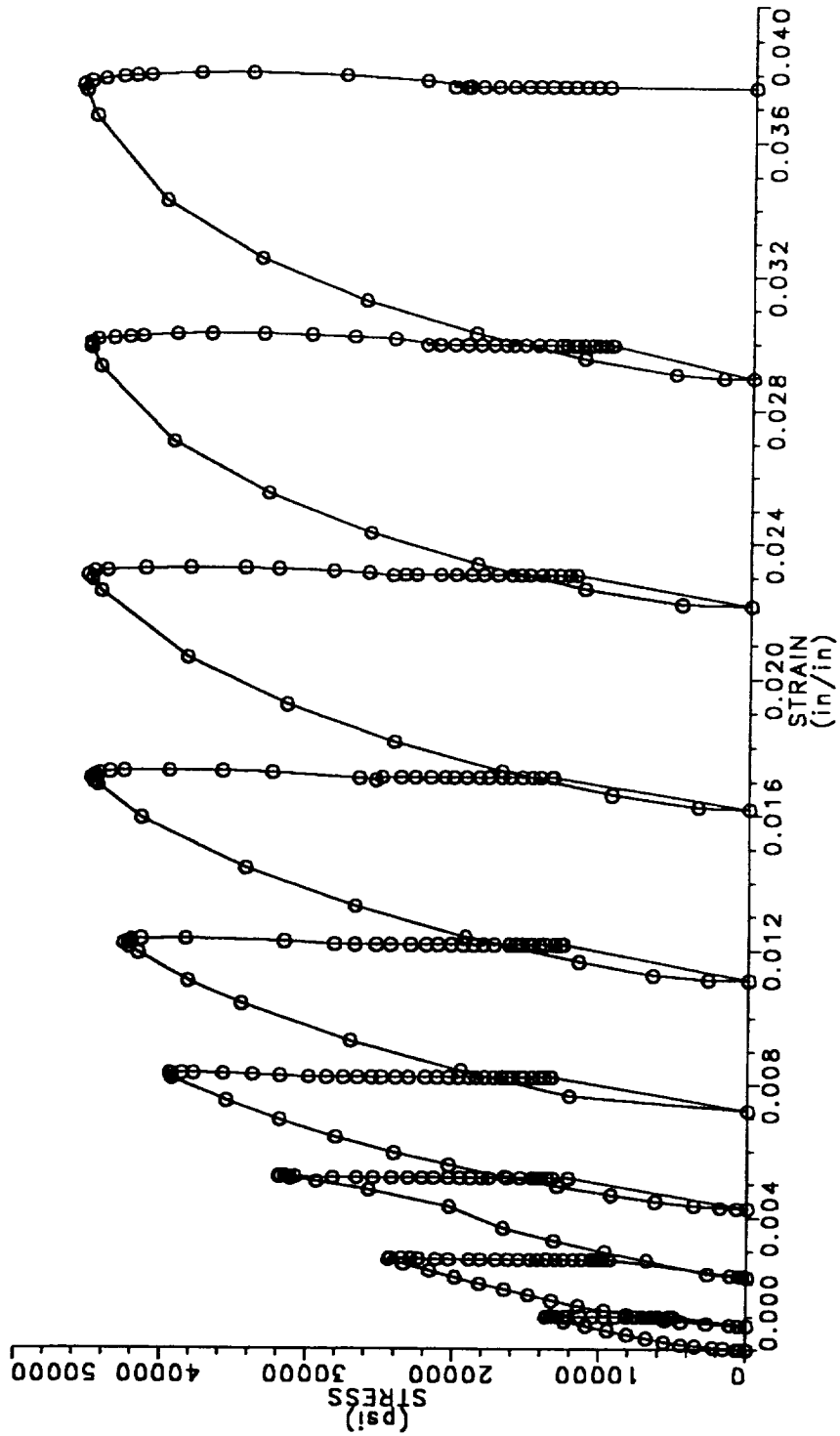
1600°F PWA 286 BULK (HIP); UNEXPOSED
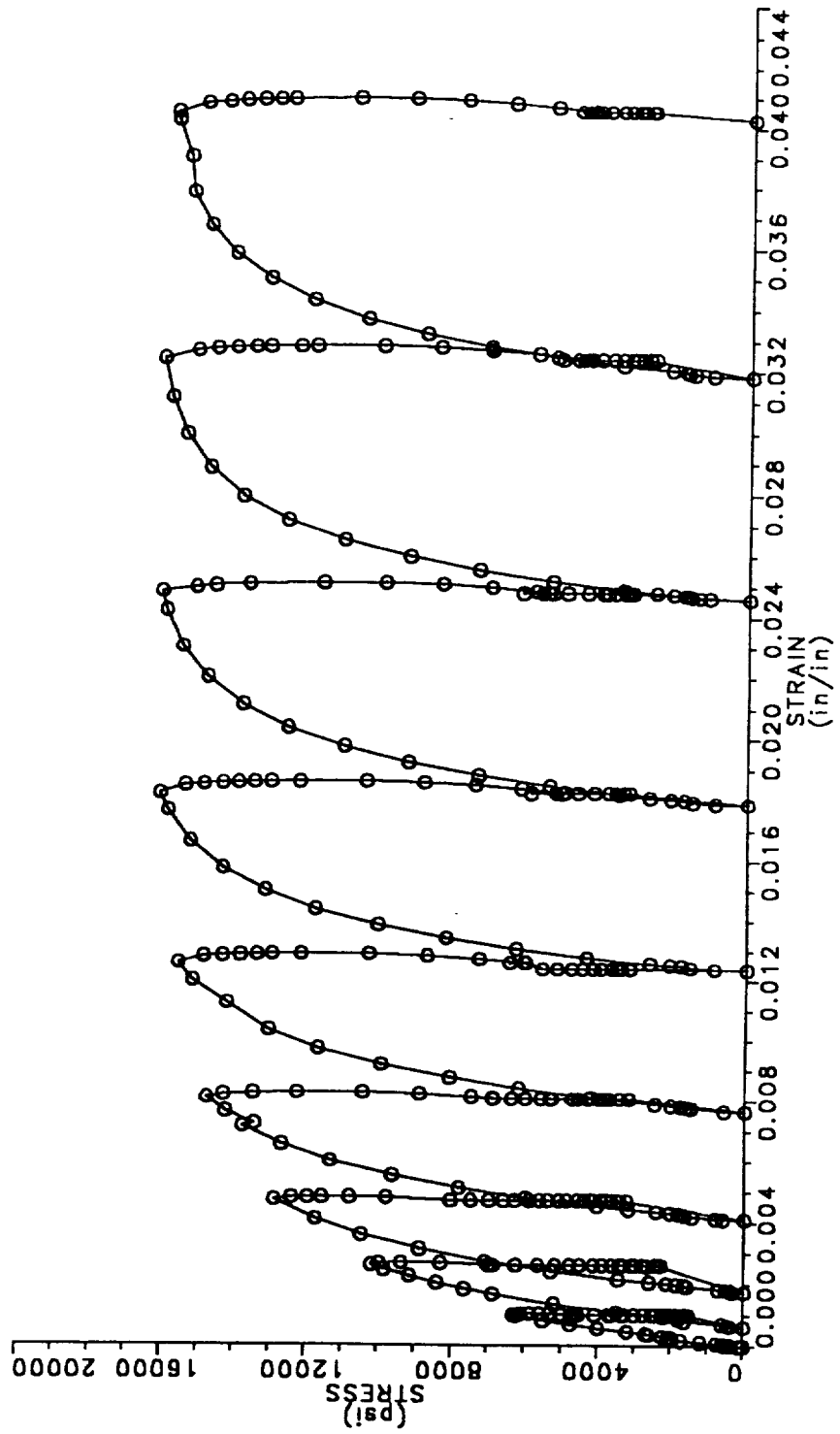
1600°F PWA 286 BULK (HIP); EXPOSED 100 HRS AT 2000°F

1600°F PWA 286 BULK (HIP); EXPOSED 100 HRS AT 2000°F

STRAIN
(in/in)

STRESS
(psi)

69
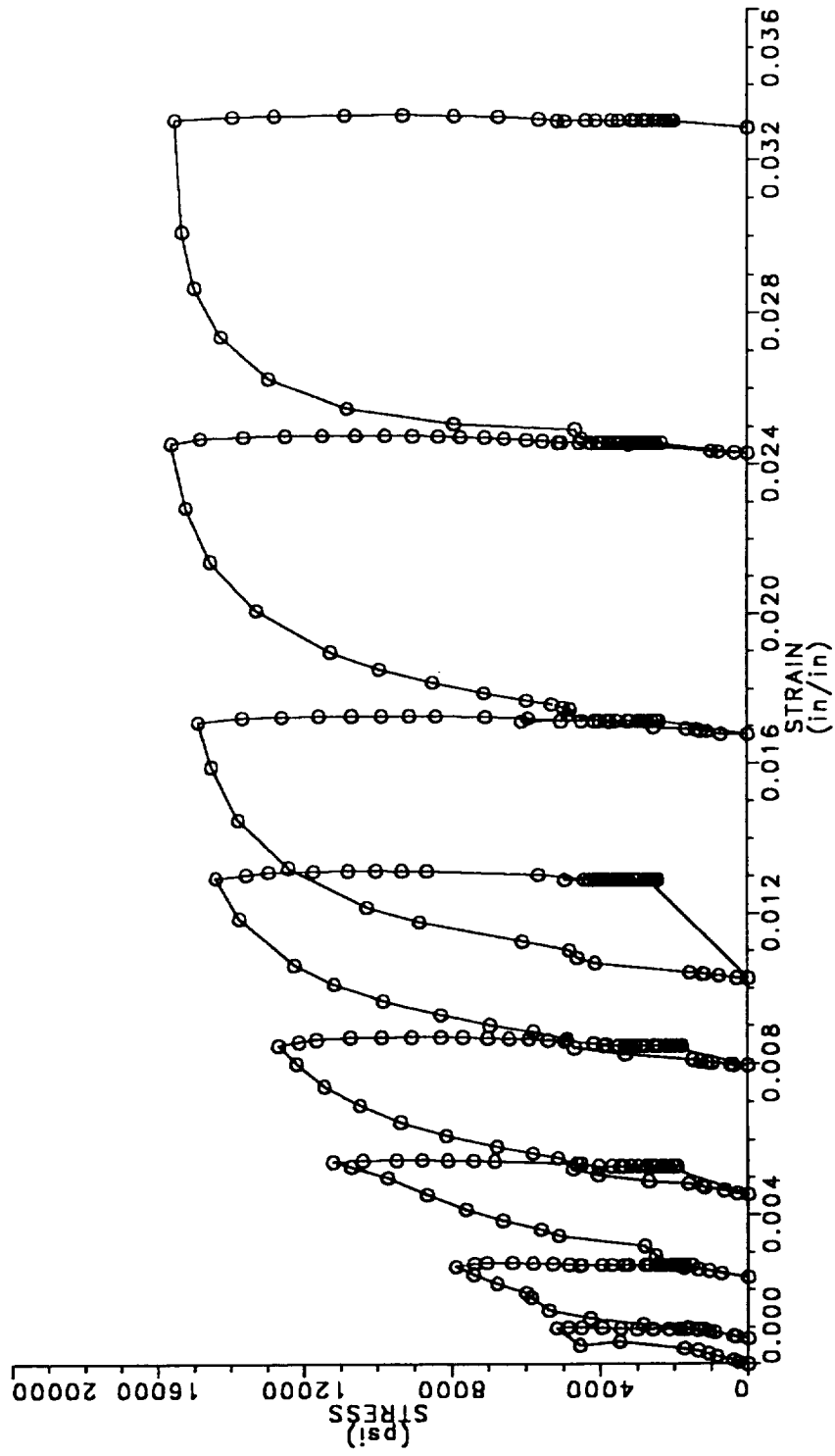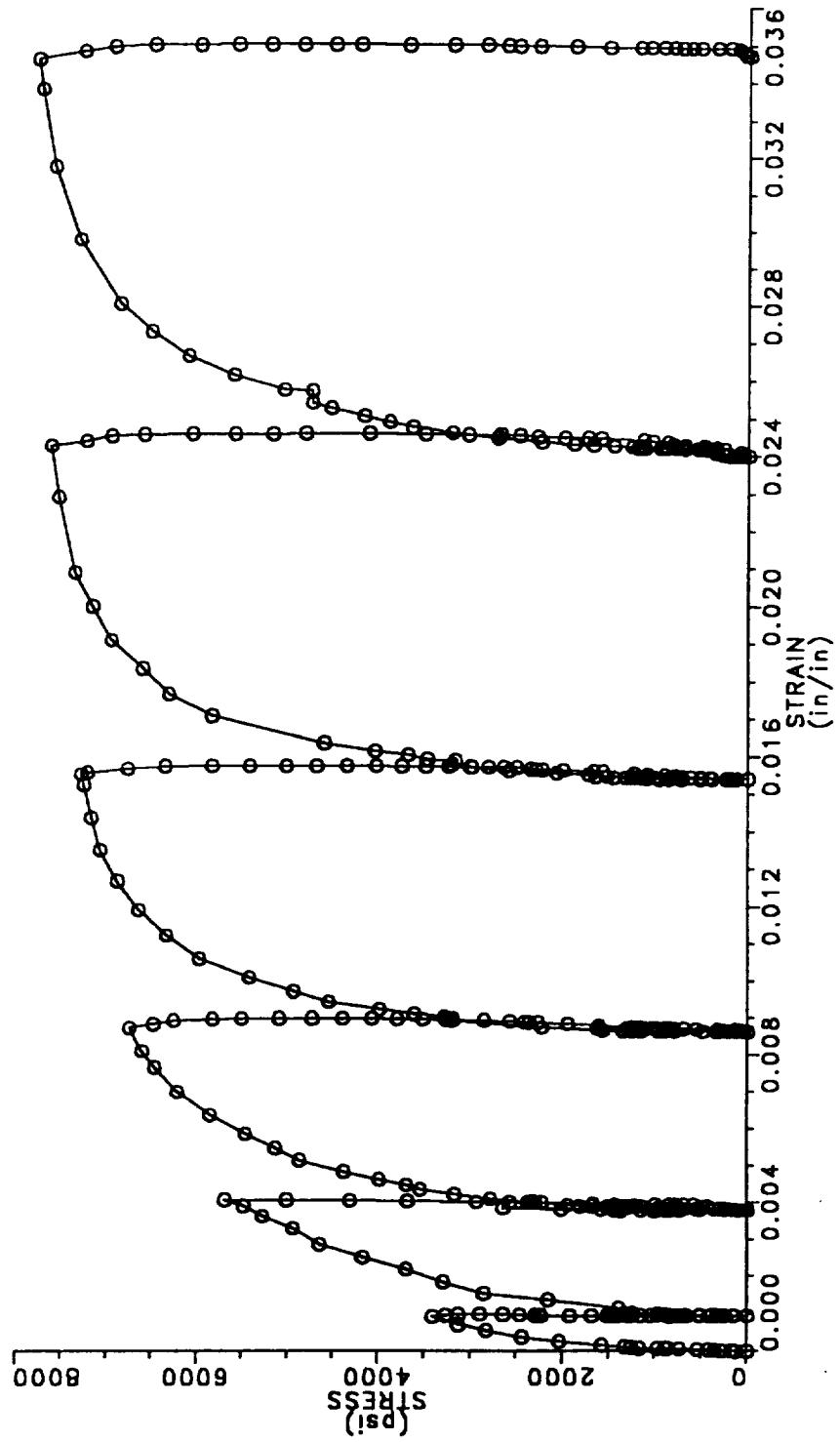
1600°F PWA 286 PLASMA SPRAY; UNEXPOSED

1800°F PWA 286 BULK (HIP); UNEXPOSED

STRESS (psi) vs STRAIN (in/in)

1800°F PWA 286 PLASMA SPRAY; UNEXPOSED

STRESS (psi)

STRAIN (in/in)

72
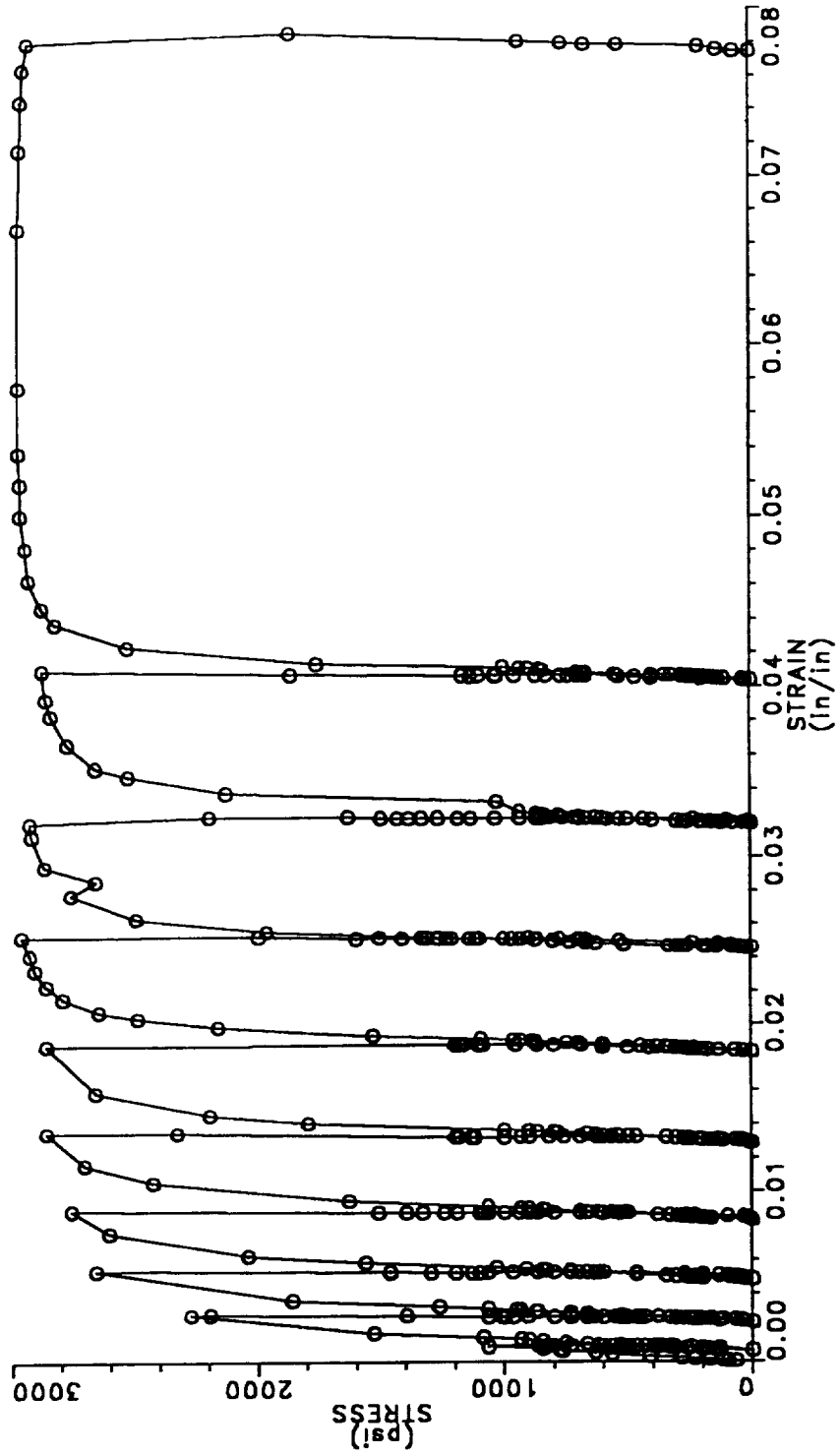
1800°F PWA 286 PLASMA SPRAY; EXPOSED 100 HRS AT 2000°F
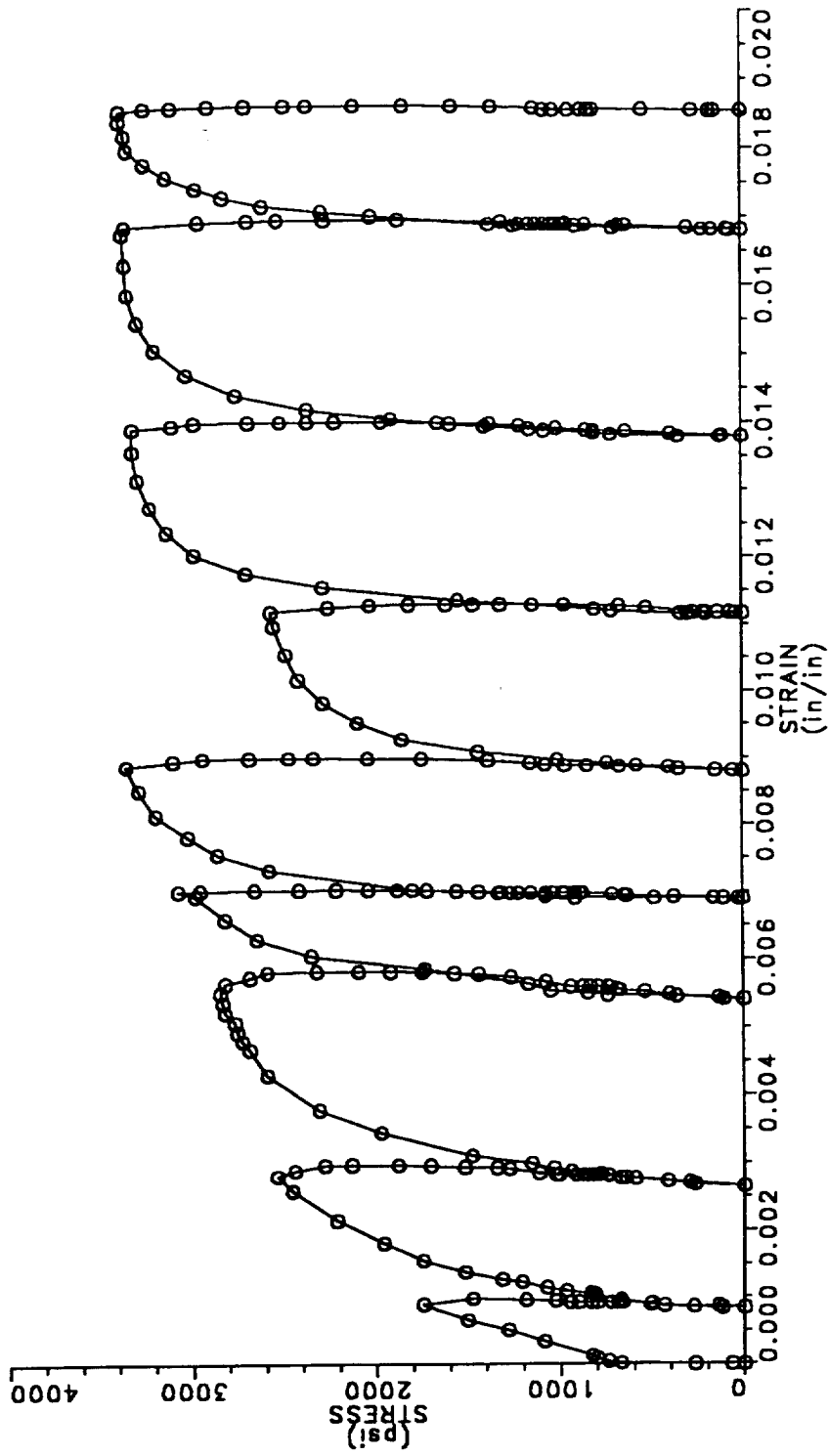
1900°F PWA 286 BULK (HIP): UNEXPOSED
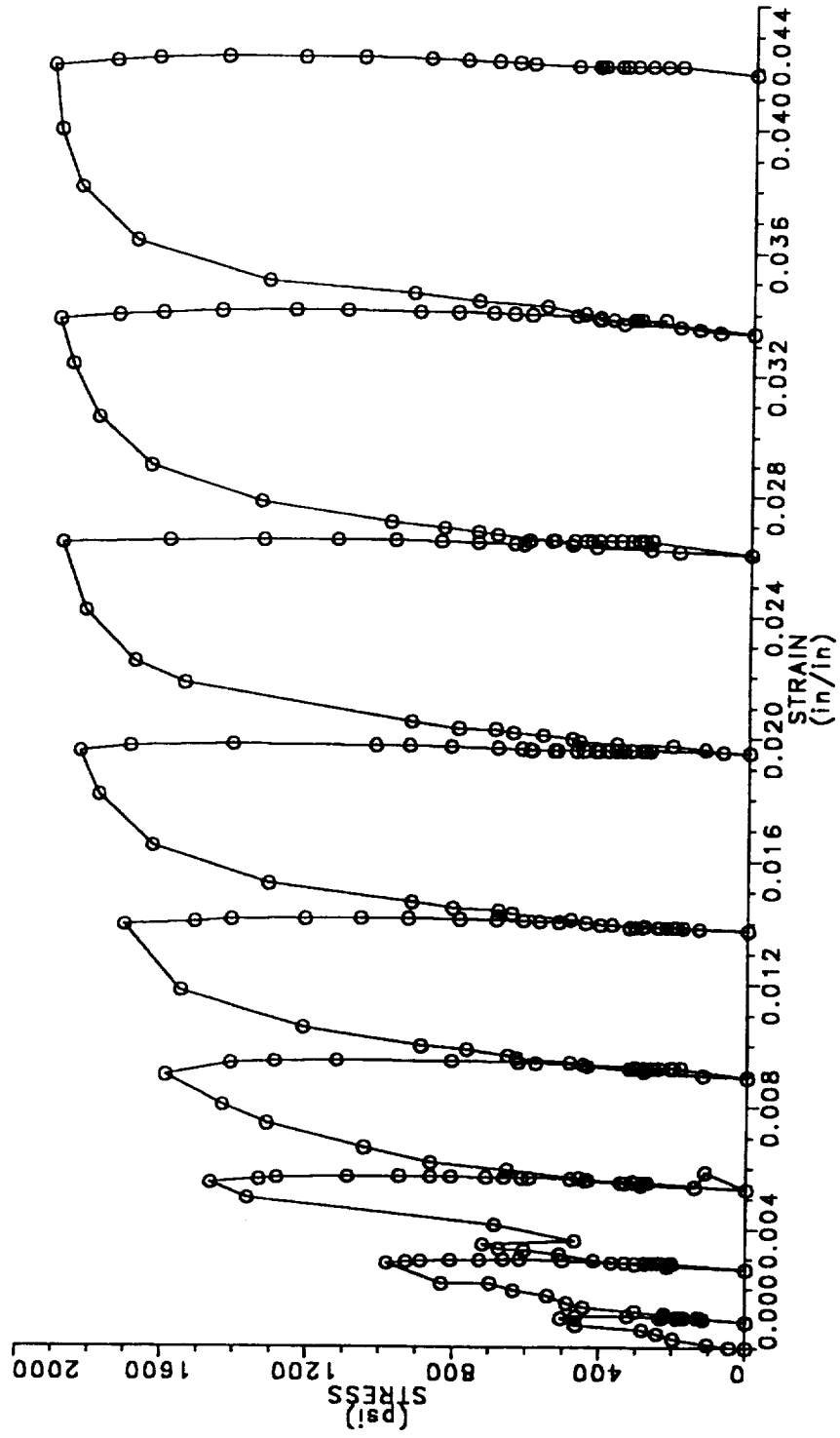
1900°F PWA 286 PLASMA SPRAY; EXPOSED 100 HRS AT 2000°F

STRAIN (in/in)

STRESS (psi)

2000°F PWA 286 BULK (HIP); UNEXPOSED

STRESS (psi) vs STRAIN (in/in)
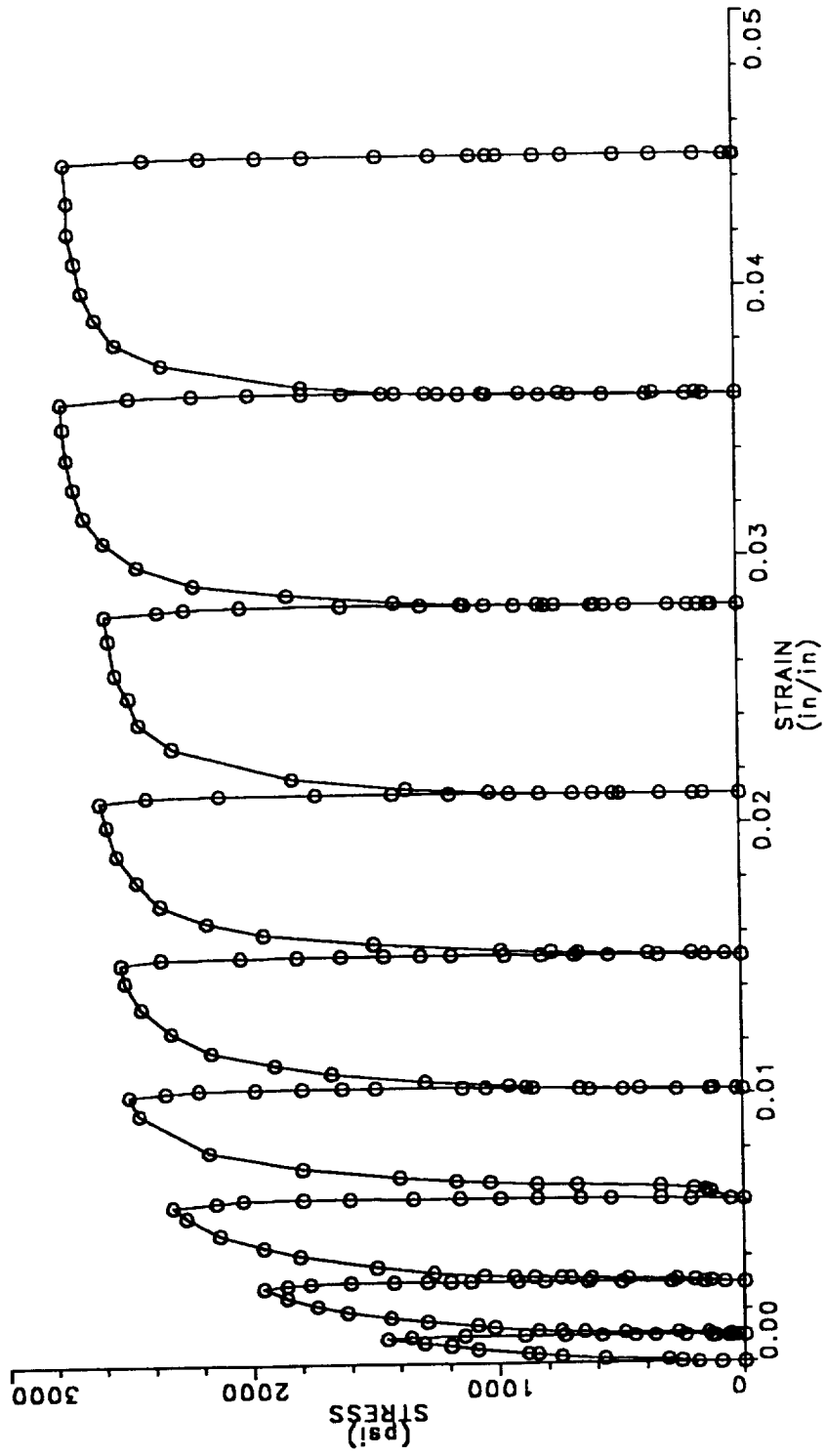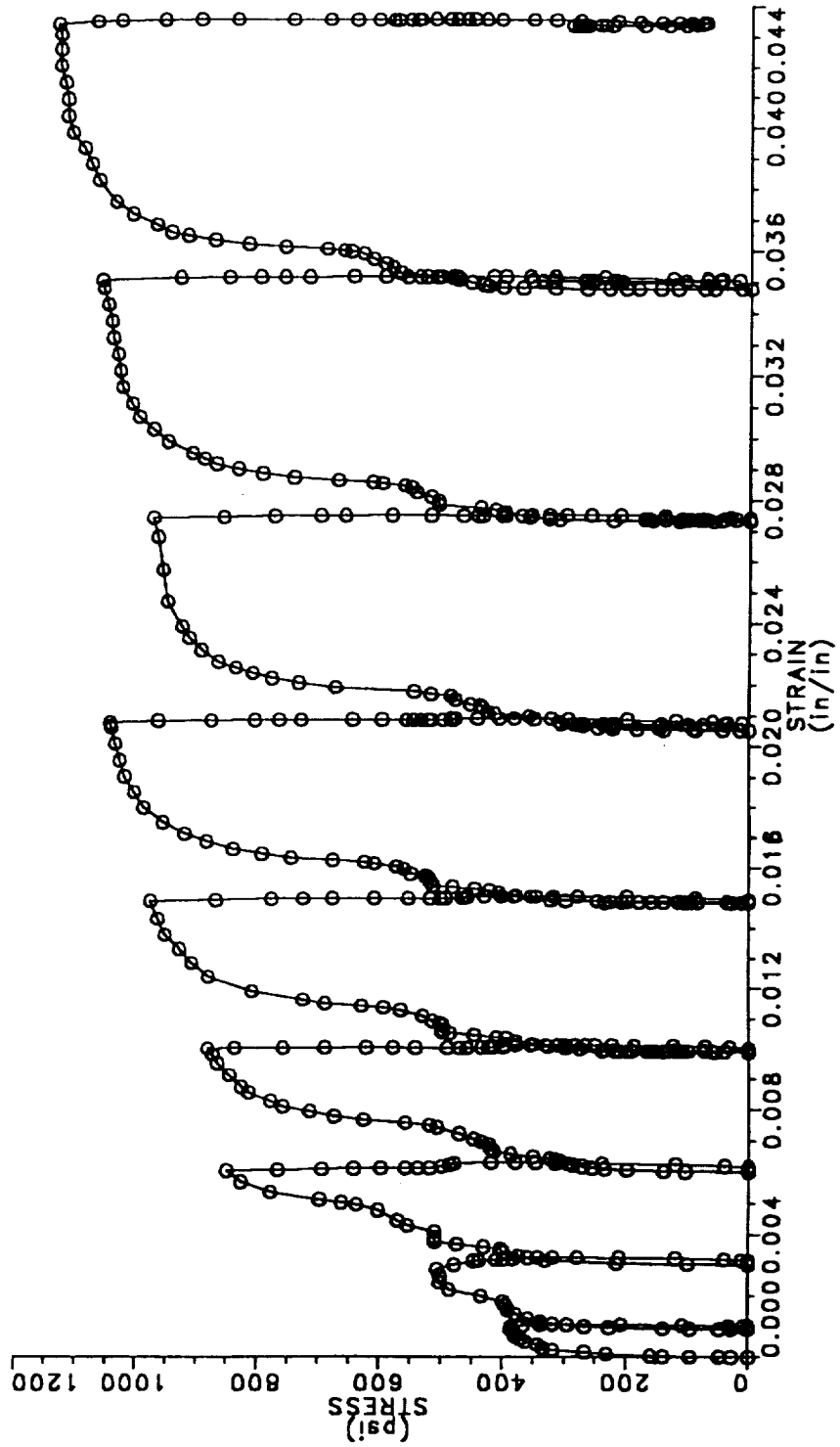
APPENDIX B

PWA 286 CONSTITUTIVE DATA

SERIES 2

USED FOR PWA 286 CONSTITUTIVE MODEL

800°F UNEXPOSED BULK HIP'PED PWA 286; SERIES 1 TEST USED AS SERIES 2

STRAIN
(in/in)

STRESS
(psi)

x10⁵

800°F PWA 286 BULK (HIP); UNEXPOSED

1000°F PWA 286 BULK (HIP); UNEXPOSED

80

C-2

1200°F PWA 286 BULK (HIP); UNEXPOSED

81

1400°F PWA 286 BULK (HIP); UNEXPOSED

STRESS
(psi)

STRAIN
(in/in)

82

1600°F PWA 286 BULK (HIP); UNEXPOSED

83
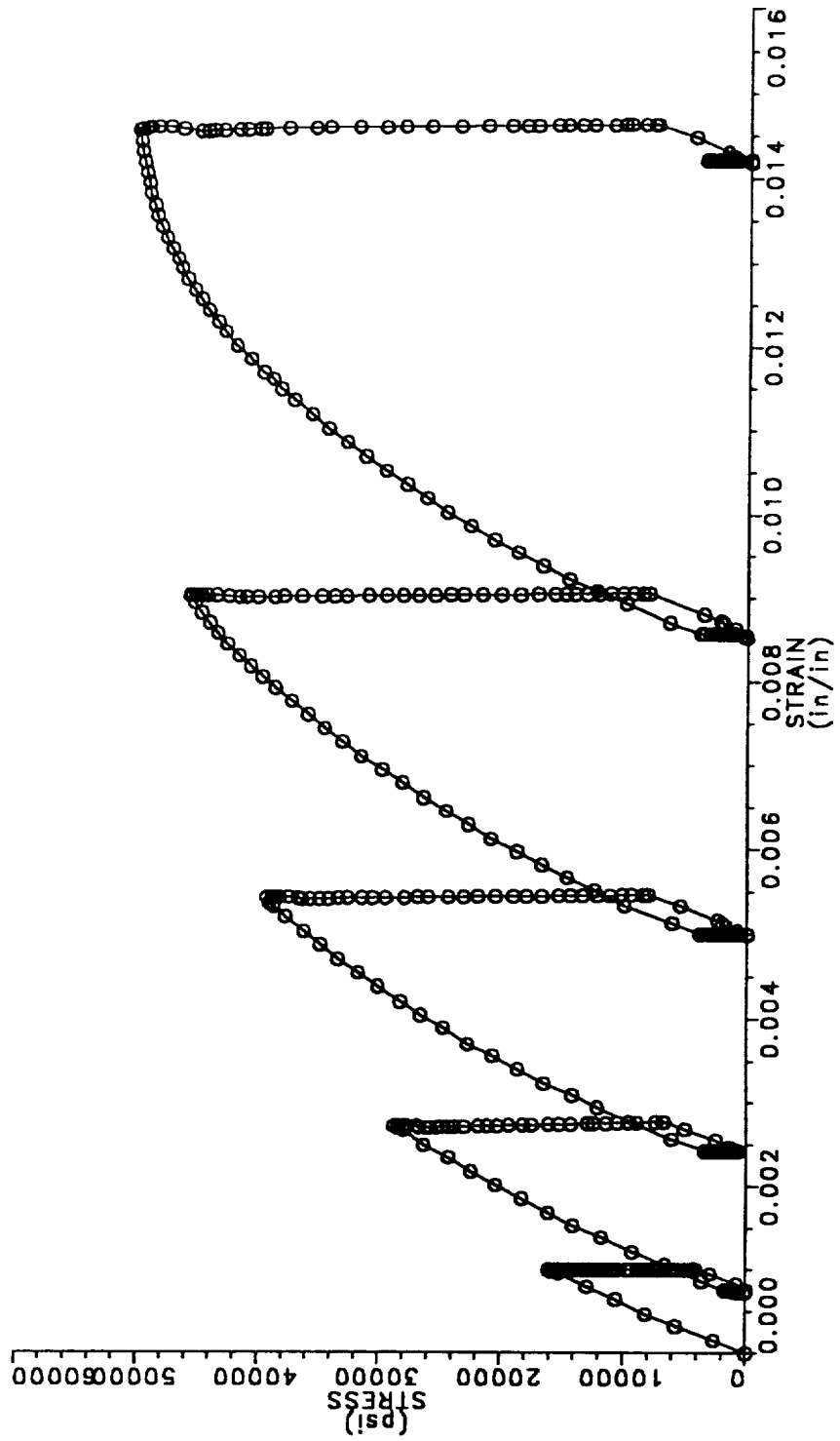
2000°F PWA 286 BULK (HIP); UNEXPOSED

PWA 286 BULK HIP OVERLAY COATING
800–1600°F OUT-OF-PHASE TMF VERIFICATION TEST
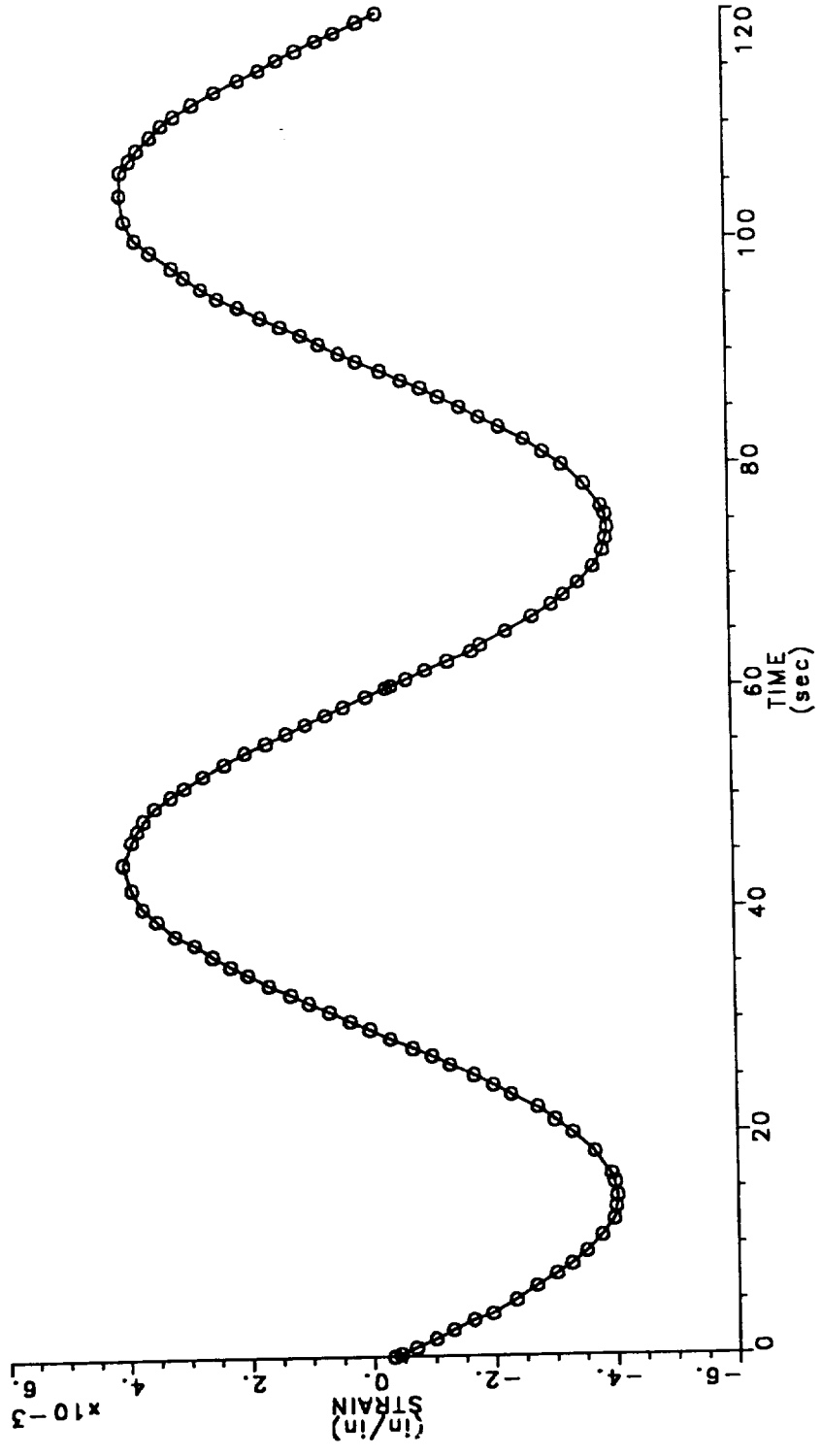
PWA 286 BULK HIP OVERLAY COATING
800–1600°F OUT-OF-PHASE TMF VERIFICATION TEST
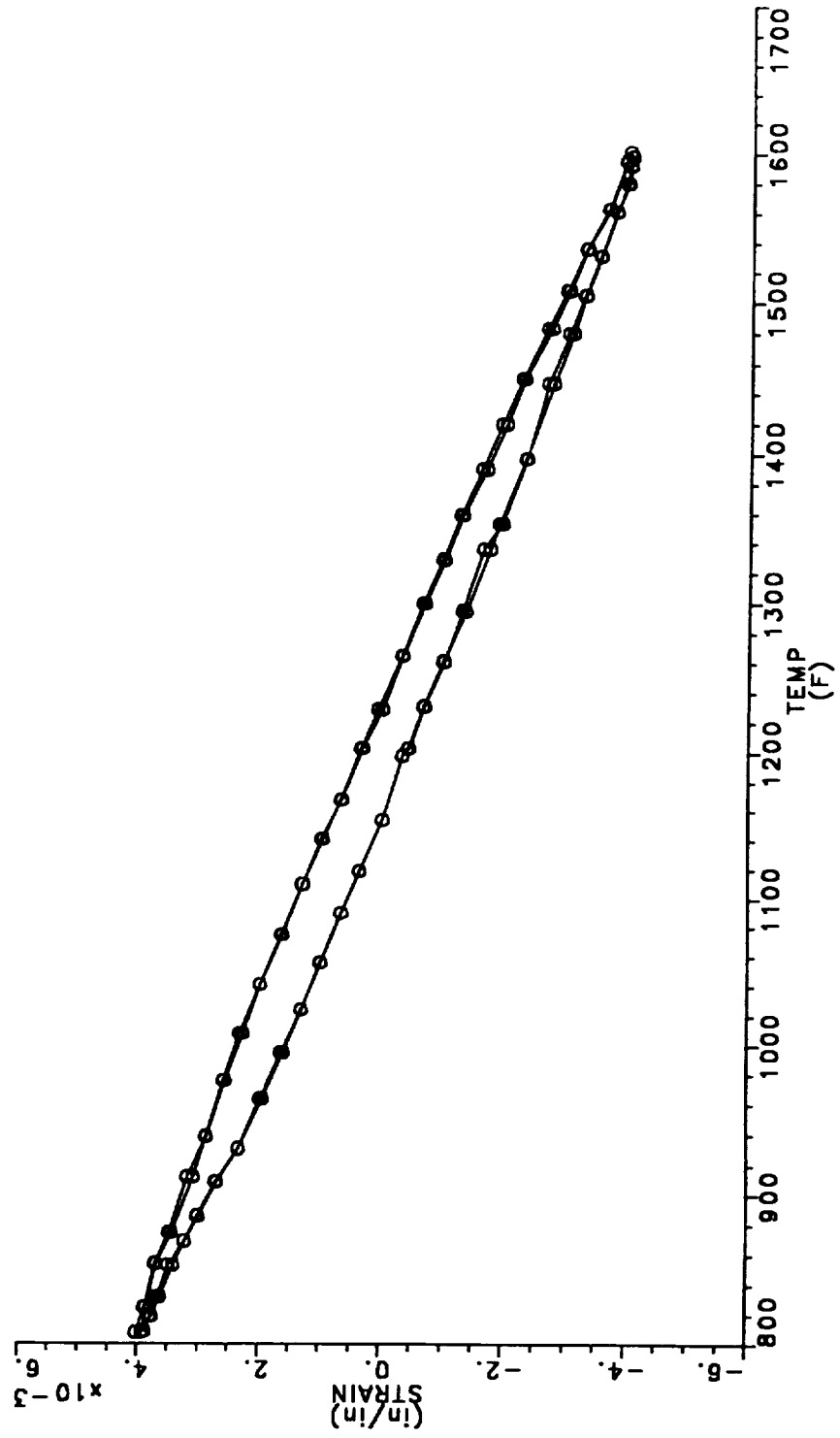
PWA 286 BULK HIP OVERLAY COATING
800–1600°F OUT–OF–PHASE TMF VERIFICATION TEST
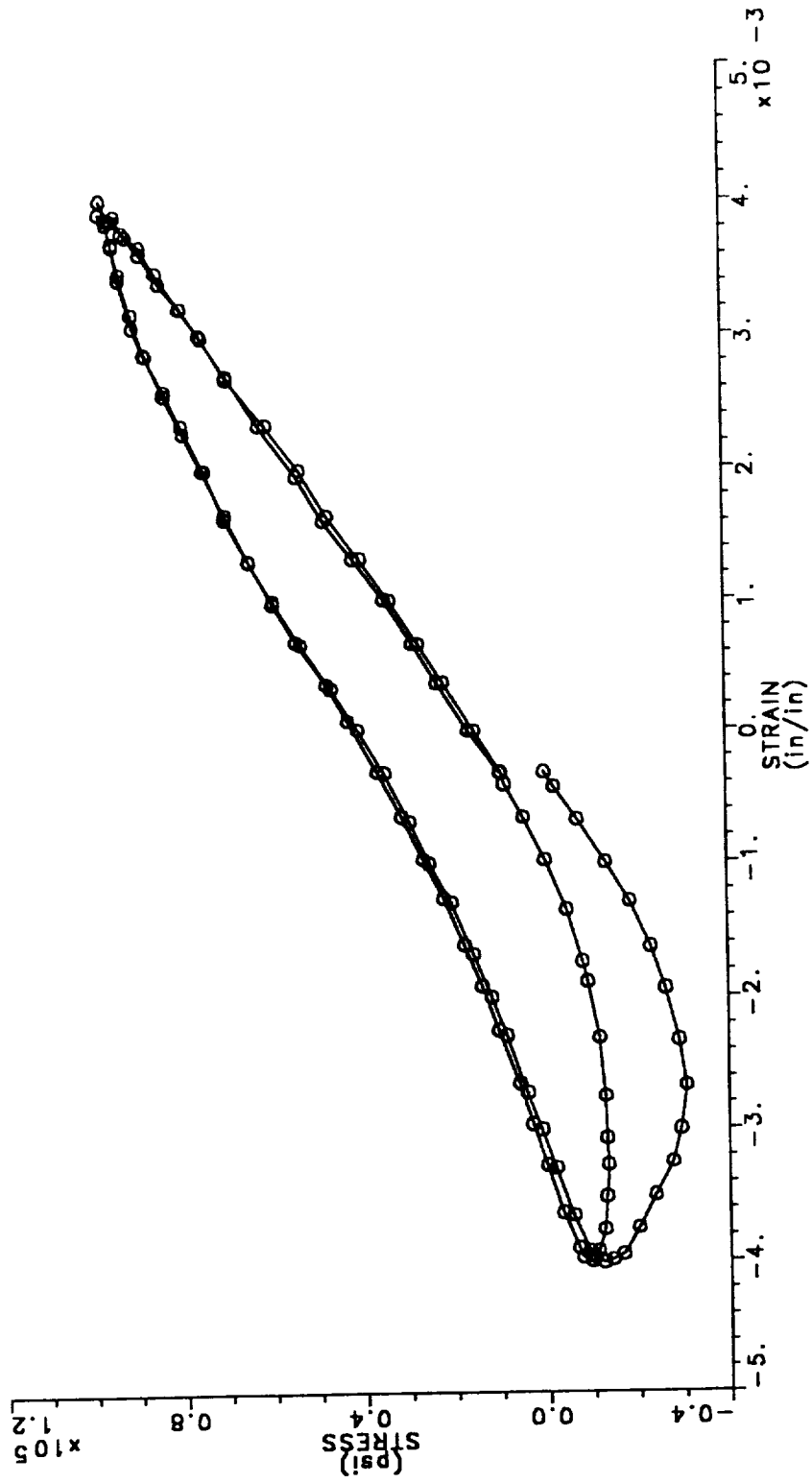
APPENDIX C

PWA 273 CONSTITUTIVE DATA

800°F STRESS RELAXATION OF SPECIMEN 55-2 0.005" NOMINAL PWA 1480; UNCOATED
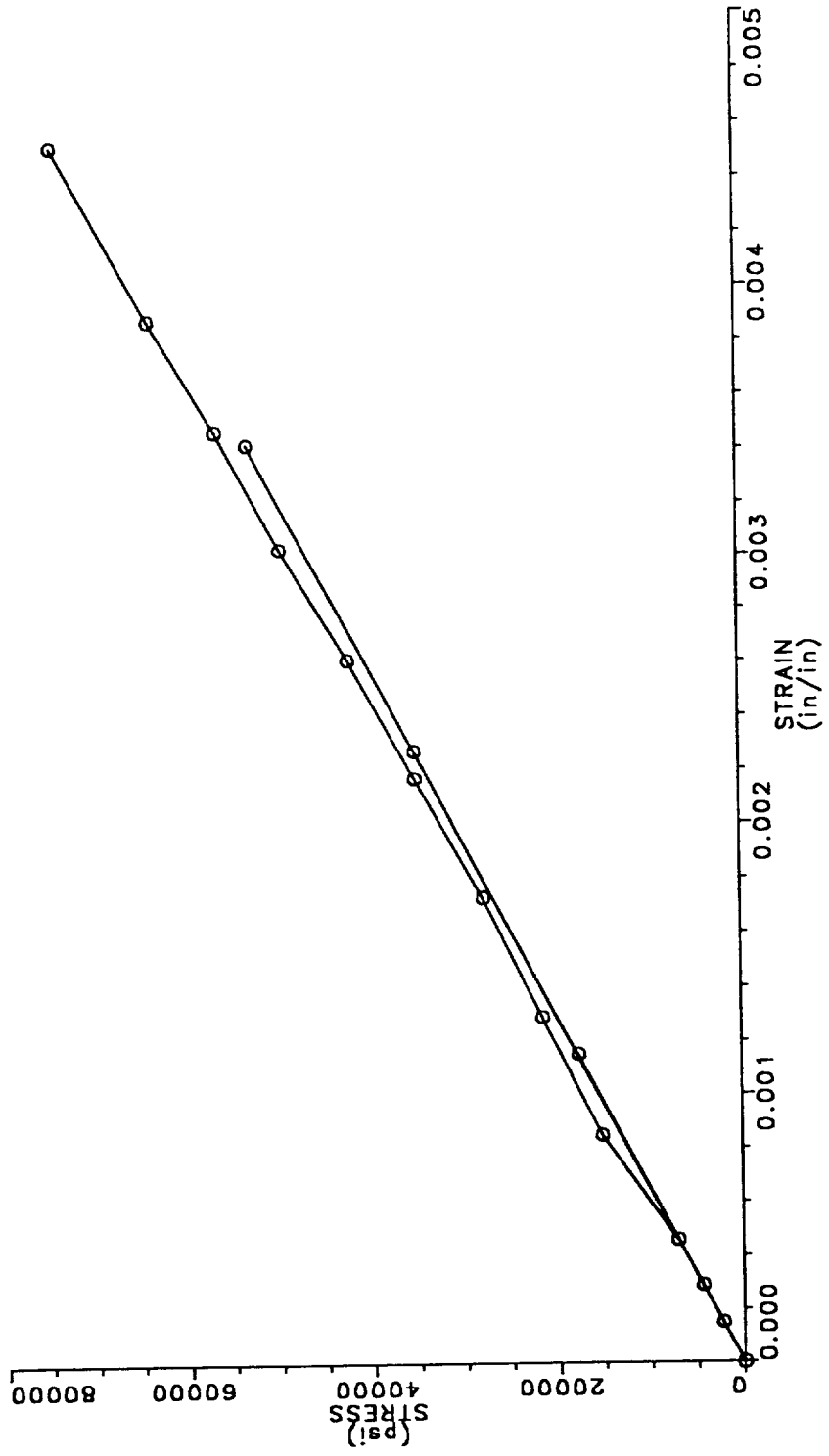
800°F STRESS RELAXATION OF SPECIMEN 78-2 0.010" NOMINAL PWA 1480 BEFORE COATING
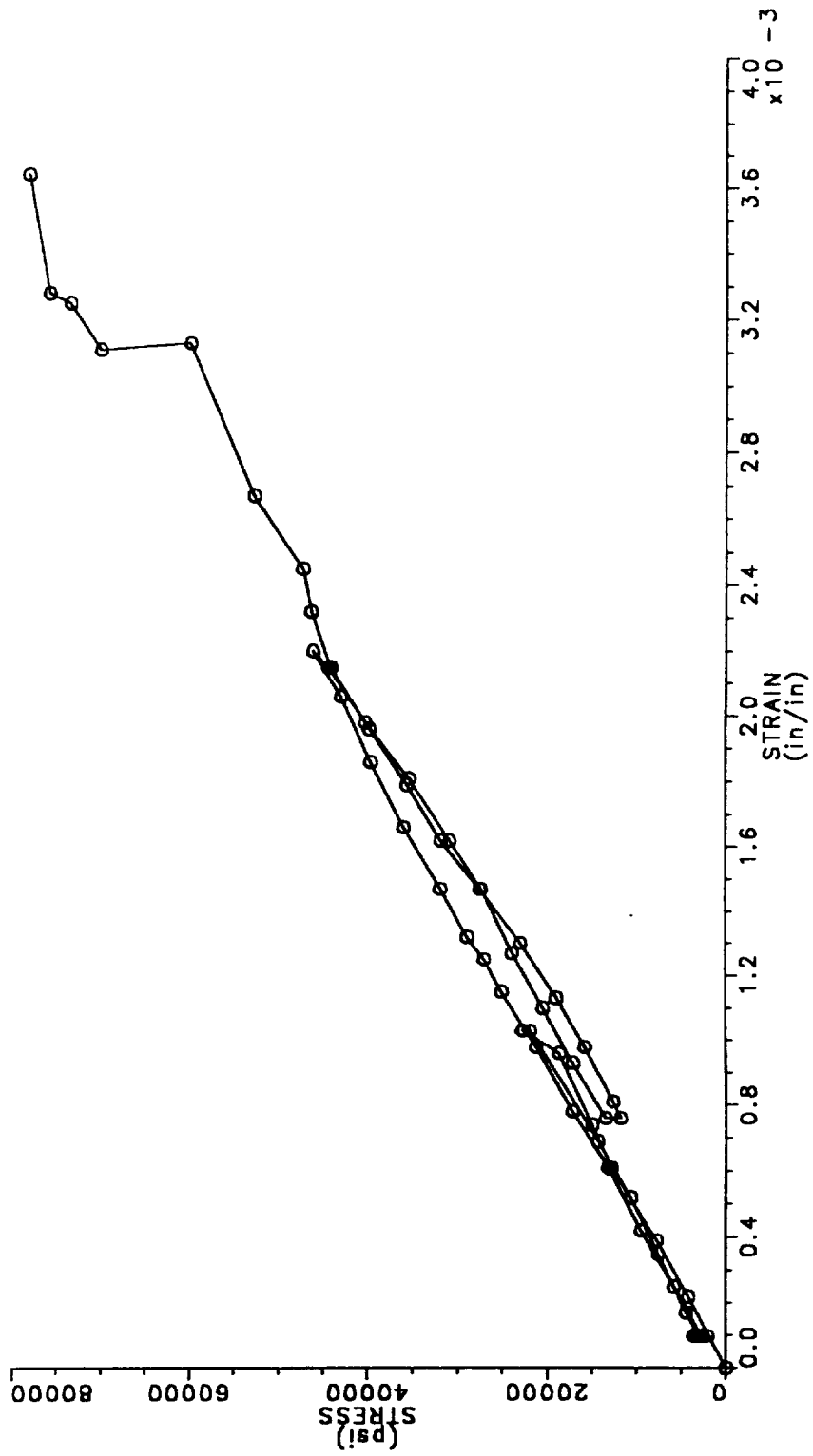
1100°F STRESS RELAXATION OF SPECIMEN 78-3 0.010" NOMINAL PWA 1480 BEFORE COATING
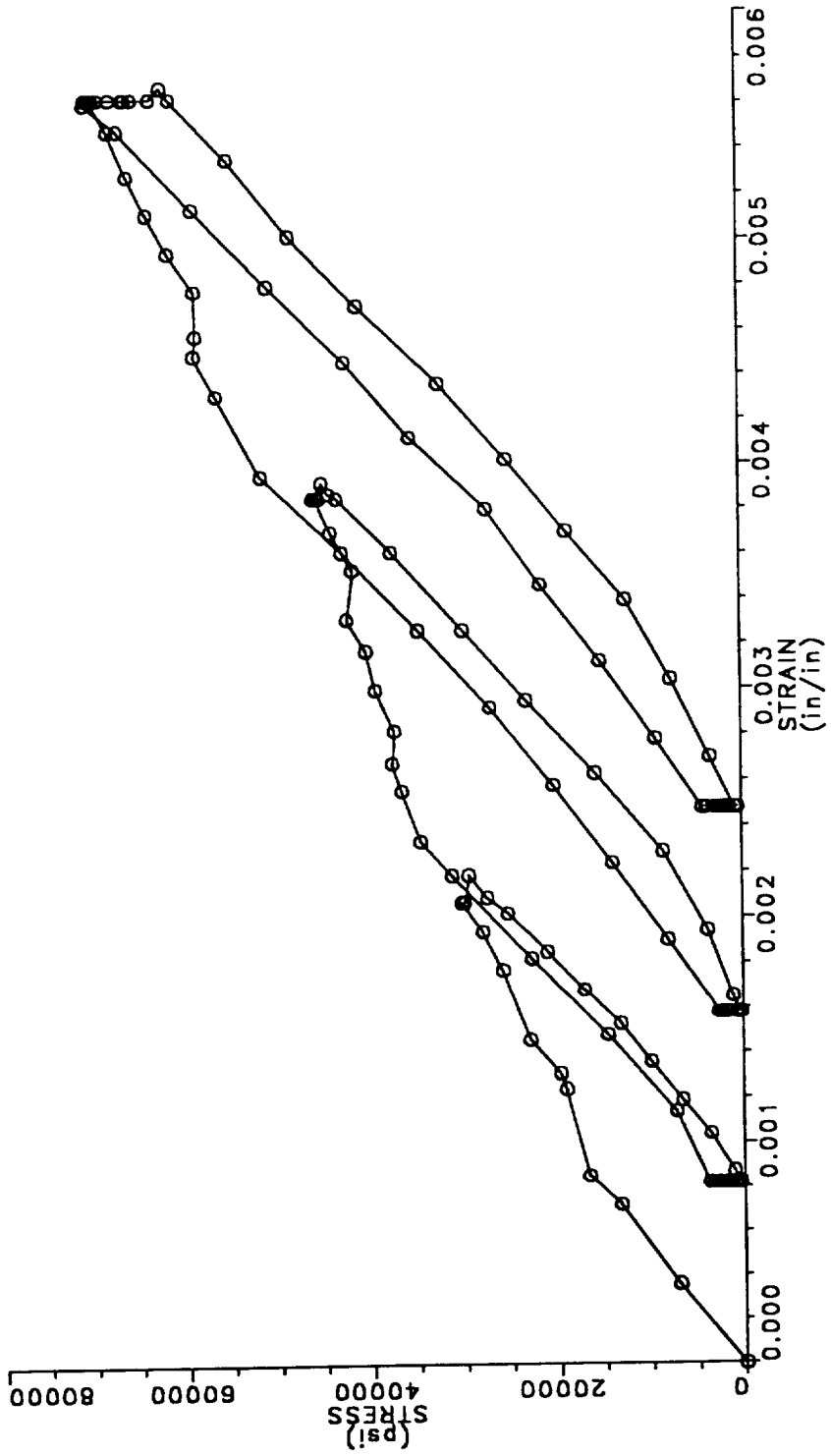
1200°F STRESS RELAXATION OF SPECIMEN 53-3 0.010" NOMINAL PWA 1480 BEFORE COATING
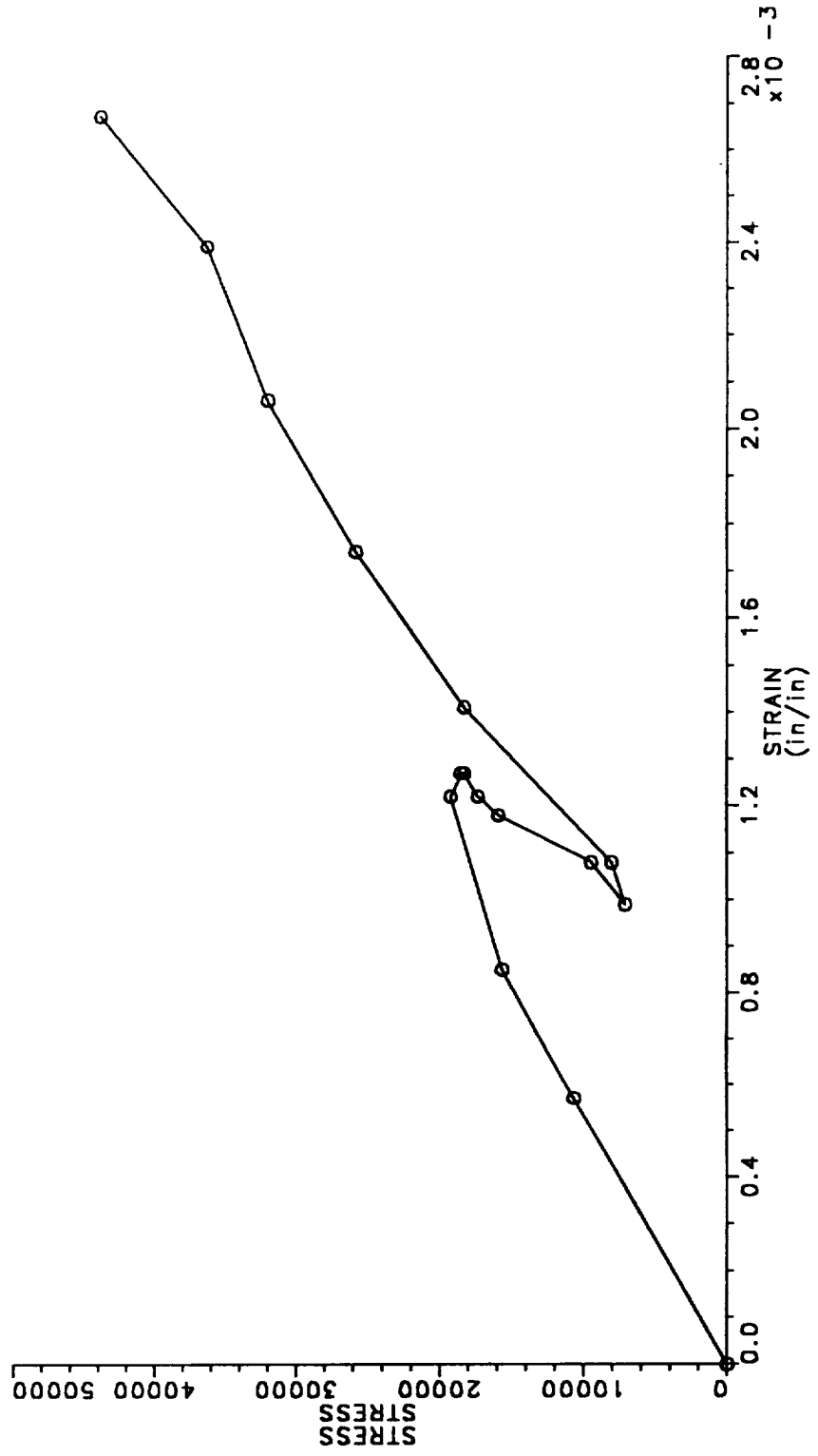
1400°F STRESS RELAXATION OF SPECIMEN 75-2 0.010" NOMINAL PWA 1480 BEFORE COATING
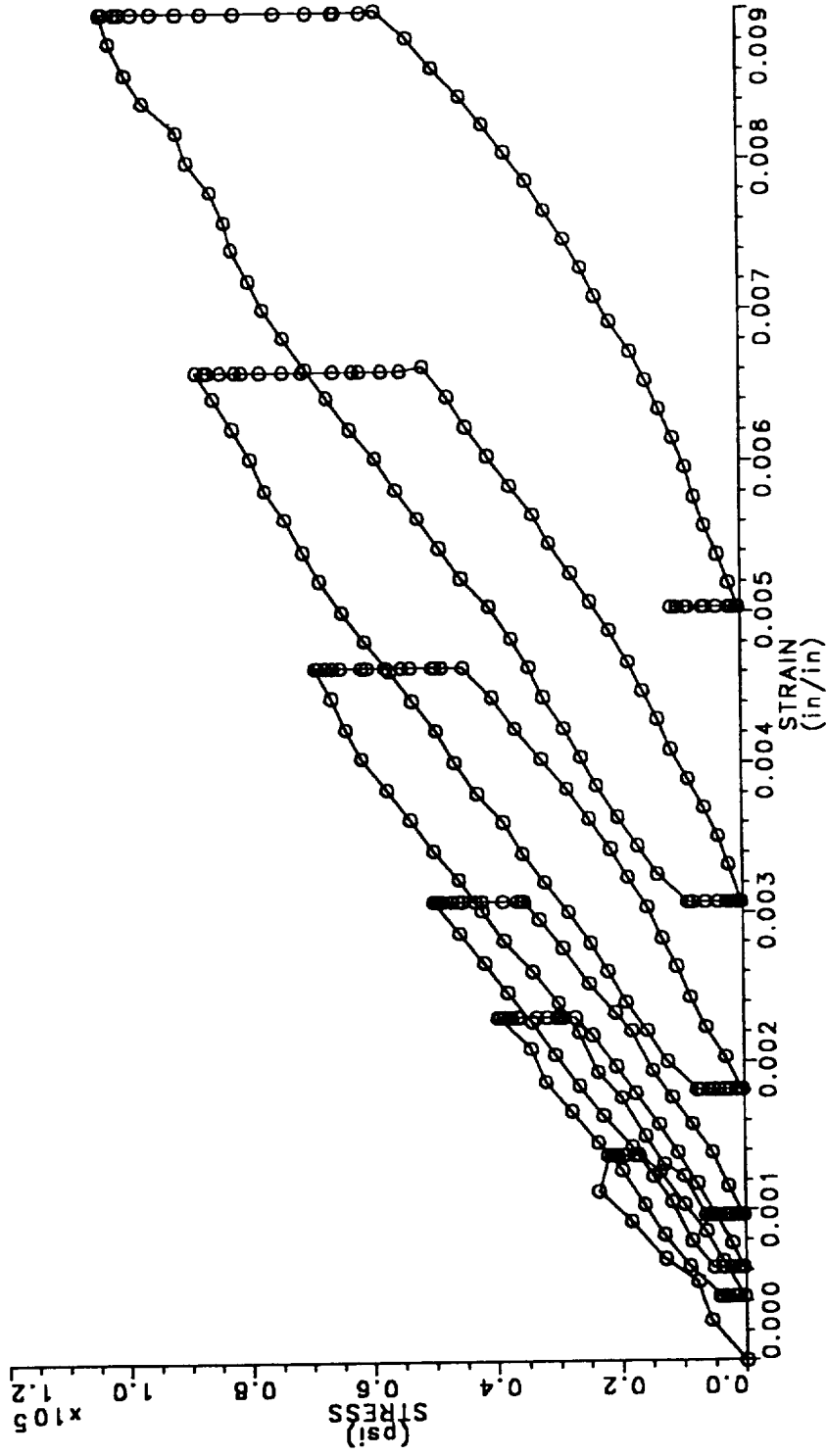
1400°F STRESS RELAXATION OF SPECIMEN 75-4 0.010" NOMINAL PWA 1480 BEFORE COATING
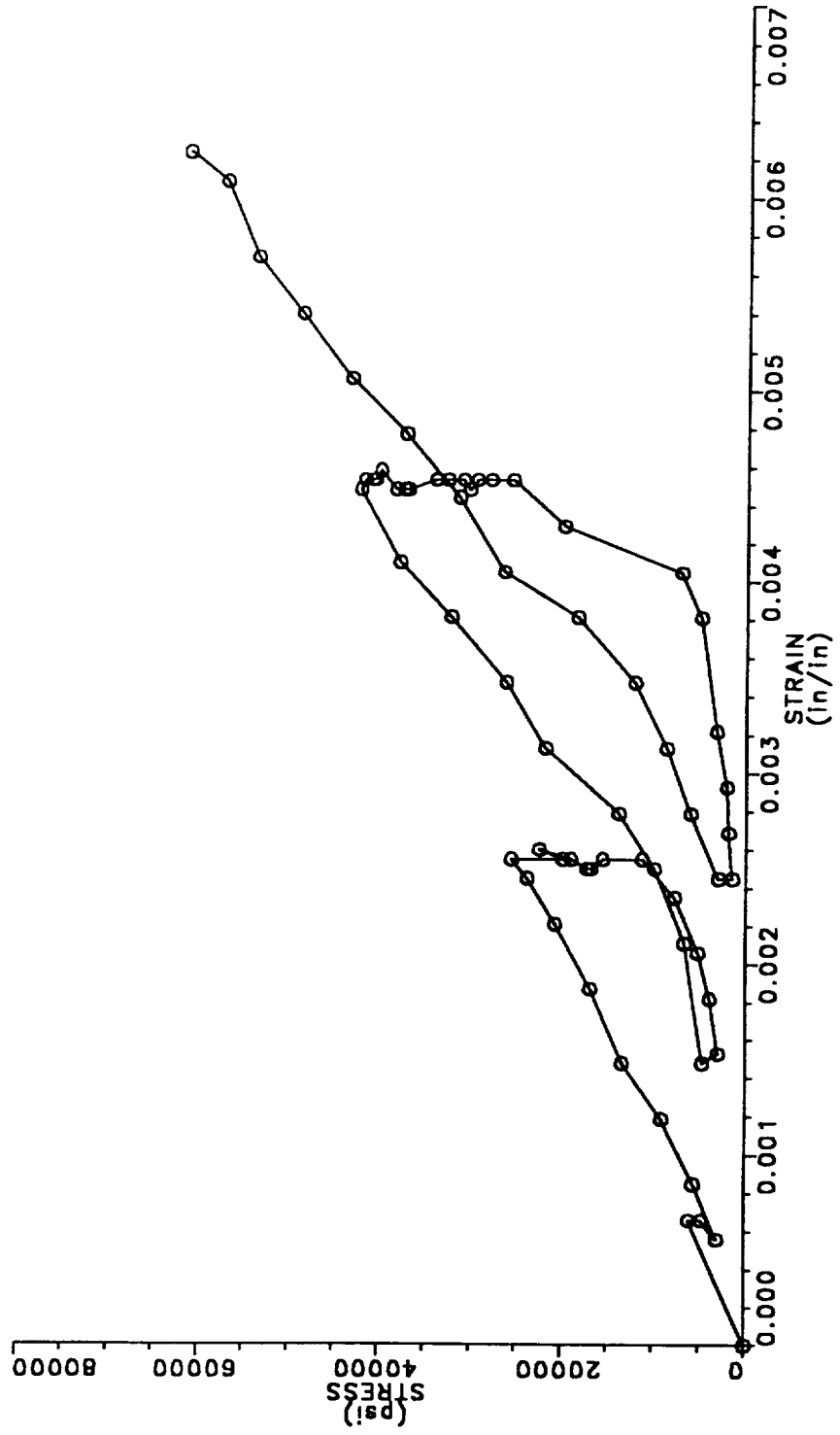
1500°F STRESS RELAXATION OF SPECIMEN 55-1 0.005" NOMINAL PWA 1480 BEFORE COATING
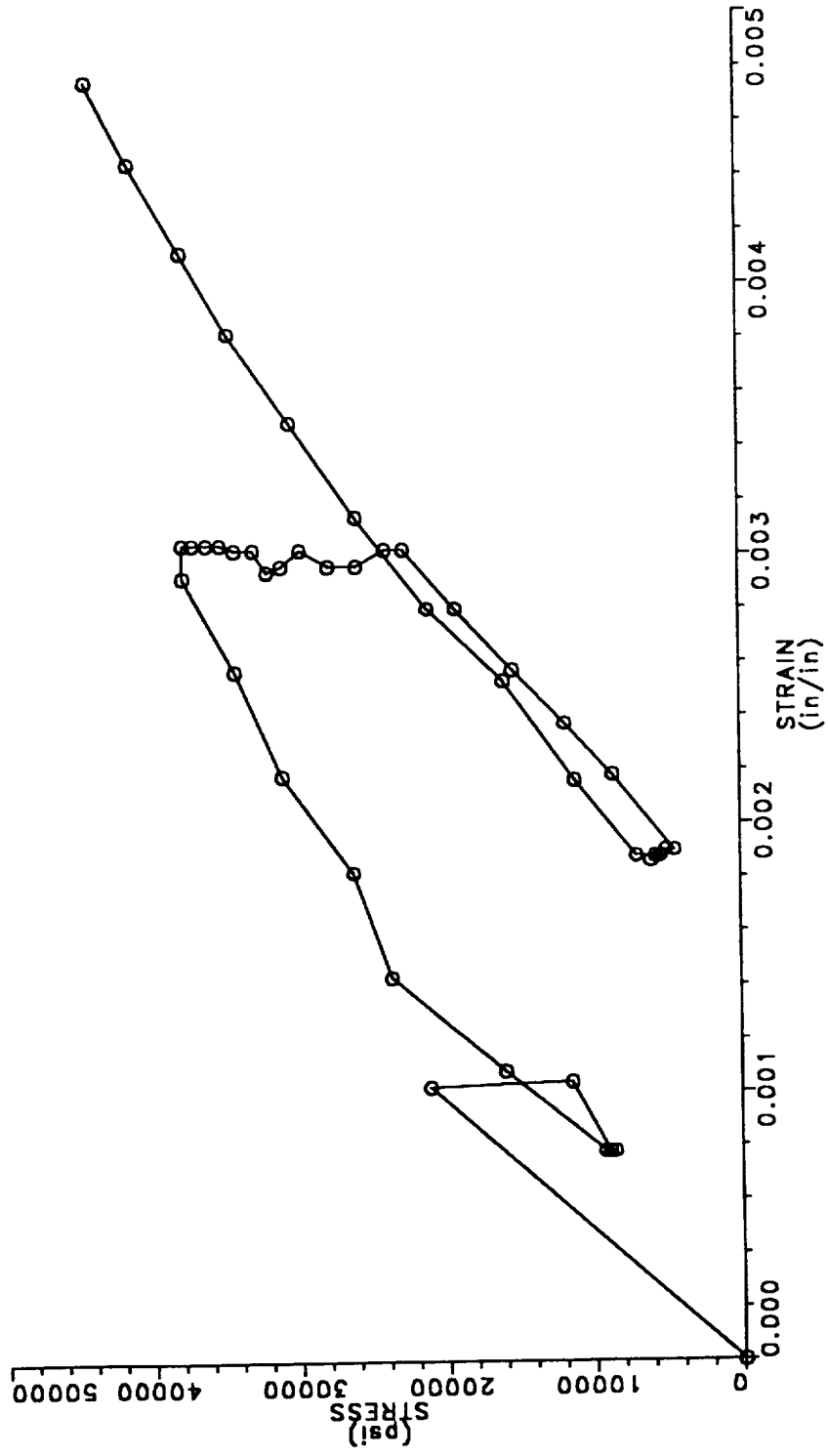
1500°F STRESS RELAXATION OF SPECIMEN 75-3 0.010" NOMINAL PWA 1480 BEFORE COATING
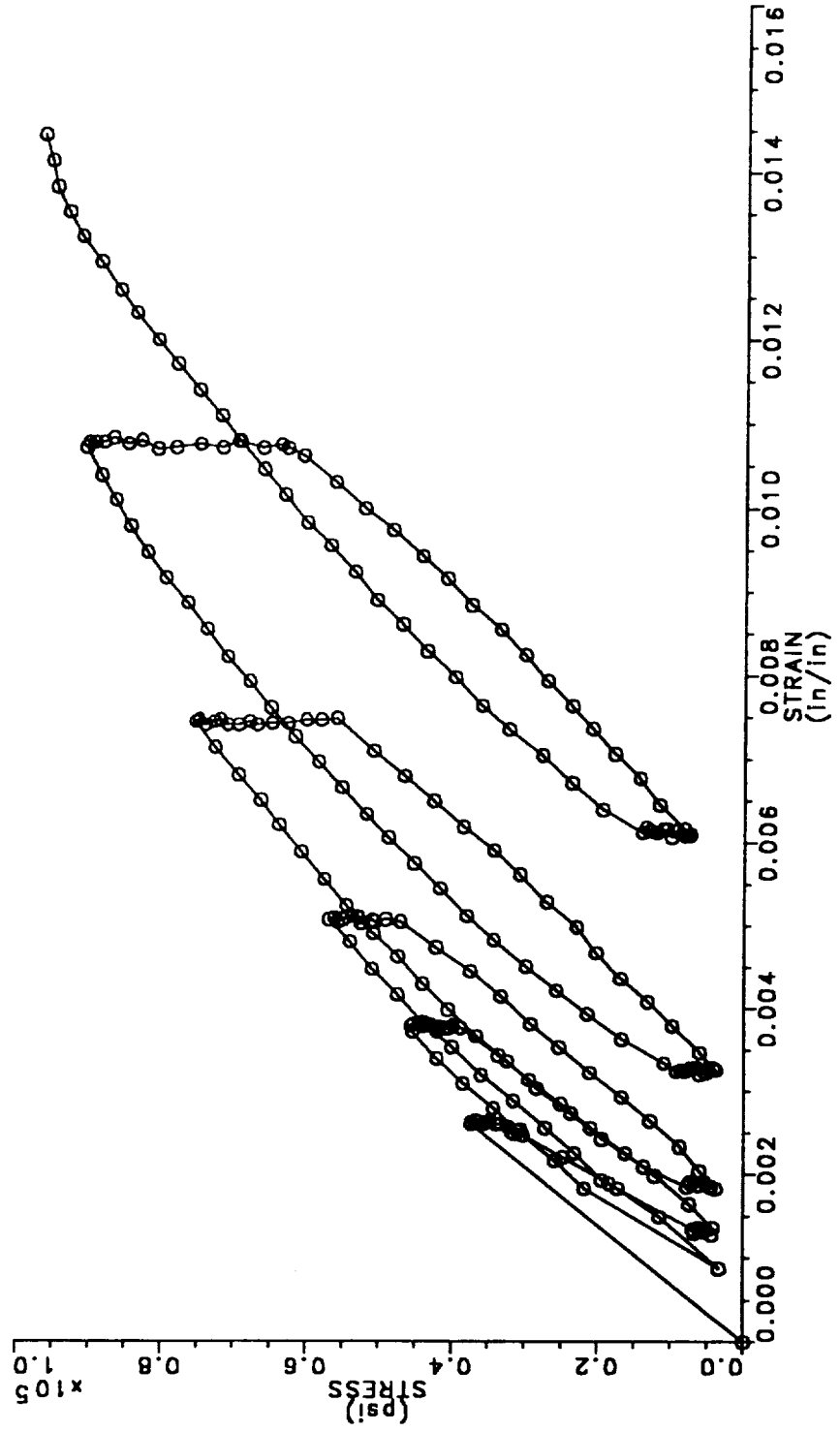
1600°F STRESS RELAXATION OF SPECIMEN 53-1 0.005" NOMINAL PWA 1480 BEFORE COATING
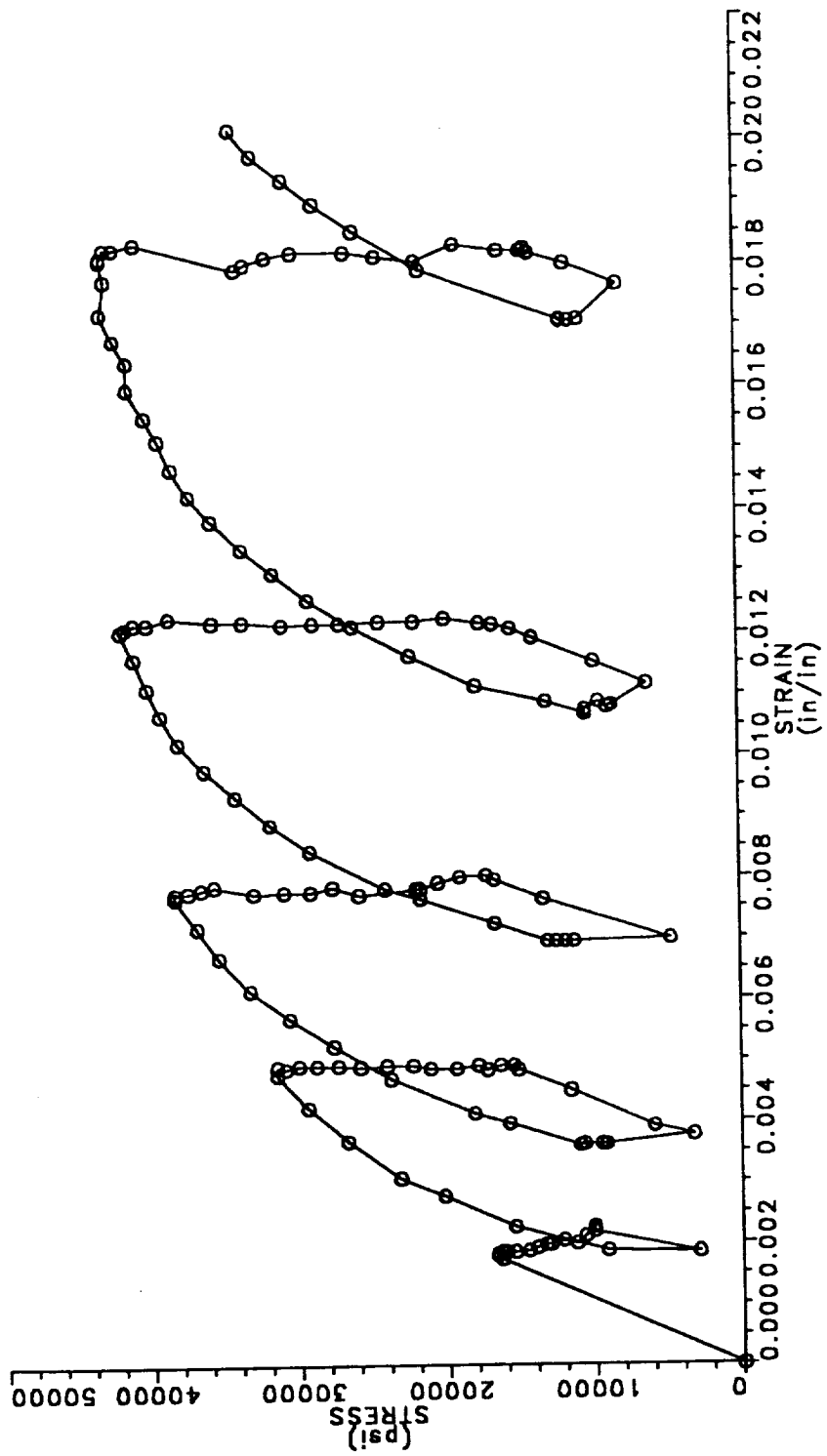
1600°F STRESS RELAXATION OF SPECIMEN 55-3 0.005" NOMINAL PWA 1480 BEFORE COATING
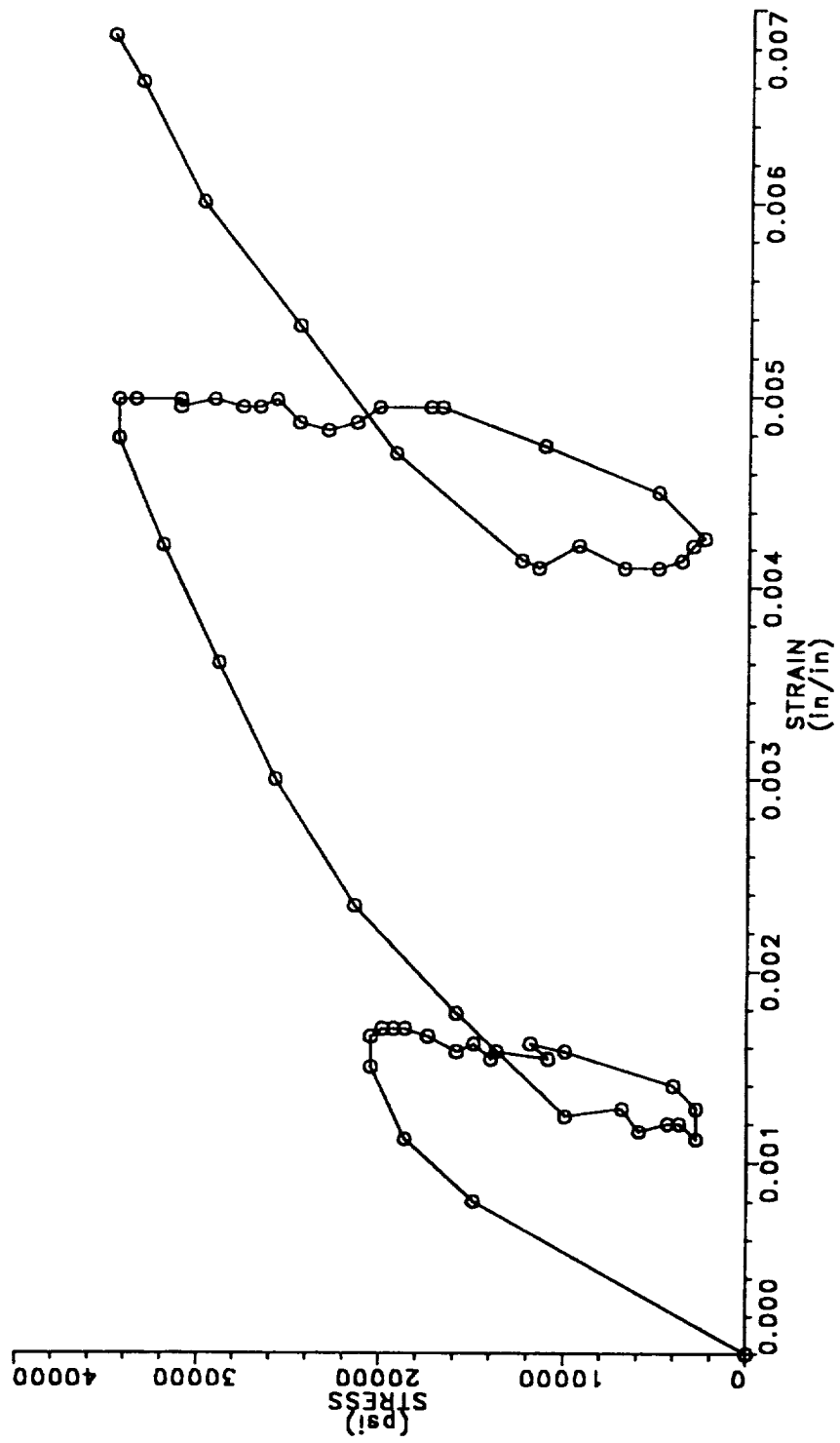
1600°F STRESS RELAXATION OF SPECIMEN 53-4 0.010" NOMINAL PWA 1480 BEFORE COATING
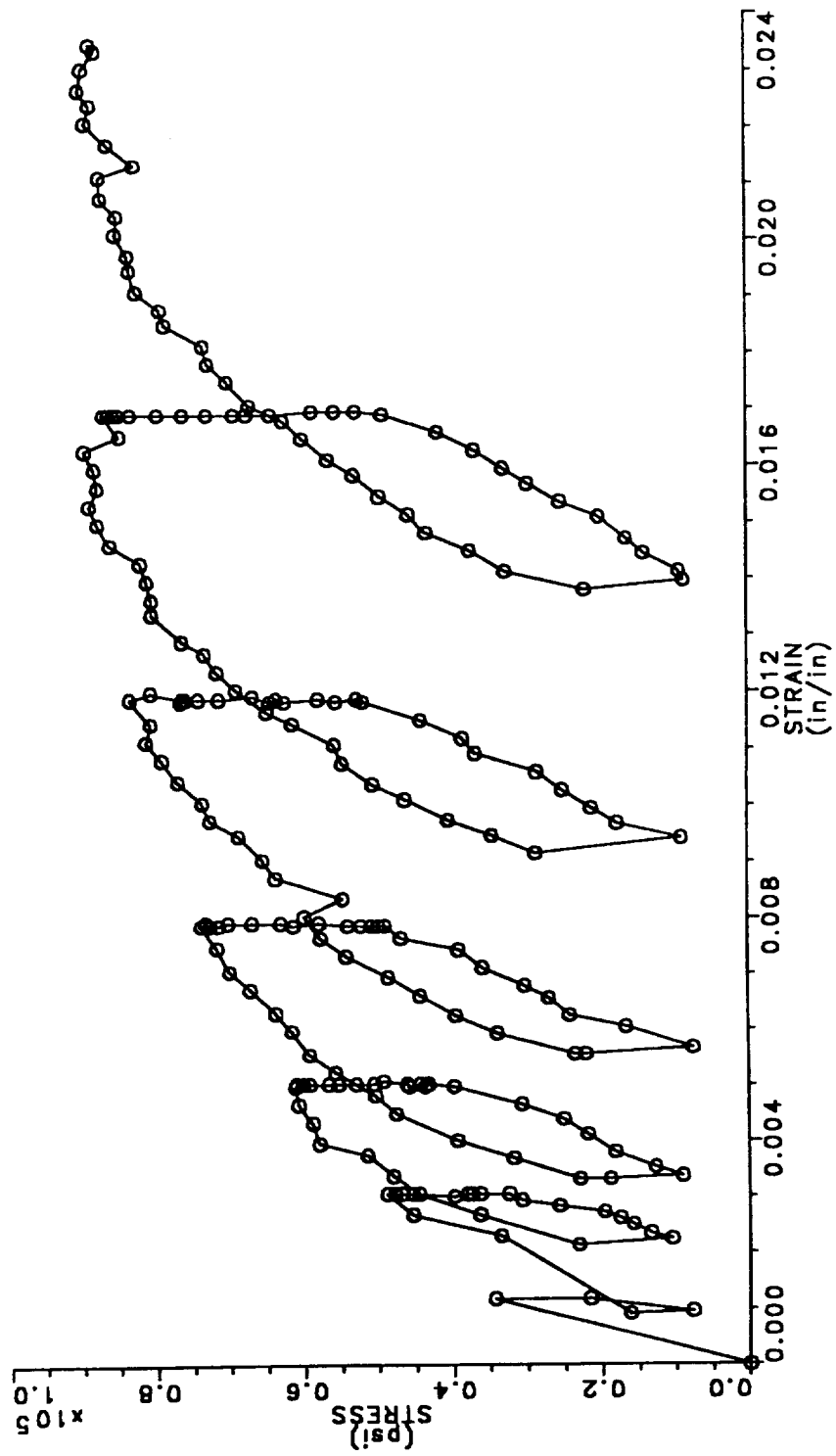
1700°F STRESS RELAXATION OF SPECIMEN 56-2 0.005" NOMINAL PWA 1480 BEFORE COATING

STRESS (psi)

STRAIN (in/in)
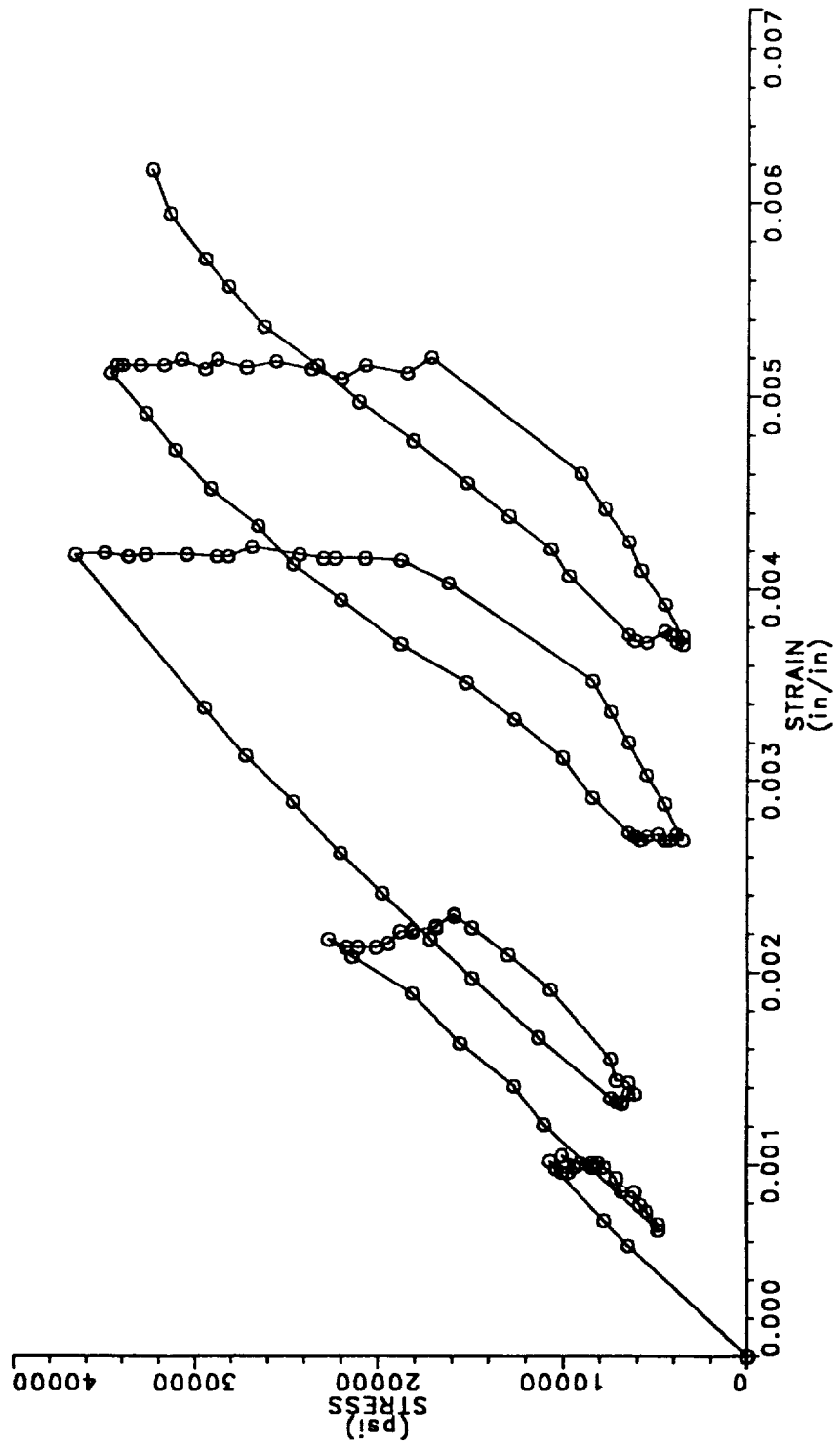
1700°F STRESS RELAXATION OF SPECIMEN 07-4 0.010" NOMINAL PWA 1480 BEFORE COATING
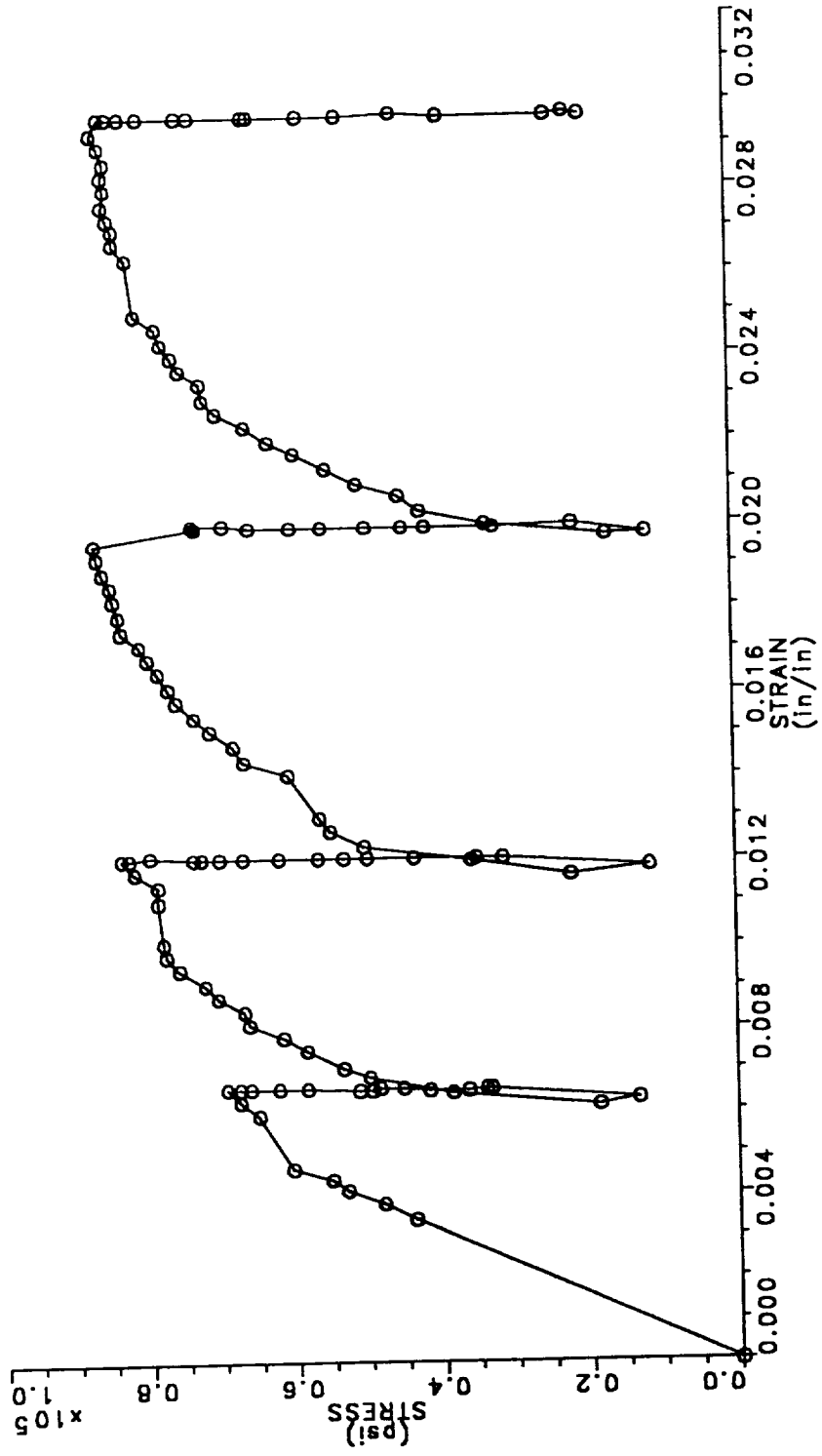
1800°F STRESS RELAXATION OF SPECIMEN 56–3 0.005" NOMINAL PWA 1480 BEFORE COATING

102
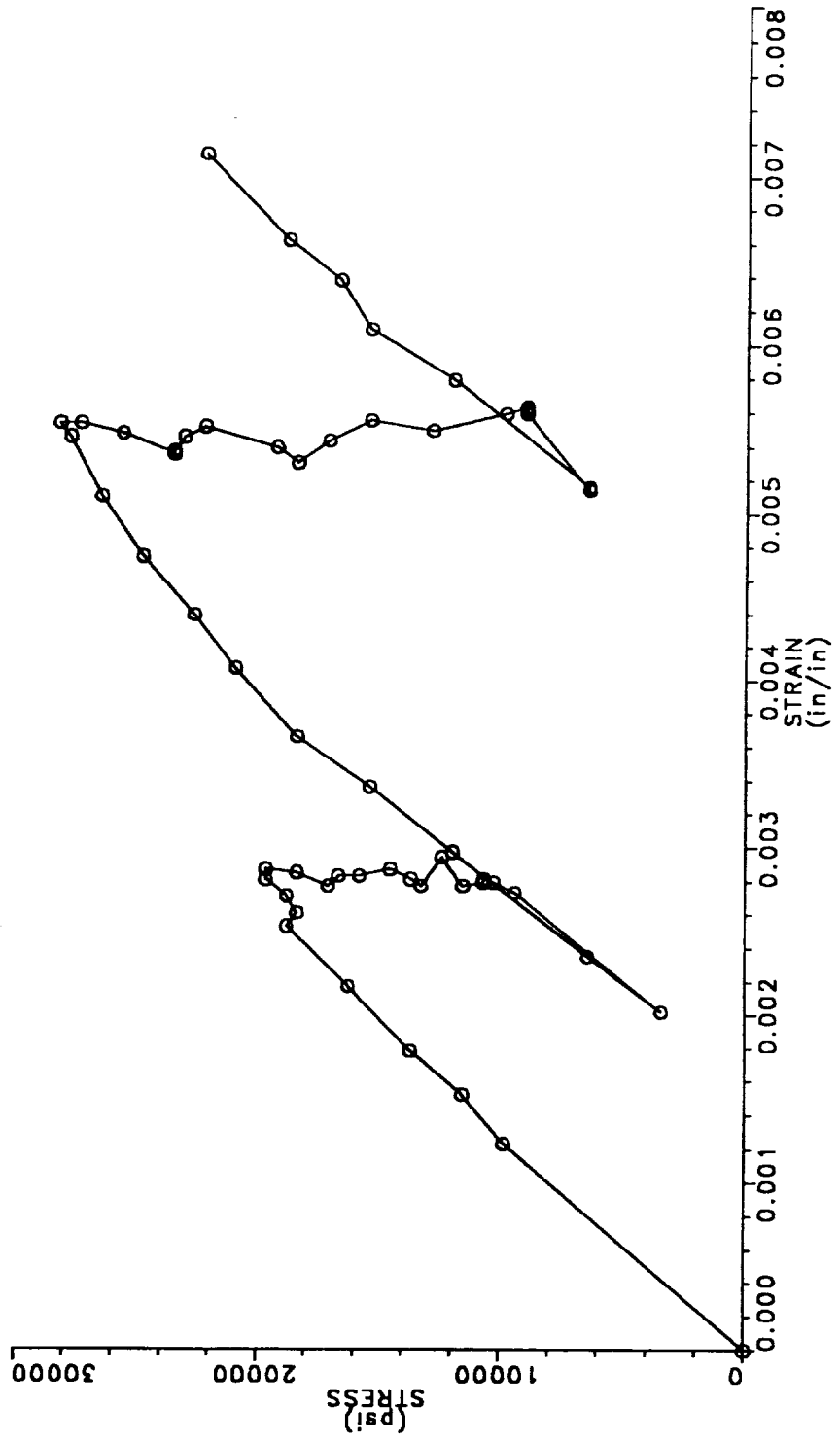
1800°F STRESS RELAXATION OF SPECIMEN 07-3 0.010" NOMINAL PWA 1480 BEFORE COATING
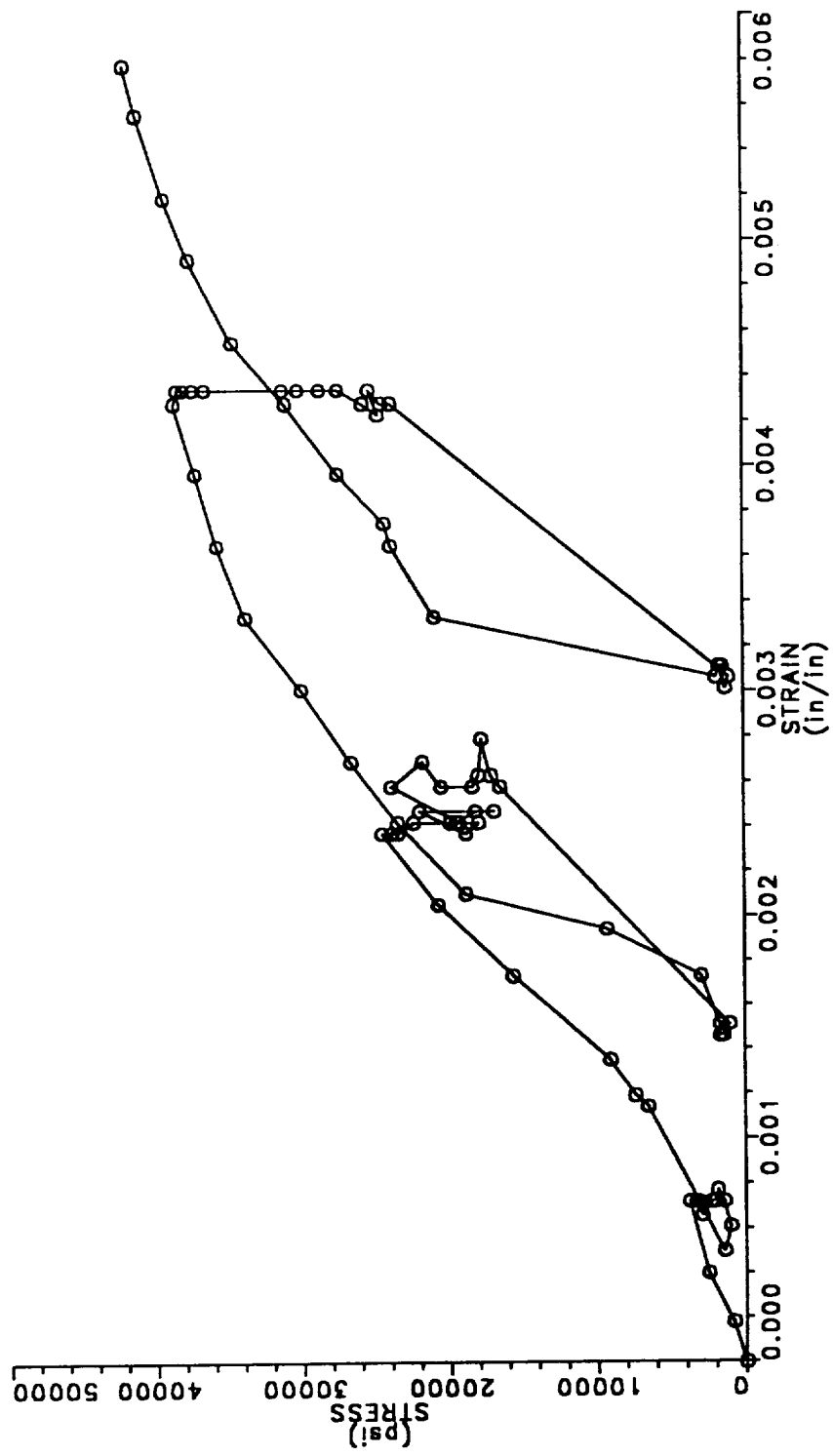
1800°F STRESS RELAXATION OF SPECIMEN 75-1 0.010" NOMINAL PWA 1480 BEFORE COATING
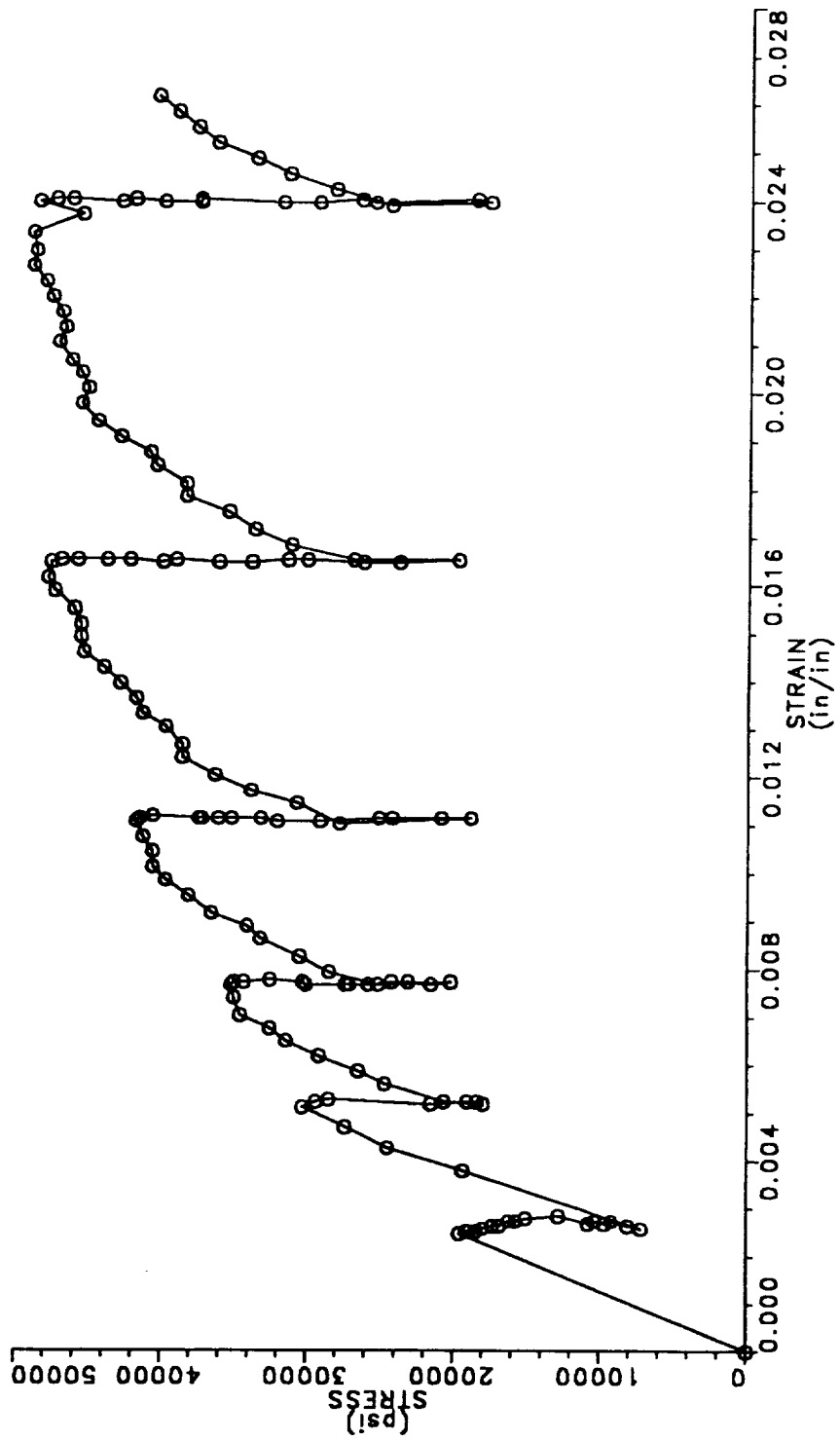
1900°F STRESS RELAXATION OF SPECIMEN 56-4 0.005" NOMINAL PWA 1480 BEFORE COATING

STRAIN (in/in)

STRESS (psi)
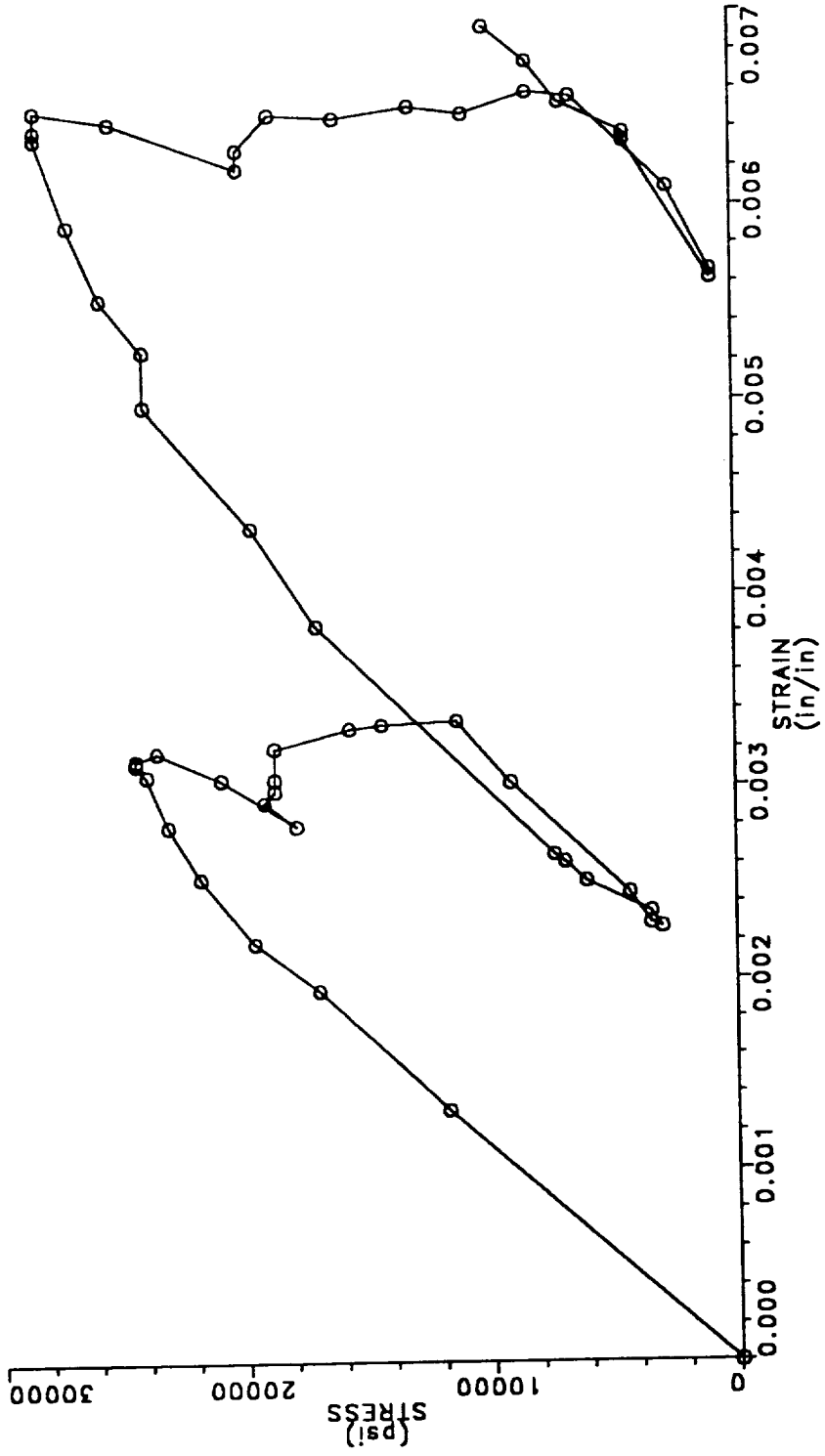
2000°F STRESS RELAXATION OF SPECIMEN 55-4 0.005" NOMINAL PWA 1480 BEFORE COATING
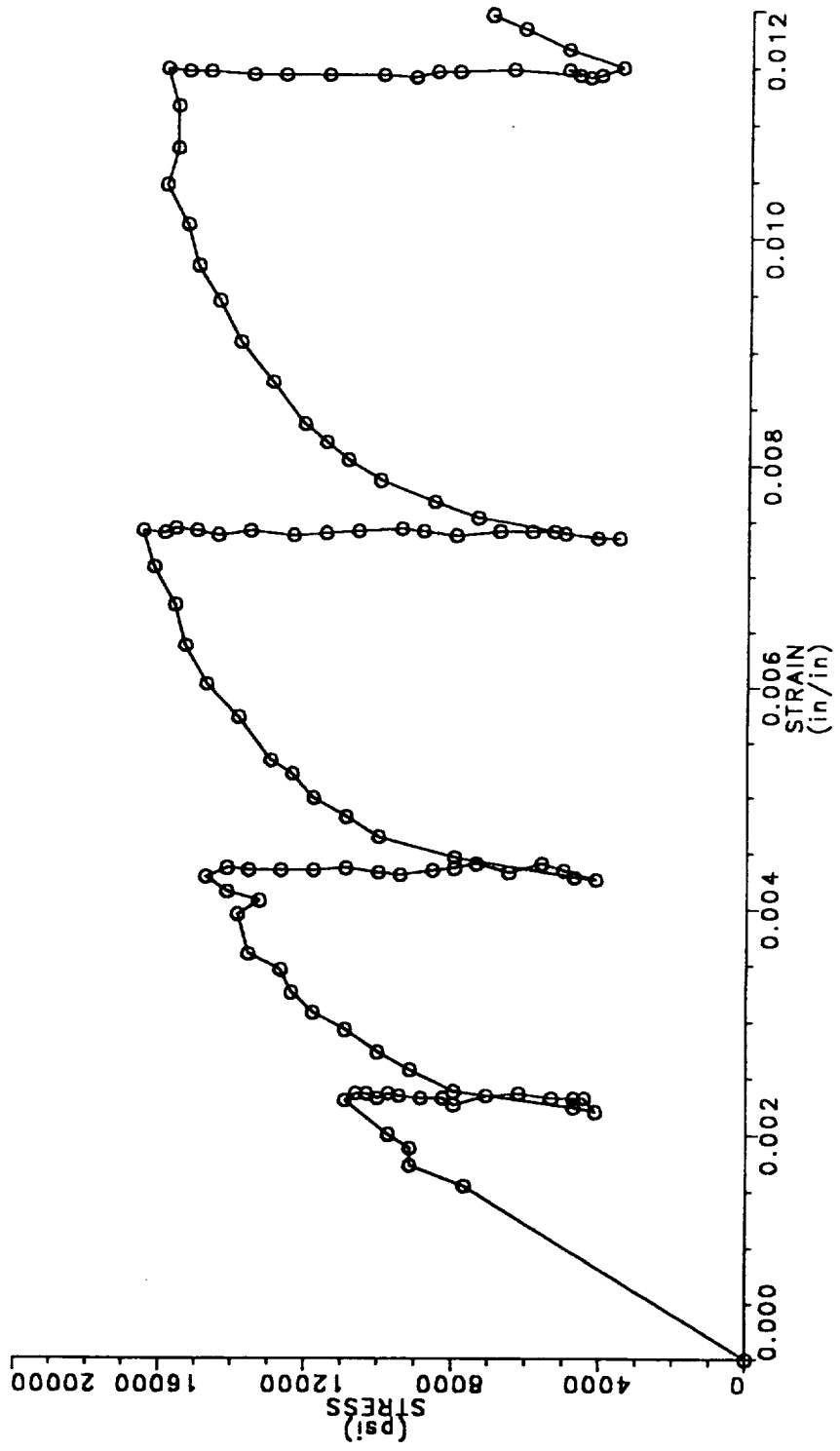
2000°F STRESS RELAXATION OF SPECIMEN 01-4 0.010" NOMINAL PWA 1480 BEFORE COATING
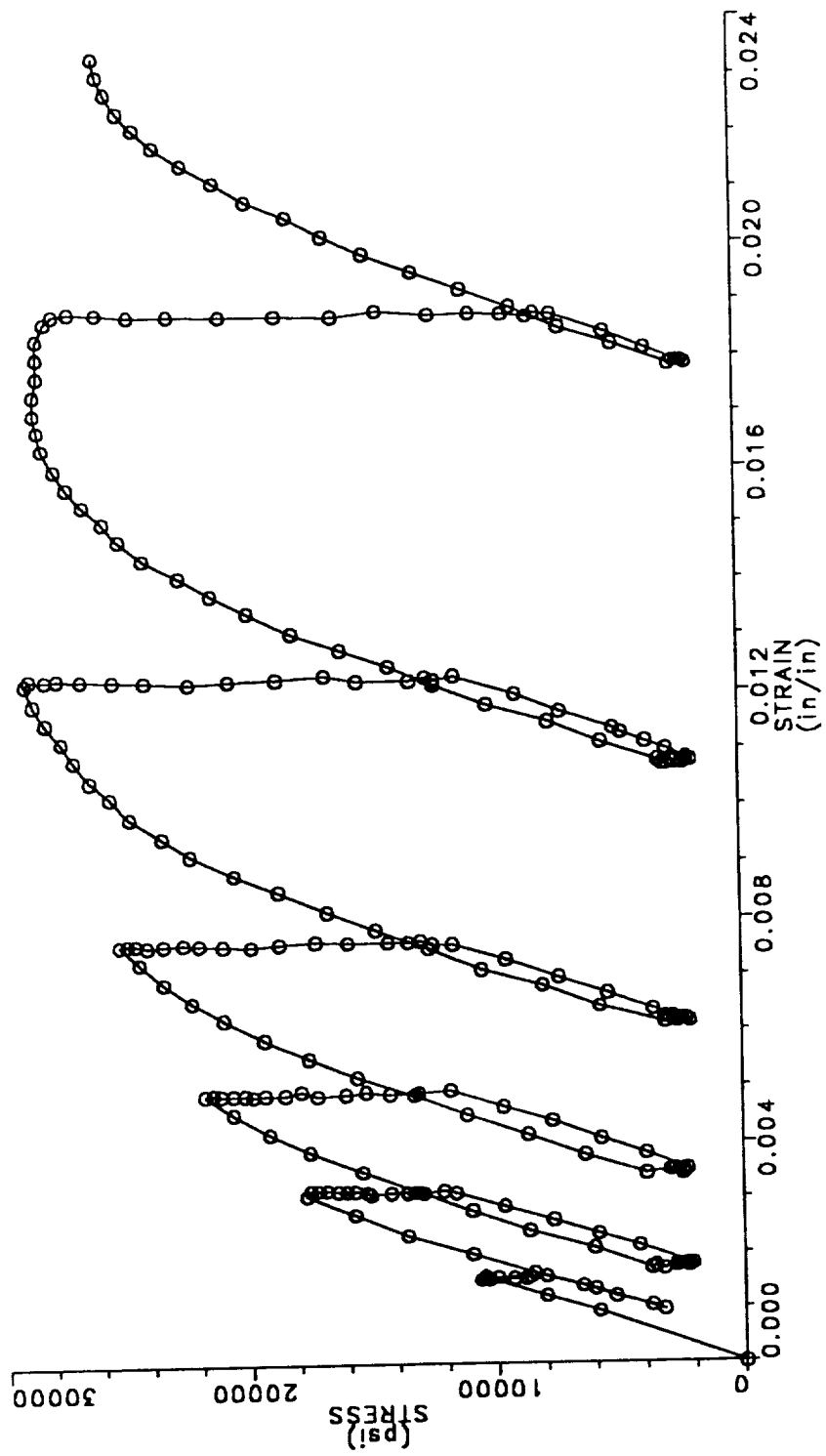
2000°F STRESS RELAXATION OF SPECIMEN 01-1 0.010" NOMINAL PWA 1480; UNCOATED
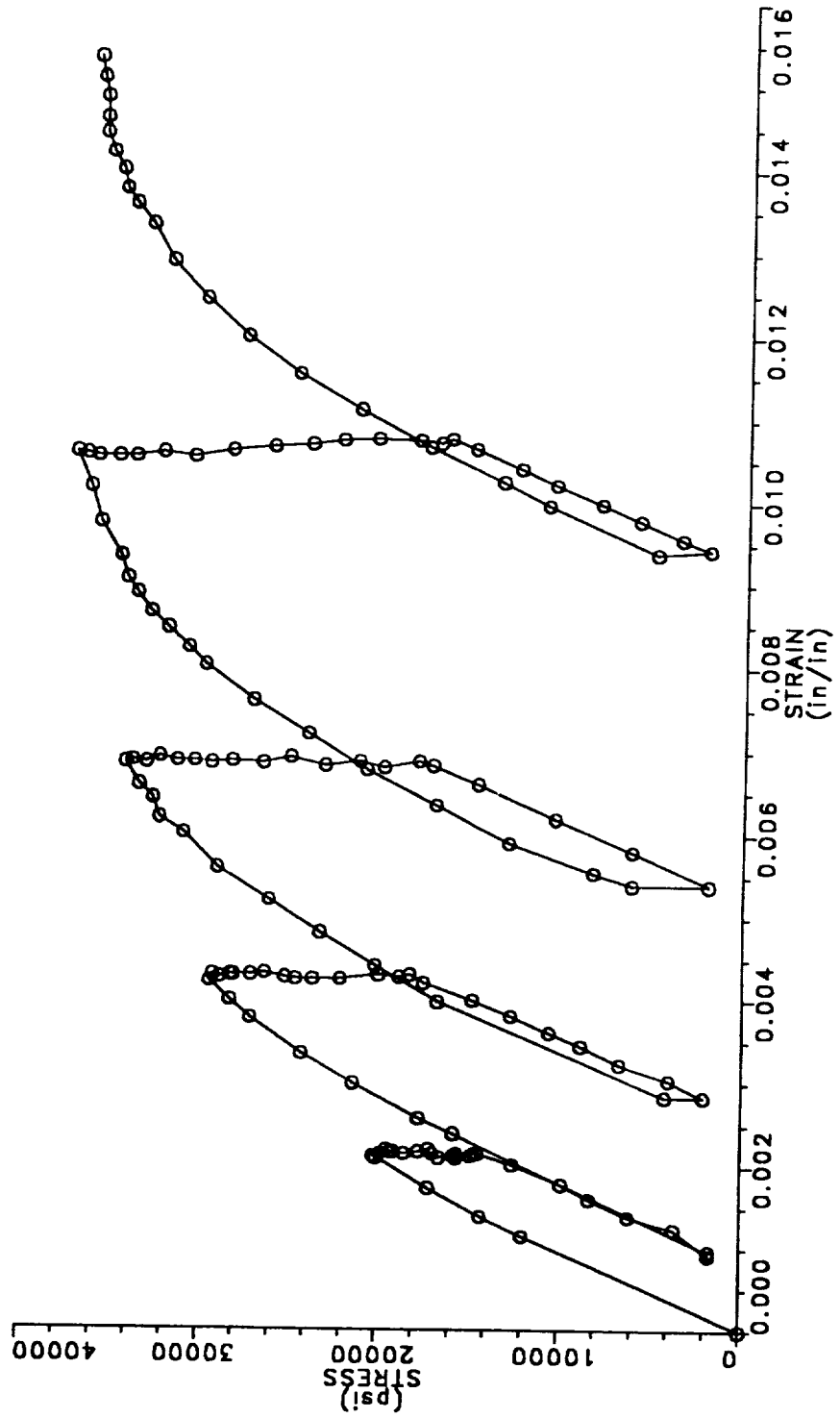
APPENDIX D

LIFE DATA SUMMARY FOR PWA 1480 FATIGUE TESTS

SCHEMATICS OF TMF CYCLES

OUT-OF-PHASE

IN-PHASE

Z-CYCLE

T-CYCLE

BASEBALL-CW

BASEBALL-CW

ELLIPTICAL-CCW

FOOTBALL-CW

110
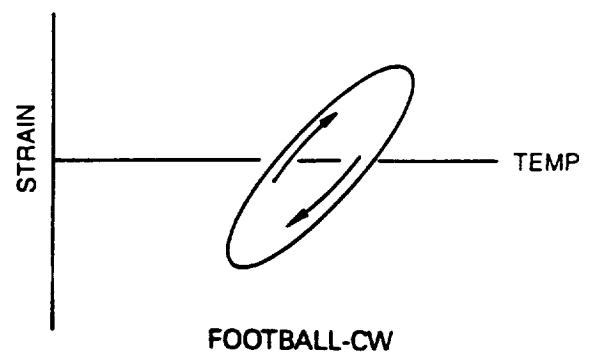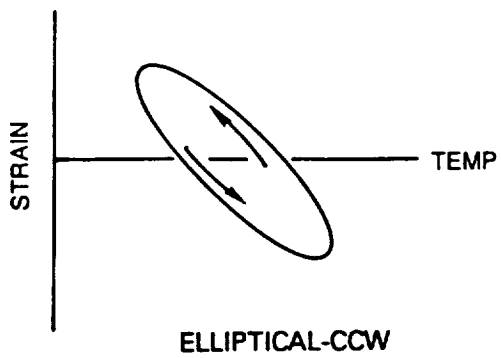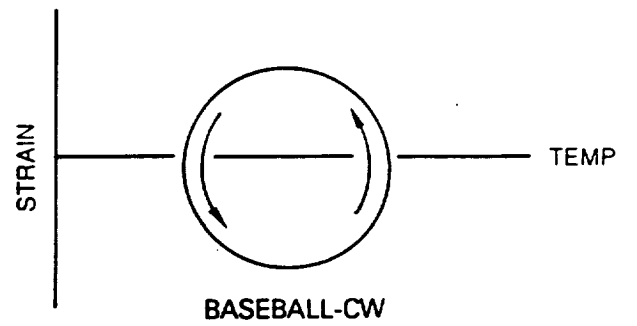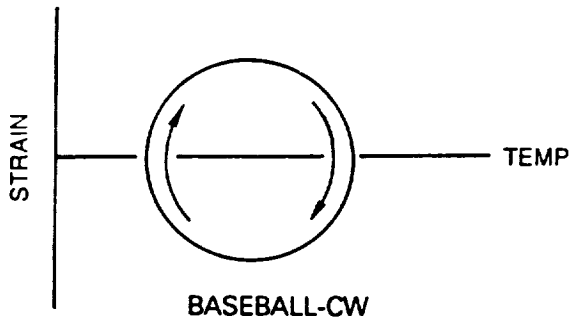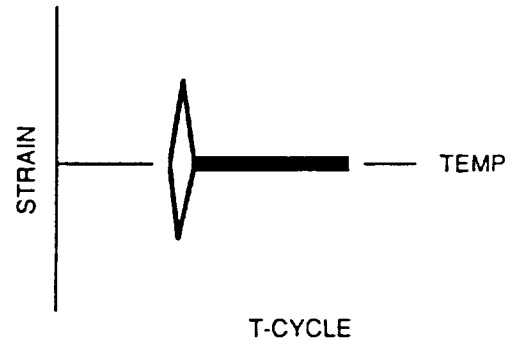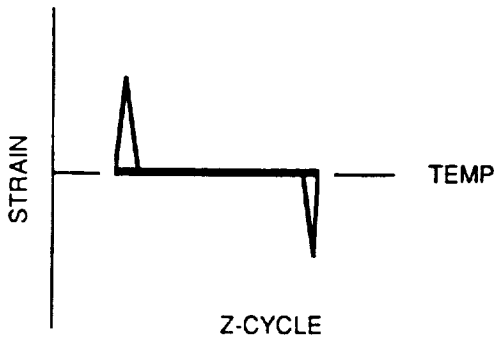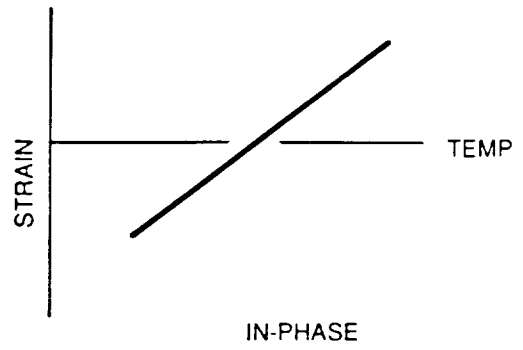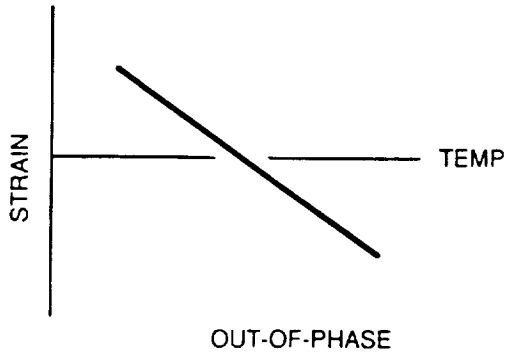
LIFE DATA SUMMARY FOR PWA 1480 FATIGUE TESTS

NOMENCLATURE

T = Task Number
S = Specimen Type
  r Internally Ridged Specimen 44C (Figure 8A).
  s Internally Ridged Specimen or Specimen 73C (Figure 8B).
      44C Specimen without Internal Ridges or Specimen 73C (Figure 8B).

Spec ID = Specimen Identification Number: JB = <001>; LB = <111>; KB = <011>; MB = <123>.
Tmax = Maximum Cycle Temperature (F), TMF Tmin = 800F.
Cycle Type = Test Waveform Information. All TMF Waveforms are 1 cpm Sine Waves Except as Noted.
DE = Test Mechanical Strain Range (%).
V = Test Strain Ratio. V=(Emax+Emin)/(Emax-Emin); Where Emax = Maximum Strain and Emin = Minimum Strain.
Init = Specimen Crack Initiation Location Which Led to Failure. Note: A "/" indicates that two modes were observed.

  c Coating
  cs Coating Diffusion Zone
  sc Coating-Substrate Interfacial Region
  s Substrate (Subsurface)
  ID Uncoated ID Surface of the Specimen; Coating Cracks Observed Along the OD Surface
  IDc Uncoated ID Surface of the Specimen; Coating Cracks Observed Along the OD Surface
  IDs Substrate (Subsurface) Initiation Near the Uncoated ID Surface
  d Test Discontinued with No Observed Cracks
  dc Test Discontinued with Coating Cracks Observed Along the OD Surface
  dcs Test Discontinued with Cracks Along OD Surface which Initiated at the Coating Diffusion Zone
  dsc Test Discontinued with Cracks Along OD Surface which Initiated at the Coating-Substrate Interfacial Region

Fail = Specimen Failure Location.
  gag Gage Section
  but Buttonhead Fillet
  ext Failure Caused by Cracking Underneath MTS Extensometer Quartz Rods
  IDr ID Ridge Region (44C Specimen Design)
  gagr OD Failure in Gage Section Near ID Ridge Region (44C Specimen Design)
  ogag Failure Occurred Outside Monitored Gage Section, but within the Constant Cross-Section Region

Exam = Inspection Technique Used to Define Initiation and Failure Locations and/or Crack Aspect Ratio and Crack Depth
  O Optical Microscopy; 7X-500X
  S Scanning Electron Microscopy; Backscatter and/or Secondary Electron Images
  T Transmission Electron Microscopy for Observing Dislocation Activity

Tc = Coating Thickness in Mils (1 Mil = .001 in).
Nc = Cycles to Initiate a Crack Through the Coating.
AR = OD Crack Aspect Ratio (Surface Length/Depth).
  E Estimated AR = Average of Specimen AR's at the Same Test Temperature
  Ring Crack AR Associated With Cracks Which "Ring" Specimen OD

Nmin = Lower Bound on (Nc+Nsc) or Nsi.
Nmax = Upper Bound on (Nc+Nsc) or Nsi.
Ind = Denotes Method Used to Determine Nmin and Nmax. See Descriptions in Section 6.3.2.
  rep Replica Data   Method 1)
  xtr Linear Extrapolation of Replica Data   Method 2))--- Nomenclature Used in Section 6.3.2.
  grf Graphical Method   Method 3))
  ld Specimen Load Drop Tangency Point   Method 4)

Nsc = Cycles to Grow a Coating Crack .010" into the Substrate.
Nsi = Cycles to Initiate a Substrate Crack Due to Macroscopic Slip, Oxidation Effects, or Defects.
5% = Cycles to 5% Stress Range Drop from Stress Range at Nf/2.
10% = Cycles to 10% Stress Range Drop from Stress Range at Nf/2.
Nf = Cycles to Specimen Failure (50% Tensile Load Drop or Separation, Whichever Comes First).

111

<001> PWA 1480 / PWA 273 ISOTHERMAL FATIGUE SUMMARY

T	S	Spec ID	Tmax (F)	Cycle Type	DE	V	Init	Fail	Exam	Tc	Nc	AR	Nmin	Ind	Nmax	Ind	Nsc	Nsi	5%	10%	Nf
5	s	JB-103	1400	PP, 8 cpm	.6	0	dc	gag	0	2.2	7200	4.0	63050	xtr	82680	xtr	56-76k	-	No load drop		>63050
5	s	JB-109	1400	PP, 8 cpm	.6	1	dc	gag	0	2.5	7700	5.0E	59800	-	-	-	>52k	-	No load drop		>59797
5	s	JB-96	1400	PP, 6 cpm	.8	0	dc	gag	0	3.2	1-2k	6.0	28254	xtr	42350	xtr	26-43k	-	No load drop		>28354
5	s	JB-23	1700	PP, 8 cpm	.6	0	c	gag	0	3.3	11500	5.6	20000	rep	20000	rep	8500	-	26000	26500	26833
5	s	JB-159	1700	CP, 8cpm+30s	.6	0	dc	gag	0	2.9	1.6-3.1k	7.0	19662	xtr	40030	xtr	16-38k	-	No load drop		>19662
5	s	JB-28	1700	PP, 7 cpm	.68	0	c	gag	0,S	2.6	1950	4.5	6600	rep	6600	rep	4650	-	12000	12500	12830
3	r	JB-31	1700	PP, 6 cpm	.8	0	c	gag	0	3.4	550	2.0	3000	rep	3000	rep	2450	-	6000	6070	6474
5	s	JB-120	1900	PP, 8 cpm	.6	0	c	gag	0	2.5	5900	2.2	11600	rep	11600	rep	5700	-	16500	-	17981
5	s	JB-65	1900	PP, 1 cpm	.6	0	IDc	gag	0	3.1	1700	2.2E	>5485	-	-	-	>3800	-	4000	5300	5485
5	s	JB-100	1900	PC, 8cpm+60s	.6	0	c	gag	0	3.0	900	2.4	1850	rep	1850	rep	950	-	3250	-	4096
5	s	JB-170	1900	CP, 8cpm+60s	.68	0	Specimen failed on loading. Loose grips caused extensometer slippage.														
5	s	JB-34	1900	PP, 7 cpm	.8	0	c	gag	0	3.3	1050	1.9	2600	rep	2600	rep	1550	-	5800	-	6183
3	r	JB-39	1900	PP, 6 cpm	.8	0	c	gag	0,S	3.1	1100	1.8	2830	rep	2830	rep	1730	-	5080	5150	5325
3	r	JB-50	1900	PP, 6 cpm	.8	0	c	gag	0,S	2.9	<770	2.7	1000	rep	1000	rep	<1000	-	4550	5100	5158
3	r	JB-37	1900	PP, 1 cpm	.8	0	IDc	gag	0	4.0	660	2.5	1970	rep	1970	rep	1310	-	3020	3300	3742
3	r	JB-36	1900	PC,10cpm+60s	.8	0	c	fDr	0	3.7	220	2.2E	>745	-	-	-	>525	-	720	730	745
3	r	JB-35	1900	CP,10cpm+60s	.8	0	c	gag	0,S	4.0	170	2.0	720	rep	720	rep	>525	-	3000	3500	3954
3	s	JB-79	1900	PP, 4.6 cpm	1.04	0	c	gag	0,S	3.4	640	3.7	1280	grf	1600	1d	640-960	-	1580	1630	1856
5	s	JB-163	2100	PP, 10 cpm	.5	0	c	gag	0	2.6	2000	2.2	5000	rep	9300	1d	3-7.3k	-	5900	6500	9652
5	s	JB-168	2100	PP, 8 cpm	.6	0	c	gag	0	2.9	1440	2.4	4000	rep	4000	rep	2560	-	3600	4400	6146

<001> PWA 1480 / PWA 286 ISOTHERMAL FATIGUE SUMMARY

T	S	Spec ID	Tmax (F)	Cycle Type	DE	V	Init	Fail	Exam	Tc	Nc	AR	Nmin	Ind	Nmax	Ind	Nsc	Nsi	5%	10%	Nf
3	s	JB-102	800	PP, 8 cpm	.6	0	d	-	0	4.1	>41578	-	10450	rep	10450	rep	4480	-	No load drop		>41578
5	s	JB-97	800	PP, 6 cpm	.8	0	c	gag	0	4.1	6000	3.0	3640	grf	3770	grf	1.5-1.7k	-	No load drop		14475
5	s	JB-99	800	PP, 5 cpm	1.0	0	c	gag	0	4.6	2120	3.0						-	No load drop		5047
5	s	JB-37	1400	PP, 6 cpm	.8	0	c	but	0	4.6	3600	3.3	23630	xtr	87120	xtr	20-84k	-	No load drop		>23630
5	s	JB-94	1400	PC, 6cpm+60s	.8	0	dc	gag	0	4.8	1920	4.2	7400	xtr	26830	xtr	5.5-25k	-	No load drop		>7400
5	s	JB-63	1400	PP, 5cpm sin	1.0	0	c	gag	0	5.2	1220	3.3	3460	grf	10836	grf	2.2-9.6k	-	No load drop		14936
5	s	JB-75	1400	PP, 5cpm sin	1.0	0	dc	gag	0	4.2	920	3.3	3409	xtr	50700	xtr	2.5-50k	-	No load drop		>3409
5	r	JB-158	1400	CP, 5cpm+300s	1.0	0	dc	gag	0	5.8	>1540	3.6E	-		-		-	-	No load drop		>1540
5	s	JB-69	1400	PP, 4.4cpm sin	1.1	0	c	gag	0	4.6	1170	3.7	2350	grf	3560	grf	1.2-2.4k	-	5620	5640	5650
5	s	JB-7	1400	PP, 4 cpm	1.2	0	IDc	but	0	5.7	1300	3.6E	-		-		-	-	No load drop		4090
5	s	JB-123	1700	PP, 8 cpm	.6	0	c	gag	0	5.3	8100	7.0	23200	grf	-		>15100	-	76000	77000	78168
5	s	JB-169	1700	PP, 6 cpm	.8	0	c	gag	0	5.8	2420	4.2	6800	grf	-		>4400	-	20000	-	21760
5	s	JB-129	1700	PP, 6 cpm	.8	0	IDc	gag	0	3.6	2820	2.8	6500	rep	6500	rep	3680	-	22100	22300	22462
3	r	JB-2	1700	PP, 1 cpm	.8	0	ID/c	IDr	0	5.1	2000	2.0	>7162	-	-		5160	-	6930	7010	7167
5	s	JB-155	1700	PP, 1 cpm	.8	0	IDc	gag	0	5.1	2820	2.5	6600	rep	6600	rep	3780	-	13800	-	13900
5	s	JB-139	1700	PC, 6cpm+60s	.8	0	c	gag	0	4.4	780	2.6	>3128	-	-		>2350	-	2980	3020	3128
5	s	JB-160	1700	CP, 5cpm+60s	1.0	0	c	gag	0	5.6	960	2.5	1640	rep	1640	rep	680	-	5200	5400	5645
5	s	JB-126	1900	PP, 10 cpm	.5	0	IDc	gag	0	6.3	8200	2.0	>27338	-	-		>19200	-	26800	27000	27338
5	s	JB-130	1900	PP, 1.33 cpm	.6	0	IDc	gag	0	5.6	2560	2.7	>7290	-	-		>4730	-	6250	7150	7290
3	s	JB-25	1900	PP, 6 cpm	.8	0	IDc	gag	0	4.6	>1750	2.6	>4285	-	-		>2500	-	4100	4200	4285
5	s	JB-85	1900	PP, 6 cpm	.8	0	IDc	gag	0	5.1	2280	2.5	>6766	-	-		>4490	-	-	-	6766
3	r	JB-5	1900	PP, 1 cpm	.8	0	IDc	IDr	0,S	4.6	550	1.8	>2595	-	-		>2045	-	2130	-	2595
5	s	JB-24	1900	PP, 1 cpm	.8	0	IDc	gag	0	4.7	1550	3.0	>4471	-	-		>2920	-	2450	3700	4471
3	s	JB-20	1900	PC, 10cpm+60s	.8	0	IDc	gag	0	4.4	1320	2.6	>2192	-	-		>870	-	1800	2010	2192
3	r	JB-6	1900	PC, 10cpm+60s	.8	0	IDc	IDr	0,S	4.7	610	2.6E	>1100	-	-		>480	-	-	-	1100
3	s	JB-71	1900	CP, 10cpm+60s	.8	0	IDc	gag	0	4.7	990	3.8	>1514	-	-		>520	-	1400	1420	1514
5	s	JB-134	1900	CP, 6cpm+120s	.8	0	IDc	gag	0	4.9	810		>1335	-	-		>540	-	-	-	1335
3	s	JB-78	1900	PP, 4.6 cpm	1.04	0	IDc	gag	0,S	5.2	1210	2.6E	>1929	-	-		>720	-	1640	1860	1929
5	s	JB-171	2100	PP, 8 cpm	.6	0	IDc	gag	0	5.0	3670	3.5	>5676	-	-		>2000	-	4250	5200	5676
5	s	JB-151	2100	PP, 1 cpm	.6	0	?	gag	0	3.5	1400	3.5E	>5690	-	-		>4290	-	5000	5470	5690
5	s	JB-162	2100	PP, 7 cpm	.68	0	IDc	gag	0	5.8	2230	3.5	>3856	-	-		>1620	-	2370	2900	3856

*The following specimens were exposed 100 hr. at 2000F prior to test.

T	S	Spec ID	Tmax (F)	Cycle Type	DE	V	Init	Fail	Exam	Tc	Nc	AR	Nmin	Ind	Nmax	Ind	Nsc	Nsi	5%	10%	Nf
5	s	JB-138	1400	PP, 6 cpm	.8	0	c	but	0	5.0	2170	3.8E	>61k	-	-		>59300	-	60890	61400	61470
5	s	JB-150	1900	PP, 6 cpm	.8	0	IDc	gag	0	5.6	1-2k	3.8	>2097	-	-		-	-	2000	2040	2097

113

<001> PWA 1480 / UNCOATED ISOTHERMAL FATIGUE SUMMARY

T	S	Spec ID	Tmax (F)	Cycle Type	DE	V	Init	Fail	Exam	Tc	Nc	AR	Nmin	Ind	Nmax	Ind	Nsc	Nsi	5%	10%	Nf
3	r	JB-42	1900	PC,10cpm+60s	.8	0	-	gag	Cracks were from OD Copper deposit from induction coil.										1730	1760	2013

<001> PWA 1480 / PWA 273 THERMOMECHANICAL FATIGUE SUMMARY

T	S	Spec ID	Tmax (F)	Cycle Type	DE	V	Init	Fail	Exam	Tc	Nc	AR	Nmin	Ind	Nmax	Ind	Nsc	Nsi	5%	10%	NF
5	s	JB-76	1700	Football,cw	.4	1	d	-	0	4.0	No cracks observed in the gage section.								No load drop		>21758
5	s	JB-125	1900	Out-of-phase +300s @Tmax	.3	0	c		0	3.1	670	21.	1270	rep	3300	1d	600-2630	-	2880	3340	3378
5	s	JB-98	1900	Out-of-phase	.4	0	c	gag	0,S	2.9	4-6k	7-9	9000	grf	13400	grf	3.0-9.4k	-	15900	-	16169
5	s	JB-61	1900	Out-of-phase	.4	0	c	gag	0	3.3	2.6-5k	Ring	-		6150	1d	<3550	-	6200	-	6216
5	s	JB-66	1900	Out-of-phase	.4	0	c	gag	0	2.9	1-2k	20.	2800	rep	4000	1d	800-3000	-	4100	4150	4162
5	s	JB-62	1900	Out-of-phase +60s @Tmax	.4	0	c	gag	0	3.9	.5-1k	10.	-		1710	xtr	<1210	-	1750	1765	1779
5	s	JB-91	1900	Out-of-phase +300s @Tmax	.5	0	c	gag	0	3.4	.6-1k	7.0	1840	grf	2730	grf	840-2130	-	-	-	3283
3	r	JB-22	1900	Out-of-phase	.52	0	c	gagr	0,S,T	3.3	400-800	14.	1960	grf	2940	grf	1.1-2.5k	-	3710	3740	3772
5	s	JB-59	1900 plus	In-phase	.7	0	dc	gag	-	3.5	1900	-	17600	-	-	-	>15700	-	-	-	>17637
				Out-of-phase	.4	0	dc	gag	0	-		5.0	3300	rep	5000	1d	3.3-5.0k	-	5160	5220	5315
3	r	JB-29	1900	In-phase	.75	0	c	gagr	0,S,T	3.4	1250	4-6	10340	xtr	92160	xtr	9.1-91k	-	No load drop		>10339
3	r	JB-19	1900	Out-of-phase	.76	0	c	gag	0,S	2.8	<12	Ring	215	xtr	570	xtr	200-560	-	572	580	580
3	r	JB-38	1900	2-cycle .5cpm	.76	0	c	gag	0	4.0	650	Ring	1060	rep	1200	rep	410-550	-	1480	-	1505
3	s	JB-81	1900	Out-of-phase	.8	-1	c	gag	0,S	3.0	<21	Ring	187	xtr	460	1d	160-440	-	530	540	541
3	s	JB-72	1900	2-cycle .5cpm	.8	0	c	gag	0,S	3.0	<50	Ring	353	xtr	870	1d	300-820	-	870	-	876
5	s	JB-64	1900	In-phase	1.0	0	c	gag	0	3.6	400	5.5	-		-		-	-	No load drop		615
5	s	JB-88	2100	Out-of-phase	.3	0	c	gag	0	4.0	<3000	3.0	8600	grf	10000	1d	<7000	-	10100	10700	12756
5	s	JB-82	2100	Out-of-phase	.5	0	c	gag	0	3.6	<<550	Ring	-		780	grf	<780	-	1300	-	1326

*The following specimens were exposed 100 hr. at 2000F prior to test.

T	S	Spec ID	Tmax (F)	Cycle Type	DE	V	Init	Fail	Exam	Tc	Nc	AR	Nmin	Ind	Nmax	Ind	Nsc	Nsi	5%	10%	NF
5	s	JB-154	1900	Out-of-phase	.4	0	c	gag	0,S	2.5	<1020	4.7	1000	rep	2000	rep	1-2k	-	5580	6200	6562
5	s	JB-161	1900	Out-of-Phase	.4	0	c	gag	0	2.7	<425	Ring	2150	xtr	2540	-	1.7-2.5k		No load drop		2543

115

<001> PWA 1480 / PWA 286 THERMOMECHANICAL FATIGUE SUMMARY

T	S	Spec ID	Tmax (F)	Cycle Type	DE	V	Init	Fail	Exam	Tc	Nc	AR	Nmin	Ind	Nmax	Ind	Nsc	Nsl	5%	10%	Nf
5	s	JB-174	1900	Out-of-phase	60	.5	c	gag	0	4.4	2050	4.6	4400	rep	4400	rep	2350	-	No load drop		9900
5	s	JB-147	1900	Out-of-phase	.45	0	c	gag	0,S	4.0	1400	4.5	2250	rep	2250	rep	850	-	7100	7900	8174
5	s	JB-121	1900	Out-of-phase	.45	-1	c	gag	0	5.4	1350	4.5	2400	rep	2400	rep	1050	-	4200	5630	6014
5	s	JB-137	1900	Out-of-phase +30s @Tmax	.45	-1	c	gag	0	4.9	1070	3.0	2050	rep	2050	rep	980	-	3830	4600	4946
7	s	JB-135	1900	Airfoil LE +60s @Tmax	.45	-1	c	gag	0	4.3	1280	4.4	2070	rep	2070	rep	790	-	3570	4730	5059
3	r	JB-10	1900	Out-of-phase .25cpm +60s @Tmax	.5	0	c	gagr	0,S	4.7	500	2.2	840	rep	3000	1d	.34-2.5k	-	3230	4050	4105
3	s	JB-104	1900	T-cycle .5cpm	.6	0	c	ext	0	4.7	3300	4.0	6000	-	6000	-	2700	-	No load drop		6032
3	r	JB-9	1900	Out-of-phase	.76	0	c	gag	0,S,T	5.0	370	2.5	820	grf	1600	1d	.5-1.2k	-	1730	1870	1878
3	r	JB-11	1900	In-phase	.79	0	-	IDr	0,S,T	5.0	>10000	-	-	-	-	-	-	-	10050	10400	10535
3	s	JB-80	1900	Out-of-phase	.8	-1	c	gag	0,S	5.5	300	2.2	600	grf	1100	1d	300-800	-	1450	1470	1472
3	s	JB-21	1900	Z-cycle .5cpm	.8	0	c	gagr	0,S	5.6	820	3.0	1380	grf	1490	grf	560-670	-	1840	-	1847
5	s	JB-102	1900	Baseball,ccw	.8	0	IDc	gag	0	4.1	1260	2.6	3430	xtr	-	-	>2170	-	No load drop		3426
5	s	JB-111	2100	Out-of-phase	.35	0	c	ext	0	5.0	3000	4.3	4830	grf	6865	grf	1.8-3.9k	-	4980	5100	7205
5	s	JB-89	2100	Out-of-phase	.5	0	c	gag	0	5.0	770	2.0	1930	grf	2320	grf	1.1-1.6k	-	2410	2730	2912
5	s	JB-146	1900	Out-of-phase	.4	0	c	gag	0	4.5	1400	4.4	3022	xtr	3610	xtr	1.6-2.2k	-	No load drop		3022
5	s	JB-133	1900	Out-of-phase	.45	0	c	gag	0,S	4.7	740	3.5	1650	rep	1650	rep	910	-	2200	2900	3804

Note: JB-174 was a load controlled test. DE = Test stress range, V = Test stress ratio

Note: JB-102 previously was run for 41578 cycles at 800F, +-.3%, 8 cpm.

*The following specimens were exposed 100 hr. at 2000F prior to test.

<001> PWA 1480 / UNCOATED THERMOMECHANICAL FATIGUE SUMMARY

T	S	Spec ID	Tmax (F)	Cycle Type	DE	V	Init	Fail	Exam	Tc	Nc	AR	Nmin	Ind	Nmax	Ind	Nsc	Nsi	5%	10%	Nf
3	s	JB-51	1900	Out-of-phase	.55	0	ID	gag 0	No data available.										11400	11700	11806
3	s	JB-46	1900	Out-of-phase	.8	0	ID	gag 0,S	No data available.										2460	2550	2589
3	s	JB-47	1900	In-phase	.8	0	ID	gag 0,S	No data available.										5000	6000	6075

T	S	Spec ID	Tmax (F)	Cycle Type	DE	V	Init	Fail	Exam	Tc	Nc	AR	Nmin	Ind	Nmax	Ind	Nsc	Nsi	5%	10%	Nf
5	s	LB-106	800	PP, 12 cpm	.4	0	-	but	0	3.1	>27800	-	-	-	-	-	-	-	No load drop		27800
5	s	LB-22	1400	PP, 10 cpm	.5	0	cs	gag	0,S	3.0	1000	8.6	-	-	7600	1d	<6600	-	No load drop		7623
3	s	LB-25	1400	PP, 8 cpm	.6	0	sc	gag	0,S	2.9	>925	Ring	-	-	1720	1d	-	<1720	1720	-	1724
3	s	LB-19	1400	PP, 8 cpm sin	.6	0	cs	gag	0,S	2.7	>1370	Ring	-	-	1800	1d	<430	-	1850	1880	1953
3	s	LB-121	1400	PP, .5 cpm	.6	0	cs	gag	0,S	2.9	300	Ring	-	-	400	1d	<100	-	420	480	565
3	s	LB-120	1400	PP, .5 cpm	.6	0	s	gag	0	2.5	>975	Ring	-	-	1202	1d	-	<1202	1200	-	1202
3	s	LB-124	1400	PP, .5 cpm	.6	0	s	gag	0,S	3.1	>1110	Ring	-	-	1320	1d	-	<1320	1320	-	1362
5	s	LB-236	1700	PP, 14 cpm	.34	0	s	gag	0,S	2.0	>11.5k	2.5	18000	rep	19400	rep	-	18-20k	20700	-	21042
5	s	LB-195	1700	PP, 12.5 cpm	.4	0	s	gag	0	2.4	>3620	2.0	5080	rep	5080	rep	-	5080	6600	7000	7680
5	s	LB-180	1700	PP, 10 cpm	.5	0	s	gag	0	2.1	>3600	-	-	-	3600	1d	-	<3600	3750	3800	3941

118

<111> PWA 1480 / PWA 286 ISOTHERMAL FATIGUE SUMMARY

T	S	Spec ID	Tmax (F)	Cycle Type	DE	V	Init	Fail	Exam	Tc	Nc	AR	Nmin	Ind	Nmax	Ind	Nsc	Nsi	5%	10%	Nf
5	s	LB-30	800	PP, 10 cpm	.5	0	-	but	0	5.5	>7130	-	-	-	-	-	-	-	No load drop		7130
5	s	LB-209	1400	PP, 12.5 cpm	.4	0	s	but	0	5.8	>38000	2.8	-	-	42600	-	-	<42600	No load drop		42603
5	s	LB-241	1400	PP, 10 cpm	.5	0	s	gag	0	5.5	>11850	-	-	-	11800	ld	-	<11800	11800	-	11850
5	s	LB-235	1400	PP, .5 cpm	.5	0	s	gag	0	5.7	>6900	2.0	6200	rep	7320	grf	-	6.2-7.3k	9200	-	9220
5	s	LB-185	1700	PP, 16 cpm	.3	0	s	gag	0	5.7	>96700	-	-	-	119000	ld	-	<119k	-	119000	120k
5	s	LB-192	1700	PP, 14 cpm	.34	0	IDs	gag	0	5.9	>42.6k	-	-	-	42600	-	-	<42600	45600	46500	46583
5	s	LB-188	1700	PP, 12.5 cpm	.4	0	s	gag	0	5.0	>8000	-	-	-	9200	ld	-	<9200	9210	9220	9233
5	s	LB-233	1900	PP, 14 cpm	.34	0	s	gag	0	4.5	>6340	2.5	6340	rep	8870	ld	-	6.3-8.9k	8700	8900	9062
5	s	LB-232	1900	PP, .5 cpm	.34	0	IDc	gag	0	5.3	10000	-	-	-	-	-	-	-	7500	10300	10761
5	s	LB-179	2100	PP, 10 cpm	.5	0	ID	gag	0	5.6	>911		Constitutive test, no replica data taken.						770	900	911

<111> PWA 1480 / UNCOATED ISOTHERMAL FATIGUE SUMMARY

T	S	Spec ID	Tmax (F)	Cycle Type	DE	V	Init Fail	Exam	Tc	Nc	AR	Nmin Ind	Nmax Ind	Nsc	Nsi	5%	10%	Nf
3	s	LB-59	1400	PP, 8 cpm	.6	0	s	gag 0	-	-	2.0	1220 rep	1300 rep	-	1.2-1.3k	-	-	1445
3	s	LB-36	1400	PP,8 cpm sin	.6	0	s	gag 0,S	-	-	2.0	1550 rep	1750 rep	-	1.5-1.8k	2260	-	2331

120

<111> PWA 1480 / PWA 273 THERMOMECHANICAL FATIGUE SUMMARY

T	S	Spec ID	Tmax (F)	Cycle Type	DE	V	Init Fail	Exam	Tc	Nc	AR	Nmin	Ind	Nmax	Ind	Nsc	Ns1	5%	10%	Nf
3	s	LB-23	1900	Out-of-phase	.25	0	ID	gag 0.5	2.4	>6900	-	-	-	1408	rep	.8-1k	-	8150	8200	8211
3	s	LB-20	1900	Out-of-phase	.3	0	cs	ogag 0.5	2.7	400	7.-10.	1220	rep	6500	1d	-	5.2-6.5k	-	-	1408
3	s	LB-21	1900	Baseball,ccw	.3	0	s	gag 0.5	3.6	>4700	-	5250	rep			-	-	6600	6650	6689
3	s	LB-156	1900	Baseball,cw	.3	0	sc/ID	gag 0.5	3.0	>860	2.2-3.4	1230	rep	1370	rep	-	370-510	-	-	1639
3	s	LB-155	1900	Baseball,cw 0.5 cpm	.6	0	-	gag 0	-	Tensile failure								No load drop		31
5	s	LB-189	2100	Out-of-phase	.25	0	c	gag 0	3.2	860	4.0	1800	rep	3700	1d	1-3k	-	3870	4000	4131
5	s	LB-240	2100	In-phase	.4	0	s	gag 0	2.0	>2233	-	1200	rep	2000	1d	-	1.2-2k	2180	-	2233

<111> PWA 1480 / PWA 286 THERMOMECHANICAL FATIGUE SUMMARY

T	S	Spec ID	Tmax (F)	Cycle Type	DE	V	Init Fail	Exam	Tc	Nc	AR	Nmin	Ind	Nmax	Ind	Nsc	Nsi	5%	10%	Nf
s	s	LB-170	1900	Out-of-phase	.25	0	c	ext 0.5	5.5	5720	2.8	6480	rep	6480	rep	760	-	6250	-	6290
s	s	LB-181	1900	Out-of-phase	.25	0	dc	gag 0.5	5.7	5720	2.4	6720	rep	6720	rep	1000	-	7630	7670	7675
s	s	LB-27	1900	Out-of-phase	.3	0	c	ext 0	4.4	2500	2.1	3030	rep	3030	rep	530	-	No load drop		2936
		Note: LB-27 encountered specimen cooling problems during testing.																		
s	s	LB-31	1900	Out-of-phase	.3	0	ID	gag 0	5.0	>3219	-	-	-	-	-	-	-	3200	-	3219
s	s	LB-32	1900	Baseball,ccw	.3	0	d	-	4.8	>11852	-	-	-	-	-	-	-	No load drop		>11852
s	s	LB-29	1900	Baseball,cw	.3	0	c	ext 0	5.3	2000	2.5-4.	2580	rep	3150	rep	.6-1.2k	-	3250	3550	3773
s	s	LB-26	1900	T-cycle .5cpm	.5	0	c	ext 0	5.2	2560	2.6E	3530	-	-	-	>1000	-	3500	-	3532
s	s	LB-216	2100	Out-of-phase	.23	0	c	ext 0	5.5	3090	2.6	3820	rep	3820	rep	730	-	3900	4200	4654
s	s	LB-239	2100	Out-of-phase	.25	0	c	ext 0	5.6	2160	2.7	2800	rep	2800	rep	640	-	No load drop		3787

<111> PWA 1480 / UNCOATED THERMOMECHANICAL FATIGUE SUMMARY

T	S	Spec ID	Tmax (F)	Cycle Type	DE	V	Init	Fail	Exam	Tc	Nc	AR	Nmin	Ind	Nmax	Ind	Nsc	Nsi	5%	10%	Nf
3	s	LB-56	1900	Out-of-phase	.3	0	s	gag	0,S	-	-	3.0	360	rep	360	rep	-	360	1530	1610	2067
3	s	LB-35	1900	Out-of-phase	.4	0	s	gag	0	-	-	-	300	-	530	-	-	300-530	535	-	537
3	s	LB-34	1900	Out-of-phase	.55	0	s	gag	0	-	Bulged specimen		110	rep	150	-	-	110-150	150	-	151
3	s	LB-33	1900	Out-of-phase	.8	0	ID	gag	0	-	Bulged specimen		100	rep	160	-	-	100-160	160	-	162

123

<011> PWA 1480 / PWA 273 ISOTHERMAL FATIGUE SUMMARY

T	S	Spec ID	Tmax (F)	Cycle Type	DE	V	Init	Fail	Exam	Tc	Nc	AR	Nmin	Ind	Nmax	Ind	Nsc	Nsi	5%	10%	Nf
5	s	KB-47	1400	PP, 8 cpm	.6	0	c	but	0	2.0	10800	3.3E	18530	-	-	-	>7730	-	No load	drop	18530
5	s	KB-64	1400	PP, 7 cpm	.68	-1	c	gag	0	2.1	4750	3.1	10500	rep	10500	rep	5750	-	19500	19800	19822
5	s	KB-67	1400	PP, 1 cpm	.68	-1	c	gag	0	3.0	3000	3.-4.	5200	rep	6000	rep	2.2-3k	-	18950	-	18987
5	s	KB-31	1700	PP, 12.5 cpm	.4	0	cs	gag	0	2.8	25-30k	4.6	-	-	40000	1d	<15000	-	52100	54100	54521
5	s	KB-23	1700	PP, 10 cpm	.5	0	s	gag	0,S	2.4	>6800	3.3	-	-	10200	1d	-	<10200	12700	12900	13000
5	s	KB-69	1700	PP, 1 cpm	.6	0	s	gag	0	3.4	2000	-	2800	rep	3000	rep	-	2.8-3k	2980	3050	3163
5	s	KB-28	1700	CP, 8cpm+60s	.6	0	s	gag	0	2.5	2200	2.4	3580	rep	3580	rep	-	3580	4350	4420	4556
5	s	KB-97	1900	PC,1.25cpm+60s	.3	0	IDc	gag	0	3.3	4300	3.8E	6300	rep	-	-	>2000	-	-	-	9234
5	s	KB-90	1900	CP,12.5cpm+60s	.4	0	ID	gag	0	2.7	>1870	-	-	-	-	-	-	-	1660	1700	1869
5	s	KB-86	1900	PP, 1 cpm	.4	0	ID/c	gag	0	3.8	2770	5.0	6200	rep	6700	grf	3.4-4k	-	4610	6190	6797
5	s	KB-35	1900	PP, 10 cpm	.5	0	s	gag	0,S	2.8	>2350	2.6	3320	rep	3320	rep	-	3320	-	-	3899

*The following specimens were exposed 100 hr. at 2000F prior to test.

T	S	Spec ID	Tmax (F)	Cycle Type	DE	V	Init	Fail	Exam	Tc	Nc	AR	Nmin	Ind	Nmax	Ind	Nsc	Nsi	5%	10%	Nf
5	s	KB-111	1700	PP, 10 cpm	.5	0	sc	gag	0	3.3	4100	5.0	4100	rep	4640	1d	-	4.1-4.7k	4900	5100	5338

<011> PWA 1480 / PWA 286 ISOTHERMAL FATIGUE SUMMARY

T	S	Spec ID	Tmax (F)	Cycle Type	DE	V	Init	Fail	Exam	Tc	Nc	AR	Nmin	Ind	Nmax	Ind	Nsc	Nsi	5%	10%	Nf
5	s	KB-89	1200	PP, 7 cpm	.68	0	c	but	0	4.4	>6516	-	-	-	-	-	-	-	6200	6400	6516
5	s	KB-85	1200	PP, 7 cpm	.68	-1	-	but	0	5.5	>8536	-	-	-	-	-	-	-	No load drop		>8535
5	s	KB-71	1400	PP, 10 cpm	.5	-1	dc	gag	0	4.3	25000	4.5	>63080	-	-	-	>38000	-	No load drop		>63080
5	s	KB-21	1400	PP, 6 cpm	.5	0	dc	gag	0	5.3	15750	10.0	61660	xtr	130500	xtr	46-115k	-	No load drop		>61660
5	s	KB-100	1400	PC,7cpm+70s	.68	-1	c	gag	0	5.4	700	2.5	1300	rep	2170	1d	.6-1.5k	-	-	-	2283
5	s	KB-98	1400	CP,7cpm+10s	.68	-1	dc	gag	0	4.6	8000	5.3E	44500	xtr	-	-	>36000	-	No load drop		>44561
5	s	KB-29	1400	PP, 6 cpm	.8	0	c	but	0	5.0	2750	4.3	3400	xtr	9200	xtr	.6-6.5k	-	-	-	3396
5	s	KB-68	1700	PP, 10 cpm	.5	0	s	gag	0	6.4	>7150	1.7	10100	rep	10100	rep	-	10100	17300	17600	17810
5	s	KB-65	1700	PP, 1 cpm	.5	0	s	gag	0	5.7	>3700	2.0	5080	rep	5080	rep	-	5080	6200	6300	6624
5	s	KB-70	1700	PC,10cpm+10s	.5	-1	s/c	gag	0	5.5	3600	2.5	-	-	3600	1d	-	<3600	3530	3600	3627
5	s	KB-96	1700	CP,10cpm+60s	.5	0	s	gag	0	4.6	>4056	-	2180	rep	3550	1d	-	2.2-3.6k	3880	3940	4056
5	s	KB-54	1700	PP, 8 cpm	.6	0	s	gag	0	6.1	>3500	2.7	-	-	4450	1d	-	<4450			4509
5	s	KB-79	1900	PP, .5 cpm	.34	0	dc	gag	0	4.3	9400	-	-	-	11000	rep	-	<11000	6700	9000	9420
5	s	KB-72	1900	PP, 12.5 cpm	.4	0	IDs/c	gag	0	6.0	8-11k	4.2	>15532	-	-	-	>4500	-	12300	12500	12929
5	s	KB-91	1900	PP, 12.5 cpm	.4	0	IDc	gag	0	3.8	12500	-	-	-	-	-	-	-	15100	15500	15532
5	s	KB-83	1900	PC,12.5cpm+10s	.4	0	IDc	gag	0	5.3	4100	-	-	-	-	-	-	-	3920	4000	4106
5	s	KB-77	1900	CP,10cpm+11s	.5	0	ID	gag	0	6.3	>2642	-	-	-	-	-	-	-	2060	2130	2642
5	s	KB-25	1900	PP, 8 cpm	.6	0	ID	gag	0	5.5	>1187	-	-	-	-	-	-	-	1140	1060	1187
5	s	KB-87	2100	PP, 2 cpm	.3	0	IDc	gag	0	5.2	3000	4.-6.	-	-	-	-	-	-	2150	2520	3266
5	s	KB-78	2100	PP, 2 cpm	.4	0	ID	gag	0	3.9	>1464	-	-	-	-	-	-	-	900	1060	1464

*The following specimens were exposed 100 hr. at 2000F prior to test.

T	S	Spec ID	Tmax (F)	Cycle Type	DE	V	Init	Fail	Exam	Tc	Nc	AR	Nmin	Ind	Nmax	Ind	Nsc	Nsi	5%	10%	Nf
5	s	KB-74	1400	PP, 10 cpm	.5	-1	c	gag	0	5.6	21000	3.5	23325	xtr	25200	rep	2.3-4.2k	-	26600	-	26833
5	s	KB-108	1700	PP, 10 cpm	.5	0	c	gag	0	5.5	5300	4.0	8100	rep	9050	1d	2.8-3.8k	-	9300	9440	9655
5	s	KB-81	1900	PP, 12.5 cpm	.4	0	c	ogag	0	4.6	10100	3.5	13100	rep	13100	rep	3000	-	24300	24700	24913

<011> PWA 1480 / PWA 273 THERMOMECHANICAL FATIGUE SUMMARY

T	S	Spec ID	Tmax (F)	Cycle Type	DE	V	Init Fail	Exam Tc	Nc	AR	Nmin Ind	Nmax Ind	Nsc Ind	Nsi	5%	10%	Nf
5	s	KB-33	1900	Out-of-phase	.3	0	d	- 0	2.5	>17003	-	-	-	-	-	No load drop		>17003
5	s	KB-80	2100	Out-of-Phase	.25	0	c	gag 0	-	-	Fracture surface melted at end of test					-	-	6335
5	s	KB-49	2100	Out-of-Phase	.25	0	c	gag 0	4.0	640	2.7	860 rep	1400	1d 220-760	-	1590	1700	1903
5	s	KB-27	2100	Out-of-phase	.35	0	cs	gag 0	2.6	620	3.-4.5	850 rep	1900	1d 230-1280	-	2360	2650	2900
5	s	KB-92	1900	Out-of-phase	.34	0	c	gag 0	4.2	<857	Ring	Test failed before first inspection				760	790	857

Note: KB-49 encountered specimen cooling problems during testing.

*The following specimens were exposed 100 hr. at 2000F prior to test.

<011> PWA 1480 / PWA 286 THERMOMECHANICAL FATIGUE SUMMARY

T	S	Spec ID	Tmax (F)	Cycle Type	DE	V	Init	Fail	Exam	Tc	Nc	AR	Nmin	Ind	Nmax	Ind	Nsc	Nsi	5%	10%	Nf
5	s	KB-32	1900	Out-of-phase	.3	0	c	gag	0	6.0	2680	3.1	5050	rep	5050	rep	2370	–	6450	6500	6569
5	s	KB-24	1900	Out-of-phase	.3	0	c	gag	0	5.9	2900	2.2	4000	rep	4000	rep	1100	–	5550	5650	5927
5	s	KB-36	1900	Ellipt.,ccw	.3	1	d	ext	0	5.1	>9743	2.5	No cracks observed in gauge section.					–	9050	9400	9743
5	s	KB-34	1900	Out-of-phase	.4	0	c	gag	0	6.0	900		1610	grf	1610	grf	710	–	2240	–	2266
5	s	KB-48	2100	Out-of-phase	.25	0	c	ext	0	6.2	2460	2.0	3400	rep	3400	rep	940	–	2760	2850	3411
5	s	KB-52	2100	Out-of-phase	.25	0	dc	ext	0	5.5	4300	3.6	5150	rep	5150	rep	850	–	No load drop		5227

*The following specimens were exposed 100 hr. at 2000F prior to test.

T	S	Spec ID	Tmax (F)	Cycle Type	DE	V	Init	Fail	Exam	Tc	Nc	AR	Nmin	Ind	Nmax	Ind	Nsc	Nsi	5%	10%	Nf
5	s	KB-93	1900	Out-of-phase	.3	0	c	gag	0	4.7	2420	3.3	–	–	2940	1d	<520	–	3010	–	3026

127

T	S	Spec ID	Tmax (F)	Cycle Type	DE	V	Init	Fail	Exam	Tc	Nc	AR	Nmin Ind	Nmax Ind	Nsc	Nsi	5%	10%	Nf
5	s	MB-21	1700	PP, 10 cpm	.5	0	cs	gag	0.5	2.0	5500	2.6	-	9000 1d	<3500	-	10400	10900	11648
5	s	MB-18	1700	PP, 8 cpm	.6	0	s	gag	0	2.4	>2500	2.7	3500 rep	3500 rep	-	3500	3750	-	3861
5	s	MB-4	1700	CP, 8cpm+60s	.6	0	sc	gag	0	2.4	>1100	2.4	1900 rep	1900 rep	-	1900	2000	2330	2407
5	s	MB-88	1900	PC,12.5cpm+60s	.3	0	ID/c	ogag	0	3.5	900	3.8	2940 rep	2940 rep	2040	-	2700	2800	2947

<123> PWA 1480 / PWA 286 ISOTHERMAL FATIGUE SUMMARY

T	S	Spec ID	Tmax (F)	Cycle Type	DE	V	Init	Fail	Exam	Tc	Nc	AR	Nmin	Ind	Nmax	Ind	Nsc	Ind	Nsi	5%	10%	Nf
5	s	MB-26	1400	PP, 10 cpm	.5	-1	dc	gag	0	5.7	18600	5.0	30000	-	-	-	>11400	-	-	No load drop		>30000
5	s	MB-64	1700	PP, 10 cpm	.5	0	s/c	gag	0	4.2	9900	3.8	14500	rep	14500	rep	4600	-	-	19200	20000	21215
5	s	MB-40	1700	PC, 10cpm+60s	.5	0	IDc	gag	0	4.8	1650	-	-	-	-	-	-	-	-	2650	2670	2683
5	s	MB-41	1900	CP, 12.5cpm+60s	.3	0	ID	gag	0	5.9	>3680	-	High porosity level; Not typical for							2780	3350	3681
5	s	MB-6	1900	PP, 10 cpm	.5	0	ID	gag	0	6.0	>2540	-	4000 rep		6000 rep		-		4-6k	PWA1480		2540
5	s	MB-38	1900	PP, 10 cpm	.5	0	s	gag	0	5.8	>8250	-	-	-	-	-	-	-	-	8050	8220	8253
5	s	MB-33	1900	PP, 8 cpm	.6	0	IDs	gag	0	5.6	>2640	-	-	-	-	-	-	-	-	2610	2630	2640
5	s	MB-2	1900	PP, 8 cpm	.6	0	ID	gag	0	6.4	>3900	-	-	-	-	-	-	-	-	3700	3780	3919

<123> PWA 1480 / PWA 273 THERMOMECHANICAL FATIGUE SUMMARY

T	S	Spec ID	Tmax (F)	Cycle Type	DE	V	Init Fail	Exam	Tc	Nc	AR	Nmin	Ind	Nmax	Ind	Nsc	Nsi	5%	10%	Nf
5	s	MB-25	1900	Out-of-phase	.3	0	ID	gag 0	2.6	>8000	8.0	-	-	-	-	-	-	8400	8500	8516
5	s	MB-1	1900	Out-of-phase	.4	0	c	gag 0.S	2.6	<<500	8.0	-	-	500	1d	<500	-	740	-	749
5	s	MB-16	2100	Out-of-phase	.25	0	c	gag 0	2.6	1400	6.5	2860	rep	3800	rep	1.4-2.4k	-	3000	3850	4961
5	s	MB-24	2100	Out-of-phase	.25	0	c	gag 0	3.0	760	4.5	1900	rep	1900	rep	1140	-	3450	3740	3910

<123> PWA 1480 / PWA 286 THERMOMECHANICAL FATIGUE SUMMARY

T	S	Spec ID	Tmax (F)	Cycle Type	DE	V	Init	Fail	Exam	Tc	Nc	AR	Nmin	Ind	Nmax	Ind	Nsc	Nsi	5%	10%	Nf
5	s	MB-17	1900	Out-of-phase	.25	0	dc	ext	0	5.5	4600	3.1	6570	rep	6570	rep	1970	-	7150	-	7294
5	s	MB-23	1900	Out-of-phase	.25	0	c	gag	0	5.6	5050	4.3	7700	rep	7700	rep	2650	-	10300	10800	12172
5	s	MB-22	1900	Out-of-phase	.3	0	c	ext	0	5.3	3500	3.0	4400	xtr	5180	xtr	.9-1.7k	-	No load	drop	4358
5	s	MB-8	1900	Out-of-phase	.3	0	c	gag	0	5.8	3930	2.5	5500	rep	5500	rep	1570	-	6500	6600	6745
5	s	MB-19	1900	Out-of-phase	.3	1	c	ext	0	6.2	3700	3.6	5540	xtr	7240	xtr	1.8-3.5k	-	4300	4530	5539
5	s	MB-62	1900	Out-of-phase	.3	0	c	gag	0	4.4	1800	3.7	3560	rep	3560	rep	1760	-	4000	4030	4098
5	s	MB-27	1900	Out-of-phase +300s @Tmax	.3	0	c	gag	0	4.7	1170	3.8	2100	rep	2100	rep	930	-	2180	2520	3002
5	s	MB-35	2100	Out-of-phase	.23	0	c	ext	0	6.1	3620	2.8	4520	rep	4520	rep	900	-	4570	4880	6786
5	s	MB-37	2100	Out-of-phase	.25	0	c	ext	0	6.0	2840	2.3	3780	rep	3780	rep	940	-	3980	4050	4130

APPENDIX E

STRESS/INELASTIC STRAIN DATA SUMMARY FOR PWA 1480 FATIGUE TESTS

STRESS/INELASTIC STRAIN DATA SUMMARY FOR PWA 1480 FATIGUE TESTS

NOMENCLATURE

Spec ID = Specimen Identification Number: JB = <001>; LB = <111>; KB = <011>; MB = <123>
Sig0 Range = Initial Stress Range (ksi).
 Sig0 Mean = Initial Mean Stress (ksi).
Ein0 Range = Initial Inelastic Strain Range (%).
SigNc Range = Stress Range at Nc Cycles (ksi).
 SigNc Mean = Mean Stress at Nc Cycles (ksi).
EinNc Range = Inelastic Strain Range at Nc Cycles (%).
SigNs Range = Stress Range at (Nc+Nsc) or Nsi, Depending on Initiation Mode (ksi).
 SigNs Mean = Mean Stress at (Nc+Nsc) or Nsi, Depending on Initiation Mode (ksi).
EinNs Range = Inelastic Strain Range at (Nc+Nsc) or Nsi, Depending on Initiation Mode (%).
Sig.5 Range = Stress Range at Nf/2 Cycles (ksi).
 Sig.5 Mean = Mean Stress at Nf/2 Cycles (ksi).
Ein.5 Range = Inelastic Strain Range at Nf/2 Cycles (%).
SNmin Range = Stress Range at Nmin (ksi).
 SNmin Mean = Mean Stress at Nmin (ksi).
SNmax Range = Stress Range at Nmax (ksi).
 SNmax Mean = Mean Stress at Nmax (ksi).
 Nc = Cycles to Initiate a Crack Through the Coating.
 Nmin = Lower Bound on (Nc+Nsc) or Nsi.
 Nmax = Upper Bound on (Nc+Nsc) or Nsi.
 Nsc = Cycles to Grow a Coating Crack .010" into the Substrate.
 Nsi = Cycles to Initiate a Substrate Crack Due to Macroscopic Slip, Oxidation Effects, or Defects.
 Nf = Cycles to Specimen Failure (50% Tensile Load Drop or Separation, Whichever Comes First).
 Dsig = Stress Change During Hold Times = Stress at End of Hold - Stress at Beginning of Hold (ksi).

*** Note : All stresses were calculated using substrate cross sectional area only.
 ===> Stress = Po/As = (observed specimen load)/(substrate area)
          As = Ao - Ac
          As = Substrate area.
          Ao = Specimen area based on measured specimen ID & OD.
          Ac = Coating area calculated based on constant coating thickness.
          Coating thicknesses assumed were: PWA 273 = .003" ; PWA 286 = .005".

133

<001> PWA 1480 / PWA 273 ISOTHERMAL FATIGUE SUMMARY

Spec ID	SigO Range (ksi)	SigO Mean (ksi)	EinO Range (%)	SigNc Range (ksi)	SigNc Mean (ksi)	EinNc Range (%)	SigNs Range (ksi)	SigNs Mean (ksi)	EinNs Range (%)	Sig.5 Range (ksi)	Sig.5 Mean (ksi)	Ein.5 Range (%)
JB-103	97.0	0.7	0.009	102.1	2.4	0.006	102.6	1.3	0.006	Test discontinued		
JB-109	94.7	-	0.010	97.2	41.3	0.010	95.9	40.3	0.008	Test discontinued		
JB-96	130.4	2.9	0.022	129.4	3.1	0.022	126.4	3.6	-	Test discontinued		
JB-23	80.8	0.5	0.029	82.8	1.4	0.032	82.4	-1.2	0.028	82.4	0.3	0.028
JB-159	83.3	0.6	0.027	78.3	-17.6	0.046	77.5	-18.9	0.048	Test discontinued		
Dsig	-2.0			-2.7			-2.9					
JB-28	90.5	-0.2	0.030	89.3	0.1	0.033	89.9	2.2	0.034	89.9	2.2	0.034
JB-31	110.7	1.0	0.043	107.6	2.5	0.051	107.1	3.4	0.055	106.1	4.0	0.055
JB-120	67.0	0.3	0.042	62.3	0.3	0.072	62.6	0.0	0.074	63.1	0.5	0.070
JB-65	65.0	-0.5	0.064	57.3	0.4	0.119	-	-	-	56.2	1.2	0.143
JB-100	68.1	0.0	0.039	64.3	8.1	0.095	63.2	10.0	0.107	62.1	9.3	0.110
Dsig	+3.0			+3.4			+3.3			+3.3		
JB-170	Specimen failed during initial loading. No data is available.											
JB-34	74.3	-0.4	0.071	70.1	-0.5	0.100	70.5	0.4	0.104	71.2	-0.1	0.106
JB-39	86.3	-0.9	0.112	75.7	1.3	0.158	71.8	0.2	0.177	71.9	0.2	0.175
JB-50	84.9	0.2	0.096	81.2	0.0	0.126	78.8	-0.7	0.131	76.2	-0.1	0.141
JB-33	71.6	0.0	0.155	64.5	0.7	0.215	58.2	0.4	0.255	58.8	0.5	0.252
JB-36	80.3	1.2	0.128	80.9	9.2	0.190	-	-	-	80.0	10.2	0.203
Dsig	+6.5			+5.9			-			+5.7		
JB-35	84.5	0.0	0.117	81.0	-7.4	0.185	76.0	-10.0	0.200	69.9	-12.4	0.210
Dsig	-6.3			-5.4			-5.7			-4.6		
JB-79	99.0	1.1	0.218	89.1	0.6	0.225	90.0	0.6	0.257	91.1	0.8	0.248
JB-163	43.6	-1.0	0.101	39.5	0.0	0.118	34.0	0.1	0.154	34.0	0.1	0.154
JB-168	50.1	-0.5	0.138	42.2	0.5	0.200	34.4	0.0	0.244	37.7	0.4	0.233

<001> PWA 1480 / PWA 286 ISOTHERMAL FATIGUE SUMMARY

<001> PWA 1480 / PWA 286 ISOTHERMAL FATIGUE SUMMARY

Spec ID	SigO Range (ksi)	SigO Mean (ksi)	EinO Range (%)	SigNc Range (ksi)	SigNc Mean (ksi)	EinNc Range (%)	SigNs Range (ksi)	SigNs Mean (ksi)	EinNs Range (%)	Sig.5 Range (ksi)	Sig.5 Mean (ksi)	Ein.5 Range (%)
JB-102	116.9	0.8	0.0	Test discontinued before			load drop. Nf/2 = 20800			115.8	0.0	0.0
JB-97	153.5	2.8	0.006	154.0	3.1	0.005	153.6	1.5	0.006	153.8	0.9	0.006
JB-99	190.0	3.3	0.010	192.2	4.7	0.011	189.8	5.1	0.007	187.7	5.3	0.010
JB-37	118.5	-1.7	0.036	119.0	2.8	0.030	117.6	3.9	0.018	117.6	3.9	0.018
JB-94	128.4	0.9	0.036	125.8	9.2	0.031	123.8	10.6	0.020	Test discontinued		
Dsig	+3.1			+1.5			+1.0			+1.3		
JB-63	157.6	1.6	0.046	155.4	3.8	–	150.0	4.3	0.027	150.0	4.3	0.027
JB-75	147.0	0.0	0.037	145.6	8.1	0.043	145.5	8.7	0.042	Test discontinued		
JB-158	154.6	1.0	0.043	149.7	-14.8	0.048	–	–		Test discontinued		
Dsig	-2.9			-2.7								
JB-69	169.3	0.0	0.049	170.9	9.9	0.047	169.9	11.4	0.042	167.7	12.5	0.042
JB-7	168.9	0.7	0.060	176.0	8.0	0.056	–	–		171.4	5.0	0.048
JB-123	76.5	0.7	0.020	79.8	2.1	–	77.9	3.0	0.023	77.9	3.0	0.021
JB-169	111.1	-1.8	0.039	109.2	1.2	0.036	108.3	2.0	0.034	106.9	2.2	0.033
JB-129	105.9	0.0	0.034	101.2	0.6	0.038	103.1	-0.2	0.037	98.7	-0.9	0.037
JB-2	103.4	0.0	0.030	99.4	-0.9	0.063	–	–		96.0	-1.8	0.077
JB-155	98.4	-1.1	0.025	96.5	-1.2	0.032	94.7	-2.5	0.045	94.7	-2.5	0.045
JB-139	109.3	2.4	0.035	108.5	23.4	0.092	–	–		108.5	24.6	0.091
Dsig	+2.9			+2.9						+2.5		
JB-160	121.0	-3.9	0.111	118.4	-25.4	0.132	113.6	-25.4	0.141	110.6	-25.3	0.142
Dsig	-6.4			-6.8			-6.6			-6.4		
JB-126	58.0	0.1	0.025	55.4	1.1	0.044	–	–	–	53.4	0.4	0.052
JB-130	80.9	0.0	0.055	70.8	0.5	0.104	–	–	–	67.5	1.3	0.129
JB-25	81.8	1.5	0.118	74.3	0.8	0.159	–	–	–	72.1	0.8	0.168
JB-85	84.4	-0.3	0.103	79.9	1.1	0.152	–	–	–	78.7	0.7	0.156
JB-5	77.8	-0.5	0.133	70.0	0.9	0.200	–	–	–	66.2	0.3	0.248
JB-24	76.7	0.0	0.143	63.5	0.9	0.260	–	–	–	62.1	1.2	0.260
JB-20	82.3	0.6	0.080	73.0	11.1	0.217	–	–	–	73.3	11.1	0.217
Dsig	+5.5			+5.1						+5.1		
JB-6	85.4	4.1	0.112	76.7	11.1	0.198	–	–	–	77.2	11.1	0.194
Dsig	+8.0			+4.9						+4.9		
JB-71	75.0	-0.5	0.112	67.9	-10.6	0.227	–	–	–	68.8	-10.4	0.224
Dsig	-5.7			-6.2						-6.6		
JB-134	85.1	-1.0	0.099	78.8	-12.9	0.196	–	–	–	78.2	-13.9	0.202
Dsig	-8.9			-6.1						-6.1		
JB-78	94.3	-1.4	0.194	78.5	1.1	0.308	–	–	–	78.5	1.1	0.308
JB-171	48.3	-1.3	0.120	39.1	0.4	0.195	–	–	–	39.1	0.4	0.195
JB-151	46.8	-0.7	0.145	30.0	-0.1	0.294	–	–	–	25.6	-0.3	0.344
JB-162	53.4	-1.5	0.164	43.8	0.3	0.240	–	–	–	42.2	0.1	0.261

*The following specimens were exposed 100 hr. at 2000F prior to test.

Spec ID	SigO Range (ksi)	SigO Mean (ksi)	EinO Range (%)	SigNc Range (ksi)	SigNc Mean (ksi)	EinNc Range (%)	SigNs Range (ksi)	SigNs Mean (ksi)	EinNs Range (%)	Sig.5 Range (ksi)	Sig.5 Mean (ksi)	Ein.5 Range (%)
JB-138	125.0	0.4	0.024	121.9	-0.3	0.021	–	–	–	114.0	-0.8	0.013
JB-150	84.1	-0.9	0.164	78.7	0.9	0.158	–	–	–	78.7	0.9	0.158

<001> PWA 1480 / UNCOATED ISOTHERMAL FATIGUE SUMMARY

Spec ID	SigO Range (ksi)	SigO Mean (ksi)	EinO Range (%)	SigNc Range (ksi)	SigNc Mean (ksi)	EinNc Range (%)	SigNs Range (ksi)	SigNs Mean (ksi)	EinNs Range (%)	Sig.5 Range (ksi)	Sig.5 Mean (ksi)	Ein.5 Range (%)
JB-42 Dsig	79.4 +5.0	4.3	0.148	- -	-	-	- -	-	-	73.7 +5.2	11.0	0.199

<001> PWA 1480 / PWA 273 THERMOMECHANICAL FATIGUE SUMMARY

Spec ID	SigO Range (ksi)	SigO Mean (ksi)	SigNc Range (ksi)	SigNc Mean (ksi)	SNmin Range (ksi)	SNmin Mean (ksi)	SNmax Range (ksi)	SNmax Mean (ksi)	Sig.5 Range (ksi)	Sig.5 Mean (ksi)
JB-76	60.5	22.0	Test discontinued before load drop. Nf/2 = 10800						60.3	-1.2
JB-125	48.6	7.0	52.8	16.9	54.6	18.3	52.8	25.0	55.8	21.0
Dsig	+2.4		+0.8		+0.7		+0.5		+0.7	
JB-98	60.9	5.7	62.5	18.4	64.3	20.3	66.3	24.6	65.7	24.6
JB-61	60.6	6.6	-	-	-	-	63.7	17.1	59.8	16.2
JB-66	65.9	10.2	66.4	26.4	70.4	28.1	69.1	31.5	69.2	30.2
Dsig	+4.7		+0.9		+0.6		+0.3		+0.6	
JB-62	65.6	9.5	73.7	33.3	74.8	37.8	77.0	38.6	73.3	34.5
Dsig	+1.5		+0.8		+0.8		+0.4		+0.8	
JB-91	79.3	10.0	81.3	21.6	81.7	25.1	83.2	25.5	81.4	24.6
JB-22	78.2	10.0	83.4	15.8	79.9	21.0	80.1	21.6	79.9	21.0
JB-59	111.1	-20.1	112.5	-35.9	101.0	-37.3	-	-	Test discontinued	
plus	57.7	9.9	-	-	58.8	22.3	58.4	23.8	58.5	21.8
JB-29	117.0	-17.3	117.7	-38.9	117.3	-44.4	113.5	33.3	Test discontinued	
JB-19	110.5	16.0	112.9	23.8	115.3	30.9	124.4	38.5	115.3	32.1
JB-38	121.7	21.0	122.2	34.9	124.4	38.5	121.4	39.6	122.6	38.0
JB-81	143.5	-8.4	123.9	25.3	123.0	36.9	123.2	36.1	122.5	38.5
JB-72	122.1	17.8	125.6	32.2	126.0	36.5	-	-	127.4	38.0
JB-64	159.4	-33.1	154.9	-48.6	-	-	-	-	154.9	-49.3
JB-88	48.1	6.1	48.0	22.0	46.2	21.7	45.4	20.9	47.0	22.7
JB-82	86.4	16.8	86.9	39.0	-	-	86.9	40.9	85.7	40.9

*The following specimens were exposed 100 hr. at 2000F prior to test.

Spec ID	SigO Range (ksi)	SigO Mean (ksi)	SigNc Range (ksi)	SigNc Mean (ksi)	SNmin Range (ksi)	SNmin Mean (ksi)	SNmax Range (ksi)	SNmax Mean (ksi)	Sig.5 Range (ksi)	Sig.5 Mean (ksi)
JB-154	64.9	10.9	65.4	15.5	65.4	15.5	66.8	19.6	66.4	22.0
JB-161	64.6	12.0	63.1	15.0	63.9	18.5	63.1	18.1	63.6	18.8

<001> PWA 1480 / PWA 286 THERMOMECHANICAL FATIGUE SUMMARY

Spec ID	SigO Range (ksi)	SigO Mean (ksi)	SigNc Range (ksi)	SigNc Mean (ksi)	SNmin Range (ksi)	SNmin Mean (ksi)	SNmax Range (ksi)	SNmax Mean (ksi)	Sig.5 Range (ksi)	Sig.5 Mean (ksi)
JB-174	58.3	14.5	58.2	14.6	58.3	14.6	58.3	14.6	58.4	14.5
JB-147	71.4	10.6	76.3	23.4	74.3	26.7	74.3	26.7	70.0	26.3
JB-121	66.6	-5.5	72.8	22.0	66.8	26.7	66.8	26.7	65.4	24.5
Dsig	+3.6		+0.5		+0.6		+0.6		+0.6	
JB-137	65.9	-7.9	72.9	25.4	70.9	27.6	70.9	27.6	68.7	32.9
Dsig	+6.0		+1.5		+1.4		+1.4		+1.2	
JB-135	61.5	-8.1	69.1	24.1	72.6	32.8	72.6	32.8	72.6	32.9
Dsig	+1.9		+1.3		+0.4		+0.4		+0.3	
JB-10	-	-	88.1	20.9	91.1	22.2	89.7	27.0	91.2	26.7
JB-104	108.6	-1.5	112.2	1.5	107.1	5.1	107.1	5.1	111.2	3.0
JB-9	115.5	17.7	122.9	36.2	123.4	36.8	121.4	37.2	124.0	36.7
JB-11	125.3	-18.2	125.1	-44.3	-	-	-	-	127.8	-44.2
JB-80	148.4	-2.6	133.6	47.8	132.6	55.8	134.7	57.9	132.6	56.3
JB-21	132.2	21.9	135.5	36.4	131.8	39.6	131.8	40.5	132.2	37.3
JB-102	135.3	-7.0	135.1	-11.9	133.5	-8.0	-	-	135.3	-10.2
JB-111	54.9	15.6	55.0	25.3	52.3	25.0	31.0	15.0	53.4	23.8
JB-89	84.7	18.3	80.4	38.3	76.8	35.6	76.8	38.1	80.9	37.6
*The following specimens were exposed 100 hr. at 2000F prior to test.										
JB-146	65.1	15.1	69.0	23.6	67.1	31.5	67.1	31.5	67.8	26.5
JB-133	77.4	14.5	79.0	23.6	77.6	25.2	77.6	25.2	76.0	24.8

<001> PWA 1480 / UNCOATED THERMOMECHANICAL FATIGUE SUMMARY

Spec ID	Sig0 Range (ksi)	Sig0 Mean (ksi)	SigNc Range (ksi)	SigNc Mean (ksi)	SNmin Range (ksi)	SNmin Mean (ksi)	SNmax Range (ksi)	SNmax Mean (ksi)	Sig.5 Range (ksi)	Sig.5 Mean (ksi)
JB-51	81.2	16.5	-	-	-	-	-	-	88.8	29.1
JB-46	112.8	23.8	-	-	-	-	-	-	113.2	35.7
JB-47	127.9	-14.0	-	-	-	-	-	-	123.5	-37.5

139

<111> PWA 1480 / PWA 273 ISOTHERMAL FATIGUE SUMMARY

Spec ID	SigO Range (ksi)	SigO Mean (ksi)	EinO Range (%)	SigNc Range (ksi)	SigNc Mean (ksi)	EinNc Range (%)	SigNs Range (ksi)	SigNs Mean (ksi)	EinNs Range (%)	Sig.5 Range (ksi)	Sig.5 Mean (ksi)	Ein.5 Range (%)
LB-106	156.1	0.1	0.002	188.7	0.7	0.009	-	-	-	172.1	11.1	0.003
LB-22	190.6	0.0	0.010				192.0	0.1	0.010	188.7	0.7	0.009
LB-25	234.5	0.0	0.011	-	-	-	231.5	0.0	0.015	230.5	3.0	0.013
LB-19	222.6	1.0	0.020	-	-	-	222.6	3.1	-	225.7	3.1	0.018
LB-121	238.7	-4.7	0.006	237.2	3.7	0.025	234.3	2.9	0.026	237.2	3.7	0.025
LB-120	229.8	-4.1	0.014	-	-	-	220.6	5.0	0.030	223.0	3.1	0.021
LB-124	232.5	-0.9	0.014	-	-	-	223.5	6.8	-	226.4	1.0	0.026
LB-236	114.3	-0.9	0.015	-	-	-	116.2	1.1	-	113.1	-0.1	0.017
LB-195	132.0	0.0	0.024	-	-	-	132.2	2.7	0.028	132.0	3.5	0.029
LB-180	152.6	-1.0	0.097	-	-	-	152.9	1.3	-	152.5	-1.3	0.106

<111> PWA 1480 / PWA 286 ISOTHERMAL FATIGUE SUMMARY

Spec ID	SigO Range (ksi)	SigO Mean (ksi)	EinO Range (%)	SigNc Range (ksi)	SigNc Mean (ksi)	EinNc Range (%)	SigNs Range (ksi)	SigNs Mean (ksi)	EinNs Range (%)	Sig.5 Range (ksi)	Sig.5 Mean (ksi)	Ein.5 Range (%)
LB-30	219.0	-3.5	0.006	-	-	-	-	-	-	212.4	-2.1	0.004
LB-209	155.1	-1.3	0.007	-	-	-	170.5	14.7	0.005	157.0	8.3	0.006
LB-241	192.5	-3.1	0.011	-	-	-	191.5	1.0	-	194.6	2.1	0.011
LB-235	182.8	-3.3	0.013	-	-	-	182.8	2.4	0.017	182.3	1.0	0.017
LB-185	103.7	-0.4	0.016	-	-	-	99.3	0.0	0.017	103.7	0.5	0.013
LB-192	115.6	1.4	0.012	-	-	-	117.9	2.2	-	117.0	3.9	0.016
LB-188	130.6	-1.3	0.031	-	-	-	133.7	0.0	-	132.3	2.5	0.036
LB-233	101.2	-1.3	0.046	-	-	-	90.5	1.7	-	90.2	1.2	0.075
LB-232	75.7	2.2	0.113	52.0	1.0	-	-	-	-	63.1	2.3	0.131
LB-179	56.6	0.4	0.292	-	-	-	-	-	-	51.1	0.1	-

<111> PWA 1480 / UNCOATED ISOTHERMAL FATIGUE SUMMARY

Spec ID	/	SigO Range (ksi)	SigO Mean (ksi)	EinO Range (%)	/	SigNc Range (ksi)	SigNc Mean (ksi)	EinNc Range (%)	/	SigNs Range (ksi)	SigNs Mean (ksi)	EinNs Range (%)	/	Sig.5 Range (ksi)	Sig.5 Mean (ksi)	Ein.5 Range (%)	/
LB-59		231.7	-0.5	0.019		-	-	-		234.0	10.1	0.005		233.5	8.5	0.007	
LB-36		219.6	0.0	0.006		-	-	-		219.5	0.0	-		225.1	3.1	0.007	

<111> PWA 1480 / PWA 273 THERMOMECHANICAL FATIGUE SUMMARY

Spec ID	SigO Range (ksi)	SigO Mean (ksi)	SigNc Range (ksi)	SigNc Mean (ksi)	SNmin Range (ksi)	SNmin Mean (ksi)	SNmax Range (ksi)	SNmax Mean (ksi)	Sig.5 Range (ksi)	Sig.5 Mean (ksi)
LB-23	102.3	18.3	116.8	39.8	-	-	-	-	95.1	29.9
LB-20	118.7	27.0	-	-	123.9	44.0	118.2	47.3	111.6	45.4
LB-21	124.4	-9.5	-	-	128.4	-16.7	129.6	-14.3	125.2	-14.3
LB-156	125.6	14.8	-	-	127.9	22.5	129.4	22.5	124.3	19.4
LB-155	220.7	33.1	-	-	-	-	-	-	209.4	35.4
LB-189	115.0	27.7	104.6	46.1	109.6	50.0	109.6	50.0	109.2	49.6
LB-240	178.6	-32.8	-	-	160.4	-48.6	154.7	-49.3	159.8	-47.4

<111> PWA 1480 / PWA 286 THERMOMECHANICAL FATIGUE SUMMARY

Spec ID	SigO Range (ksi)	SigO Mean (ksi)	SigNc Range (ksi)	SigNc Mean (ksi)	SNmin Range (ksi)	SNmin Mean (ksi)	SNmax Range (ksi)	SNmax Mean (ksi)	Sig.5 Range (ksi)	Sig.5 Mean (ksi)
LB-170	97.5	17.1	101.3	57.6	86.6	49.1	86.6	49.1	99.1	54.5
LB-181	100.1	17.5	105.7	56.7	100.2	60.6	100.2	60.6	99.8	49.9
LB-27	121.7	18.7	124.6	43.8	132.5	45.3	132.5	45.3	121.2	39.9
LB-31	124.6	17.2	-	-	Test discontinued before load drop, $Nf/2 = 6000$				117.7	52.7
LB-32	122.2	-13.4	113.3	9.7	112.2	7.1	112.2	7.1	117.3	-5.4
LB-29	126.5	7.1	209.7	0.0	217.4	1.9	-	-	113.3	8.2
LB-26	212.4	-8.5							203.9	1.0
LB-216	95.4	25.5	94.5	40.5	92.0	37.6	92.0	37.6	90.5	40.1
LB-239	119.6	23.8	94.1	45.7	103.1	45.3	103.1	45.3	94.2	45.7

<111> PWA 1480 / UNCOATED THERMOMECHANICAL FATIGUE SUMMARY

Spec ID	Sig0 Range (ksi)	Sig0 Mean (ksi)	SigNc Range (ksi)	SigNc Mean (ksi)	SNmin Range (ksi)	SNmin Mean (ksi)	SNmax Range (ksi)	SNmax Mean (ksi)	Sig.5 Range (ksi)	Sig.5 Mean (ksi)
LB-56	114.1	31.3	-	-	118.9	46.3	118.9	46.3	120.3	52.9
LB-35	143.2	48.0	-	-	161.2	46.7	156.1	43.9	160.3	46.7
LB-34	180.8	38.4	-	-	189.0	45.1	183.7	41.2	192.8	45.6
LB-33	215.2	31.6	-	-	236.9	42.4	226.3	37.8	236.0	42.5

Spec ID	SigO Range (ksi)	SigO Mean (ksi)	EinO Range (%)	SigNc Range (ksi)	SigNc Mean (ksi)	EinNc Range (%)	SigNs Range (ksi)	SigNs Mean (ksi)	EinNs Range (%)	Sig.5 Range (ksi)	Sig.5 Mean (ksi)	Ein.5 Range (%)
KB-47	185.0	-2.1	0.026	178.6	-2.6	0.014	181.9	-3.1	0.016	186.4	-4.5	0.011
KB-64	190.7	-59.1	0.017	186.4	-35.6	0.012	179.3	-35.6	-	179.3	-35.6	-
KB-67	164.8	-80.5	0.029	174.1	-32.8	0.020	173.4	-25.9	0.021	172.0	-21.8	0.023
KB-31	101.5	-1.8	0.018	101.9	-0.2	0.014	100.3	0.4	0.014	101.9	-0.2	0.014
KB-23	118.9	-0.1	0.023	-	-	-	120.1	2.4	0.024	120.3	1.6	0.026
KB-69	125.8	-3.3	0.062	124.0	-0.7	0.067	122.9	-0.4	0.075	123.6	0.0	0.067
KB-28	138.5	-1.5	0.043	133.0	-22.5	-	130.0	-23.0	-	133.8	-22.6	0.090
Dsig	-3.8			-9.1			-9.0			-9.1		
KB-97	63.7	2.7	0.023	48.7	1.6	0.064	47.6	2.3	-	48.7	1.6	0.064
Dsig	+1.6			+3.2			+3.0			+3.2		
KB-90	82.6	-0.7	0.036	-	-	-	-	-	-	72.2	-7.3	0.101
Dsig	-7.7									-7.2		
KB-86	74.4	-1.3	0.056	59.9	0.0	0.106	52.7	-1.5	0.130	58.8	-1.7	0.116
KB-35	98.2	-2.9	0.070	-	-	-	-	-	-	94.0	-1.3	0.078

*The following specimens were exposed 100 hr. at 2000F prior to test.

Spec ID	SigO Range (ksi)	SigO Mean (ksi)	EinO Range (%)	SigNc Range (ksi)	SigNc Mean (ksi)	EinNc Range (%)	SigNs Range (ksi)	SigNs Mean (ksi)	EinNs Range (%)	Sig.5 Range (ksi)	Sig.5 Mean (ksi)	Ein.5 Range (%)
KB-111	108.6	-2.1	0.065	105.0	0.3	0.057	105.0	0.3	0.057	106.5	0.3	0.059

<011> PWA 1480 / PWA 286 ISOTHERMAL FATIGUE SUMMARY

Spec ID	SigO Range (ksi)	SigO Mean (ksi)	EinO Range (%)	SigNc Range (ksi)	SigNc Mean (ksi)	EinNc Range (%)	SigNs Range (ksi)	SigNs Mean (ksi)	EinNs Range (%)	Sig.5 Range (ksi)	Sig.5 Mean (ksi)	Ein.5 Range (%)
KB-89	199.2	-5.6	0.011	--	--	--	--	--	--	195.9	-0.6	0.012
KB-85	208.6	-60.0	0.024	--	--	--	--	--	--	205.0	-26.9	0.014
KB-71	141.0	-60.8	0.011	140.4	-49.0	0.009	--	--	--	Test discontinued		
KB-21	138.5	-1.6	0.010	140.7	-3.2	0.010	144.2	-5.5	0.010	Test discontinued		
KB-100	192.7	-67.7	0.025	178.9	21.7	0.037	176.8	28.4	0.045	176.7	24.2	0.043
Dsig	+26.0			+7.6			+7.5			+7.2		
KB-98	190.5	-69.3	0.104	183.7	-46.1	0.029	180.9	-39.7	0.023	Test discontinued		
Dsig	-4.6			-4.3			-3.5					
KB-29	220.0	-2.9	0.020	221.5	-3.4	0.024	221.0	-1.3	0.025	221.5	-3.4	0.024
KB-68	129.0	0.1	0.030	--	--	--	122.2	0.9	0.031	122.8	1.1	0.031
KB-65	104.3	-1.4	0.030	--	--	--	105.7	1.5	--	106.7	-0.5	0.129
KB-70	113.0	-30.3	0.061	120.3	15.3	--	120.3	15.5	--	116.9	14.3	0.052
Dsig	+4.8			+4.8			+4.8			+4.8		
KB-96	115.1	-3.9	0.031	--	--	--	111.3	20.5	0.060	113.2	23.6	0.057
Dsig	-6.8			--			-6.0			-5.7		
KB-54	145.6	-0.9	0.049	--	--	--	144.6	-0.9	0.049	141.7	1.0	0.049
KB-79	68.6	0.0	0.024	47.5	0.0	0.108	80.6	2.0	--	Test discontinued		
KB-72	87.7	0.7	0.017	80.8	2.0	--	--	--	--	83.5	1.7	0.035
KB-91	84.8	0.5	0.037	77.3	0.7	0.056	--	--	--	78.0	0.2	0.053
KB-83	82.3	-0.3	0.042	75.5	4.9	0.075	--	--	--	75.5	4.9	0.075
Dsig	+6.3			+4.7						+5.1		
KB-77	89.2	-1.5	0.088	--	--	--	--	--	--	83.8	-5.1	0.121
Dsig	-6.7			--						-7.7		
KB-25	110.8	0.3	0.118	--	--	--	--	--	--	106.8	-0.3	0.133
KB-87	46.0	-0.4	0.053	--	--	--	--	--	--	34.5	0.0	0.113
KB-78	54.8	-0.6	0.134	--	--	--	--	--	--	47.4	0.0	0.169

*The following specimens were exposed 100 hr. at 2000F prior to test.

Spec ID	SigO Range (ksi)	SigO Mean (ksi)	EinO Range (%)	SigNc Range (ksi)	SigNc Mean (ksi)	EinNc Range (%)	SigNs Range (ksi)	SigNs Mean (ksi)	EinNs Range (%)	Sig.5 Range (ksi)	Sig.5 Mean (ksi)	Ein.5 Range (%)
KB-74	134.3	0.0	0.009	134.7	2.4	0.009	134.3	5.1	0.009	134.0	2.2	0.009
KB-108	107.3	-4.5	0.062	105.5	-1.4	0.053	104.4	-2.3	--	105.5	-1.4	0.053
KB-81	75.0	-1.1	0.081	70.3	-0.2	0.087	69.6	-0.2	0.089	69.8	-0.1	0.089

<011> PWA 1480 / PWA 273 THERMOMECHANICAL FATIGUE SUMMARY

Spec ID	SigO Range (ksi)	SigO Mean (ksi)	SigNc Range (ksi)	SigNc Mean (ksi)	SNmin Range (ksi)	SNmin Mean (ksi)	SNmax Range (ksi)	SNmax Mean (ksi)	Sig.5 Range (ksi)	Sig.5 Mean (ksi)
KB-33	85.9	10.7	Test discontinued before load drop. Nf/2 = 8500						87.5	39.2
KB-80	71.7	28.8	-	-	-	-	-	-	49.9	-2.8
KB-49	69.6	20.1	96.2	41.2	90.0	39.9	90.7	40.1	89.3	38.7
KB-27	101.7	22.7	96.0	42.2	98.0	41.5	97.3	42.6	99.5	44.2

*The following specimens were exposed 100 hr. at 2000F prior to test.

Spec ID	SigO Range (ksi)	SigO Mean (ksi)	SigNc Range (ksi)	SigNc Mean (ksi)	SNmin Range (ksi)	SNmin Mean (ksi)	SNmax Range (ksi)	SNmax Mean (ksi)	Sig.5 Range (ksi)	Sig.5 Mean (ksi)
KB-92	94.3	16.9	-	-	-	-	-	-	98.9	27.7

Spec ID	SigO Range (ksi)	SigO Mean (ksi)	SigNc Range (ksi)	SigNc Mean (ksi)	SNmin Range (ksi)	SNmin Mean (ksi)	SNmax Range (ksi)	SNmax Mean (ksi)	Sig.5 Range (ksi)	Sig.5 Mean (ksi)
KB-32	81.1	10.5	83.3	15.4	88.6	25.0	88.6	25.0	81.4	25.7
KB-24	87.7	14.1	91.8	41.0	84.1	48.1	89.1	48.1	91.4	41.0
KB-36	85.6	42.7	-	-	-	-	-	-	89.0	42.3
KB-34	120.8	18.4	127.0	35.2	128.0	51.1	128.0	51.1	128.2	43.1
KB-48	74.1	10.0	78.8	38.1	53.3	26.6	53.3	26.6	75.3	36.9
KB-52	75.3	8.0	69.2	27.2	76.5	33.2	76.5	33.2	Test discontinued	

*The following specimens were exposed 100 hr. at 2000F prior to test.

Spec ID	SigO Range (ksi)	SigO Mean (ksi)	SigNc Range (ksi)	SigNc Mean (ksi)	SNmin Range (ksi)	SNmin Mean (ksi)	SNmax Range (ksi)	SNmax Mean (ksi)	Sig.5 Range (ksi)	Sig.5 Mean (ksi)
KB-93	92.9	18.3	101.2	38.1	-	-	103.6	38.9	103.6	38.9

<123> PWA 1480 / PWA 273 ISOTHERMAL FATIGUE SUMMARY

Spec ID	SigO Range (ksi)	SigO Mean (ksi)	EinO Range (%)	SigNc Range (ksi)	SigNc Mean (ksi)	EinNc Range (%)	SigNs Range (ksi)	SigNs Mean (ksi)	EinNs Range (%)	Sig.5 Range (ksi)	Sig.5 Mean (ksi)	Ein.5 Range (%)
MB-21	119.3	-3.3	0.026	119.1	2.2	0.032	119.3	2.4	0.029	119.1	2.2	0.032
MB-18	143.9	-2.0	0.055	-	-	-	144.7	3.1	-	144.9	3.6	0.052
MB-4	155.8	-2.3	0.065	-	-	-	142.4	-18.7	0.144	145.2	-18.4	0.137
Dsig	-			-			-14.5			-15.1		
MB-88	60.2	1.3	0.016	57.2	4.4	0.040	41.6	1.5	0.073	55.0	6.6	0.046
Dsig	+2.8			+3.6			+3.6			+4.3		

\<123\> PWA 1480 / PWA 286 ISOTHERMAL FATIGUE SUMMARY

Spec ID	SigO Range (ksi)	SigO Mean (ksi)	EinO Range (%)	//	SigNc Range (ksi)	SigNc Mean (ksi)	EinNc Range (%)	//	SigNs Range (ksi)	SigNs Mean (ksi)	EinNs Range (%)	//	Sig.5 Range (ksi)	Sig.5 Mean (ksi)	Ein.5 Range (%)	//
MB-26	140.7	-63.6	0.016		138.6	-29.5	0.017		135.6	-27.6	0.014		Test discontinued			
MB-64	119.0	2.0	0.018		117.6	-2.0	0.027		116.2	5.0	0.024		117.6	-2.0	0.027	
MB-40	118.3	-0.8	0.031		110.8	20.7	0.075		-	-	-		112.5	18.1	0.073	
Dsig	+13.2				+7.3								+7.7			
MB-41	68.3	-1.6	0.031		-	-	-		-	-	-		61.2	-4.8	0.071	
Dsig	-4.5												-6.0			
MB-6	105.2	-0.7	0.082		-	-	-		-	-	-		99.3	0.9	0.102	
MB-38	90.2	-2.6	0.108		-	-	-		81.7	0.7	0.123		81.4	0.7	0.122	
MB-33	103.3	-1.4	0.164		-	-	-		-	-	-		99.3	0.9	0.167	
MB-2	105.4	0.6	0.141		-	-	-		-	-	-		98.0	0.3	0.161	

\<123> PWA 1480 / PWA 273 THERMOMECHANICAL FATIGUE SUMMARY

Spec ID	SigO Range (ksi)	SigO Mean (ksi)	SigNc Range (ksi)	SigNc Mean (ksi)	SNmin Range (ksi)	SNmin Mean (ksi)	SNmax Range (ksi)	SNmax Mean (ksi)	Sig.5 Range (ksi)	Sig.5 Mean (ksi)
MB-25	92.8	11.9	-	-	-	-	-	-	97.2	42.1
MB-1	129.2	22.2	-	-	-	-	130.2	38.8	130.2	38.3
MB-16	86.2	9.6	77.7	32.7	84.9	39.2	84.9	39.2	89.5	40.1
MB-24	69.1	10.0	70.6	26.5	73.1	29.4	73.1	29.4	69.5	30.6

<123> PWA 1480 / PWA 286 THERMOMECHANICAL FATIGUE SUMMARY

Spec ID	SigO Range (ksi)	SigO Mean (ksi)	SigNc Range (ksi)	SigNc Mean (ksi)	SNmin Range (ksi)	SNmin Mean (ksi)	SNmax Range (ksi)	SNmax Mean (ksi)	Sig.5 Range (ksi)	Sig.5 Mean (ksi)
MB-17	73.3	10.1	82.8	47.4	82.7	47.8	82.7	47.8	82.5	47.6
MB-23	61.3	6.0	64.9	21.2	65.0	21.2	65.0	21.2	62.4	21.0
MB-22	89.5	11.0	92.8	36.8	107.2	43.4	-	-	92.3	32.2
MB-8	86.6	12.5	88.6	32.3	93.2	41.4	93.2	41.4	89.1	31.6
MB-19	85.0	13.5	83.2	30.5	38.8	17.0	-	-	83.2	29.2
MB-62	100.0	52.8	95.9	47.3	98.7	50.3	98.4	50.3	94.7	47.3
MB-27	88.1	14.4	93.6	47.2	92.6	50.3	92.6	50.3	96.9	54.1
Dsig	+4.9		-2.9		-2.4		-2.4		-1.4	
MB-35	78.3	10.1	76.9	38.1	79.6	39.5	79.6	39.5	77.1	37.3
MB-37	68.7	16.1	82.1	39.0	81.5	43.1	81.5	43.1	83.0	38.7

APPENDIX F

LIFE DATA SUMMARY FOR ALLOY 185 FATIGUE TESTS

AND

STRESS/INELASTIC STRAIN DATA SUMMARY FOR ALLOY 185 FATIGUE TESTS

\<001\> ALLOY 185 / PWA 286 THERMOMECHANICAL FATIGUE SUMMARY

T	S	Spec ID	Tmax (F)	Cycle Type	DE	V	Init	Fail Exam	Tc	Nc	AR	Nmin	Ind	Nmax	Ind	Nsc	Nsi	5%	10%	Nf
8	s	HJB-4	1900	Out-of-phase	.3	0	c	gag 0	4.6	1880	12.	3240	rep	3240	rep	1360	-	11170	12970	16030
8	s	HJB-1	1900	Out-of-phase	.5	0	c	gag 0	4.5	510	4.5	1020	rep	1020	rep	510	-	5110	5270	5399
8	s	HJB-8	1900	Out-of-phase	.7	0	c	gag 0	4.6	110	4.3	390	rep	390	rep	280	-	960	1090	1095

\<001\> ALLOY 185 / PWA 286 THERMOMECHANICAL FATIGUE SUMMARY

Spec ID	/ / /	Sig0 Range (ksi)	Sig0 Mean (ksi)	/ / /	SigNc Range (ksi)	SigNc Mean (ksi)	/ / /	SNmin Range (ksi)	SNmin Mean (ksi)	/ / /	SNmax Range (ksi)	SNmax Mean (ksi)	/ / /	Sig.5 Range (ksi)	Sig.5 Mean (ksi)	/ / /
HJB-4		52.0	5.0		52.2	14.4		49.2	15.8		49.2	15.8		43.6	13.8	
HJB-1		81.0	11.2		86.1	31.6		81.4	33.5		81.4	33.5		74.6	28.2	
HJB-8		115.1	16.2		116.6	33.3		116.1	37.7		116.1	37.7		114.1	38.7	

APPENDIX G

PWA 1480 SMOOTH SPECIMEN LOW CYCLE FATIGUE STRAIN CONTROLLED

PWA 1480 SMOOTH SPECIMEN LOW CYCLE FATIGUE STRAIN CONTROLLED

0.1% PER SEC. 1200°F (Unless Noted Otherwise)

Spec	Strain %		PL Range	Stress (KSI)		Life	Comments
	Max.	Min.		Max.	Min.	(Cycles)	
<001> Orientation							
JJB49	1.509	0.014	0.025	158.0	−76.5	1326.	
JJB43	1.120	0.020	0.000	149.0	−35.0	4414.	
JJB50	1.202	0.008	0.000	159.5	−39.3	5673.	
JJB45	1.740	0.270	0.020	165.5	−61.0	1593.	
JJB101	0.891	0.018	0.000	153.0	−8.5	29516.	
JJB109	0.726	0.000	0.000	114.2	0.2	365072.	SUS
JJB170	0.678	0.000	0.000	112.0	5.6	212570.	LDC
<111> Orientation							
JLB58	0.809	0.008	0.140	138.1	−138.8	1016.	
JLB56	0.600	0.000	0.010	120.0	−104.0	3410.	
JLB66	0.591	0.015	0.010	126.1	−105.0	7356.	
JLB57	0.960	0.150	0.080	148.3	−150.3	843.	
JLB59	1.205	0.625	0.000	132.9	−91.5	7904.	
JLB60	1.219	−0.603	1.020	171.7	−168.7	26.	
JLB61	0.291	−0.284	0.000	119.7	−118.4	7101.	
<213> Orientation							
JMB29	1.212	0.000	0.270	130.6	−140.6	79.	
JMB41	0.795	0.013	0.000	122.9	−120.4	4175.	
JMB35	0.600	0.000	0.000	113.7	−48.8	114789.	
JMB32	0.602	0.008	0.000	117.7	−61.5	45640.	SUS
JMB36	0.601	0.005	0.000	132.8	−6.5	34676.	
<011> Orientation							
JJB112	0.896	0.013	0.000	127.1	−90.8	7532.	
JKB21	0.920	0.040	0.000	119.2	−127.1	2672.	
JKB24	0.695	0.019	0.000	122.4	−60.2	30220.	
<001> Orientation							
JJB41	1.120	0.030	0.000	153.0	−13.0	4912.	1400°F
JJB46	1.160	0.000	0.060	119.7	−28.0	5431.	1600°F

PWA 1480 SMOOTH SPECIMEN LOW CYCLE FATIGUE STRAIN CONTROLLED
(Continued)

Spec	Strain % Max.	Strain % Min.	PL Range	Stress (KSI) Max.	Stress (KSI) Min.	Life (Cycles)	Comments
<111> Orientation							
JLB64	0.602	0.007	0.070	116.9	−79.4	3354.	1600°F
<213> Orientation							
JMB39	1.170	0.005	0.211	133.1	−113.0	350.	1600°F
<001> Orientation							
JJB74	1.814	0.015	0.054	186.8	−100.6	1471.	HIP
JJB75B	1.508	0.011	0.016	180.0	−68.0	2964.	HIP
JJB79	1.202	0.010	0.000	167.8	−31.9	20051.	HIP
JJB80	1.103	0.021	0.000	160.2	−19.7	32448.	HIP
<111> Orientation							
JLB25B	0.811	0.003	0.126	145.5	−144.2	1166.	HIP
JLB25A	0.590	0.014	0.000	137.2	−101.3	27410.	HIP
JLB26A	0.492	0.019	0.000	125.1	−70.7	325570.	HIP
<011> Orientation							
JKB13A	0.902	0.016	0.000	126.4	−112.2	1806.	HIP
JKB13B	0.890	0.027	0.000	131.1	−110.5	737.	HIP
<001> Orientation							
JJB78	1.164	0.007	0.060	133.1	−26.9	12413.	HIP, 1600°F
JJB81	1.160	0.011	0.055	134.4	−24.9	13174.	HIP, 1600°F
<111> Orientation							
JLB26B	0.598	0.007	0.052	123.9	−82.1	4269.	HIP, 1600°F

Notes: SUS = Test suspended without failure
        LDC = Test conducted in load control

159

APPENDIX H

PWA 1480 NOTCHED FATIGUE TESTS LOAD CONTROL

PWA 1480 NOTCHED FATIGUE TESTS LOAD CONTROL

1 CPS, 1200°F (Unless Noted Otherwise)

Specmen	Lot No.	Smax (Ksi)	Smin/ Smax	Life (Cycles)	Comments
<001> <100> Thin, Mild Notched Specimen					
JJB105A	1160	140.0	0.05	30.	
JJB125A	1160	125.0	0.05	14340.	
JJB108A	1160	125.0	0.05	23740.	
JJB106A	1160	125.0	0.05	22940.	
JJB125B	1160EP	125.0	0.05	54470.	
JJB106B	1160	125.0	0.25	93850.	
JJB128B	1160	125.0	0.40	535200.	
JJB121A	1160	120.0	0.05	18880.	
JJB121B	1160	120.0	0.04	14260.	
JJB26B	7590	115.0	0.05	2860.	
JJB18A	7590	115.0	0.05	17227.	
JJB127B	1160	115.0	0.05	10010.	
JB30A	7590	115.0	0.50	1122917.	
JB30B	7590	95.0	0.05	62119.	
JB18B	7590	95.0	0.05	84626.	
JJB127A	1160	95.0	0.05	198930.	
<001> <210> Thin, Mild Notched Specimen					
JJB48A	316B	115.0	0.05	3434.	
JJB48B	316B	95.0	0.05	16427.	
JJB56B	316B	95.0	0.05	85040.	
JJB52A	316B	95.0	0.05	43090.	
<111> <01-1> Thin, Mild Notched Specimen					
JLB79B	1535	100.0	0.05	157320.	
JLB67B	1535	100.0	0.05	333380.	
JLB72B	316B	100.0	0.05	18490.	
JLB69B	316B	100.0	0.05	4178.	
JLB69A	316B	85.0	0.05	97870.	
JLB71A	316B	85.0	0.05	347360.	

PWA 1480 NOTCHED FATIGUE TESTS LOAD CONTROL
(Continued)

Specmen	Lot No.	Smax (Ksi)	Smin/ Smax	Life (Cycles)	Comments
JLB71B	316B	85.0	0.05	413050.	
JLB67A	1535	85.0	0.05	1000000.	Upload to 100.0 for 870.
JLB79A	1535	85.0	0.05	1166580.	Upload to 130.0 for 14450.
<011> <01-1> Thin, Mild Notched Specimen					
JKB25A	1535	95.0	0.05	13220.	
JKB26A	1535	95.0	0.05	23040.	
JKB25B	1535EP	95.0	0.05	18370.	
<001> <100> Thin, Mild Notched Specimen					
JB26A	7590	115.0	0.05	2476.	1400°F
JB132B	7590	115.0	0.05	1128.	1600°F
JB58B	7590	95.0	0.05	3402.	1600°F
<001> <100> Thin, Mild Notched Specimen					
JLB70A	316B	100.0	0.05	930.	1600°F
JLB70B	316B	85.0	0.05	1952.	1600°F
<001> <100> Thin, Sharp Notched Specimen					
JJB137A	1535	100.0	0.05	53030.	
JJB122A	1535	100.0	0.05	6940.	
830-4B	7590	100.0	0.05	4190.	
JJB4B	7590	100.0	0.05	6157.	
789-3B	7590	88.0	0.05	16015.	
789-4B	7590	88.0	0.05	117596.	
JJB4A	7590	75.0	0.05	1070000.	Upload to 88.0 for 4485.
<111> <01-1> Thin, Sharp Notched Specimen					
JLB73A	316B	83.0	0.05	5286.	
JLB73B	316B	73.0	0.05	5154.	
JLB74A	316B	73.0	0.05	6888.	
JLB74B	316B	57.0	0.05	1250000.	Test Suspended
<001> <100> Thick, Mild Notched Specimen					
789-2	7590	115.0	0.05	12048.	

PWA 1480 NOTCHED FATIGUE TESTS LOAD CONTROL
(Continued)

Specmen	Lot No.	Smax (Ksi)	Smin/ Smax	Life (Cycles)	Comments
830–2	7590	97.3	0.05	8253.	
830–3	7590	97.3	0.05	17232.	
JJB130	1160	107.0	0.05	10730.	
JJB132	1160	81.0	0.05	76210.	
JJB133	1160	81.0	0.05	500450.	
<111> <01–1> Thick, Mild Notched Specimen					
JLB75	316B	94.2	0.05	6343.	
JLB76	316B	79.5	0.05	20918.	
JLB78	316B	79.5	0.05	396570.	
JLB77	316B	66.0	0.05	1044340.	Upload to 79.5 for 396570.
<001> <100> Single Tooth Firtree (STFT) Specimen					
JJB180A	1534	23.26	0.05	27354.	
<001> <100> Thin, Mild Notched Specimen					
JJB86A	900	140.0	0.05	170.	HIP
JJB88A	900	130.0	0.05	33770.	HIP
JJB84B	900	120.0	0.05	94400.	HIP
JJB82A	900	115.0	0.05	413610.	HIP
JJB82B	900	115.0	0.05	327143.	HIP
JJB84A	900	95.0	0.05	1060620.	HIP, Load Increase to 115.0 Ksi for 137130.
<001> <210> Thin, Mild Notched Specimen					
JJB93A	900	115.0	0.05	87030.	HIP
JJB104	900	95.0	0.05	1334290.	HIP, Load Increased to 115.0 Ksi for 2860.
<001> <100> Thin, Sharp Notched Specimen					
JJB96B	900	120.0	0.05	19550.	HIP
JJB95A	900	120.0	0.05	48190.	HIP
JJB96A	900	120.0	0.05	142330.	HIP
<111> <01–1> Thin, Sharp Notched Specimen					
JLB81A	1535	108.0	0.05	52190.	HIP
JLB80B	1535	93.0	0.05	73040.	HIP, Test Suspended
JLB80A	1535	83.0	0.05	612930.	HIP, Test Suspended

Table 1

Single Crystal Superalloys

Alloy Composition (Weight Percent)

Alloy	Heat Code	Ni	Cr	Co	Ti	Elements Al	Ta	W	Mo	C
PWA 1480	Nominal	Bal*	10.0	5.0	1.5	5.0	12.0	4.0	--	--
	P9866 (Heat A)	Bal*	10.35	5.5	1.44	4.95	12.2	3.9	--	0.01
	P9867 (Heat B)	Bal*	10.3	5.3	1.44	4.9	10.2	4.0	--	0.004
Alloy 185	Nominal	Bal*	--	--	--	6.8	--	6.0	14.0	0.04
	P9921	Bal*	--	--	0.001	6.82	--	6.10	13.85	0.04

*Balance

Table 2

Coating Compositions and Application Processes

Coating	Type	Composition	Deposition Process
PWA 286	Overlay	NiCoCrAlY+Si+Hf	Vacuum Plasma Spray
PWA 273	Aluminide (Outward Diffusion)	NiAl	Pack Cementation

Table 3

Dynamic Elastic Constants
and Apparent Modulus for PWA 1480 Uniaxial Bars In Four Orientations

TEMP °F	CONSTANTS REFERRED TO CRYSTAL AXES						APPARENT MODULUS			
	C11 Msi	C12 Msi	C44 Msi	S11	S12	S44	<001> Msi	<101> Msi	<213> Msi	<111> Msi
				$\times 10^{-9}$ Psi^{-1}						
0.	36.5	23.6	19.0	55.6	-21.8	52.7	18.0	33.3	33.3	46.4
100.	36.3	23.6	18.7	56.5	-22.3	53.3	17.7	32.8	32.8	45.9
200.	36.0	23.4	18.5	56.9	-22.4	54.0	17.6	32.5	32.5	45.4
300.	35.7	23.2	18.3	57.4	-22.6	54.7	17.4	32.2	32.2	44.8
400.	35.4	23.1	18.0	58.0	-22.9	55.5	17.2	31.8	31.8	44.3
500.	35.1	22.9	17.8	58.9	-23.3	56.3	17.0	31.4	31.4	43.7
600.	34.8	22.8	17.5	59.7	-23.7	57.2	16.7	30.9	30.9	43.1
700.	34.5	22.7	17.2	60.8	-24.1	58.1	16.4	30.4	30.4	42.5
800.	34.1	22.6	16.9	61.9	-24.7	59.0	16.1	29.9	29.9	41.9
900.	33.8	22.4	16.6	63.0	-25.2	60.1	15.9	29.5	29.5	41.2
1000.	33.4	22.3	16.4	64.2	-25.7	61.1	15.6	29.0	29.0	40.6
1100.	33.0	22.1	16.1	65.5	-26.3	62.2	15.3	28.4	28.4	39.9
1200.	32.7	22.0	15.8	66.9	-26.9	63.4	15.0	27.9	27.9	39.3
1300.	32.3	21.9	15.5	68.6	-27.7	64.6	14.6	27.3	27.3	38.6
1400.	31.8	21.8	15.2	70.6	-28.7	65.9	14.2	26.7	26.7	37.9
1500.	31.4	21.7	14.8	72.9	-29.8	67.3	13.7	26.0	26.0	37.2
1600.	30.9	21.6	14.5	75.6	-31.0	68.9	13.2	25.3	25.3	36.4
1700.	30.4	21.4	14.1	78.5	-32.4	70.7	12.7	24.6	24.6	35.6
1800.	29.9	21.2	13.7	81.9	-34.0	72.8	12.2	23.7	23.7	34.6
1900.	29.2	21.0	13.3	86.0	-36.0	75.2	11.6	22.8	22.8	33.6
2000.	28.5	20.8	12.8	91.4	-38.6	78.1	10.9	21.8	21.8	32.5
2100.	27.8	20.7	12.3	99.4	-42.5	81.4	10.1	20.5	20.5	31.3
2200.	27.0	20.6	11.8	108.9	-47.1	85.0	9.2	19.2	19.2	30.1

1 MPa = 1.45 x 10^{-4} Msi = 145 Psi
C = 1.8 x (F-32)

Table 4

Summary of PWA 1480 Tensile Tests

Temp. °C(°F)	Spec. ID	Orient	Coat Type	$Ex10^{-3}$ MPa(KSI)	.2% Yield MPa(KSI)	Ult. MPa(KSI)	Elong %	RA %
427(800)	JA-16	100	---	113.8(16.5)	989.4(143.5)	1118.4(162.2)	5.7	3.2
	KA-2	110	---	221.3(32.1)	921.9(133.7)	957.0(138.8)	14.3	23.2
	LA-36	111	---	239.3(34.7)	897.0(130.1)	1393.5(202.1)	11.7	11.9
	MA-1	123	---	198.6(28.8)	837.7(121.5)	1218.3(176.7)	19.1	18.2
649(1200)	JA-33	100	---	POROSITY FAILURE				
	KA-3	110	---	176.5(25.6)	929.4(134.8)	1081.1(156.8)	4.7	5.6
	LA-51	111	---	253.7(36.8)	849.5(123.2)	1245.2(180.6)	23.7	25.6
	MA-3	123	---	193.7(28.1)	824.0(119.5)	1082.5(157.0)	22.7	25.1
760(1400)	JA-34	100	---	101.4(14.7)	1177.0(170.7)	1324.5(192.1)	14.1	13.0
	JA-22		$273^{1,2}$	103.4(15.0)	1159.7(168.2)	1293.5(187.6)	4.8	7.3
	JA-11		$286^{1,3}$	94.5(13.7)	1163.2(168.7)	1290.1(187.1)	8.0	15.1
	KA-4	110	---	174.4(25.3)	948.1(137.5)	1108.7(160.8)	10.5	23.9
	LA-52	111	---	200.0(29.0)	879.8(127.6)	1093.5(158.6)	22.1	24.2
	LA-25		$273^{1,2}$	220.6(32.0)	920.5(133.5)	1030.1(149.4)	16.8	20.9
	LA-13		$286^{1,3}$	171.7(24.9)	908.1(131.7)	1106.6(160.5)	21.4	29.7
	MA-4	123	---	180.0(26.1)	891.5(129.3)	985.3(142.9)	17.8	18.5
871(1600)	JA-36	100	---	102.0(14.8)	715.0(103.7)	1021.1(148.1)	13.7	23.6
	JA-24		$273^{1,2}$	92.4(13.4)	756.4(109.7)	991.5(143.8)	18.7	25.4
	JA-12		$286^{1,3}$	91.7(13.3)	755.7(109.6)	961.9(139.5)	21.7	26.2
	KA-6	110	---	149.6(21.7)	786.0(114.0)	910.1(132.0)	13.1	26.0
	LA-53	111	---	190.3(27.6)	696.4(101.0)	819.8(118.9)	19.0	22.1
	LA-26		$273^{1,2}$	201.3(29.2)	682.6(99.0)	812.2(117.8)	20.3	24.4
	LA-14		$286^{1,3}$	181.3(26.3)	671.6(97.4)	812.2(117.8)	22.1	22.1
	MA-5	123	---	179.3(26.0)	626.1(90.8)	764.7(110.9)	18.0	21.1
982(1800)	JA-37	100	---	88.3(12.8)	452.3(65.6)	695.0(100.8)	23.0	32.5
	JA-25		$273^{1,2}$	92.4(13.4)	437.1(63.4)	659.9(95.7)	24.0	34.3
	JA-13		$286^{1,3}$	102.0(14.8)	428.9(62.2)	642.6(93.2)	22.9	35.4
	KA-8	110	---	133.1(19.3)	519.9(75.4)	628.8(91.2)	16.7	36.1
	LA-54	111	---	189.6(27.5)	427.5(62.0)	557.8(80.9)	22.2	28.0
	LA-28		$273^{1,2}$	175.1(25.4)	448.2(65.0)	575.7(83.5)	18.3	26.3
	LA-16		$286^{1,3}$	120.0(17.4)	455.1(66.0)	557.1(80.8)	23.7	28.2
	MA-6	123	---	164.8(23.9)	431.6(62.6)	539.9(78.3)	25.9	25.0
1093(2000)	JA-38	100	---	72.4(10.5)	275.1(39.9)	371.6(53.9)	30.0	53.8
	JA-26		$273^{1,2}$	52.4(7.6)	272.4(39.5)	368.2(53.4)	31.3	56.8
	JA-14		$286^{1,3}$	68.9(10.0)	269.6(39.1)	353.7(51.3)	43.0	59.2
	KA-9	110	---	91.7(13.3)	315.8(45.8)	385.4(55.9)	18.7	28.1
	LA-55	111	---	132.4(19.2)	259.9(37.7)	328.9(47.7)	41.7	35.5
	LA-29		$273^{1,2}$	97.9(14.2)	253.0(36.7)	315.1(45.7)	28.0	42.1
	LA-18		$286^{1,3}$	85.5(12.4)	262.7(38.1)	321.3(46.6)	29.2	46.6
	MA-9	123	---	125.5(18.2)	273.0(39.6)	319.2(46.3)	24.9	35.3

1 X-sectional area used to calculate stress excludes coating area
2 Aluminide diffusion
3 NiCoCrAlY overlay

Table 5

Summary of PWA 1480 Creep Tests

Temperature °C (°F)	Spec. ID	Orient.	Coat Type	Stress MPa	(ksi)	% of 0.2% Yield	Life (hours)	Creep Rate (minutes)$^{-1}$	Elong. (%)	RA (%)
871 (1600)	JA-40	<001>	--	413.7	(60)	57.8	462.9	8.84E-07	12.0	20.1
	JA-41		--	517.1	(75)	72.3	79.0	8.82E-06	15.3	28.9
	KA-10	<011>	--	413.7	(60)	52.6	330.7	7.33E-07	3.2	1.6
	KA-11		--	482.6	(70)	61.4	83.5	3.79E-06	3.2	4.6
	MA-10	<123>	--	413.7	(60)	66.0	167.1	4.66E-06	7.5	9.7
	MA-11		--	482.6	(70)	77.1	42.6	3.22E-05	15.5	19.1
	LA-56	<111>	--	413.7	(60)	59.4	373.7	4.18E-07	13.0	16.7
	LA-57		--	482.6	(70)	69.3	67.1	2.90E-05	14.9	22.8
982 (1800)	JA-42	<001>	--	220.6	(32)	48.8	Stopped at 5.4 hours for TEM[1]			
	JA-27		273[2,3]	231.7	(33.6)	53.0	89.1	3.94E-06	25.2	44.2
	JA-15		286[2,4]	237.9	(34.5)	55.5	105.5	3.65E-06	20.0	42.3
	JA-45		--	248.2	(36)	54.9	80.5	4.74E-06	20.7	41.4
	JA-28		273[2,3]	260.6	(37.8)	59.6	53.3	8.74E-06	24.3	40.6
	JA-17		286[2,4]	268.2	(38.9)	62.5	51.7	8.48E-06	20.7	36.3
	KA-14	<011>	--	248.2	(36)	47.7	75.4	1.79E-06	Failed outside gage	
	KA-13		--	248.2	(36)	47.7	88.7	1.31E-06	8.6	39.8
	MA-12	<123>	--	206.9	(30)	63.8	277.1	5.87E-07	23.5	57.4
	MA-13		--	248.2	(36)	76.6	76.6	3.12E-06	23.5	33.1
	LA-58	<111>	--	220.6	(32)	51.6	678.6	9.37E-07	17.1	19.9
	LA-30		273[2,3]	230.5	(33.4)	53.9	Stopped at 17.3 hours for TEM[1]			
	LA-20		286[2,4]	239.7	(34.8)	56.2	274.4	3.61E-06	17.5	24.1
	LA-59		--	248.2	(36)	58.1	258.1	3.58E-06	12.9	17.2
	LA-31		273[2,3]	259.6	(37.6)	60.7	156.3	9.06E-06	19.6	22.4
	LA-21		286[2,4]	266.0	(38.6)	62.3	Stopped at 44.8 hours for TEM[1]			
1093 (2000)	JA-46	<001>	--	117.2	(17)	42.6	132.2	9.24E-07	13.2	49.5
	JA-48		--	117.2	(17)	42.6	137.1	9.03E-07	16.1	50.9
	JA-29		273[2,3]	108.5	(15.7)	39.4	Stopped at 29.8 hours for TEM[1]			
	JA-18		286[2,4]	112.9	(16.4)	41.1	223.9	5.73E-07	13.5	48.2
	JA-30		273[2,3]	123.1	(17.8)	44.7	76.4	2.97E-06	20.6	58.1
	JA-19		286[2,4]	297.4	(43.1)	108.1	Stopped at 0.4 hour for TEM[1]			
	KA-15	<011>	--	89.6	(13)	28.4	197.6	7.70E-08	2.7	4.9
	KA-16		--	103.4	(15)	32.8	138.7	3.02E-07	6.0	30.3
	MA-14	<123>	--	89.6	(13)	32.9	251.2	3.29E-07	11.9	37.1
	MA-17		--	103.4	(15)	37.9	130.7	6.59E-07	14.0	19.8
	LA-60	<111>	--	89.6	(13)	34.5	825.7	2.38E-07	13.0	17.0
	LA-32		273[2,3]	144.6	(21)	55.7	83.2	Not available	12.0	17.1
	LA-22		286[2,4]	111.0	(16.1)	42.7	Stopped at 132.3 hours for TEM[1]			
	LA-61		--	103.4	(15)	39.8	372.4	1.81E-07	Failed outside gage	
	LA-34		273[2,3]	180.8	(26.2)	69.5	14.6	4.05E-05	18.5	22.3
	LA-23		286[2,4]	111.5	(16.2)	43.0	322.4	8.37E-07	9.6	19.7

Notes:

1. Transmission electron microscopy (TEM)
2. Cross sectional area used to calculate stresses excludes coating area
3. Aluminide diffusion
4. NiCoCrAlY overlay

Table 6

Summary of Bulk HIP PWA 286 Creep Tests

Temp. °C(°F)	Spec. ID	Stress MPa(KSI)	Life (Hrs)	Secondary Creep Rate (Min^{-1})	Elong %	RA %	Comments
649(1200)	9-T	68.9(10)	1700	2.99 E-07	N/A	N/A	Discontinued At 1700 hrs.
	9-B	103.4(15)	1130	1.25 E-06	N/A	N/A	Discontinued At 1130 hrs.
760(1400)	17-T	34.5(5)	446	6.53 E-06	93.2	87.1	
	12-T	20.7/55.2(3/8)	92.1	2.64 E-06/4.60 E-05	166.1	23.7	Uploaded from 20.7 MPa/3 ksi to 55.2 MPa/8 ksi at 48 hrs.
871(1600)	18-B	6.9/13.8(1/2)	280.5	9.38 E-07/2.31 E-05	77.1	84.9	Uploaded from 6.9 MPa/1 ksi to 13.8 MPa/2 ksi at 160 hrs.
	17-B	20.7(3)	26.8	1.40 E-04	206.0	86.7	
982(1800)	15-B	3.45(.5)	---	---	139.1	66.1	Failed on loading

N/A = Not available

Table 7

Base Program Cyclic Constitutive Tests

Nominal Orientation	R.T.	800°F (427°C)	1200°F (649°C)	1400°F (760°C)	1600°F (871°C)	1800°F (982°C)	1900°F (1038°C)	1975°F (1079°C)	2000°F (1093°C)	2100°F (1149°C)
<001>		JA61	JA64	JA44	JA63 JA67	JA58 JA66 JA68	JA69	JB44*	JB1*	JA65
<011>		KA27	KA31	KA26	KA23 KA33	KA22				KB107*
<111>		LA66	LA71	LA63 LA67	LA65 LA68	LA64 LA69	LA62		LB300*	LB94* LB179*†
<213>	MA27	MA26 MA28 MA30		MA25	MA35	MA23 MA30				

* MERL 73C Tube Specimen. All others are LED41784 solid round specimens.
† Coated

169

Table 8

Summary of Walker Constitutive Model Regressed
Temperature Dependent Constants for Unexposed, Bulk HIP PWA 286

6.895 kPa = 1 psi

	427°C (800°F)	538°C (1000°F)	649°C (1200°F)	760°C (1400°F)	871°C (1600°F)	1093°C (2000°F)
E, psi	0.2180E8	0.2133E8	0.1902E8	0.1550E8	0.9502E7	0.1500E7
WALKER						
n	0.5143E2	0.2070E2	0.3300E1	0.2130E1	0.1705E1	0.1345E1
n1, psi	0.	0.	0.	0.	0.	0.
n2, psi	0.3130E8	0.3130E8	0.3017E8	0.1334E8	0.3467E7	0.7292E5
n3	0.5000E3	0.7000E3	0.9000E3	0.1000E4	0.8786E3	0.2516E3
n4	0.	0.	0.	0.	0.	0.
n5	0.	0.	0.	0.	0.	0.
n6	0.1488E-8	0.3162E-7	0.3162E-6	0.1110E-5	0.2109E-5	0.3437E-5
n7	0.	0.	0.	0.	0.	0.
K1, psi	0.9548E5	0.1240E6	0.1253E7	0.2488E7	0.1543E7	0.3950E6
K2, psi	0.	0.	0.	0.	0.	0.
m	0.1200E1	0.1320E1	0.1492E1	0.1788E1	0.2042E1	0.2202E1
Ω_0, psi	0.	0.	0.	0.	0.	0.

Table 9

Unexposed, Bulk HIP PWA 286 Creep Rates
Data Vs. Prediction

| | | Secondary Creep Rate (in/in/hr) | |
| | | | Predicted |
Temp. °C (°F)	Stress MPa (ksi)	Data	Walker
649 (1200)	68.9 (10)	0.266E-4	0.305E-4
649 (1200)	103.4 (15)	0.173E-3	0.574E-4
760 (1400)	20.7 (3)	0.139E-3	0.256E-3
760 (1400)	34.5 (5)	0.388E-3	0.732E-3
871 (1600)	6.9 (1)	0.461E-4	0.171E-2
871 (1600)	20.7 (3)	0.103E-1	0.179E-1

Table 10

PWA 286 Overlay Coating TMF Life Model
Correlation Data Set
Note: All ε–T cycles are out–of–phase

Spec ID	Substrate Orientation	Tmax (°F)	Compression Hold Time (sec)	Cycle Period (sec)	Actual Life (cycles)	Nc Correlated Life (cycles)
JB-147	<001>	1900	0	60	1400	1111
JB-121	<001>	1900	30	90	1350	1061
JB-137	<001>	1900	60	120	1070	878
JB-10	<001>	1900	0	60	500	881
JB-9	<001>	1900	0	60	370	347
JB-80	<001>	1900	0	60	300	318
JB-111	<001>	2100	0	60	3000	2124
JB-89	<001>	2100	0	60	770	648
LB-170	<111>	1900	0	60	5720	4299
LB-181	<111>	1900	0	60	5720	4310
LB-27	<111>	1900	0	60	2500	2894
LB-216	<111>	2100	0	60	3090	3592
LB-236	<111>	2100	0	60	2160	3248
KB-32	<011>	1900	0	60	2680	3542
KB-24	<011>	1900	0	60	2900	3539
KB-34	<011>	1900	0	60	900	1506
KB-48	<011>	2100	0	60	2460	3629
KB-52	<011>	2100	0	60	4300	3620
MB-17	<213>	1900	0	60	4600	4252
MB-23	<213>	1900	0	60	5050	4252
MB-22	<213>	1900	0	60	3500	2628
MB-8	<213>	1900	0	60	3930	2634
MB-19	<213>	1900	0	60	3700	2642
MB-62	<213>	1900	0	60	1800	2619
MB-27	<213>	1900	300	360	1170	1186
MB-35	<213>	2100	0	60	3620	3655
MB-37	<213>	2100	0	60	2840	3285

Table 11

PWA 286 Overlay Coating TMF Life Model
Verification Data Set

Spec ID	Substrate Orienta- tion	ε-T cycle	Tmax (°F)	Compression Hold Time (sec)	Cycle Period (sec)	Actual Life (cycles)	Nc Predicted Life (cycles)
JB-174	<001>	Out-of-phase	1900	0	60	2050	2297
JB-104	<001>	T-cycle	1900	0	120	3300	2545
JB-11	<001>	In-phase	1900	0	60	>10000	10872
JB-21	<001>	Z-cycle	1900	0	120	820	965
JB-102	<001>	Baseball-ccw	1900	0	60	1260	2182
JB-146[e]	<001>	Out-of-phase	1900	0	60	1400	1540
JB-133[e]	<001>	Out-of-phase	1900	0	60	740	1134
JB-135	<001>	Airfoil L.E.	1900	60	300	1280	1994
LB-29	<111>	Baseball-cw	1900	0	60	2000	1150
LB-26	<111>	T-cycle	1900	0	120	2560	6703
LB-31	<111>	Out-of-phase	1900	0	60	>3219	2950
LB-32	<111>	Baseball-ccw	1900	0	60	>11852	6343
KB-36	<011>	Elliptical-ccw	1900	0	60	>9743	4926
KB-93[e]	<011>	Out-of-phase	1900	0	60	2420	3490

Superscript e = Specimen was exposed 100 hours at 2000°F before testing.

Table 12

Relative Quality Loss Function Values for the
Nominal—Is—Best Quality Characteristic
Calculated for Each PWA 1480 TMF Life Model

Data Set	Base Model a)	Model b)	Model c)	Model d)
Correlation	(1.0)	1.20	1.20	1.13
Verification	1.0	0.92	1.11	(0.87)
All <001> data	(1.0)	1.58	1.57	1.52
All <111> data	1.0	(0.72)	0.98	0.96
All <011> data	1.0	0.90	1.11	(0.64)
All <213> data	1.0	1.09	1.09	(0.90)
All 1900°F data without hold times	(1.0)	1.09	1.15	1.12
All 2100°F data	1.0	0.92	1.18	(0.69)
All 1900°F data with hold times	1.0	1.17	1.12	(0.86)
All overlay coated	(1.0)	1.30	1.32	1.19
All aluminide coated	1.0	0.83	1.00	(0.81)
All data	1.0	1.05	1.15	(0.99)
Rank	2	3	4	1

Table 13

PWA 1480 TMF Life Model
Correlation Data Set

Notes: All ε-T cycles are out-of-phase
         All specimens oriented along the <001> direction

Spec ID	Tmax (°F)	Coating Type	Compression Hold Time (sec)	Cycle Period (sec)	Actual Life (cycles)	Correlated Life (cycles)
JB-147	1900	Overlay	0	60	850	1391
JB-121	1900	Overlay	30	90	1050	1472
JB-137	1900	Overlay	60	120	980	1850
JB-10	1900	Overlay	0	60	340-2500	2265
JB-9	1900	Overlay	0	60	500-1200	696
JB-80	1900	Overlay	0	60	300-800	480
JB-111	2100	Overlay	0	60	1800-3900	2622
JB-89	2100	Overlay	0	60	1100-1600	1420
JB-125	1900	Aluminide	300	360	600–2650	1369
JB-98	1900	Aluminide	0	60	3000–9400	1568
JB-66	1900	Aluminide	60	120	800–3000	789
JB-62	1900	Aluminide	300	360	<1210	476
JB-91	1900	Aluminide	0	60	840–2130	937
JB-22	1900	Aluminide	0	60	1100–2500	963
JB-59	1900	Aluminide	0	60	3300–5000	1824
JB-19	1900	Aluminide	0	60	200–560	378
JB-81	1900	Aluminide	0	60	160–440	299

Table 14

PWA 1480 TMF Life Model Verification Data Set

Spec ID	⟨hkl⟩	Coating Type	-T Cycle	Tmax (°F)	Compression Hold Time (sec)	Cycle Period (sec)	Actual Life (cycles)	Predicted Life (cycles)
JB-174	⟨001⟩	Overlay	Out-of-phase	1900	0	60	2350	4008
JB-135	⟨001⟩	Overlay	Airfoil L.E.	1900	60	300	790	1013
JB-104	⟨001⟩	Overlay	T-cycle	1900	0	120	2700	1526
JB-21	⟨001⟩	Overlay	Z-cycle	1900	0	120	560-670	411
JB-102	⟨001⟩	Overlay	Baseball-ccw	1900	0	60	>2170	2043
JB-146[e]	⟨001⟩	Overlay	Out-of-phase	1900	0	60	1600-2200	1400
JB-133[e]	⟨001⟩	Overlay	Out-of-phase	1900	0	60	910	1592
JB-61	⟨001⟩	Aluminide	Out-of-phase	1900	0	60	<3550	1286
JB-59	⟨001⟩	Aluminide	In-phase	1900	0	60	>15700	100000
JB-29	⟨001⟩	Aluminide	In-phase	1900	0	60	9100-91000	52320
JB-38	⟨001⟩	Aluminide	Z-cycle	1900	0	120	410-550	198
JB-72	⟨001⟩	Aluminide	Z-cycle	1900	0	120	300-820	237
JB-154[e]	⟨001⟩	Aluminide	Out-of-phase	1900	0	60	1000-2000	2667
JB-161[e]	⟨001⟩	Aluminide	Out-of-phase	1900	0	60	1700-2500	1473
JB-88	⟨001⟩	Aluminide	Out-of-phase	2100	0	60	<7000	2878
JB-82	⟨001⟩	Aluminide	Out-of-phase	2100	0	60	<780	279
LB-170	⟨111⟩	Overlay	Out-of-phase	1900	0	60	760	562
LB-181	⟨111⟩	Overlay	Out-of-phase	1900	0	60	1000	517
LB-27	⟨111⟩	Overlay	Out-of-phase	1900	0	60	530	725
LB-29	⟨111⟩	Overlay	Baseball-cw	1900	0	60	600-1200	1184
LB-26	⟨111⟩	Overlay	T-cycle	1900	0	120	>1000	476
LB-216	⟨111⟩	Overlay	Out-of-phase	2100	0	60	730	704
LB-239	⟨111⟩	Overlay	Out-of-phase	2100	0	60	640	562
LB-20	⟨111⟩	Aluminide	Out-of-phase	1900	0	60	800-1000	353
LB-189	⟨111⟩	Aluminide	Out-of-phase	2100	0	60	1000-3000	390
KB-32	⟨011⟩	Overlay	Out-of-phase	1900	0	60	2370	1624
KB-24	⟨011⟩	Overlay	Out-of-phase	1900	0	60	1100	916
KB-34	⟨011⟩	Overlay	Out-of-phase	1900	0	60	710	499
KB-48	⟨011⟩	Overlay	Out-of-phase	2100	0	60	940	2019
KB-52	⟨011⟩	Overlay	Out-of-phase	2100	0	60	850	1005
KB-93[e]	⟨011⟩	Overlay	Out-of-phase	1900	0	60	<520	641
KB-49	⟨011⟩	Aluminide	Out-of-phase	2100	0	60	220-760	624
KB-27	⟨011⟩	Aluminide	Out-of-phase	2100	0	60	230-1280	561
KB-92[e]	⟨011⟩	Aluminide	Out-of-phase	1900	0	60	<760	373
MB-17	⟨213⟩	Overlay	Out-of-phase	1900	0	60	1970	829
MB-23	⟨213⟩	Overlay	Out-of-phase	1900	0	60	2650	2572
MB-22	⟨213⟩	Overlay	Out-of-phase	1900	0	60	900-1700	857
MB-8	⟨213⟩	Overlay	Out-of-phase	1900	0	60	1570	1292
MB-19	⟨213⟩	Overlay	Out-of-phase	1900	0	60	1800-3500	3020
MB-62	⟨213⟩	Overlay	Out-of-phase	1900	0	60	1760	629
MB-27	⟨213⟩	Overlay	Out-of-phase	1900	300	360	930	568
MB-35	⟨213⟩	Overlay	Out-of-phase	2100	0	60	900	1042
MB-37	⟨213⟩	Overlay	Out-of-phase	2100	0	60	940	1162
MB-1	⟨213⟩	Aluminide	Out-of-phase	1900	0	60	<500	432
MB-16	⟨213⟩	Aluminide	Out-of-phase	2100	0	60	1400-2400	755
MB-24	⟨213⟩	Aluminide	Out-of-phase	2100	0	60	1140	1307

Superscript e = Specimen was exposed 100 hours at 2000°F before testing.

Table 15

Description of Airfoil Leading Edge Transient Flight Cycle

Point Number	Strain (in/in)	Temp (F)	Comment
A	-0.00041	930	Steady state ground idle
B	-0.00339	1966	End of takeoff
C	-0.00228	1779	End of climb
D	-0.00129	1535	End of cruise
E	-0.00047	818	Decent
F	-0.00077	929	Steady state ground idle
G	-0.00036	805	Shutdown (200 rpm)

Table 16

Summary of Alloy 185 Specimens

Specimen Design	Specimen Type	Orientation	Coating	Number
LED 41784	solid bar	<001>	none	4
		<111>	none	2
M26	solid bar	<001>	none	7
		<111>	none	5
73C	cylindrical tube	<001>	PWA 286	7
		<111>	PWA 286	3

C-3

Table 17

Summary of Uncoated Alloy 185 Tensile Tests

Test Strain Rate = 0.005 / min

Temp C(F)	Spec. ID	Orient	E x 10⁻³ MPa(KSI)	0.2% Yield MPa(KSI)	Ultimate MPa(KSI)	Elong. %	RA %
RT	HJA-5	<001>	139.3 (20.2)	757.8 (109.9)	1025.3 (148.7)	7.0	5.5
427 (800)	HJA-7	<001>	133.1 (19.3)	886.0 (128.5)	1057.7 (153.4)	6.3	4.7
760 (1400)	HJA-9	<001>	117.2 (17.0)	1008.0 (146.2)	1070.8 (155.3)	6.0	7.0
982 (1800)	HJB-3	<001>	90.8 (13.0)	711.8 (101.9)	714.6 (102.3)	18.0	18.2
1093 (2000)	HJB-17	<001>	71.9 (10.3)	440.8 (63.1)	458.9 (65.7)	29.3	36.5
427 (800)	HLB-29	<111>	266.1 (38.6)	950.1 (137.8)	1474.1 (213.8)	9.6	7.8
760 (1400)	HLB-33	<111>	246.1 (35.7)	852.9 (123.7)	1070.8 (155.3)	25.0	15.3
1093 (2000)	HLB-35	<111>	131.9 (19.1)	455.1 (66.0)	466.1 (67.6)	19.0	17.0

Table 18

Summary of Uncoated Alloy 185 Creep Tests

Temp C(F)	Spec. ID	Orient	Stress MPa (KSI)	Percent of 0.2% Yield	Life (hr)	Creep Rate (1/min)	Elong %	RA %
982 (1800)	HJA-1	<001>	193.1 (28.0)	27.5	165.1	9.23E-7	16.0	22.5
1093 (2000)	HJA-3	<001>	68.9 (10.0)	15.8	1080.2	2.24E-8	-	-
Uploaded @ 1080.2 hrs.			103.4 (15.0)	23.8	+131.8	5.07E-7	6.0	23.8
982 (1800)	HLA-10	<111>	248.2 (36.0)	NA	142.3	6.84E-7	9.3	11.6
1093 (2000)	HLB-27	<111>	172.4 (25.0)	37.9	64.2	1.35E-6	3.3	3.2

179

Table 19

PWA 1480 Monotonic Tensile Data

Temp °C(°F)	Spec ID	⟨hkl⟩	Modulus		0.2% Offset		UTS		EL %
			MPa	(Msi)	MPa	(Ksi)	MPa	(Ksi)	
	JB49	001	123.4	(17.9)	1013.0	(146.9)	**	**	**
21	JJB17	001	123.4	(17.9)	1011.7	(146.7)	1219.3	(176.8)	7.2
(70)	JJB28	001	130.3	(18.9)	993.1	(144.0)	1090.3	(158.1)	8.2
	JJB21	001	128.3	(18.6)	1024.1	(148.5)	1195.2	(173.3)	5.6
	JKB5B	011	220.0	(31.9)	980.7	(142.2)	1033.8	(149.9)	13.0
	KB20	011	217.9	(31.6)	958.4	(139.0)	***	***	***
427	JA16*	001	113.8	(16.5)	989.4	(143.5)	1118.4	(162.2)	5.7
(800)	KA2*	011	221.3	(32.1)	921.9	(133.7)	957.0	(138.8)	14.3
	LA36*	111	239.3	(34.7)	897.0	(130.1)	1393.5	(202.1)	11.7
	JLB18A	111	300.7	(43.6)	844.8	(122.5)	1395.9	(202.4)	13.5
	MA1*	123	198.6	(28.8)	837.7	(121.5)	1218.3	(176.7)	19.1
	JMB2A	123	210.3	(30.5)	799.3	(115.9)	932.4	(135.2)	5.3
649	KA3*	011	176.5	(25.6)	929.4	(134.8)	1081.1	(156.8)	4.7
(1200)	LA51*	111	253.7	(36.8)	849.5	(123.2)	1245.2	(180.6)	23.7
	JLB14B	111	293.8	(42.6)	944.8	(137.0)	1175.2	(170.4)	4.2
	MA3*	123	193.7	(28.1)	824.0	(119.5)	1082.5	(157.0)	22.7
	JMB2B	123	193.8	(28.1)	793.1	(115.0)	1023.4	(148.4)	7.4
	JMB4B	123	189.0	(27.4)	773.1	(112.1)	944.8	(137.0)	8.8
760	JA34*	001	101.4	(14.7)	1177.0	(170.7)	1324.5	(192.1)	14.1
(1400)	JJB22	001	100.7	(14.6)	1186.9	(172.1)	1271.7	(184.4)	12.8
	KA4*	011	174.4	(25.3)	948.1	(137.5)	1108.7	(160.8)	10.5
	LA52*	111	200.0	(29.0)	879.8	(127.6)	1093.5	(158.6)	22.1
	MA4*	123	180.0	(26.1)	891.5	(129.3)	985.3	(142.9)	17.8
871	JA36*	001	102.0	(14.8)	715.0	(103.7)	1021.1	(148.1)	13.7
(1600)	KA6*	011	149.6	(21.7)	786.0	(114.0)	910.1	(132.0)	13.1
	LA53*	111	190.3	(27.6)	696.4	(101.0)	819.8	(118.9)	19.1
	MA5*	123	179.3	(26.0)	626.1	(90.8)	764.7	(110.9)	18.0
	JMB4A	123	183.4	(26.6)	842.8	(122.2)	884.8	(128.3)	9.4
982	JA37*	001	88.3	(12.8)	452.3	(65.6)	695.0	(100.8)	23.0
(1800)	KA8*	011	133.1	(19.3)	519.9	(75.4)	628.8	(91.2)	16.7
	LA54*	111	189.6	(27.5)	427.5	(62.0)	557.8	(80.9)	22.2
	MA6*	123	164.8	(23.9)	431.6	(62.6)	539.9	(78.3)	25.9
1093	JA38*	001	72.4	(10.5)	275.1	(39.9)	371.6	(53.9)	30.0
(2000)	KA9*	011	91.7	(13.3)	315.8	(45.8)	385.4	(55.9)	18.7
	LA55*	111	132.4	(19.2)	259.9	(37.7)	328.9	(47.7)	41.7
	MA9*	123	125.5	(18.2)	273.0	(39.6)	319.2	(46.3)	24.9

* Tests conducted at a strain rate of 0.0083 %/sec. All other
tests were conducted at a strain rate of 0.1000 %/sec.
** Tube specimen. Interrupted tensile test @ 1.37%
*** Tube specimen. Interrupted tensile test @ 0.67%

Table 20

BEST3D Elastic Analysis Results for Notched Specimens

Specimen Type	Material and Orientation	Location in Notch (degrees)	Stress Concentration Kt	
Thin Sharp Notch	Isotropic	0.	2.59	
(TM3387)	Single Crystal <001><100>	0. 15.	2.14 2.26	
Thin Mild Notch	Isotropic	0.	2.00	
(TM3487)	Single Crystal <001><100>	0. 30.	1.64 1.73	
Thick Mild Notch	Isotropic	0.	2.06	
(LED3587)	Single Crystal <001><100>	0. 30.	1.74 } 1.79 }	mid plane
		0. 30.	1.50 } 1.58 }	lateral surface

Notes: 1. Angular location in the notch measured from the minimum section
2. Kt = principal stress / net section stress

181

Table 21

Summary of Secondary Orientation At the Crack Initiation Site

Spec No.	Temp (°F)	Strain Range (in/in)	Stress Range (Ksi)	Life (cycles)	Initiation Site (degress from <010>)	
JJB49	1200	0.015	235	1326	5	
JJB45	1200	0.017	227	1593	5	
JJB50	1200	0.012	199	5673	6	
JJB43	1200	0.011	184	4414	25	
JJB41	1400	0.011	169	4912	10	
JJB46	1600	0.012	148	5431	40	
JJB74	1200	0.018	287	1471	9	HIP'd
JJB75B	1200	0.015	248	2964	30	HIP'd
JJB79	1200	0.012	200	20051	42	HIP'd
JJB80	1200	0.011	180	32448	2	HIP'd
JJB78	1600	0.012	160	12413	7	HIP'd

Table 22

Summary of Secondary Orientation At the Crack Initiation Site

Spec No.	Temp (°F)	Strain Range (in/in)	Stress Range (Ksi)	Life (cycles)	Initiation Site Degrees from <011>	<112>	
JLB58	1200	0.008	276.9	1016	11		
JLB66	1200	0.006	231.1	7356		3	
JLB59	1200	0.006	224.4	7904		10	
JLB61	1200	0.006	238.1	7101	3		
JLB64	1600	0.006	196.3	3354	15	15	
JLB25A	1200	0.006	238.5	27410		5	HIP'd
JLB26B	1600	0.006	206.0	4269		0	HIP'd

TABLE 23

Actual and Calculated Fatigue Lives
1200°F, PWA 1480 Smooth Specimens

Spec	Stress Range (PSI)	Mean Stress (PSI)	Plastic Strain Range (IN/IN)	Actual Life (Cycles)	Calculated Life (Cycles)
<001> Specimens					
JJB49	234500.	40750.	0.00025	1326.	2000.
JJB43	184000.	57000.	0.00000	4414.	9300.
JJB50	198800.	60100.	0.00000	5673.	5000.
JJB45	226500.	52250.	0.00020	1593.	2100.
JJB101	161500.	72250.	0.00000	29516.	18000.
JJB109	114000.	57200.	0.00000	365072.+	310000.
JJB170	106400.	58800.	0.00000	212570.	500000.
<111> Specimens					
JLB58	276900.	−350.	0.00140	1016.	970.
JLB56	224000.	8000.	0.00010	3410.	5800.
JLB66	231100.	10550.	0.00010	7356.	4300.
JLB57	298600.	−1000.	0.00080	843.	680.
JLB59	224400.	20700.	0.00000	7904.	4500.
JLB60	340400.	1500.	0.01020	26.	14.
JLB61	238100.	650.	0.00000	7101.	4400.
<213> Specimens					
JMB29	271200.	−5000.	0.00270	79.	830.
JMB41	243300.	1250.	0.00000	4175.	3700.
JMB35	162500.	32450.	0.00000	114789.	38000.
JMB32	179200.	28100.	0.00000	45640.+	20000.
JMB36	139300.	63150.	0.00000	34676.	63000.
<011>					
JJB112	217900.	18150.	0.00000	7532.	5900.

Table 23 (Continued)

Spec	Stress Range (PSI)	Mean Stress (PSI)	Plastic Strain Range (IN/IN)	Actual Life (Cycles)	Calculated Life (Cycles)
JKB21	246300.	-3950.	0.00000	2672.	3800.
JKB24	182600.	31100.	0.00000	30220.	17000.
<001> Specimens, HIP PWA 1480					
JJB74	287400.	43100.	0.00054	1471.	400.
JJB75B	248000.	56000.	0.00016	2964.	1000.
JJB79	199700.	67950.	0.00000	20051.	4100.
JJB80	179900.	70250.	0.00000	32448.	8400.
<111> Specimens, HIP PWA 1480					
JLB25B	289700.	650.	0.00126	1166.	710.
JLB25A	238500.	17950.	0.00000	27410.	3100.
JLB26A	195800.	27200.	0.00000	325570.	11000.
<011> Specimens, HIP PWA 1480					
JKB13A	238600.	7100.	0.00000	1806.	3800.
JKB13B	241600.	10300.	0.00000	737.	3200.

Note: "+" indicates testing was stopped prior to failure.

Table 24

Distribution of Manufacturing Lots

SPECIMEN ORIENTATION	LOT 7590 THIN MILD	LOT 7590 THIN SHARP	LOT 7590 THICK MILD	LOT 3168 THIN MILD	LOT 3168 THIN SHARP	LOT 3168 THICK MILD	LOT 1160 THIN MILD	LOT 1160 THIN SHARP	LOT 1160 THICK MILD	LOT 1535 THIN MILD	LOT 1535 THIN SHARP	LOT 1535 THICK MILD	LOT 900 THIN MILD	LOT 900 THIN SHARP	LOT 900 THICK MILD
NO-HIP															
<001><100>	X	X	X				X	X	X		X	X			
<001><21̄0>				X	X	X									
<011><01̄1̄>											X				
<111><01̄1̄>				X	X	X					X				
HIP															
<001><100>													X	X	X
<001><210>													X		X
<111><01̄1̄>											X				

184

Table 25

Stress and Strain Concentration Factors and Local Crystal Orientations
Used In the Neuber Calculation

Specimen		Stress and Strain Normalized to a Reference Nominal Stress		Crystal Direction at Maximum Stress Location	Uniaxial Test Orientation Used In Neuber Calculation
Type	Orientation	Stress (Dimensionless)	Strain $(Psi)^{-1}$		
Thin, Mild Notch	<001><100>	1.82	7.49E–8	24 Degrees From <001>	<001>
	<001><210>	1.79	7.30E–8	24 Degrees From <001>	<001>
	<111><01$\bar{1}$>	2.46	5.24E–8	<111>	<111>
	<011><01$\bar{1}$>	2.58	7.41E–8	<011>	<011>
Thin, Sharp Notch	<001><100>	2.48	11.60E–8	<001>	<001>
	<111><01$\bar{1}$>	2.95	6.17E–8	<111>	<111>
Thick, Mild Notch	<001><100>	2.08	7.41E–8	24 Degrees From <001>	<001>
	<111><01$\bar{1}$>	2.54	5.36E–8	<111>	<111>

Table 26

Actual and Calculated Notched Specimen Fatigue Lives
1200°F Data

Specimen	Stress Range (PSI)	Mean Stress (PSI)	Actual Life (Cycles)	Calculated Life (Cycles)
<001><100> Thin, Mild Notched Specimen				
JJB105A	242060.	81649.	30.	6700.
JJB125A	216125.	76113.	14340.	17000.
JJB108A	216125.	76113.	23740.	17000.
JJB106A	216125.	76113.	22940.	17000.
JJB125B	216125.	76113.	54470.	17000.
JJB106B	170625.	98863.	93850.	59000.
JJB128B	136500.	115925.	535200.	210000.
JJB121A	207480.	74176.	18880.	23000.
JJB121B	209664.	73084.	14260.	22000.
JJB26B	198835.	72716.	2860.	33000.
JJB18A	198835.	72716.	17227.	33000.
JJB127B	198835.	72716.	10010.	33000.
JB30A	104650.	119809.	1122917.	1300000.
JB30B	164255.	67139.	62119.	140000.
JB18B	164255.	67139.	84626.	140000.
JJB127A	164255.	67139.	198930.	140000.
<001><210> Thin, Mild Notched Specimen				
JJB48A	195557.	71609.	3434.	37000.
JJB48B	161547.	65223.	16427.	170000.
JJB56B	161547.	65223.	85040.	170000.
JJB52A	161547.	65223.	43090.	170000.
<111><01-1> Thin, Mild Notched Specimen				
JLB79B	233700.	27501.	157320.	25000.
JLB67B	233700.	27501.	333380.	25000.
JLB72B	233700.	27501.	18490.	25000.

Table 26 (Continued)

Specimen	Stress Range (PSI)	Mean Stress (PSI)	Actual Life (Cycles)	Calculated Life (Cycles)
JLB69B	233700.	27501.	4178.	25000.
JLB69A	198645.	39836.	97870.	62000.
JLB71A	198645.	39836.	347360.	62000.
JLB71B	198645.	39836.	413050.	62000.
JLB67A	198645.	39836.	1000000.+	62000.
JLB79A	198645.	39836.	1166580.+	62000.

<011><01-1> Thin, Mild Notched Specimen

JKB25A	232845.	35906.	13220.	21000.
JKB26A	232845.	35906.	23040.	21000.
JKB25B	232845.	35906.	18370.	21000.

<001><100> Thin, Sharp Notched Specimen

JJB137A	235600.	91925.	53030.	6600.
JJB122A	235600.	91925.	6940.	6600.
830-4B	235600.	91925.	4190.	6600.
JJB4B	235600.	91925.	6157.	6600.
789-3B	207328.	84309.	16015.	19000.
789-4B	207328.	84309.	117596.	19000.
JJB4A	176700.	77054.	1070000.+	70000.

<111><01-1> Thin, Sharp Notched Specimen

JLB73A	232608.	27525.	5286.	25000.
JLB73B	204583.	37415.	5154.	53000.
JLB74A	204583.	37415.	6888.	53000.
JLB74B	159743.	54470.	1250000.+	220000.

<001><100> Thick, Mild Notched Specimen

789-2	227240.	67050.	12048.	14000.
830-2	192265.	63749.	8253.	49000.
830-3	192265.	63749.	17232.	49000.

Table 26 (Continued)

Specimen	Stress Range (PSI)	Mean Stress (PSI)	Actual Life (Cycles)	Calculated Life (Cycles)
JJB130	211432.	65010.	10730.	24000.
JJB132	160056.	55361.	76210.	220000.
JJB133	160056.	55361.	500450.	220000.

<111><01-1> Thick, Mild Notched Specimen

JLB75	227305.	29500.	6343.	29000.
JLB76	191833.	42245.	20918.	76000.
JLB78	191833.	42245.	396570.	76000.
JLB77	159258.	54736.	1044340.+	230000.

<001><100> Single Tooth Firtree Specimen

JJB180A	162192.	61300.	27354.	180000.

<001><100> Thin, Mild Notched Specimen,   HIP

JJB86A	242060.	81649.	170.	6700.
JJB88A	224770.	78247.	33770.	12000.
JJB84B	207480.	74176.	94400.	23000.
JJB82A	198835.	72716.	413610.	33000.
JJB82B	198835.	72716.	327143.	33000.
JJB84A	164255.	67139.	1060620.+	140000.

<001><210> Thin, Mild Notched Specimen,   HIP

JJB93A	195557.	71609.	87030.	37000.
JJB104	161547.	65223.	1334290.+	170000.

<001><100> Thin, Sharp Notched Specimen,   HIP

JJB96B	282720.	101409.	19550.	1500.
JJB95A	282720.	101409.	48190.	1500.
JJB96A	282720.	101409.	142330.	1500.

<111><01-1> Thin, Sharp Notched Specimen,   HIP

JLB81A	302670.	11234.	52190.	5300.
JLB80B	260633.	19749.	73040.+	13000.
JLB80A	232608.	27525.	612930.+	25000.

NOTE: "+" Indicates testing was stopped prior to failure.
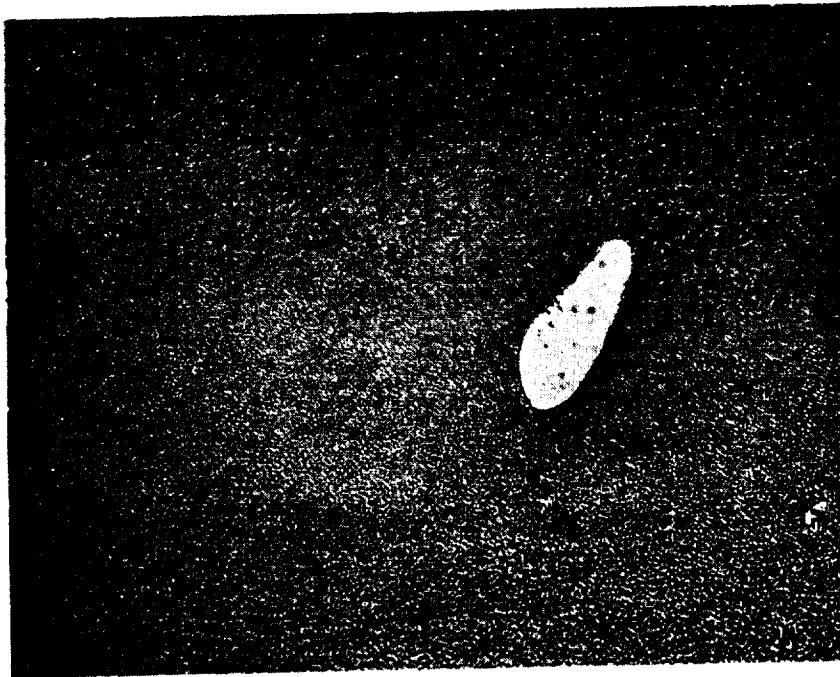
A
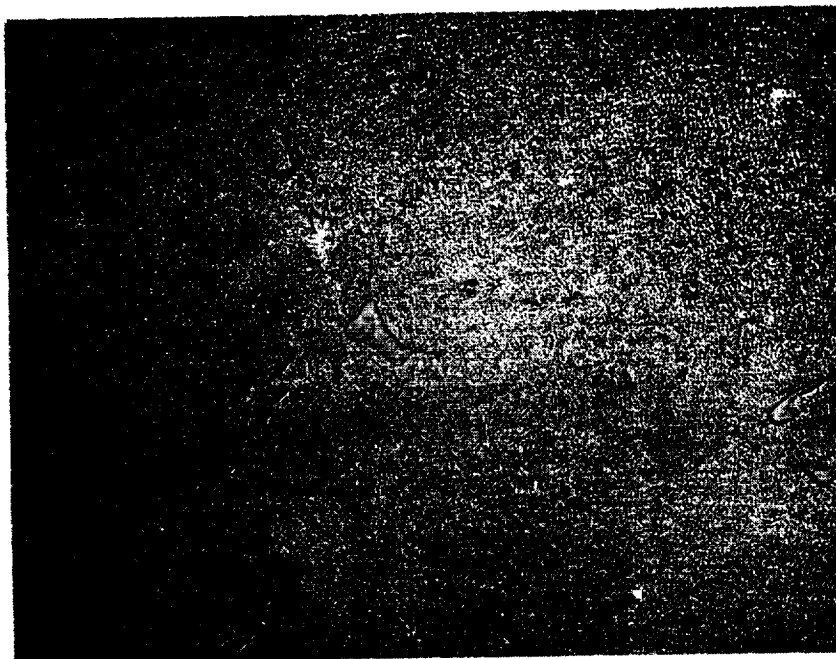
B

Figure 1   *Typical Solution Heat Treated Microstructure Illustrating Gamma/Gamma Prime Eutectic Islands in Gamma Matrix With Fine Unresolved Gamma Prime Precipitates of: A) PWA 1480, and B) Alloy 185. (500X Mag., Etchant: Mixed Acids)*
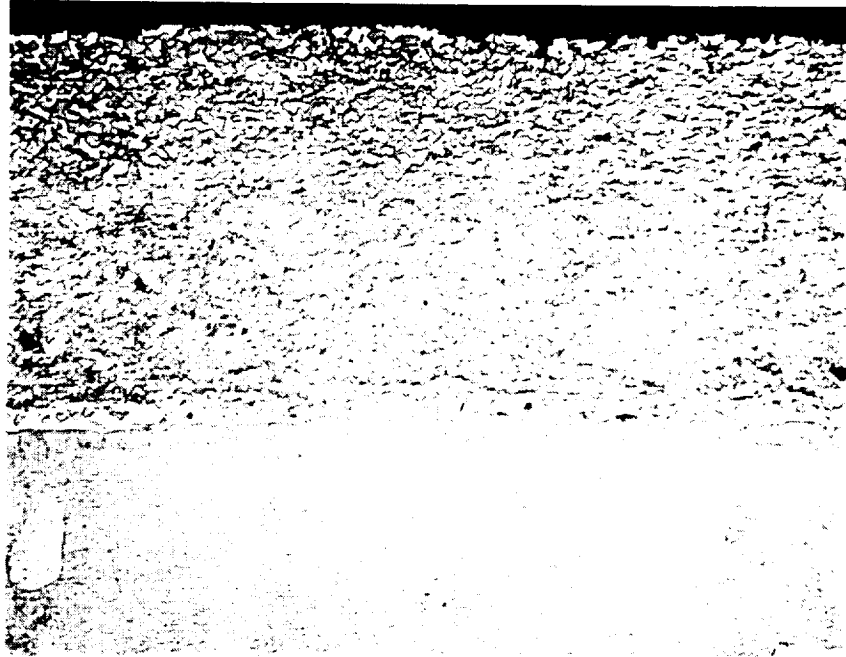
(A)
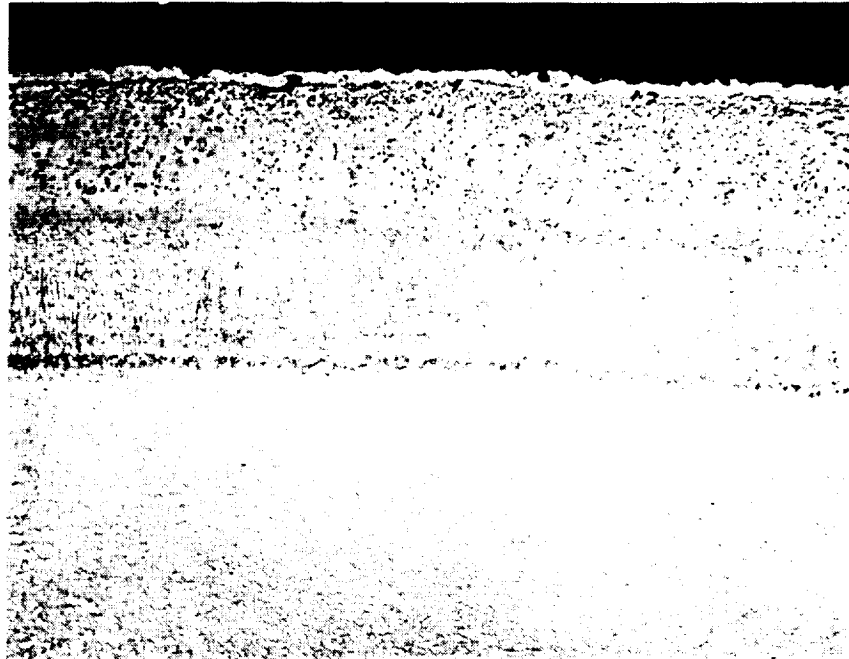
(B)

Figure 2   *Typical Micrographs of: (A) PWA 286 Overlay Coating, and (B) PWA 273 Diffusion Coating Illustrating the Microstructural Differences Between the Coatings. Note the small interdiffusion zone associated with the overlay coating compared to that of the diffusion coating. The substrate is PWA 1480. (500X Mag., Etchant: Mixed Acids)*

A) TENSILE, RELAXATION, AND STRESS-RUPTURE SPECIMEN FABRICATED FROM HOT ISOSTATICALLY PRESSED POWDER

8.33 cm
(3.28 in)

3.56 cm
(1.40 in)

0.95 cm
(0.375 in)

0.91 cm
(0.357 in)

0.45 cm
(0.178 in)
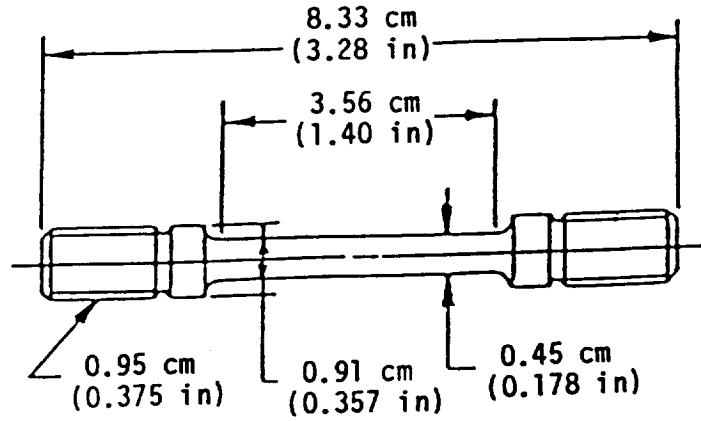
B) TENSILE, RELAXATION, AND STRESS-RUPTURE SPECIMEN FABRICATED FROM PLASMA SPRAYED SHEETS

10.16 cm
(4.00 in)

3.81 cm
(1.50 in)

0.48 cm
(0.19 in)

1.84 cm
(0.725 in)

2.54 cm
(1.00 in)
GAGE LENGTH

0.63 cm
(0.25 in)
DIA.

0.10 cm
(0.04 in)
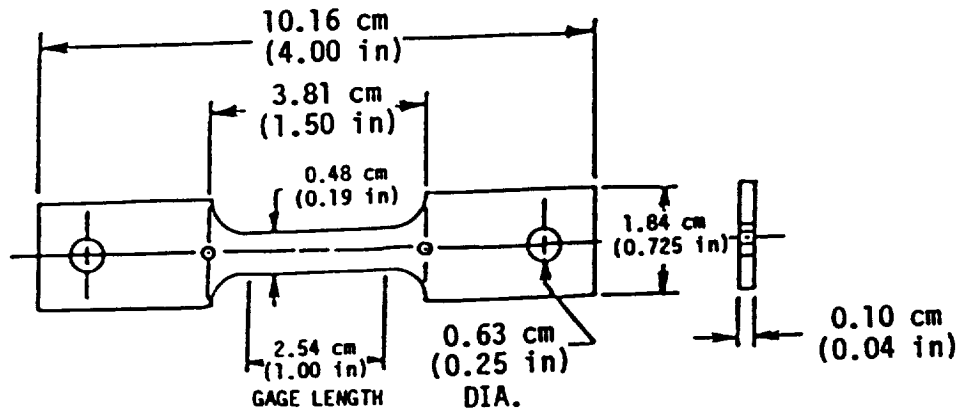
Figure 3   *Specimen Designs for Bulk PWA 286 Coating Material Mechanical Property Tests*

191
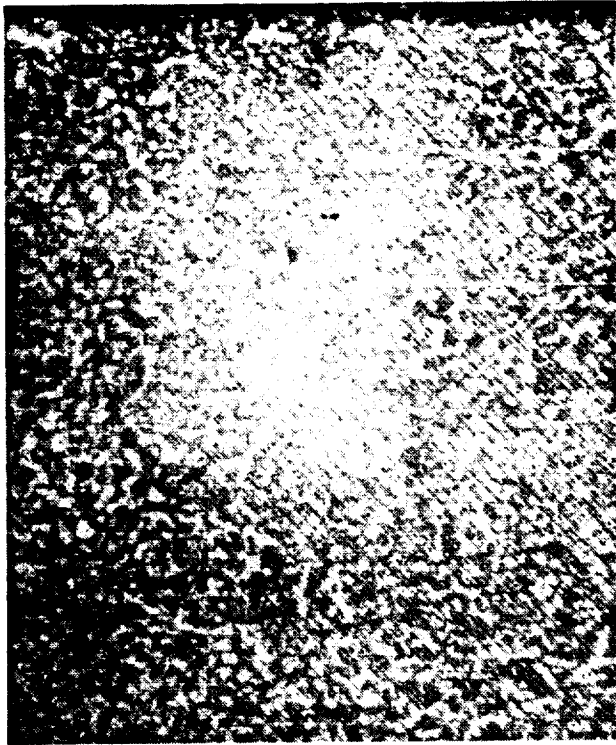
(A)
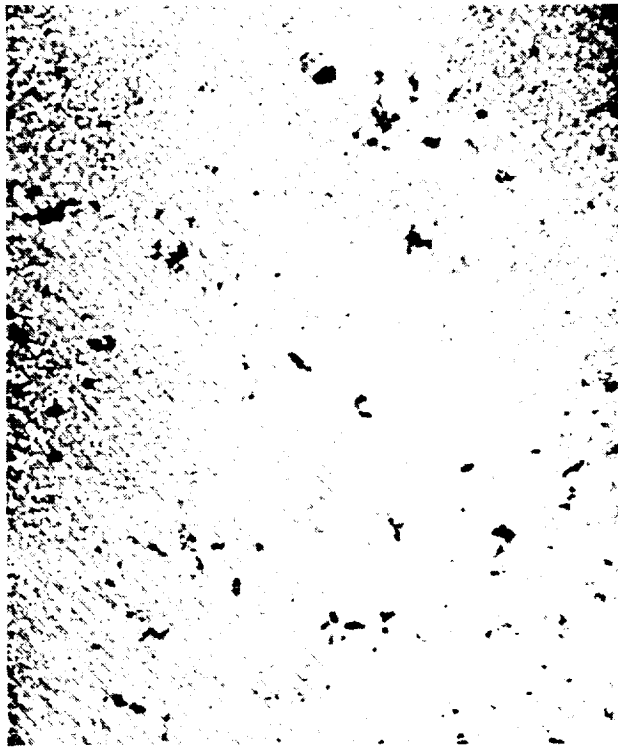
(B)

Figure 4   *PWA 286 Bulk Specimen Microstructure: A) Hot Isostatic Pressed and B) Plasma Sprayed*

UNCOATED DIMENSIONS ~ CM (IN)

(001)

(100)

PWA 1480
ORIENTATION
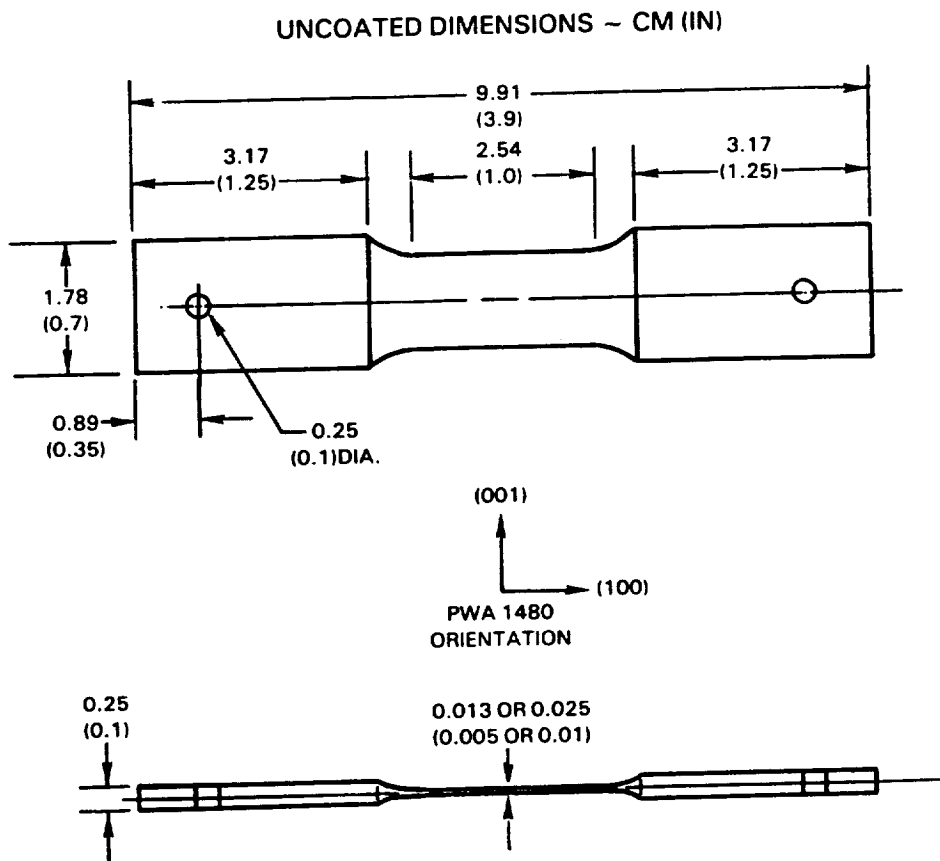
Figure 5   *Substrate Design for Diffused Aluminide Coating Mechanical Property Tests*
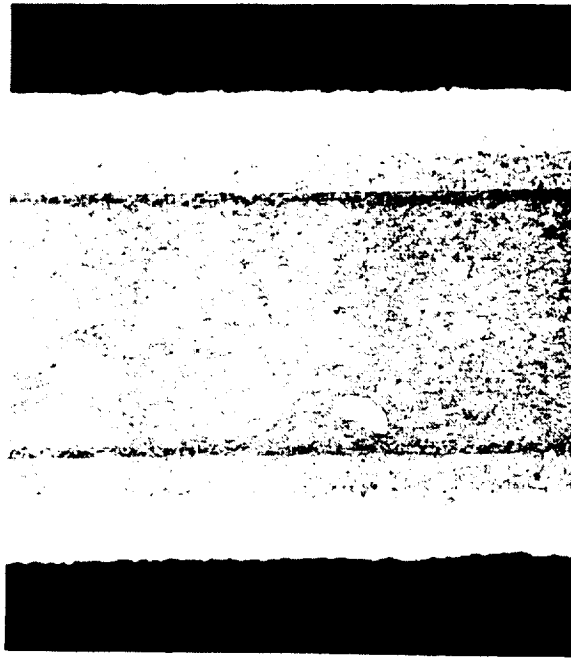
(A)
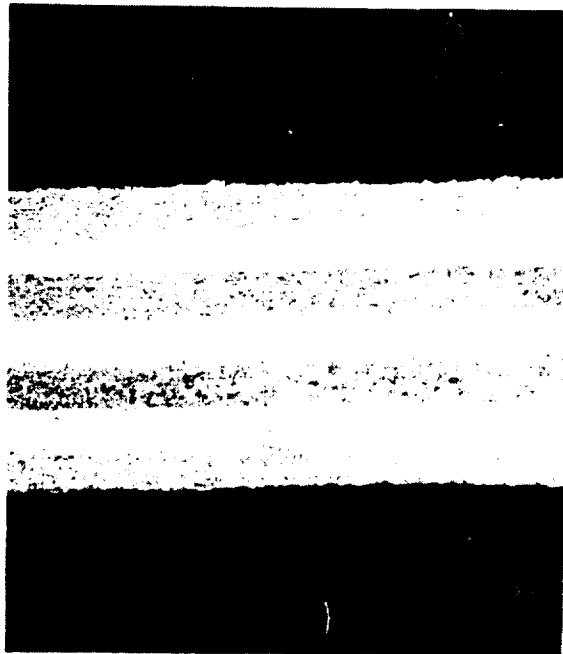
(B)

Figure 6   *Microstructure of PWA 273 Coated Difference Method Specimens with (A) 0.25 mm (0.010 in.) and (B) 0.13 mm (0.005 in.) Original PWA 1480 Substrates. The center bands represent the remaining substrate after coating. (250X Mag., Etchant: Mixed Acids)*

194

A) TENSILE AND CREEP TEST SPECIMEN

10.65 cm
(4.192 in)

3.80 cm
(1.495 in)

1.27 cm
(0.50 in)

0.64 cm
(0.252 in)

B) CYCLIC CONSTITUTIVE TEST SPECIMEN

8.89 cm
(3.50 in)

6.35 cm
(2.50 in)

2.79 cm
(1.10 in)

1.02 cm
(0.40 in)

0.76 cm
(0.30 in)

1.27 cm
(0.50 in)
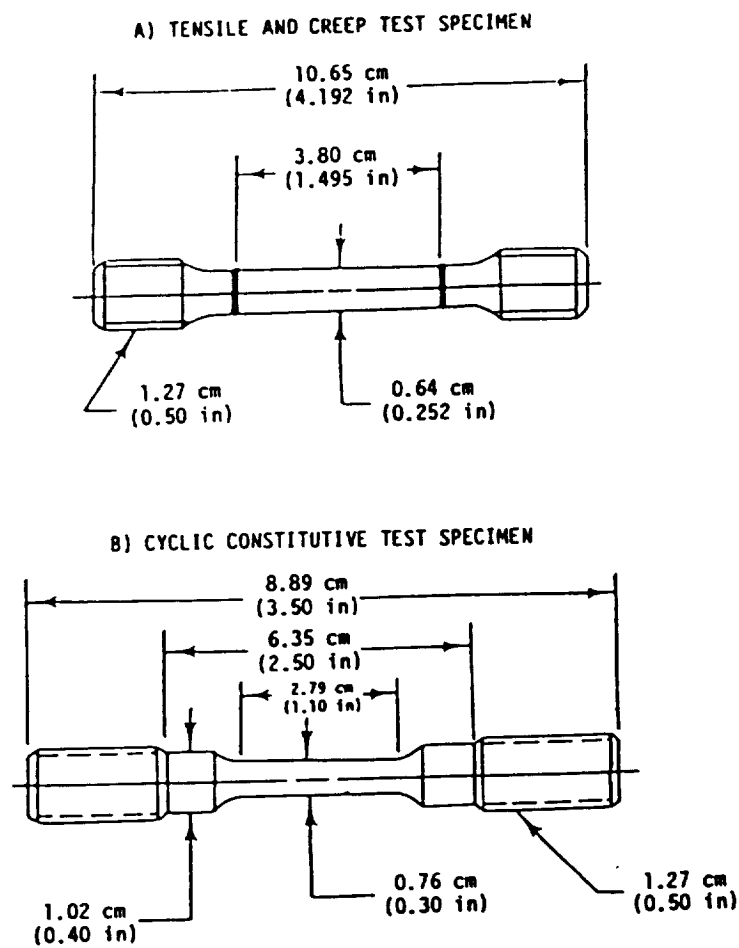
Figure 7   *Specimen Designs for Single Crystal PWA 1480 Mechanical Property Tests*

195

(A) OLD FATIGUE SPECIMEN DESIGN — TYPE 44C
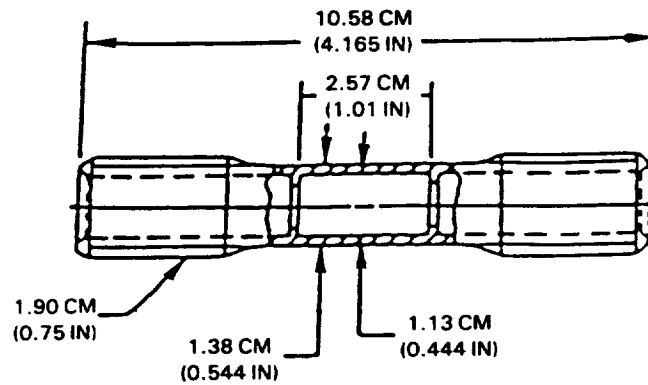
(B) NEW FATIGUE SPECIMEN DESIGN — TYPE 73C
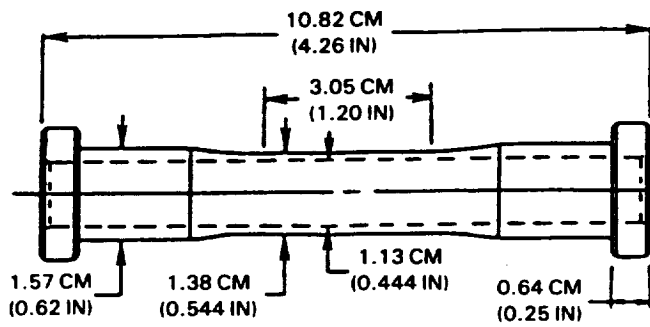
Figure 8   Geometries of Uniaxial Tubular Specimens for Fatigue Testing
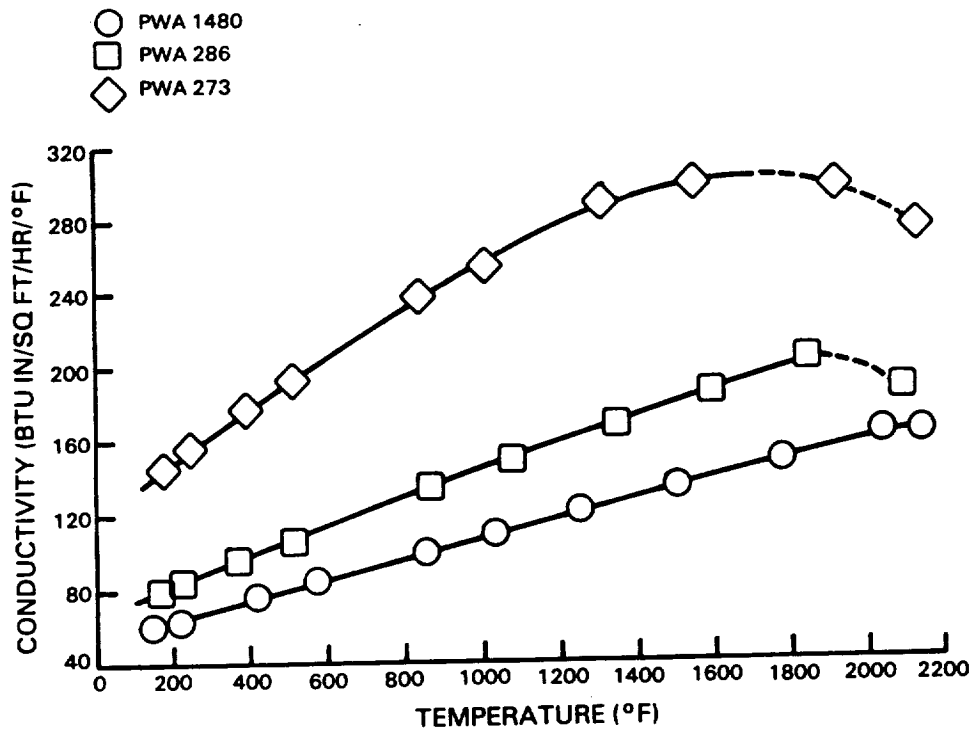
Figure 9   Measured Thermal Conductivity of PWA 273, PWA 286 and PWA 1480
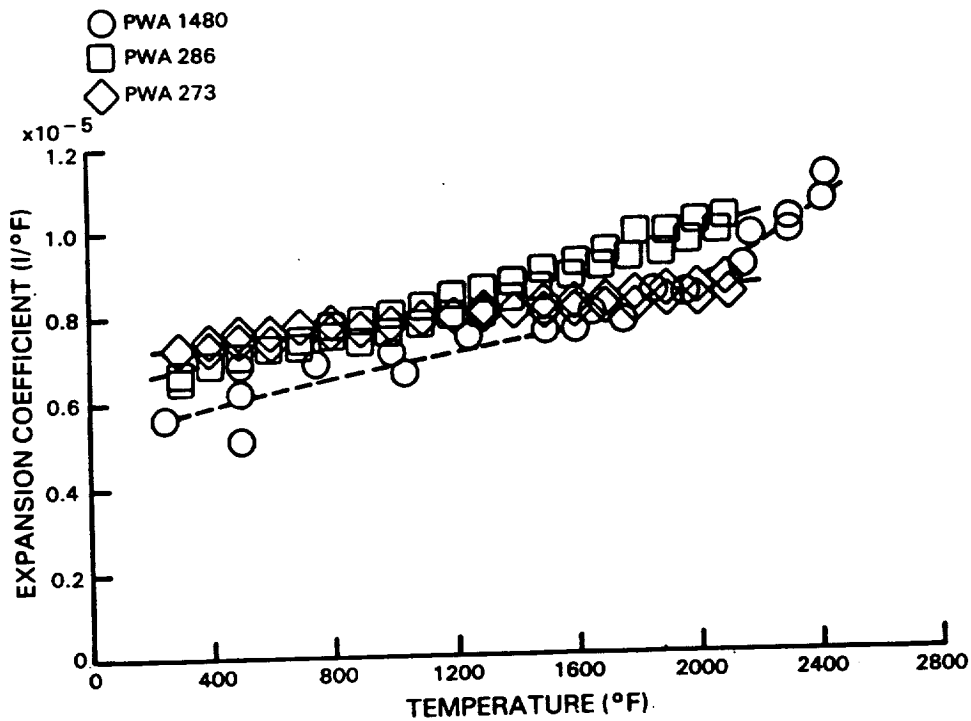
Figure 10   Mean Coefficient of Linear Thermal Expansion for PWA 273, PWA 286 and PWA 1480

197
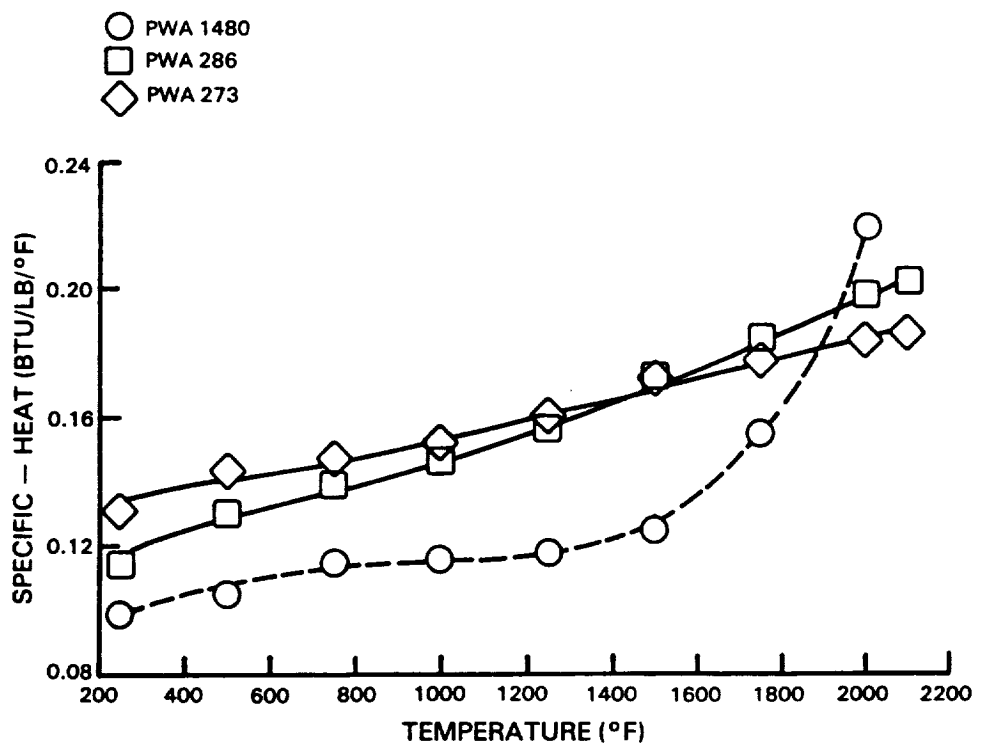
Figure 11   *Measured Specific Heat of PWA 273, PWA 286 and PWA 1480*
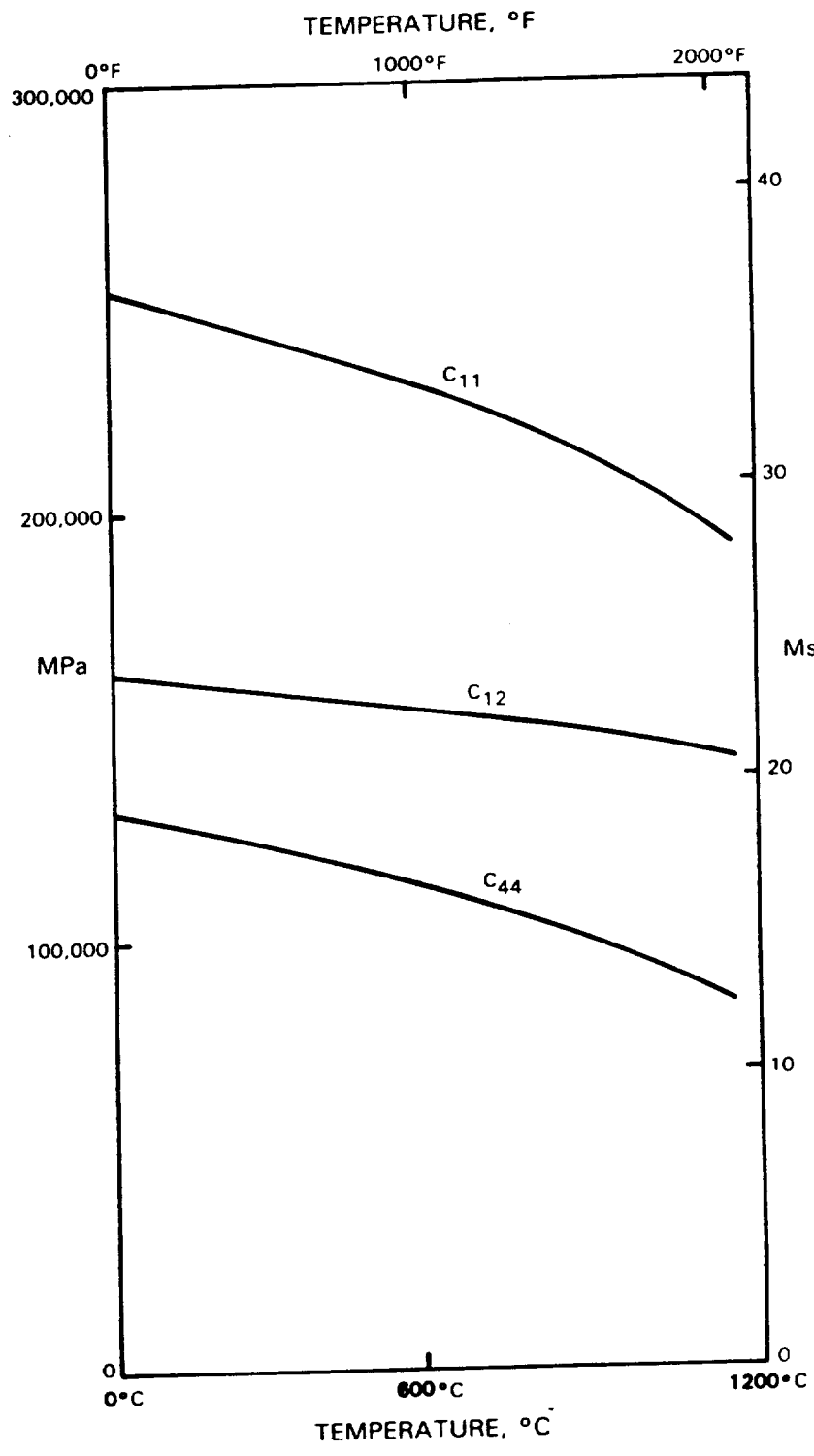
Figure 12   *PWA 1480 Dynamic Stiffnesses Vs. Temperature*

<001>

TENSILE DIRECTION

α

<010>

β

<100>
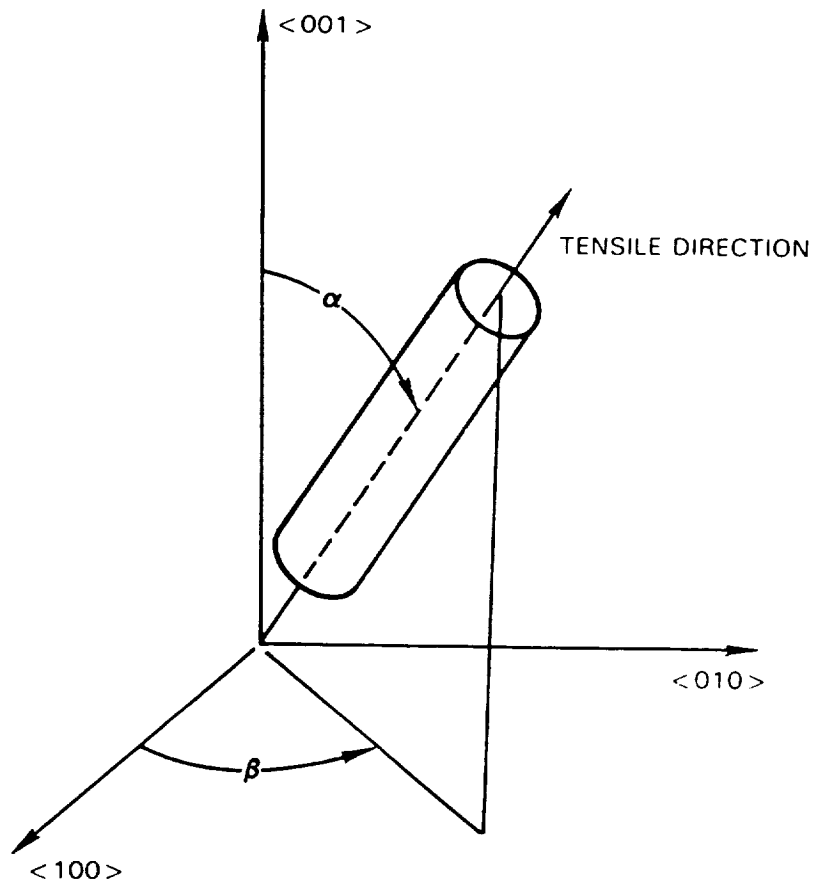
ANGLES α AND β DEFINE THE TENSILE DIRECTION

Figure 13   *Definition of PWA 1480 Orientation Angles* α *and* β

<111> APPARENT MODULUS

DYNAMIC

STATIC MODULUS
▲ 0.1%/SEC
△ 0.008%/SEC

MPa

Msi

TEMPERATURE
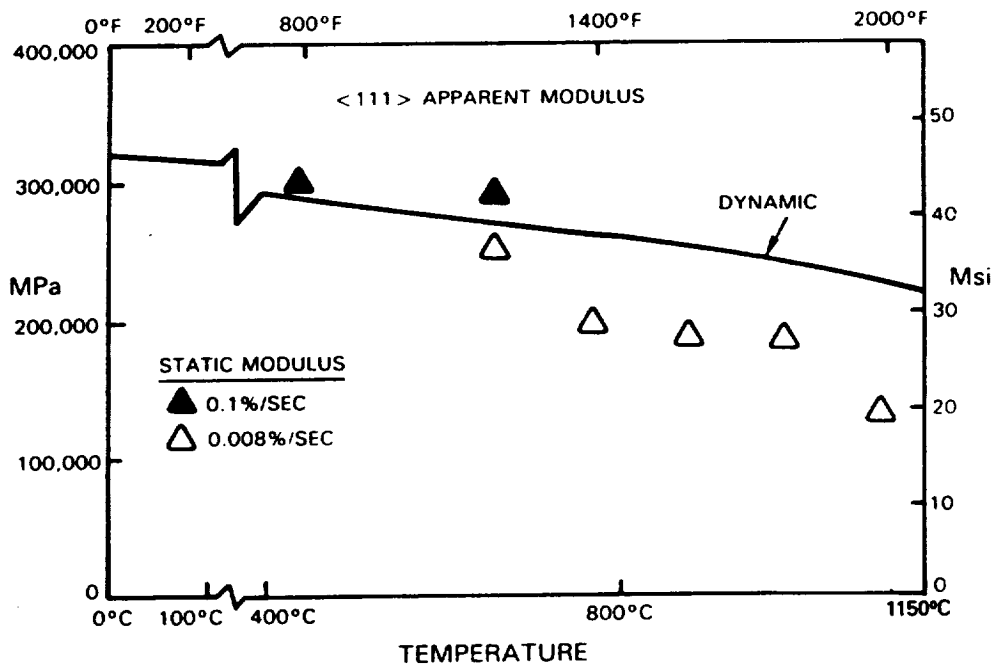
Figure 14   *Comparison of <111> PWA 1480 Static and Dynamic Moduli*

200
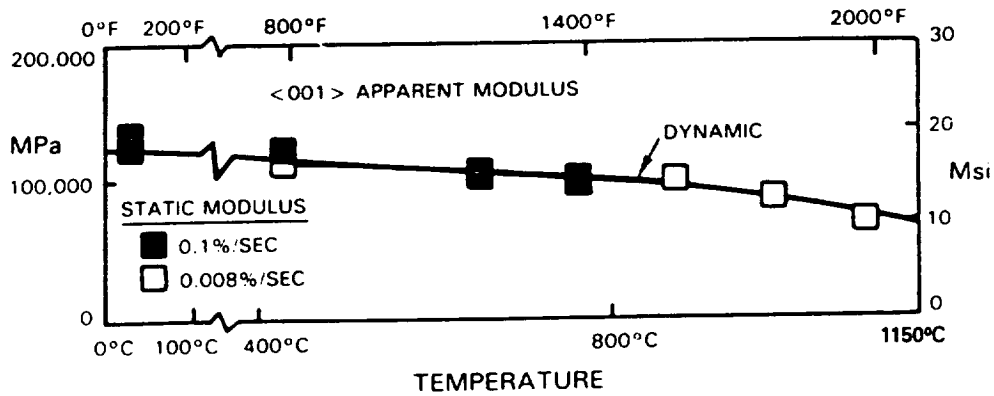
Figure 15   *Comparison of <001> PWA 1480 Static and Dynamic Moduli*
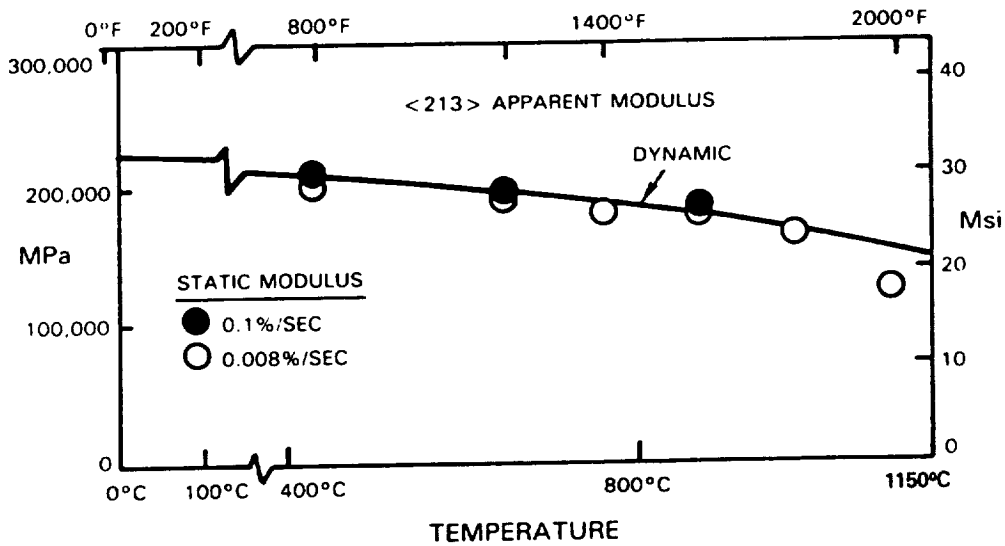
Figure 16   *Comparison of <213> PWA 1480 Static and Dynamic Moduli*
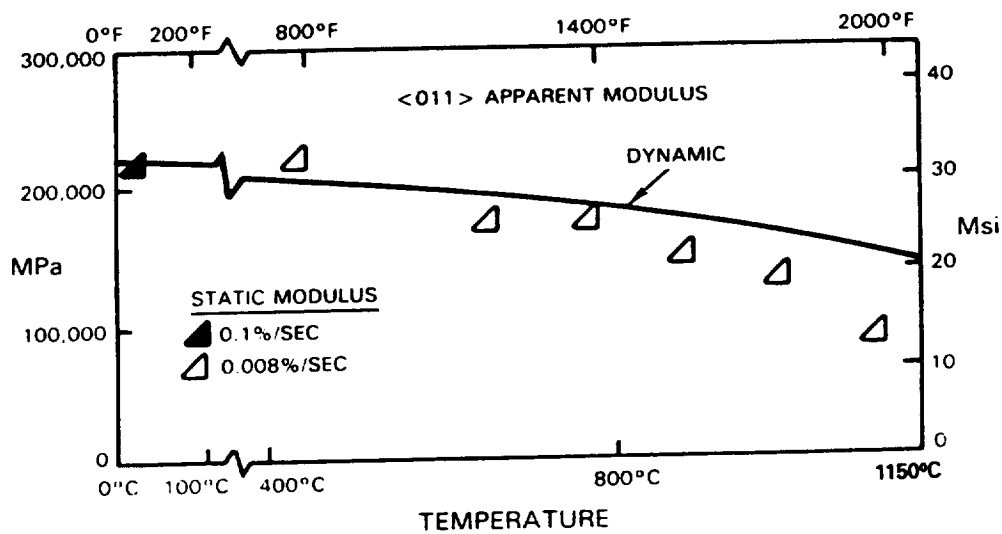
Figure 17   *Comparison of <011> PWA 1480 Static and Dynamic Moduli*

201

760°C (1400°F)   871°C (1600°F)
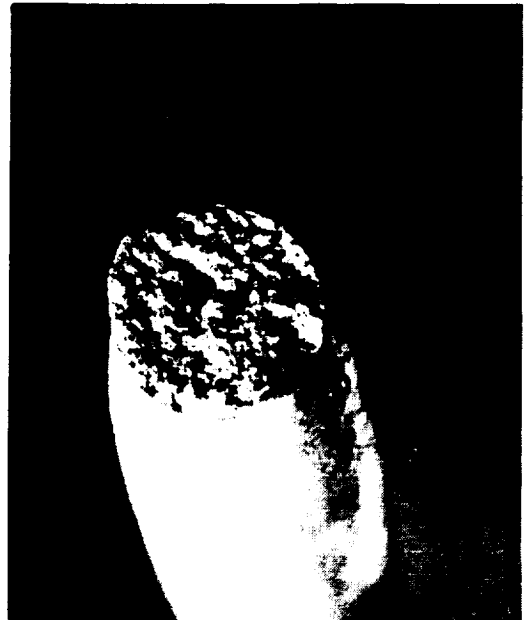
982°C (1800°F)   1093°C (2000°F)

Figure 18   *Fracture Surfaces of < 001 > PWA 1480 Tensile Specimens. Note the pronounced facet-*
ing at 760°C (1400°F) is reduced with increased temperature.

202
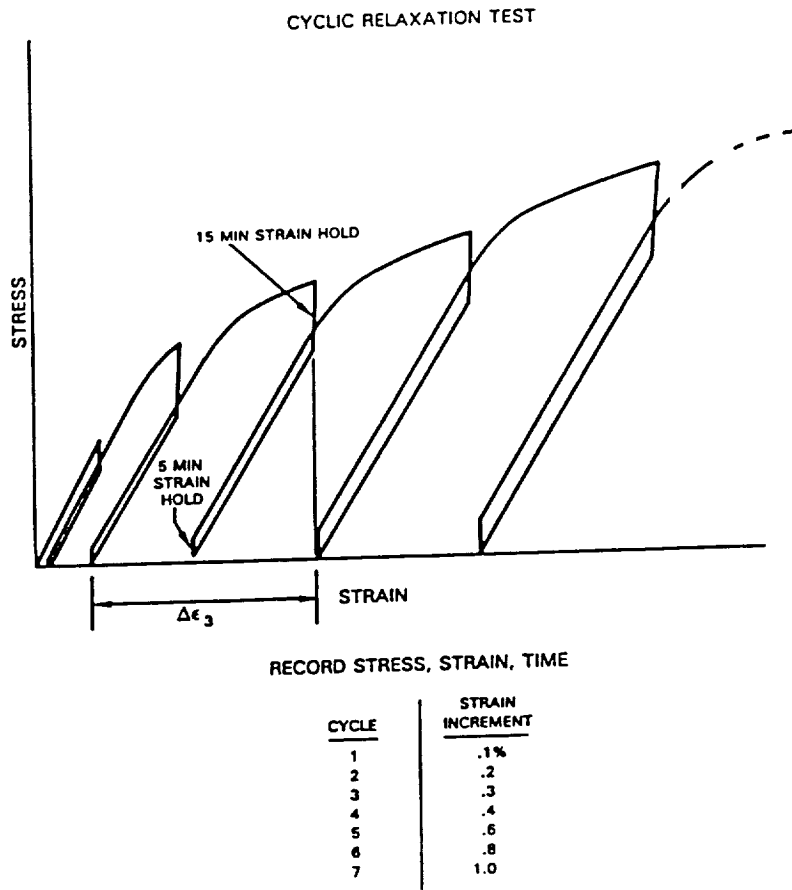
Figure 19   Representative Stress Relaxation Test Used to Obtain Coating Behavior
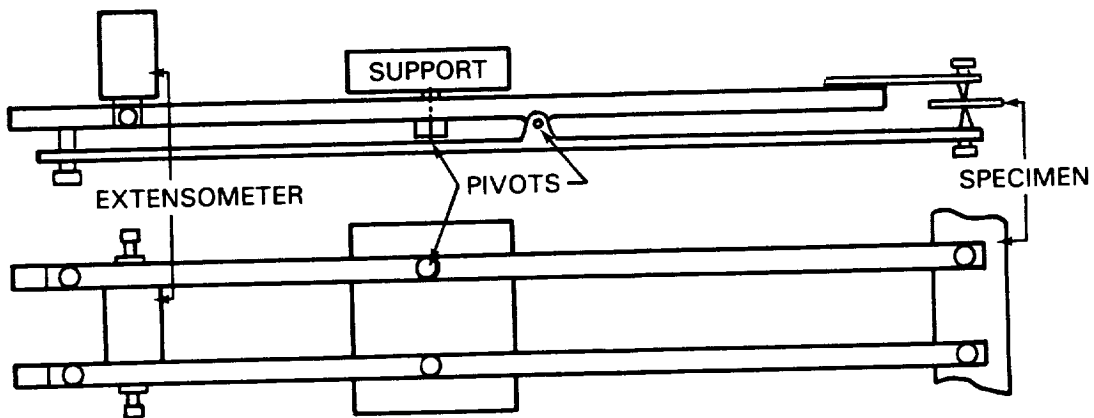
Figure 20   Schematic of Extensometer Arrangement Used to Obtain Deflection Data From Initial
               0.25 mm (0.01 in.) Thick Aluminide Coating Constitutive Specimens
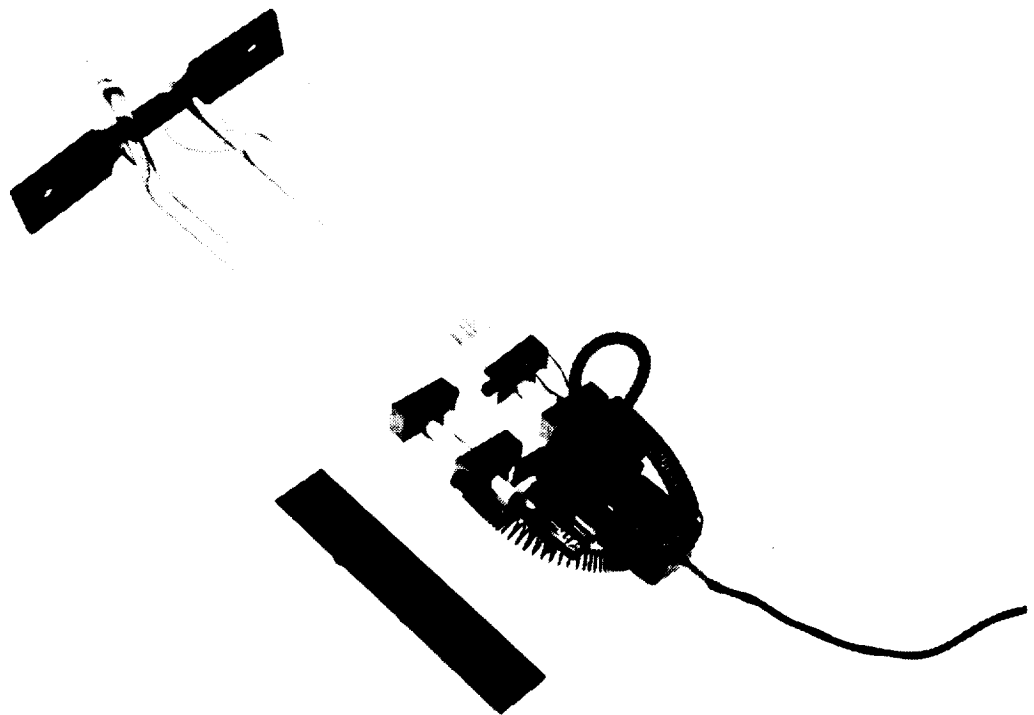
Figure 21   *Extensometer Setup Used to Obtain Deflection Data From 0.13 mm (0.005 in.) and High Temperature 0.25 mm (0.01 in.) Aluminide Coating Constitutive Specimens*

- L.V.D.T. – INTERNAL EXT.
- LOCKING NUT
- UPPER PLATEN
- HIGH TEMPERATURE SPRING
- UPPER PULL ROD

QUARTZ RODS
SPRING LOADED
AGAINST SPECIMEN

MTS

EXTERNAL
EXTENSOMETER

- QUARTZ TUBE
- SPECIMEN
- QUARTZ ROD

INTERNAL
EXT.

- HIGH TEMPERATURE SPRING
- LOWER PULL ROD
- LOAD CELL
- HYDRAULIC RAM
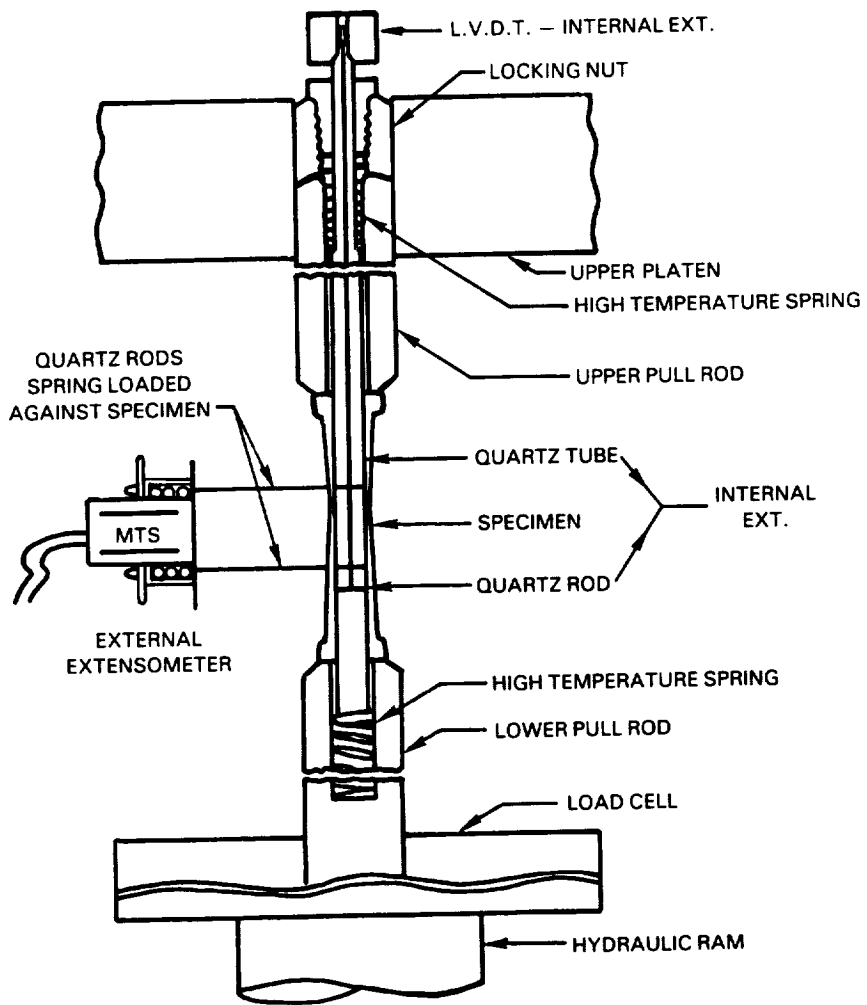
Figure 22   ***Extensometry Setup for Fatigue Testing***
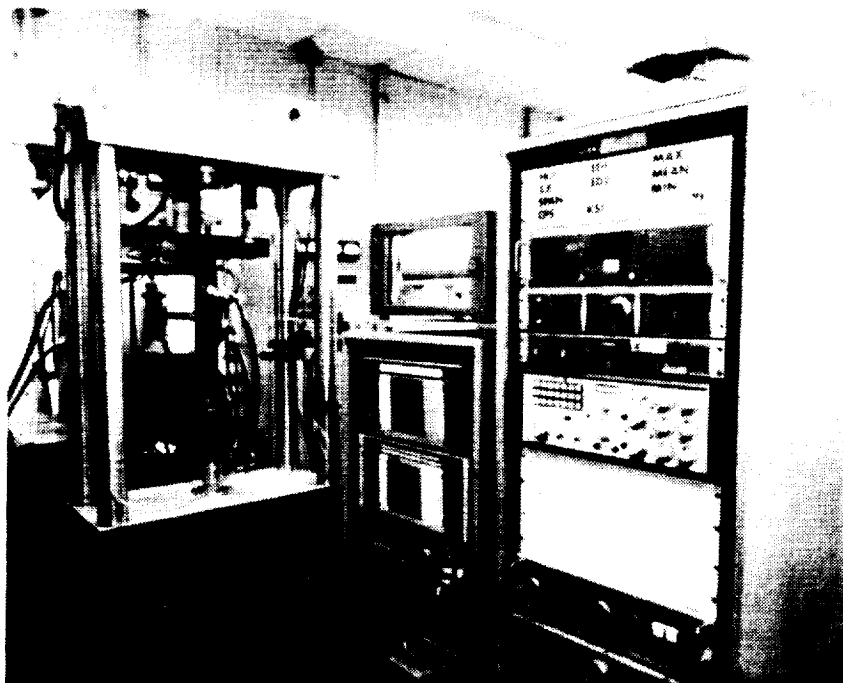
Figure 23   *Thermomechanical Fatigue Test Rig*
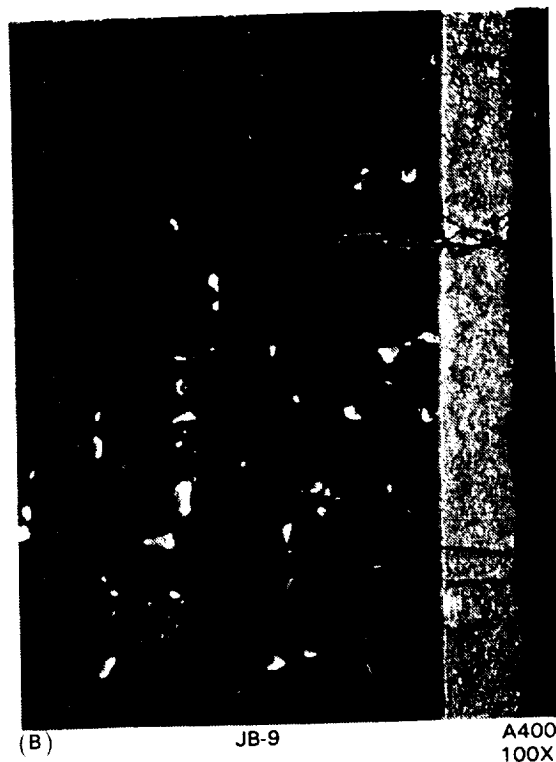
Figure 24   *Representative Coating Cracks: (A) PWA 286, 1038°C (1900°F) LCF; (B) PWA 286, 427°C to 1038°C (800°F to 1900°F) Out–of–Phase TMF; (C) PWA 273, 1038°C (1900°F) LCF; and (D) PWA 273, 427°C to 1038°C (800°F to 1900°F) Out–of–Phase TMF*

207
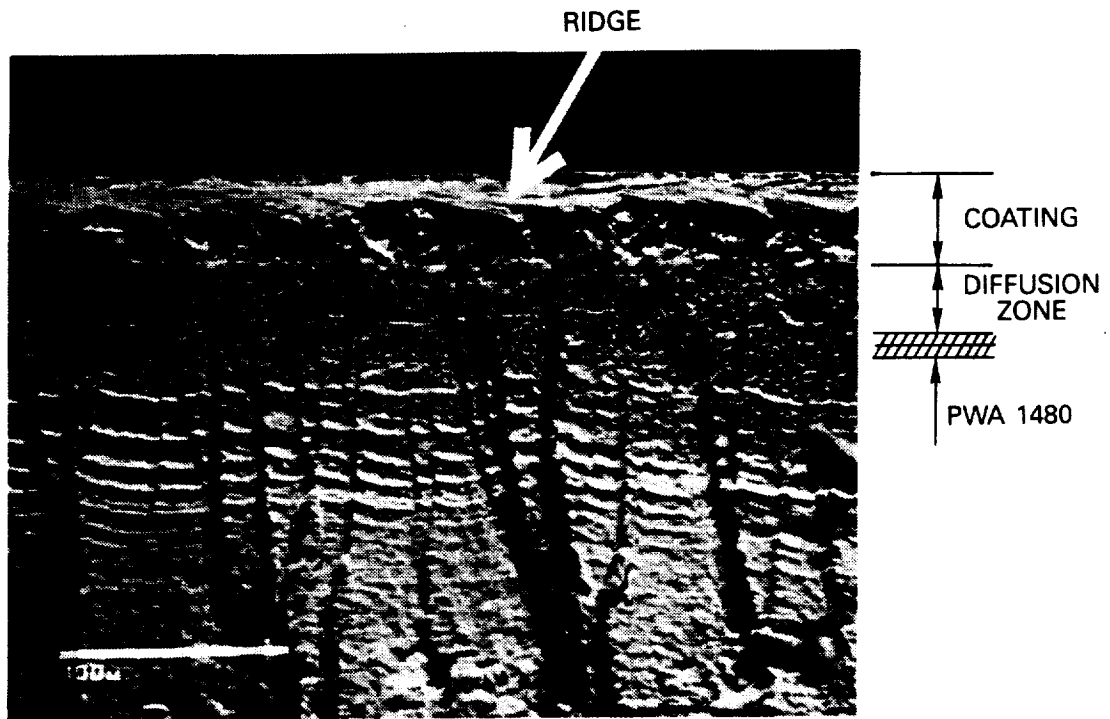
Figure 25   *Backscatter Electron Image of Primary Crack Initiation Region In Specimen MB–1 After Fatigue Testing at 427–1038°C (800–1900°F),   ±0.2%, 1 cpm, Out–of–Phase for 749 Cycles. Initiation occurred at ridge inside coating layer. Failure mode = "C".*
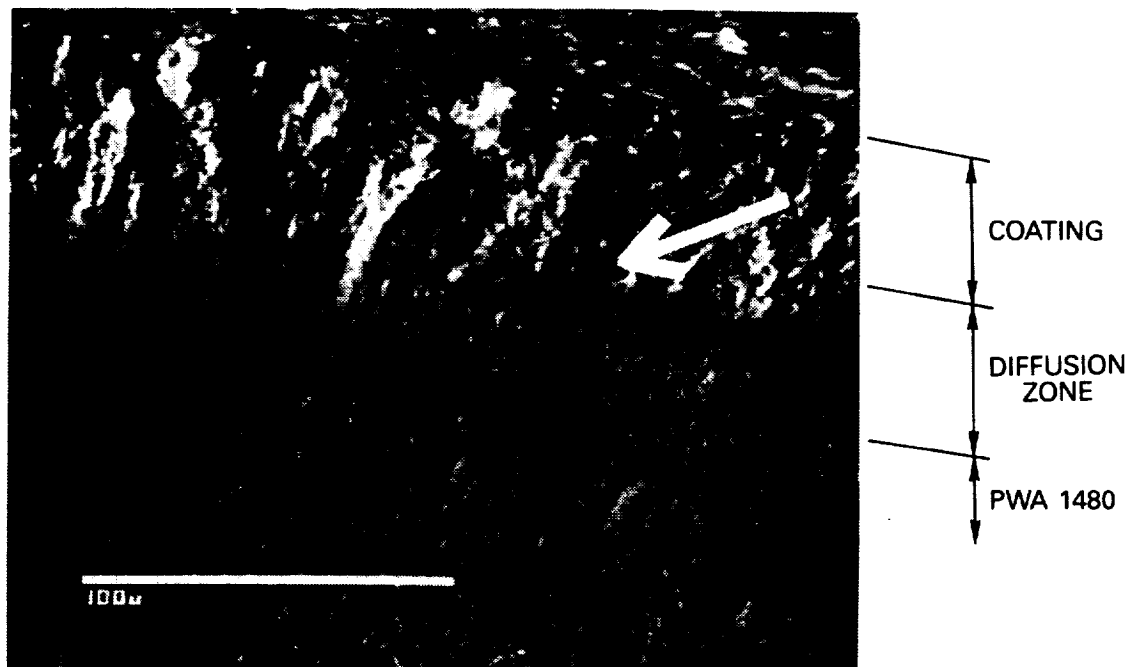
Figure 26   *Backscatter Electron Image of Primary Crack Initiation Region In Specimen MB–21 After Fatigue Testing at 927°C (1700°F), ±0.25%, 10 cpm for 11648 cycles. Arrow indicates initiation site. Failure mode = "CS".*

SUBSTRATE

COATING

500X

Figure 27   *Secondary Electron Image of Primary OD Surface Crack In Specimen LB–156 After Fatigue Testing at 427–1038°C (800–1900°F), ±0.15%, 1 cpm, Clockwise Baseball Cycle for 1639 Cycles. Initiation occurred at coating–substrate interfacial region. Failure mode = "SC".*

100µ
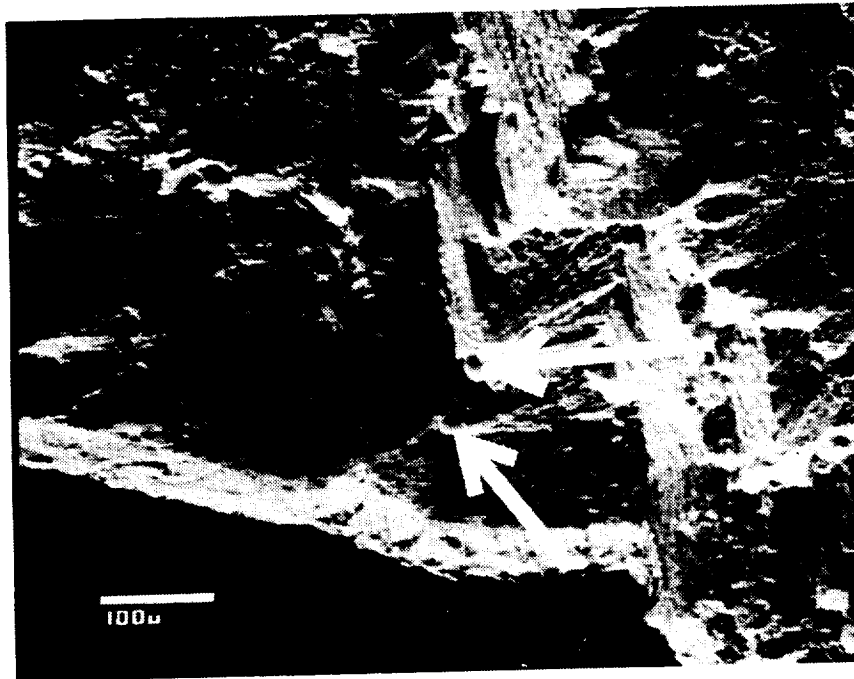
Figure 28   *Backscatter Electron Image of Primary Crack Initiation Region In Specimen LB–180 After Fatigue Testing at 927°C (1700°F), ±0.25%, 10 cpm for 3941 Cycles. Arrows indicate porosity initiation sites in PWA 1480. Failure mode = "S".*

209
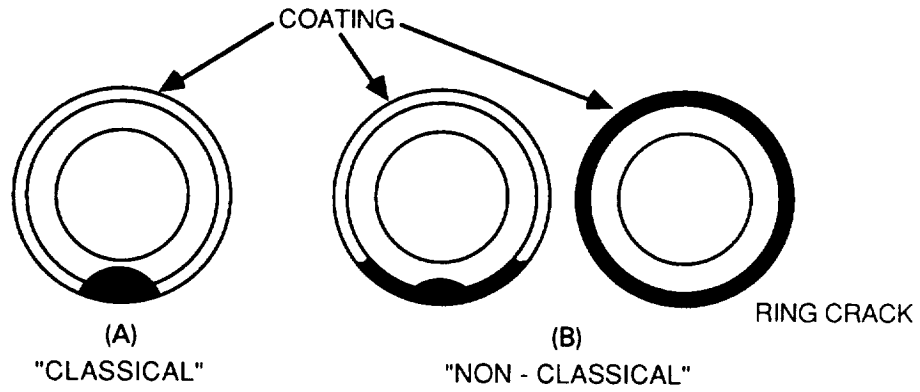
Figure 29   *Types of O.D. Initiated Cracking Observed From Coated PWA 1480 Specimens*
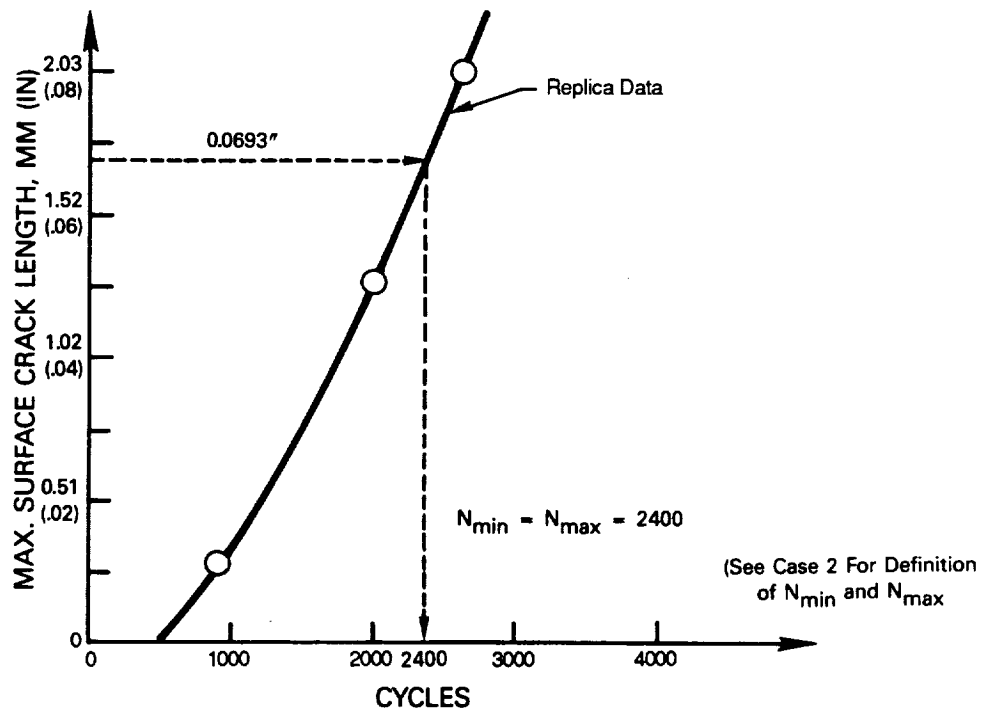
Figure 30   *Method 1 Application to Specimen JB–121. Crack aspect ratio = 4.5; desired crack length = 4.5 (0.0154 in.) = 0.0693 in.*
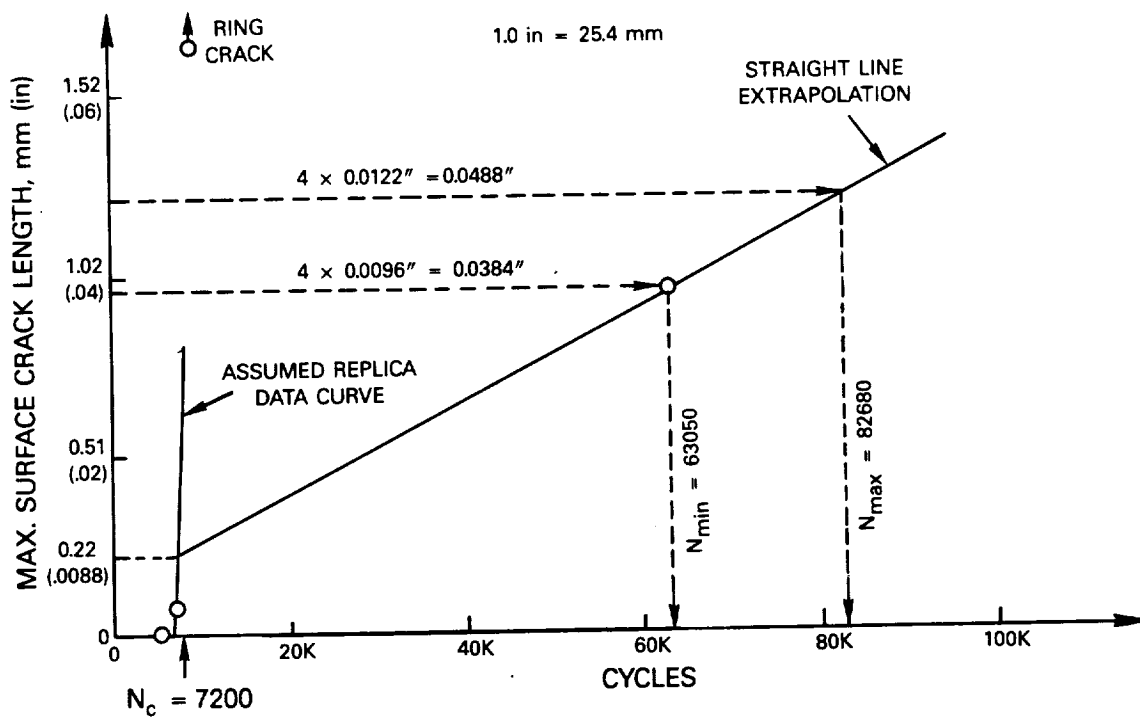
Figure 31   *Method 2 Application to Specimen JB-103. Coating initiation appeared as a ring crack. Estimated substrate crack aspect ratio = 4.0. N_c was determined at 4x (coating thickness) = 4(0.0022 in.) = 0.0088 in. Maximum crack penetration = 0.0096 in. at 63050 cycles. Desired crack length = 4.0 (0.010 in. + 0.0022 in.) = 0.0488 in.*
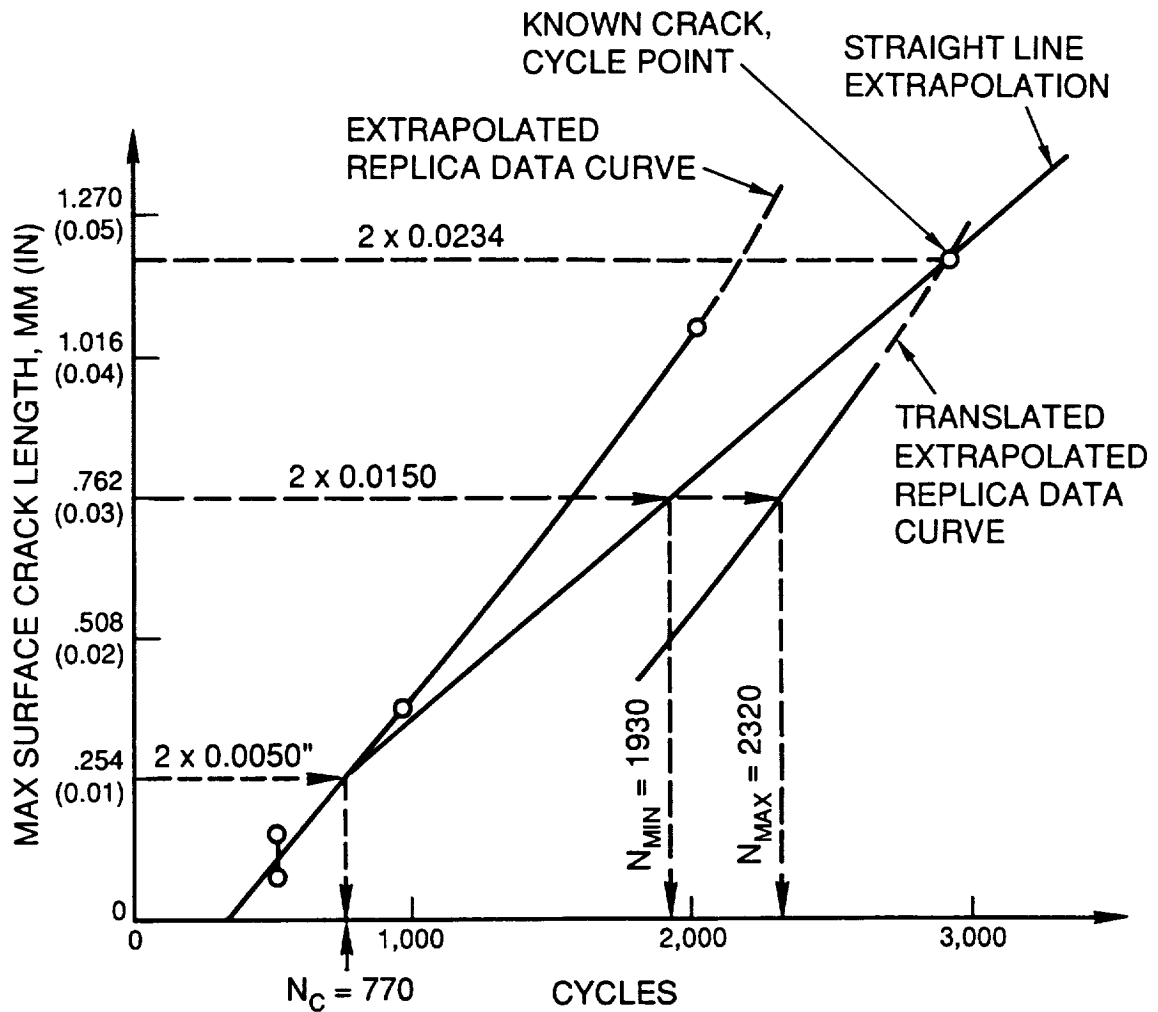
Figure 32   *Method 3 Application to Specimen JB–89. Estimated crack aspect ratio = 2.0. N_c was determined at 2 x (coating thickness) = 2 x (0.0050 in.) = 0.0100 in. Maximum crack penetration = 0.0234 in. at 2912 cycles (N_f). Desired crack length = 2 (0.0150 in.) = 0.0300 in. From straight line extrapolation, N_{min} = 1930 cycles. From translated extrapolated replica data curve, N_{max} = 2320 cycles.*
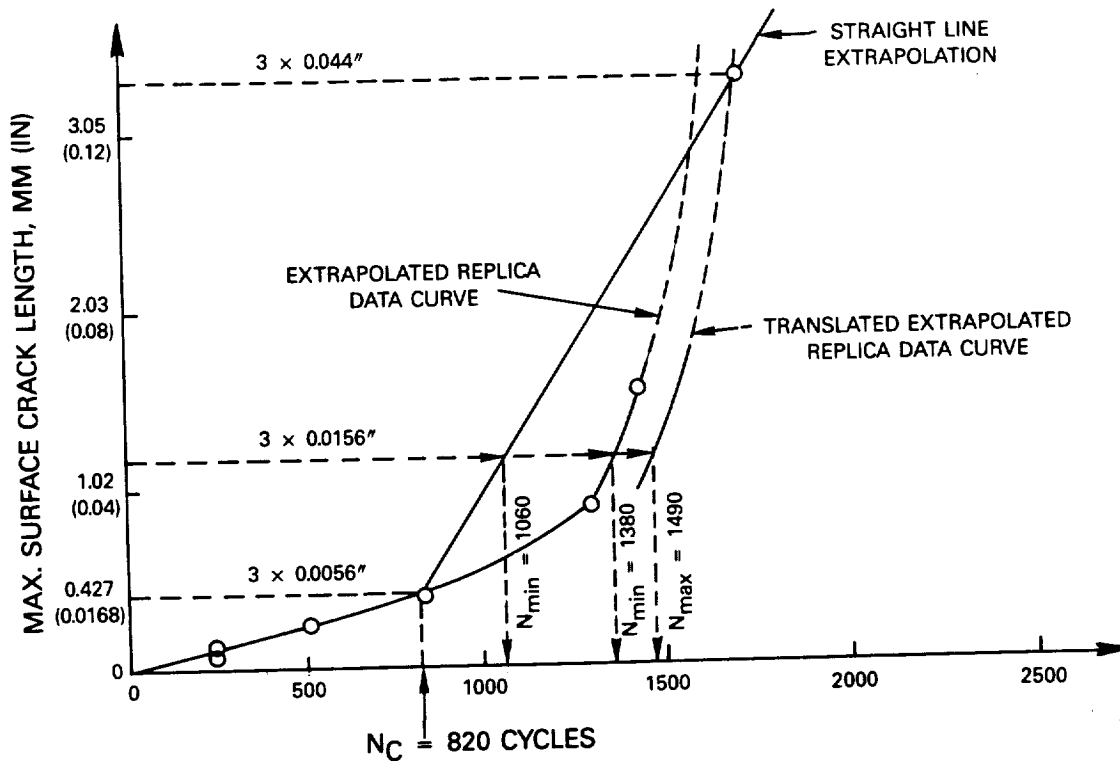
Figure 33   *Method 3 Application to Specimen JB-21. Estimated crack aspect ratio = 3.0. N_c was determined at 3 x (coating thickness) = 3 (0.0056 in.) = 0.0168 in. Maximum crack penetration = 0.044 in. at 1847 cycles (N_f). Desired crack length = 3 (0.0156 in.) = 0.0468 in. From straight line extrapolation, N_{min} = 1060 cycles, but N_{min} = 1380 cycles from replica data. Use N_{min} = 1380 cycles. From translated extrapolated replica data curve, N_{max} = 1490 cycles.*

213
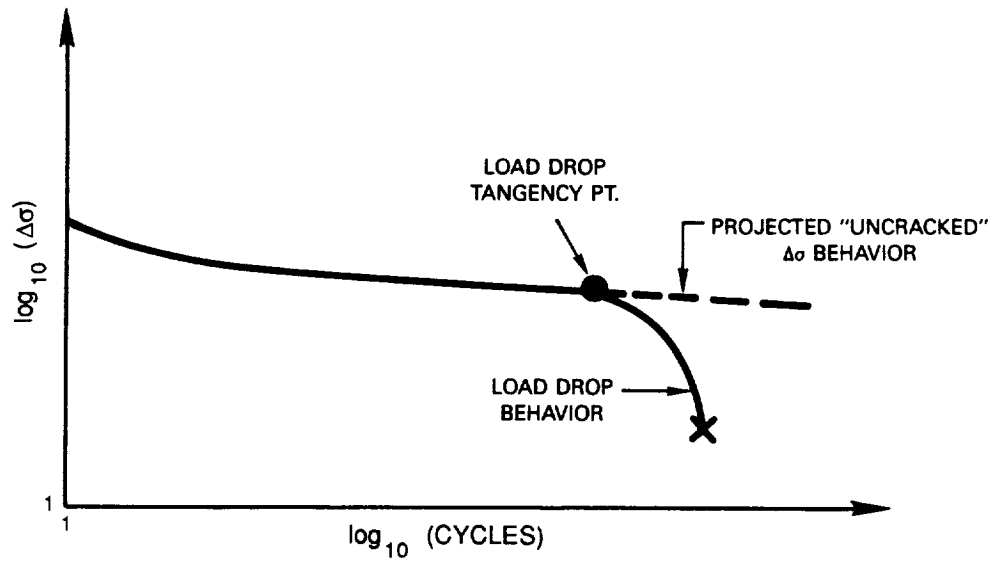
Figure 34   *Method 4 Check of N_{max} Calculation. It is assumed that a crack which has penetrated into the PWA 1480 at least 0.010 in. exists at the load drop tangency point.*
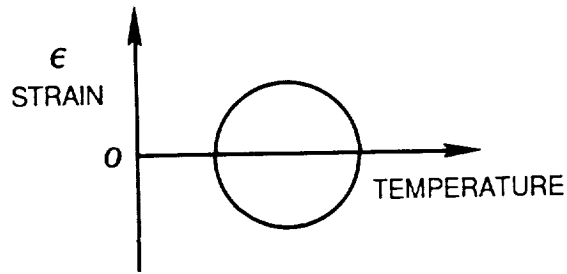
Figure 35   *Schematic of Mechanical Strain Vs. Temperature Cycle Used In TMF Testing of Specimens LB-21 and LB-156. This cycle type is called a "baseball" cycle.*
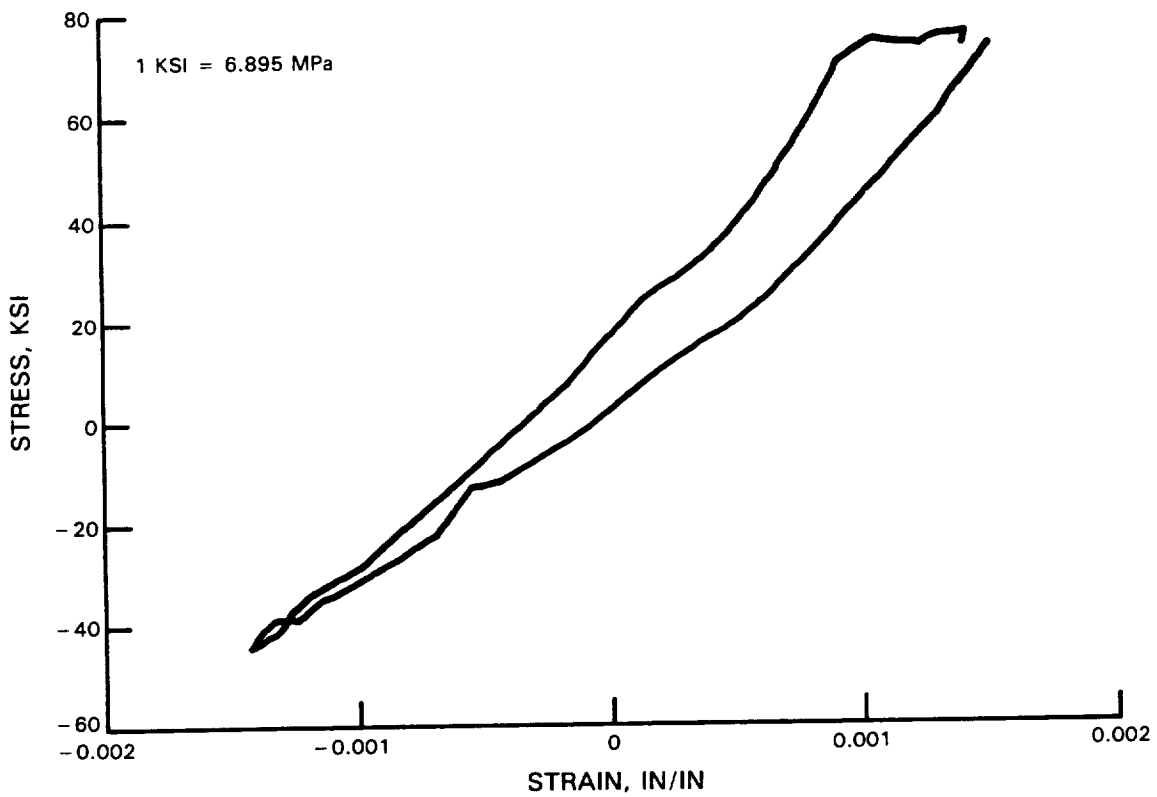
Figure 36   *Stress Vs. Mechanical Strain Response of Specimen LB-156 – Clockwise "Baseball" TMF Cycle*

60
1 KSI = 6.895 MPa
40
20
STRESS, KSI
0
−20
−40
−60
−80
−0.002   −0.001   0   0.001   0.002
STRAIN, IN/IN
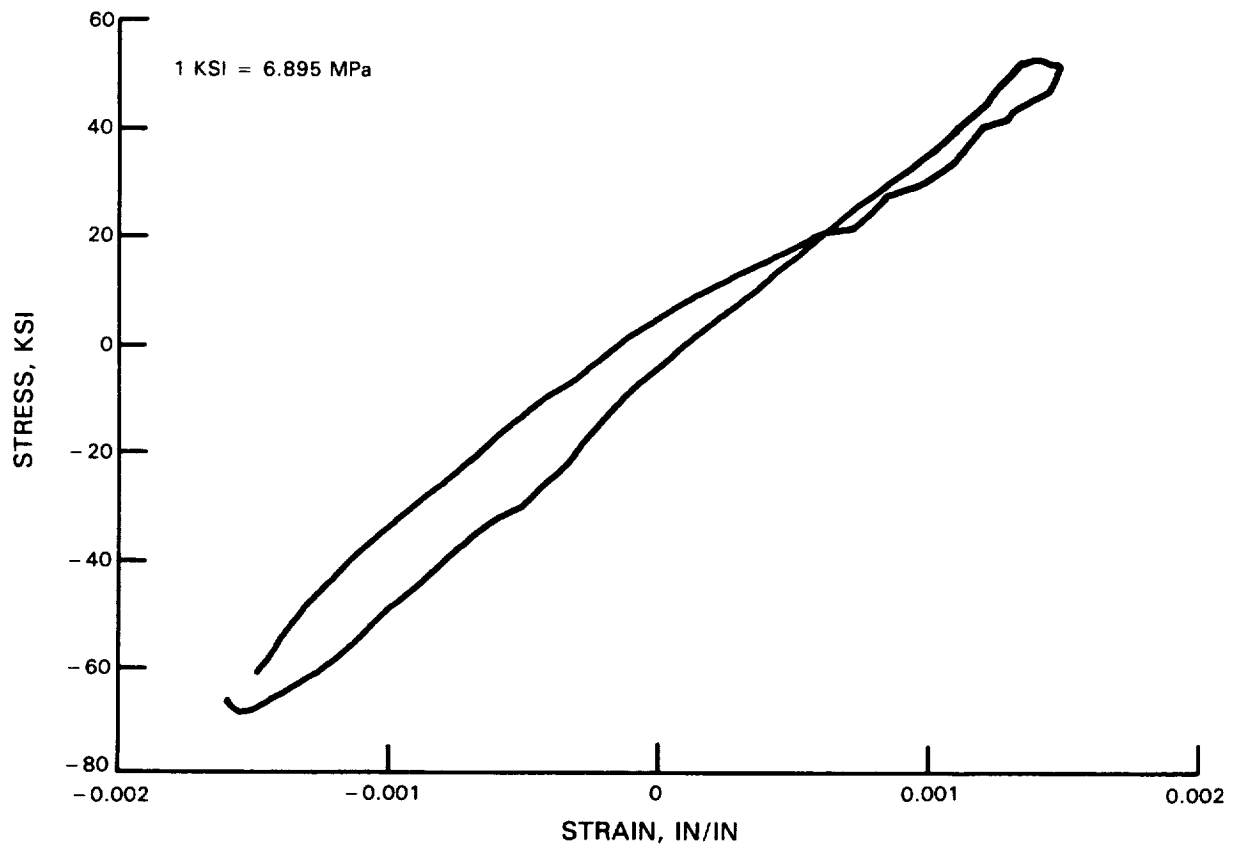
Figure 37   *Stress Vs. Mechanical Strain Response of Specimen LB-21 – Counter–Clockwise "Base-ball" TMF Cycle*
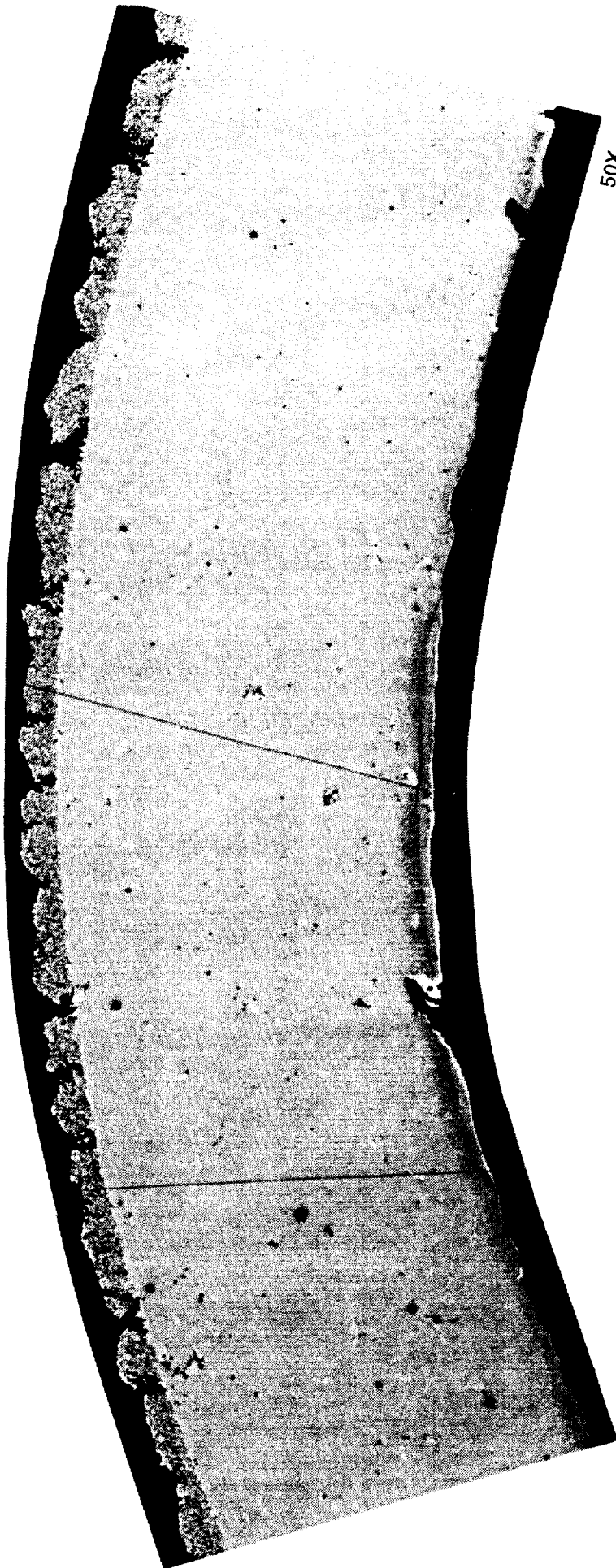
Figure 38   Transverse Micrograph of Specimen JB-102 Showing Coating Crack Morphology

50X

217

200X

Figure 39   *Secondary Electron Image of PWA 273 Aluminide Coated <111> PWA 1480 Specimen LB–124 After Isothermal LCF Testing At 760°C (1400°F), ±0.3%, 0.5 cpm for 1372 cycles. Arrow indicates location of subsurface PWA 1480 porosity where crack initiation occurred.*
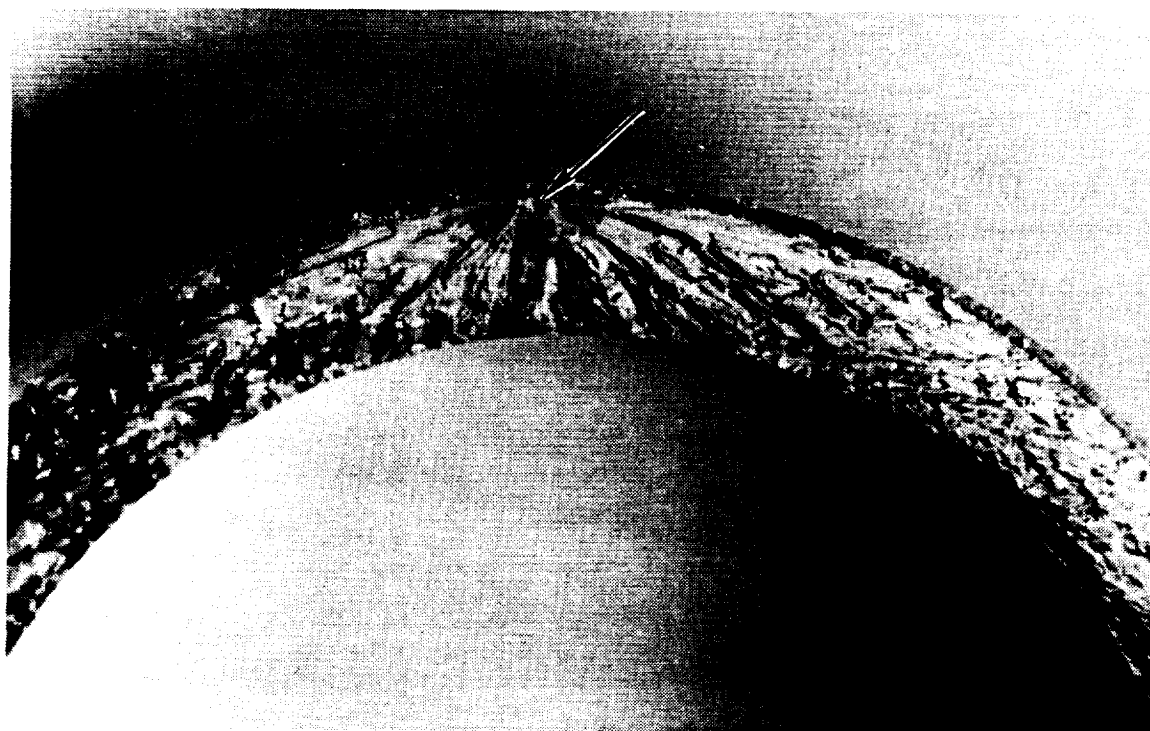
Figure 40   *Optical Microscopy Image of PWA 286 Overlay Coated <011> PWA 1480 Specimen KB–65 After Isothermal LCF Testing At 927°C (1700°F), ±0.25%, 1 cpm for 6624 cycles. Arrow indicates location of subsurface PWA porosity where crack initiation occurred.*

218
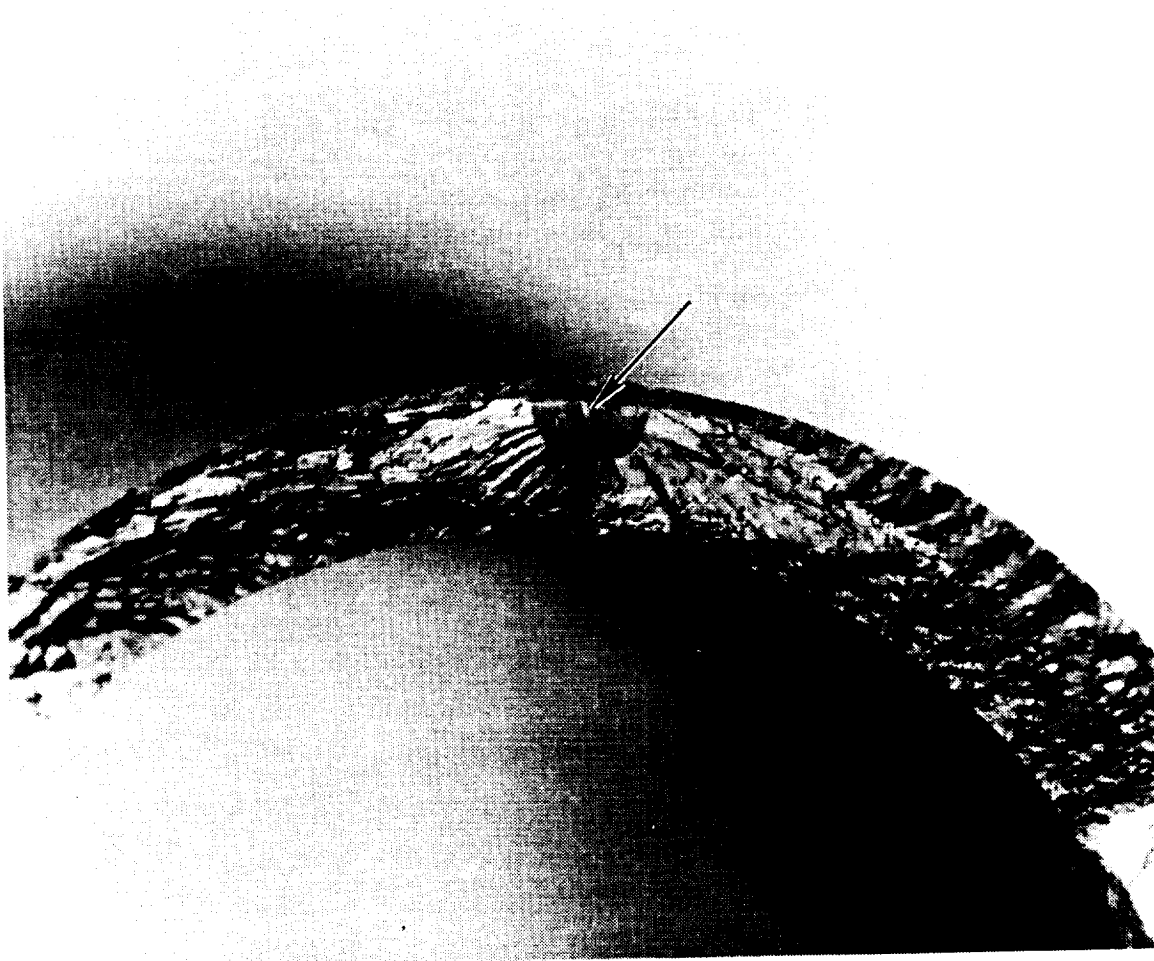
Figure 41   *Optical Microscopy Image of PWA 286 Overlay Coated <213> PWA 1480 Specimen MB-38 After Isothermal LCF At 1038°C (1900°F), ±0.25%, 10 cpm for 8253 Cycles. Arrow indicates location of subsurface PWA 1480 porosity where crack initiation occurred.*
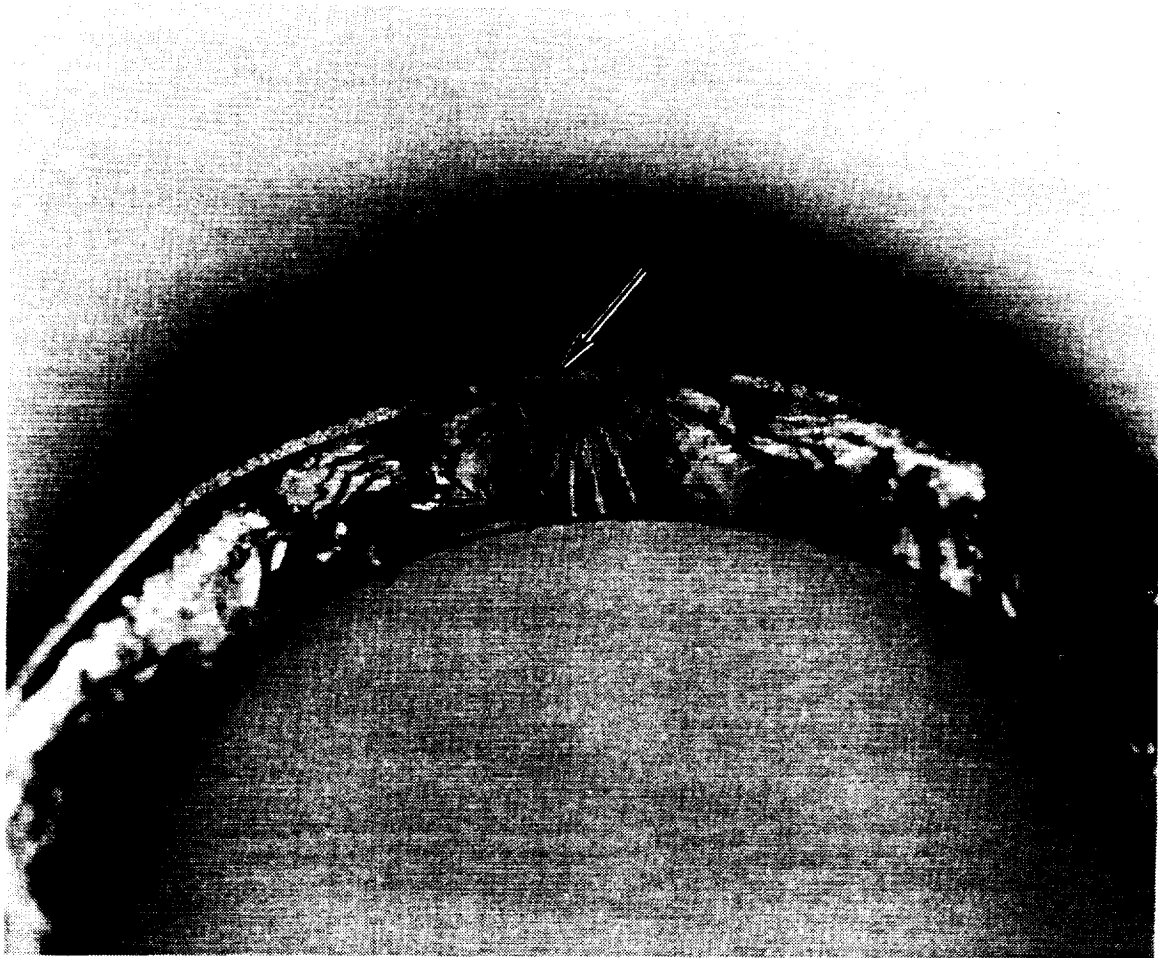
Figure 42   *Optical Microscopy Image of PWA 286 Overlay Coated <111> PWA 1480 Specimen LB–181 After Out–of–Phase TMF Testing At 427–1038°C (800–1900°F), ±0.125%, 1 cpm for 7675 Cycles. Arrow indicates typical coating initiated crack.*
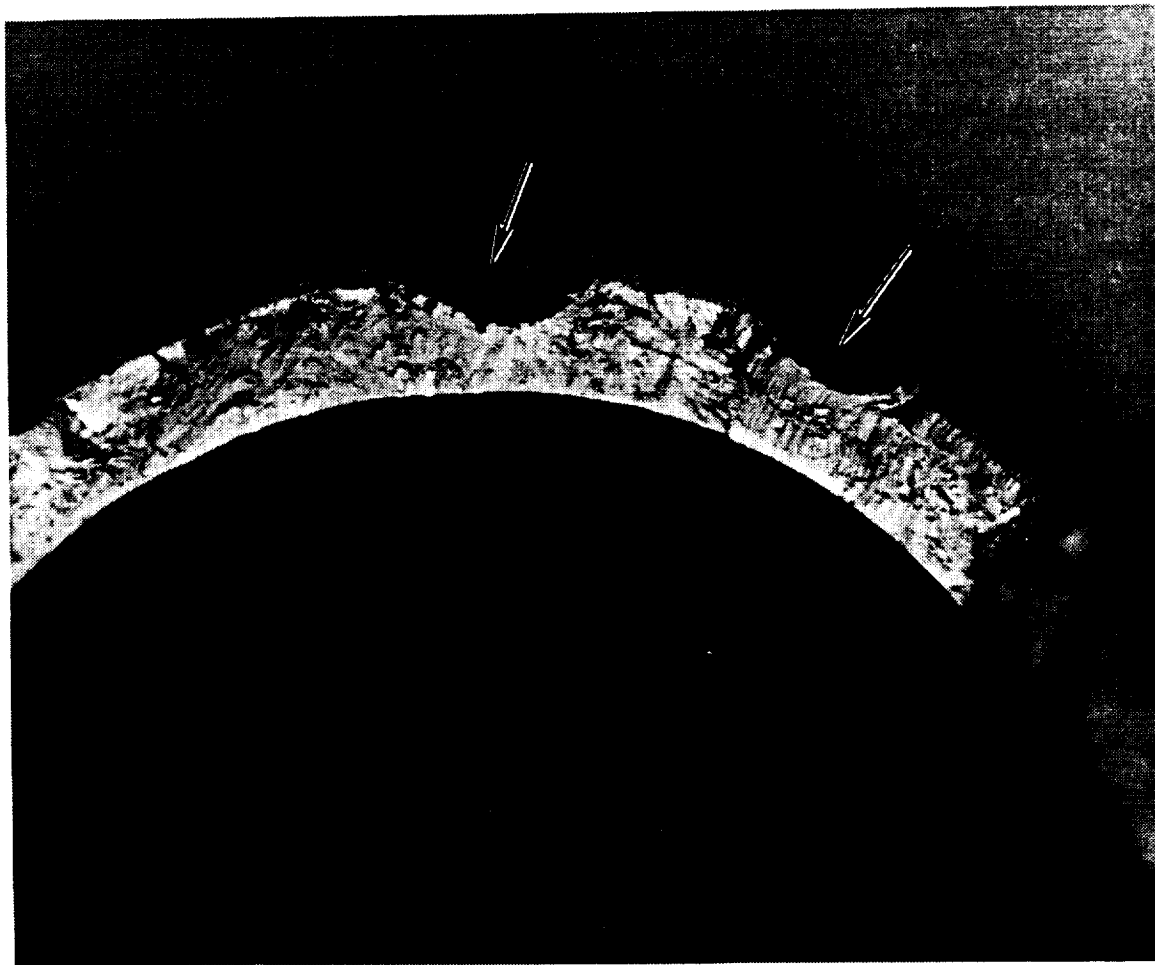
Figure 43   Optical Microscopy Image of PWA 286 Overlay Coated <011> PWA 1480 Specimen
KB-24 After Out-of-Phase TMF Testing At 427–1038°C (800–1900°F) ±0.15%, 1 cpm
for 5927 cycles. Arrow indicates typical coating initiated crack.

Figure 44   *Optical Microscopy Image of PWA 286 Overlay Coated <213> PWA 1480 Specimen MB-17 After Out-of-Phase TMF Testing At 427-1038°C (800-1900°F), ±0.125%, 1 cpm for 7294 Cycles. Arrow indicates typical coating initiated crack.*
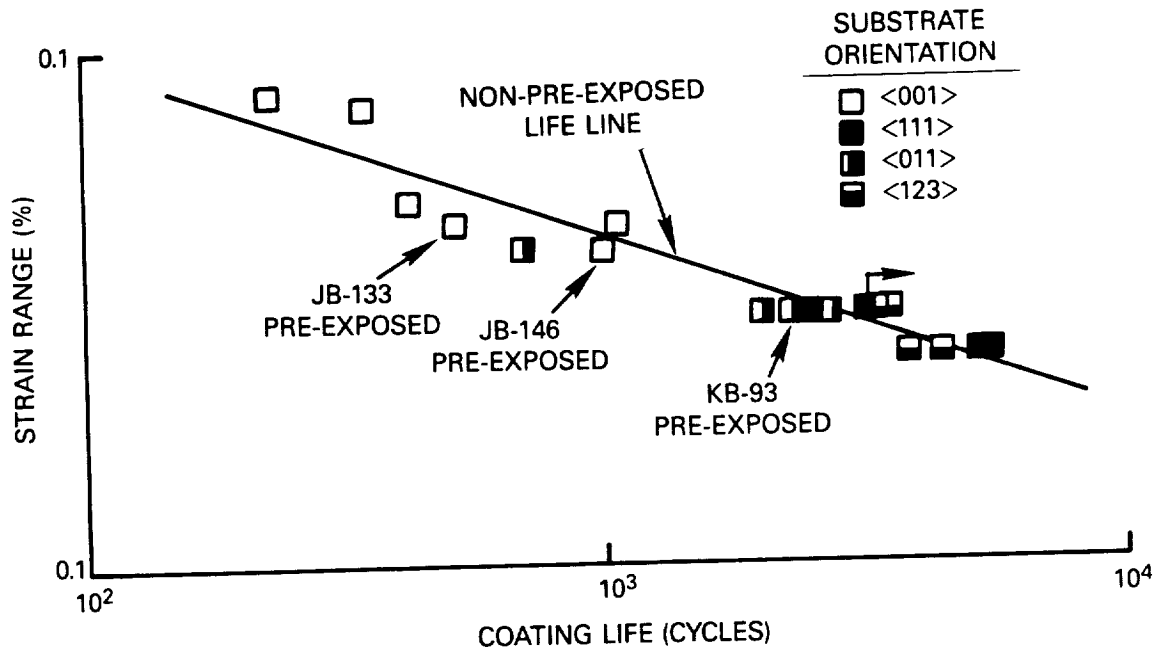
Figure 45   *Strain Range Vs. Coating Life for PWA 286 Overlay Coated PWA 1480. All tests are 427–1038°C (800–1900°F), 1 cpm, Out–of–Phase TMF.*
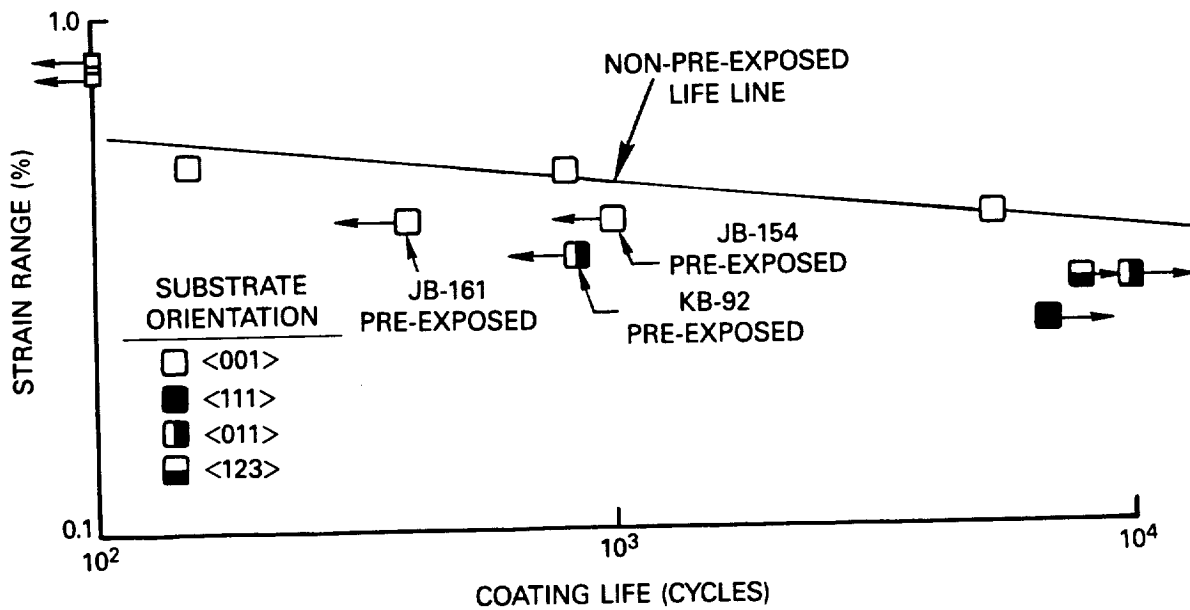
Figure 46   *Strain Range Vs. Coating Life for PWA 273 Aluminide Coated PWA 1480. All tests are 427–1038°C (800–1900°F), 1 cpm, Out–of–Phase TMF.*
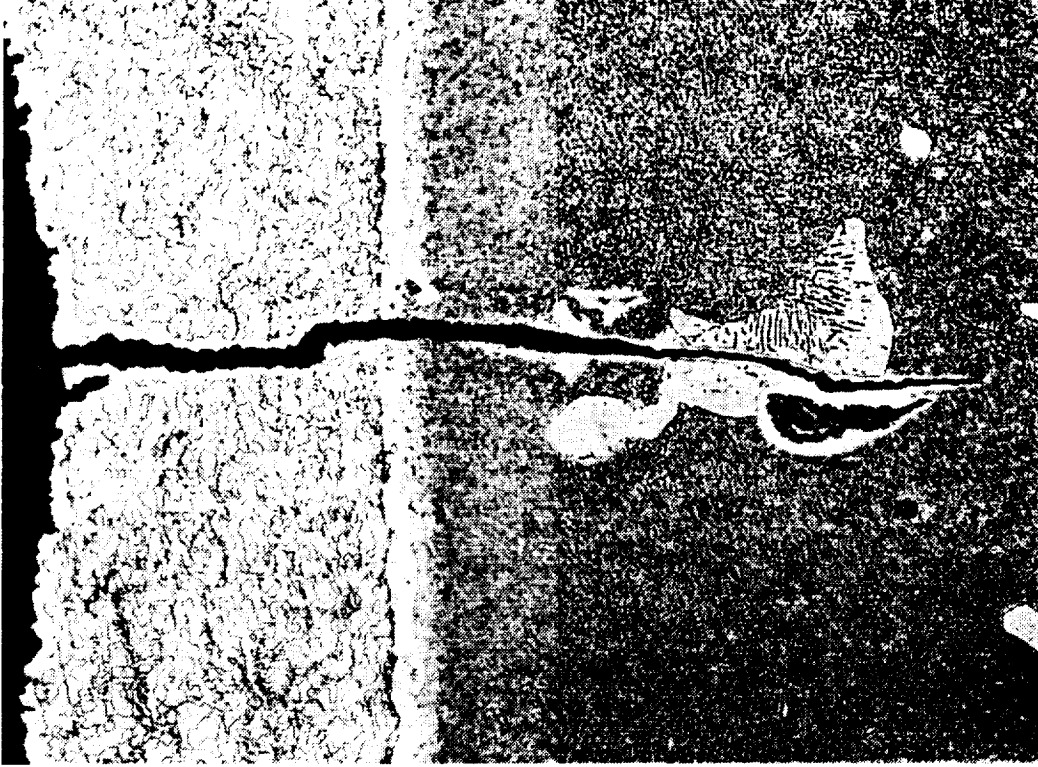
MAG: 500X

b)

MAG: 500X

a)

Figure 47   Overlay Coating Microstructure of a) Pre-exposed Specimen JB-133 and b) Non-pre-ex-posed Specimen JB-147 TMF Tested at 427–1038° C (800–1900° F), ± 0.225%, 1 cpm, Out-of-Phase

MAG: 500X

a)

MAG: 500X

b)
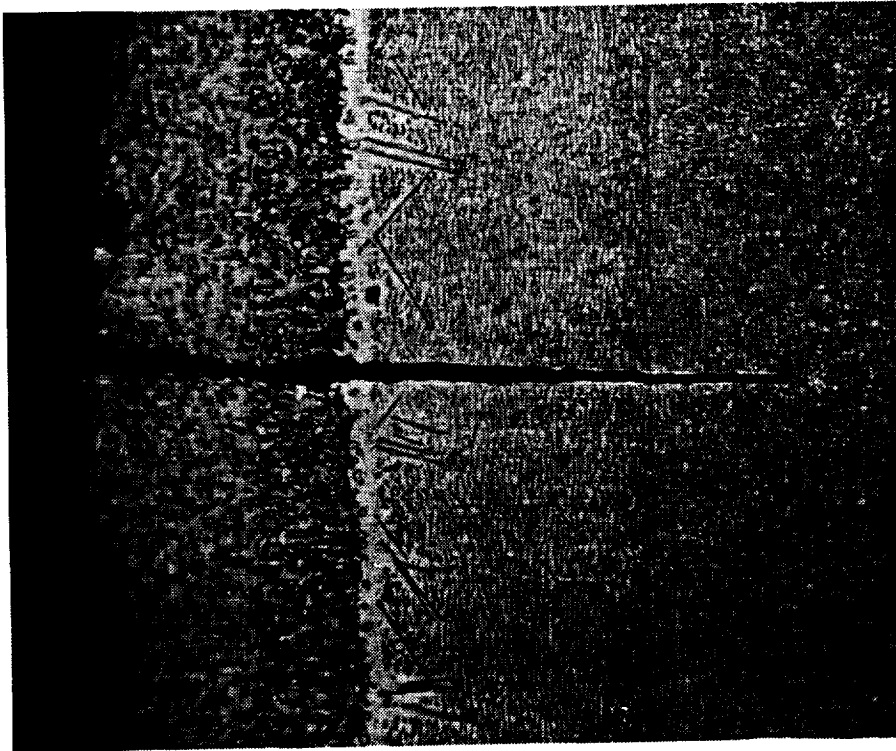
Figure 48   *Aluminide Coating Microstructure of a) Pre–exposed Specimen JB–154 and b) Non–pre–exposed Specimen JB–98 TMF Tested at 427–1038°C (800–1900°F), ±0.2%, 1 cpm, Out–of–Phase*

225
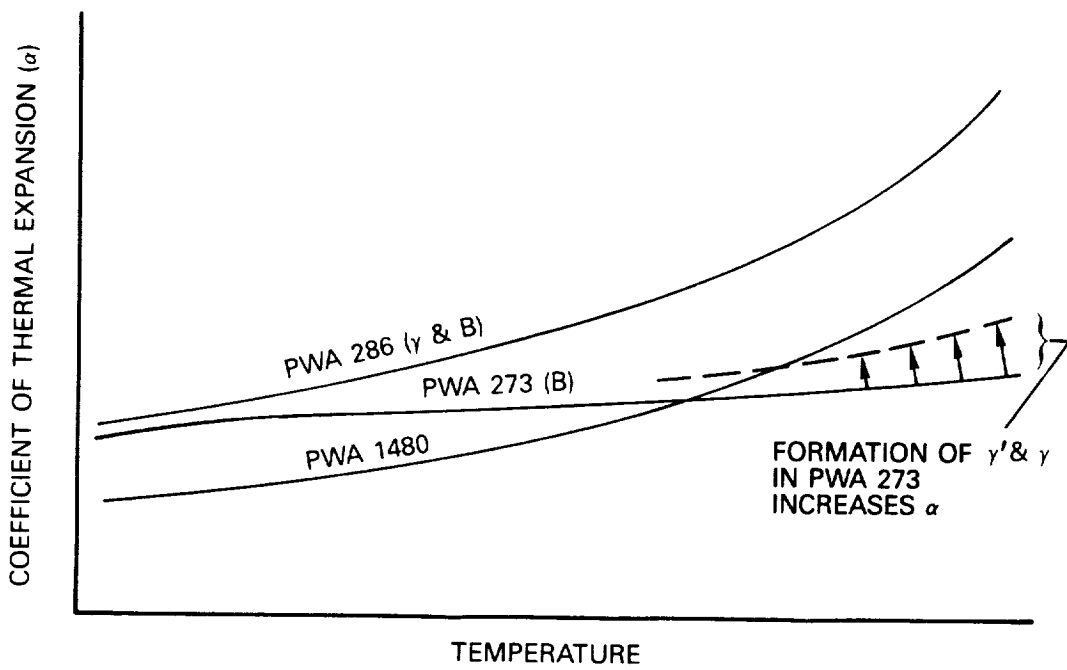
Figure 49   *Coefficient of Thermal Expansion Vs. Temperature Trends*
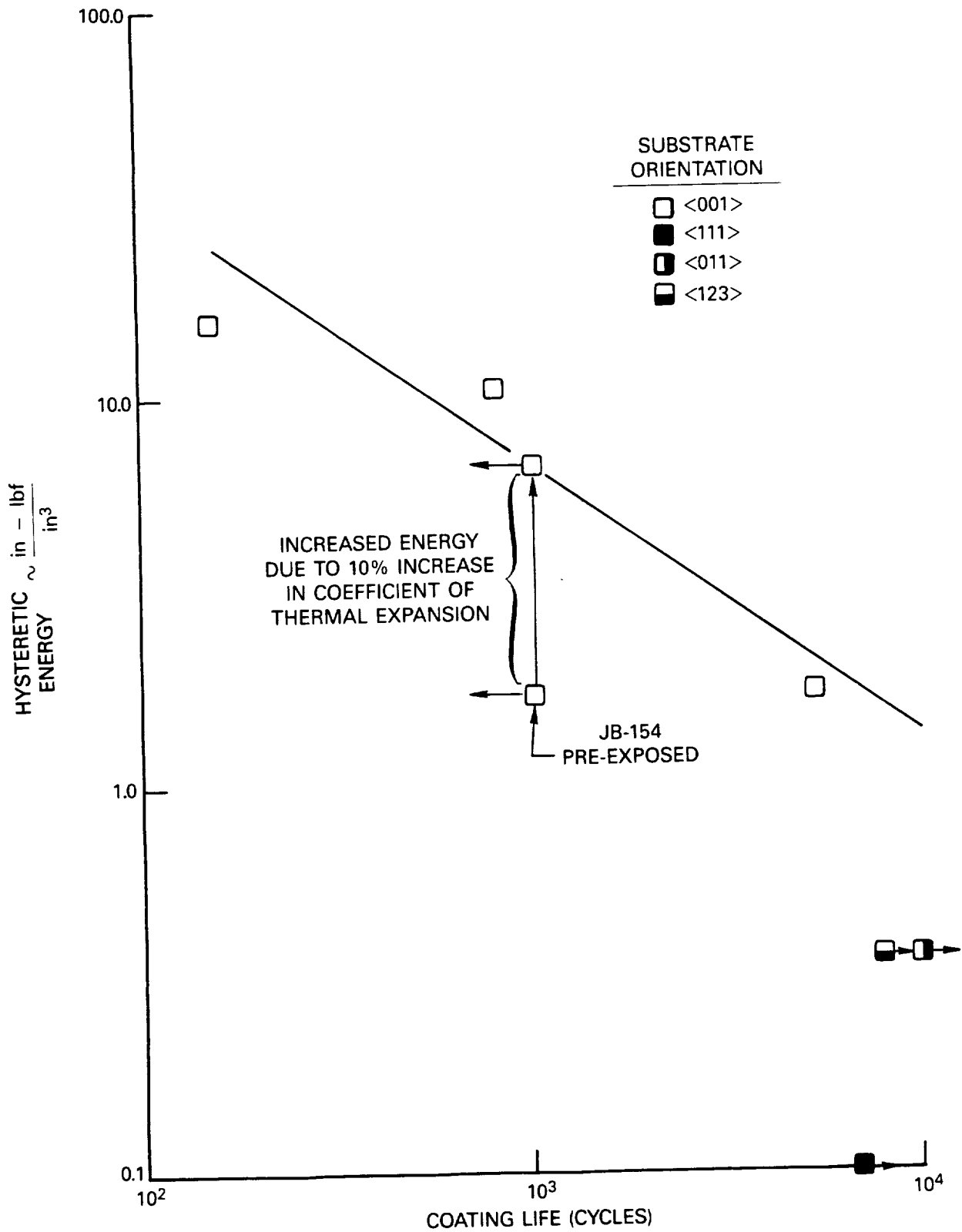
Figure 50   *Hysteretic Energy Vs. Coating Life for PWA 273 Aluminide Coated PWA 1480. All tests are 427–1038° C (800–1900° F), 1 cpm, Out–of–Phase TMF.*

227
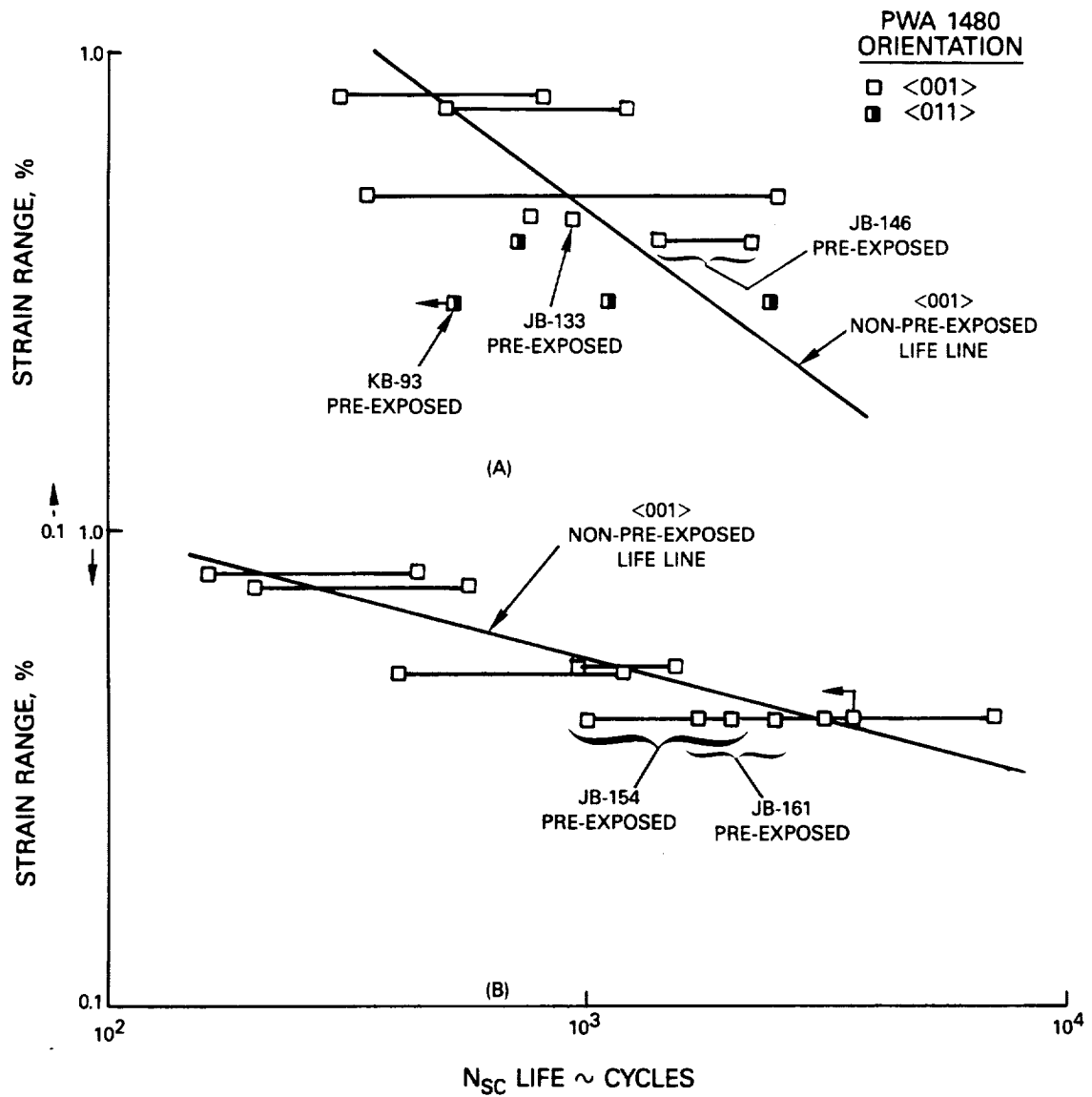
Figure 51   *Strain Range Vs. PWA 1480 Crack Initiation Life (N_{sc}) for A) Overlay Coated Specimens and B) Aluminide Coated Specimens Subjected to 427–1038° C (800–1900° F), 1 cpm, Out–of–Phase TMF*

228
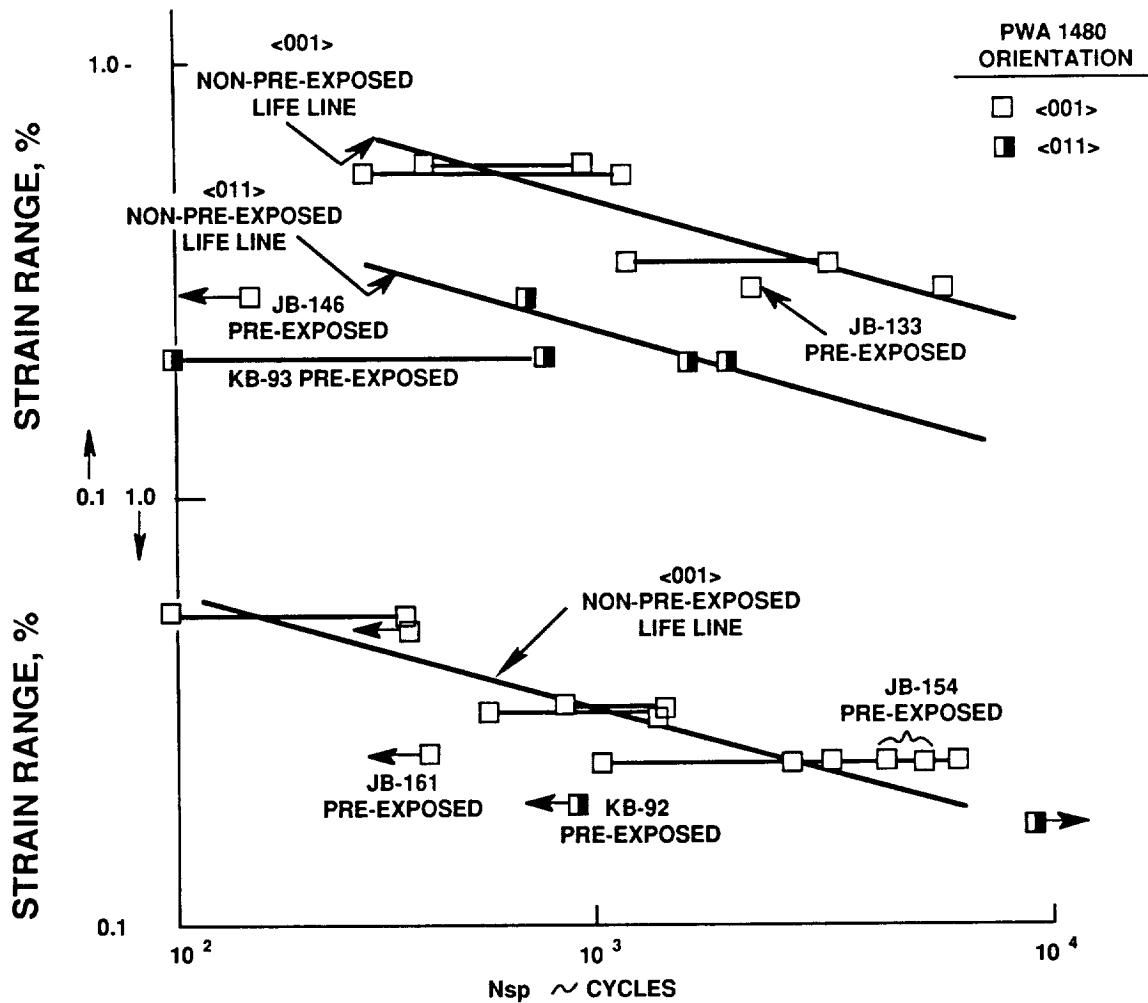
Figure 52 *Strain Range Vs. PWA 1480 Propagation Life (N$_{sp}$) for A) Overlay Coated Specimens and B) Aluminide Coated Specimens Subjected to 427–1038°C (800–1900°F), 1 cpm, Out–of–Phase TMF*

···DATA ─CORRELATION
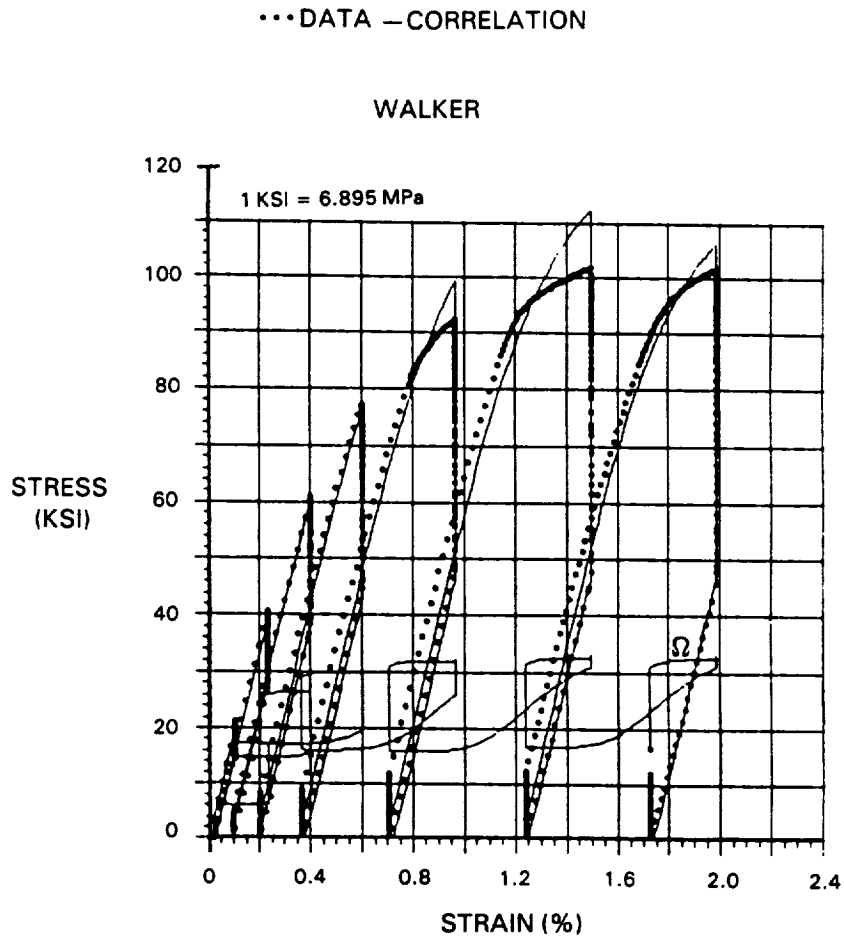
WALKER

Figure 53 *Walker Model Correlation of 649°C (1200°F) Isothermal Stress Relaxation Test*

230
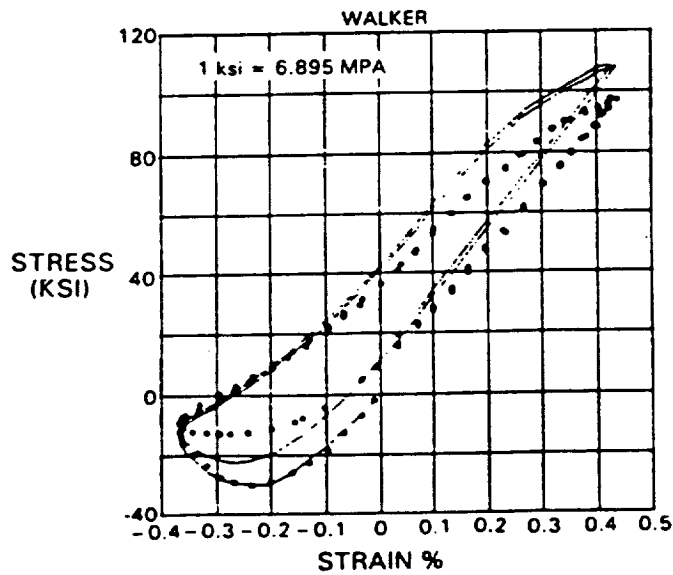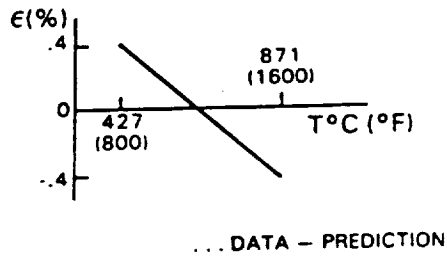
Figure 54   *Walker Model Prediction of Out–of–Phase TMF Test*

231
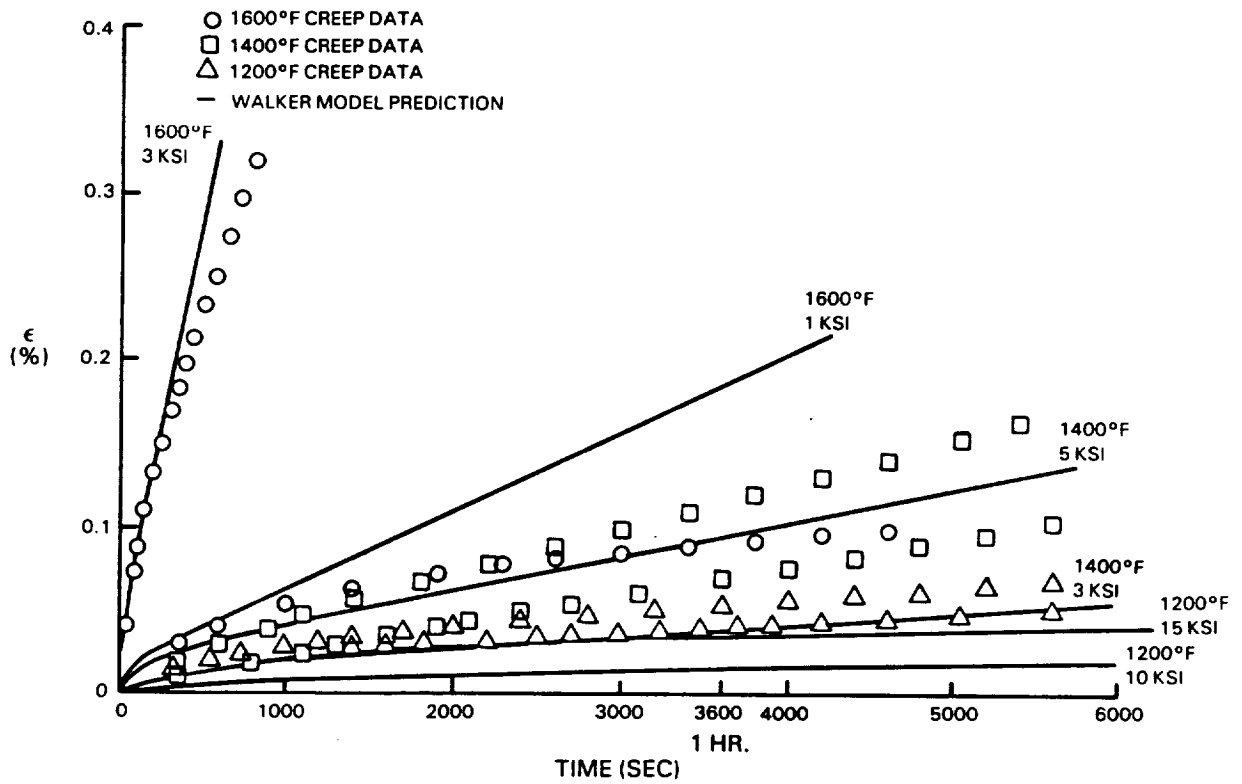
Figure 55   *Walker Model Prediction of Monotonic Creep Behavior of Unexposed, Bulk HIP PWA 286.*
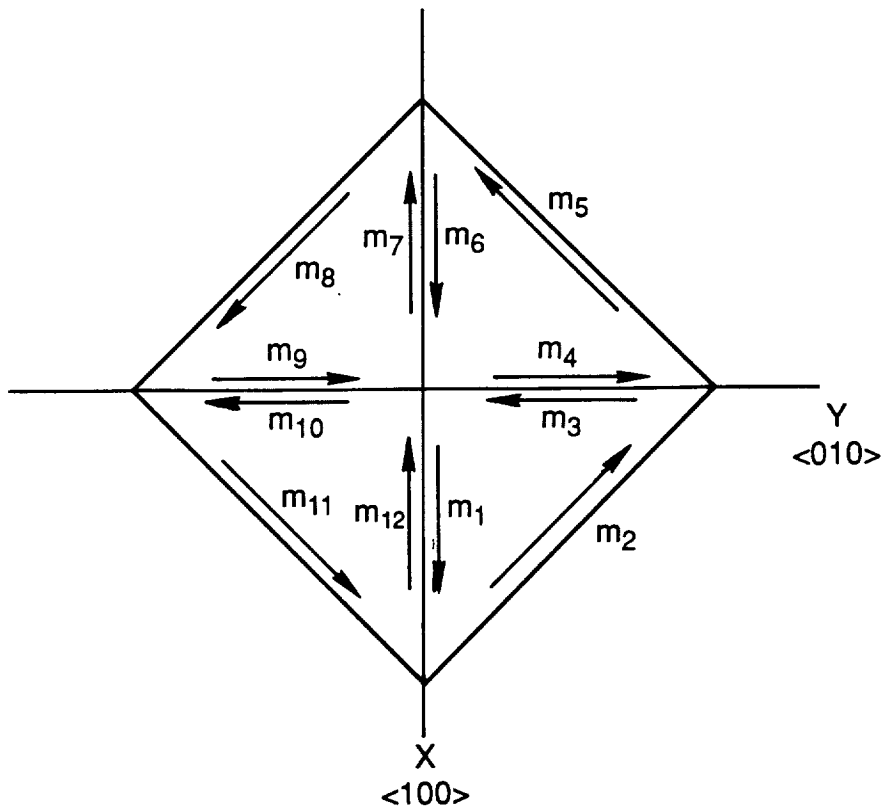
OCTAHEDRON VIEWED FROM POSITIVE
Z <001> AXIS

Figure 56   *The Twelve <110> Slip Directions m_i On the Four Octahedral {111} Planes*

233
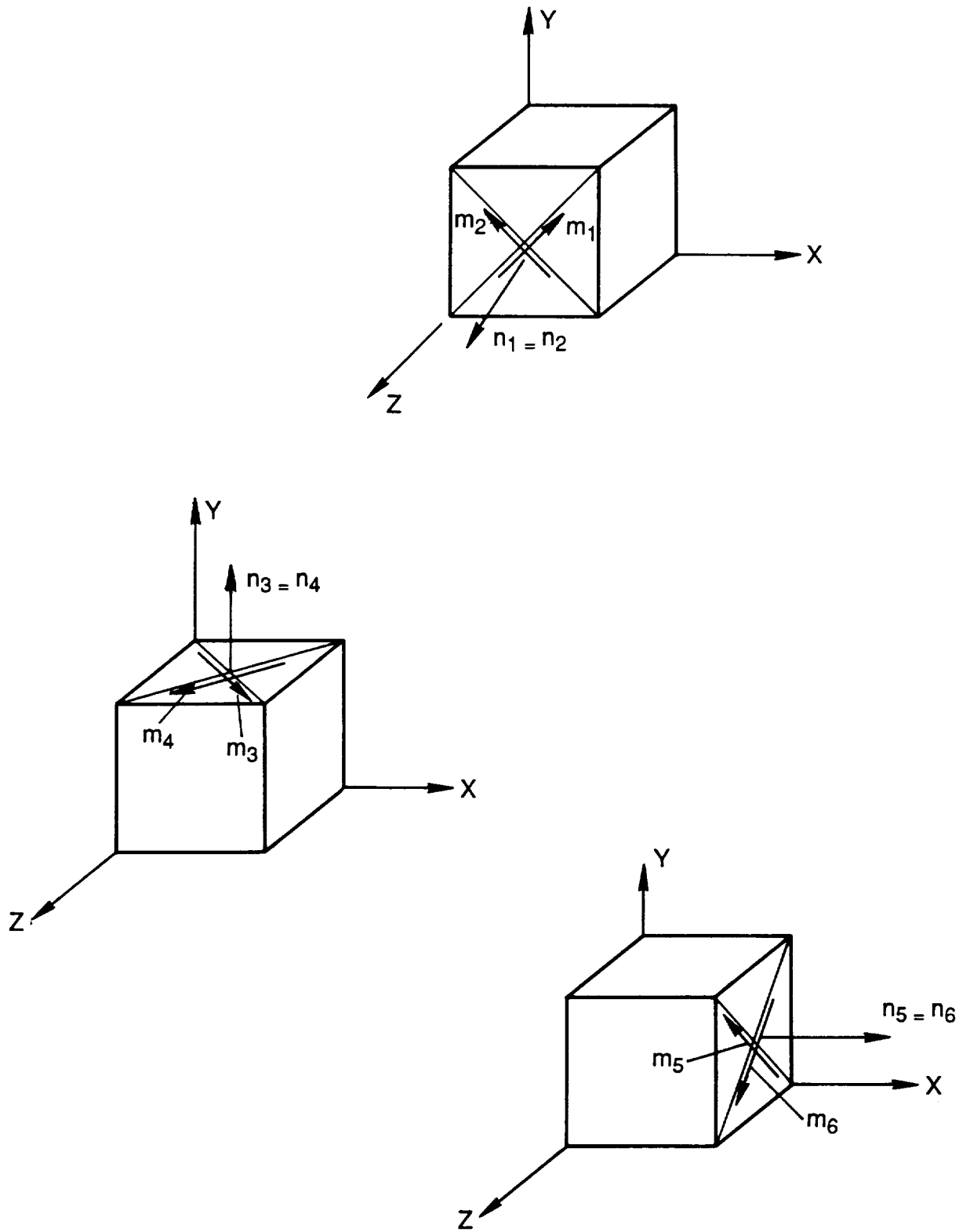
Figure 57   *The Six Cube* $<011>$ *Slip Directions* m_i *On the Three Cube* $\{100\}$ *Planes*

GLOBAL AXES

CRYSTALLOGRAPHIC AXES

SINGLE CRYSTAL BAR SPECIMEN
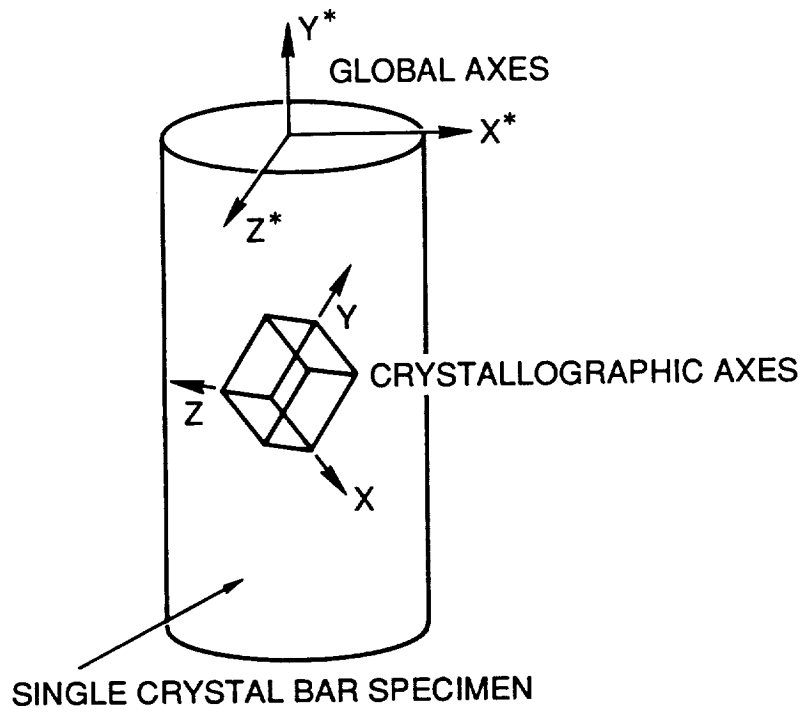
Figure 58   *The Relations Between the Global Axes of the Single Crystal Specimen and the Crystallo-graphic Axes of the Specimen*

(11) $\quad \dot{\gamma}_r = \dfrac{(\pi_r - \omega_r) \ |\pi_r - \omega_r|^{\,P-1}}{K_{rt}^{\,P}}$

(12) $\quad \pi_r = \pi_{mn}^r + \alpha_{mm}\pi_{mm}^r + \alpha_{nn}\pi_{nn}^r + \alpha_{zz}\pi_{zz}^r + 2\alpha_{mz}\pi_{mz}^r + 2\alpha_{nz}\pi_{nz}^r$ ◄── SCHMID AND NON-SCHMID STRESS COMPONENTS

(13) $\quad \dot{\omega}_r = \underbrace{\rho_1\,\dot{\gamma}_r - \rho_2\,|\dot{\gamma}_r|\,\omega_r}_{} - \underbrace{\rho_3\,|\omega_r|^{\,m-1}\,\omega_r}_{}$ ◄── ADAPTED FROM ISOTROPIC MATERIALS

<div align="center">

DYNAMIC   STATIC
RECOVERY   RECOVERY
"BAUSCHINGER   "ANNEALING"
EFFECT"

</div>

$\qquad\qquad (+\,.005\,\{1 - e^{-a R \gamma}\}\ [\dfrac{\rho_1}{\rho_2}\ \dfrac{\Delta\gamma_r}{|\Delta\gamma_r|} - \omega_r]\,|\,\Delta\theta\,|)^{(2)}$

(20) $\quad K_{rt} = K_{ro} + \int \dot{K}_r\,dt$

(18) $\quad K_{ro} = K_1 + \underbrace{\rho_4\,\pi_{nz}^r}_{} + \underbrace{\rho_5\,|\psi_r|}_{\text{CUBE CROSS SLIP}}$

CORE WIDTH TERM FOR SHOCKLEY PARTIALS;
TENSION-COMPRESSION ASSYMMETRY
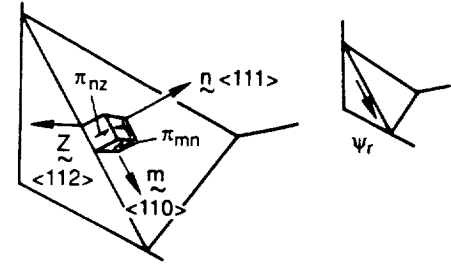
(17) $\quad \dot{K}_r = \{\sum\limits_{k=1}^{12} \underbrace{[\beta_1\,[q + (1 - q)\,\delta_{rk}] - \eta_1\,(K_{rt} - K_{ro})\,]\,|\dot{\gamma}_k|\,}_{}\} - h_1\,(K_{rt} - K_{ro})^s$

"HARDENING MODULUS"
ACCOUNTS FOR LATENT HARDENING ON OTHER SLIP SYSTEMS,
FROM HUTCHINSON TAYLOR HARDENING (EQUAL RATES ON ALL
SYSTEMS) WHEN q = 1

[1] EQUATION NUMBERS ARE THOSE REFERENCED IN THE PWA 1480 HYPELA
COMPUTER PROGRAM (REFERENCE 4).

[2] THIS TERM AVAILABLE TO CONTROL CYCLIC RELAXATION OF NONISOTHERMAL
LOOPS FOR USE IN FATIGUE LIFE PREDICTION CODE.
THE TERM IS NOT ACTIVE UNLESS ACTION IS TAKEN BY USER.

Figure 59   *Octahedral Slip System Equations*

EQUATION
NUMBER [1]

(21) $\quad \dot{\alpha}_r = \dfrac{(\tau_r - \Omega_r)|\tau_r - \Omega_r|^{d-1}}{L_{rt}^d}$

(10) $\quad \tau_r = \tau_{mn}^r$

(22) $\quad \dot{\Omega}_r = \rho_6 \, \dot{\alpha}_r - \rho_7 |\alpha_r|\Omega_r - \rho_8 |\Omega_r|^{n-1}\Omega_r$

$\left(+0.005 \, \{1 - e^{-bR\alpha}\} \left[\dfrac{\rho_6}{\rho_7} \dfrac{\Delta\alpha_r}{|\Delta\alpha_r|} - \Omega_r \right]|\Delta\theta| \right)$ [2]
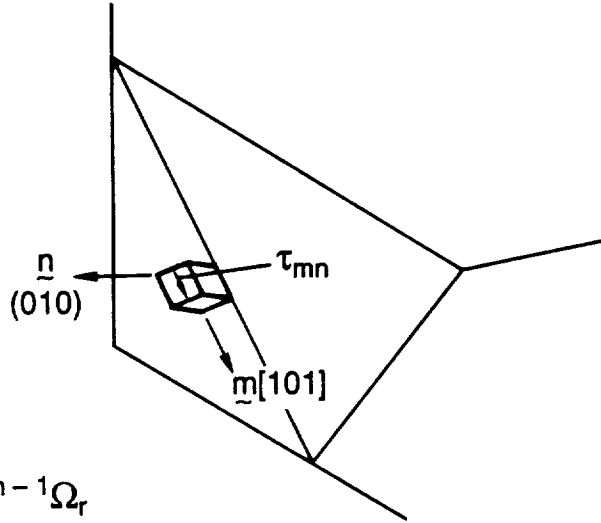
(25) $\quad L_{rt} = L_{ro} + \int \dot{L}_r \, dt$

$\quad L_{ro} = L_1$

(23) $\quad \dot{L}_r = \{\sum\limits_{k=1}^{6} [\beta_2 - \eta_2 \, (L_{rt} - L_{ro})] \, |\dot{\alpha}_k| \} - h_2 \, (L_{rt} - L_{ro})^u$

[1] EQUATION NUMBERS ARE THOSE REFERENCED IN THE PWA 1480 HYPELA COMPUTER PROGRAM (REFERENCE 4).

[2] THIS TERM IS AVAILABLE TO CONTROL CYCLIC RELAXATION OF NONISOTHERMAL LOOPS FOR USE IN A FATIGUE LIFE PREDICTION CODE. THE TERM IS NOT ACTIVE UNLESS ACTION IS TAKEN BY THE USER.

Figure 60   Cube Slip System Equations

237

$$\dot{\gamma}_r = \frac{(\pi_r - \omega_r) \mid \pi_r - \omega_r \mid^{P-1}}{K_{rt}^P}$$ $$\dot{\alpha}_r = \frac{(\tau_r - \Omega_r) \mid \tau_r - \Omega_r \mid^{d-1}}{L_{rt}^d}$$

$K_{rt} = K_1$ (NOT EVOLUTIONARY) $L_{rt} = L_1$ (NOT EVOLUTIONARY)

$$\dot{\omega}_r = \rho_1 \dot{\gamma}_r - \rho_2 \mid \dot{\gamma}_r \mid \omega - \rho_3 \mid \omega_r \mid^{m-1} \omega_r$$ $$\dot{\Omega}_r = \rho_6 \dot{\alpha}_r - \rho_7 \mid \dot{\alpha}_r \mid \Omega_r - \rho_8 \mid \Omega_r \mid^{n-1} \Omega_r$$

$$\left(+ 0.005 \left\{ 1 - e^{-aR\gamma} \right\} \left[\frac{\rho_1}{\rho_2} \frac{\Delta\gamma_r}{\mid \Delta\gamma_r \mid} - \omega_r \right] \mid \Delta\theta \mid \right)^{(1)}$$ $$\left(+ 0.005 \left\{ 1 - e^{-bR}\alpha \right\} \left[\frac{\rho_6}{\rho_7} \frac{\Delta\alpha_r}{\mid \Delta\alpha_r \mid} - \Omega_r \right] \mid \Delta\theta \mid \right)^{(1)}$$

TEMPERATURE DEPENDENT CONSTANTS	TEMPERATURE INDEPENDENT CONSTANTS	TEMPERATURE DEPENDENT CONSTANTS	TEMPERATURE INDEPENDENT CONSTANTS
P, K, ρ_1, ρ_2	$\rho_3 = 10^{-12}$ $m = 3$	d, L, ρ_6, ρ_7	$\rho_8 = 10^{-12}$ $n = 3$

(1) THESE TERMS ARE AVAILABLE TO CONTROL CYCLE-BY-CYCLE
RELAXATION/DRIFT OF NONISOTHERMAL LOOPS FOR USE IN A
FATIGUE LIFE PREDICTION CODE. THESE TERMS ARE NOT ACTIVE
UNLESS ACTION IS TAKEN BY THE USER.

Figure 61   *Active Terms In the Constitutive Model for PWA 1480*
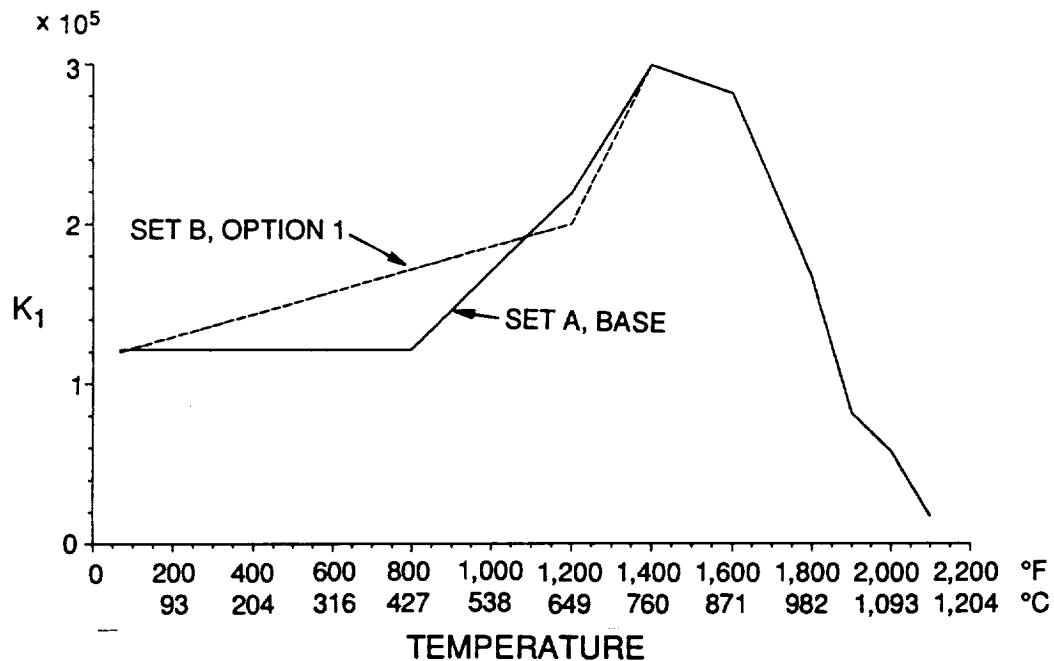
Figure 62   *PWA 1480 Octahedral Slip System Drag Stress Constant, K_1, Vs. Temperature*

238
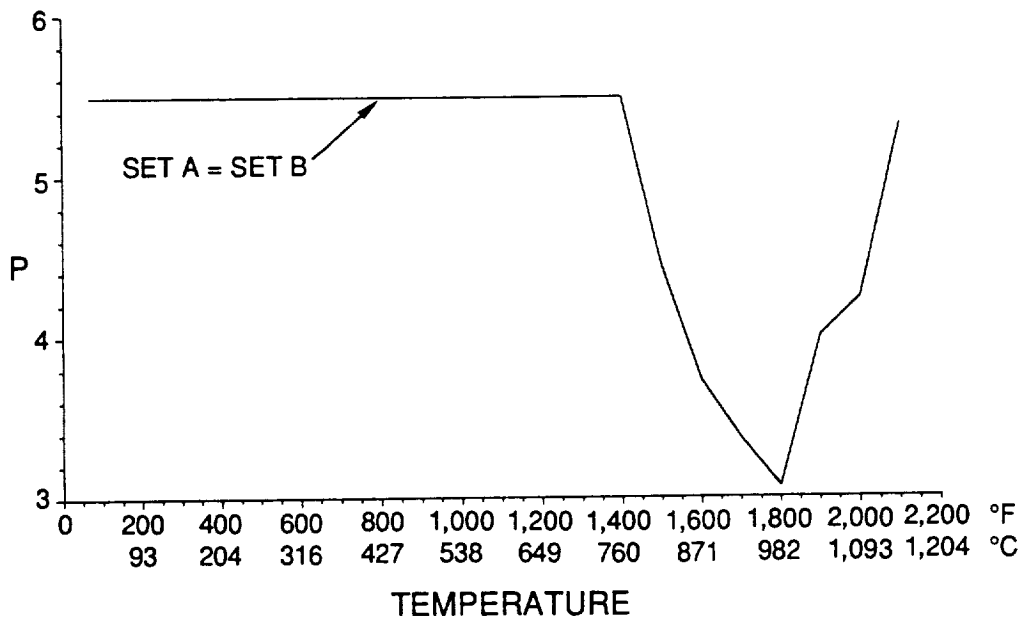
Figure 63   *PWA 1480 Octahedral Slip System Inelastic Strain Rate Exponent, p, Vs. Temperature*
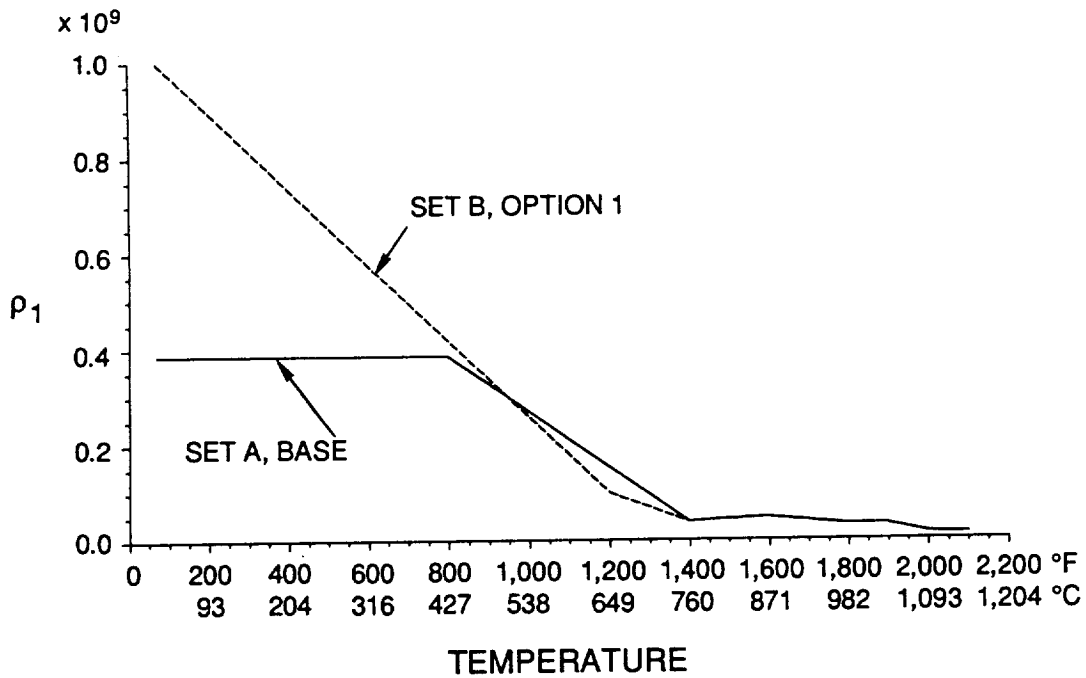
Figure 64   *PWA 1480 Octahedral Slip System Kinematic Hardening Constant, p_1, Vs. Temperature*

239
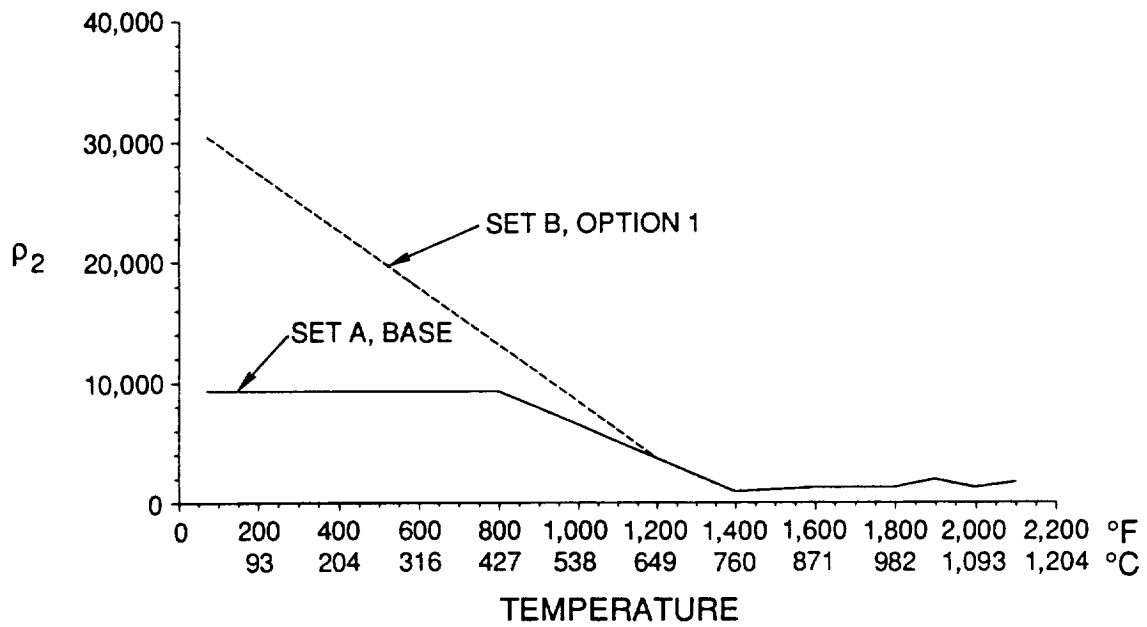
Figure 65   *PWA 1480 Octahedral Slip System Dynamic Equilibrium Stress Recovery Constant, ρ_2, Vs. Temperature*
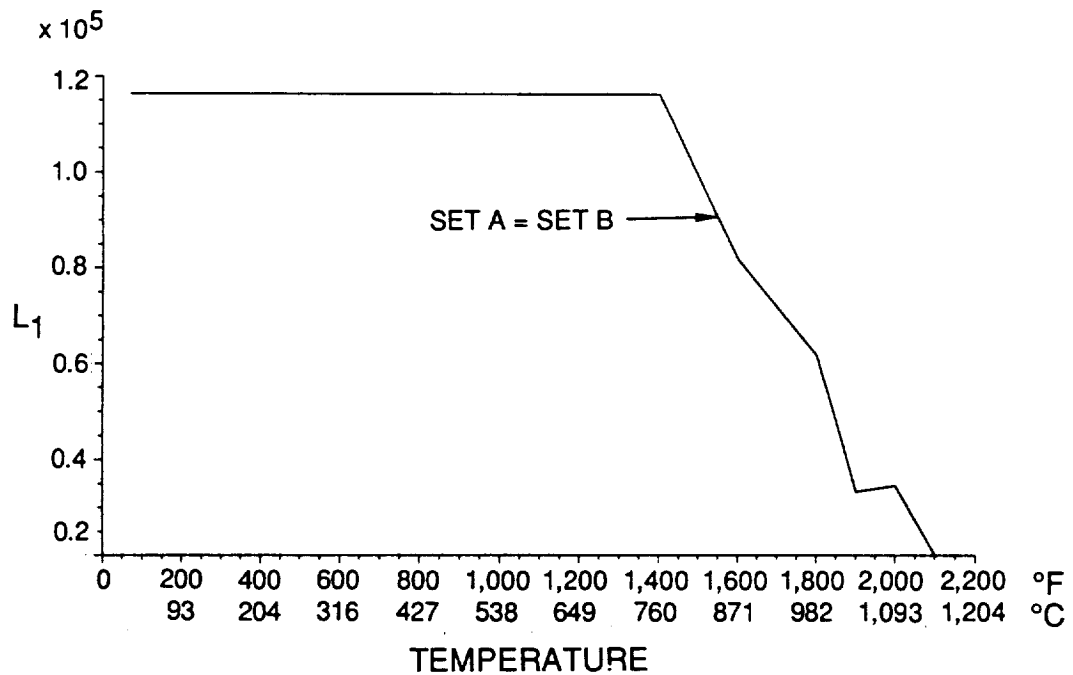
Figure 66   *PWA 1480 Cube Slip System Drag Stress Constant, L_1, Vs. Temperature*
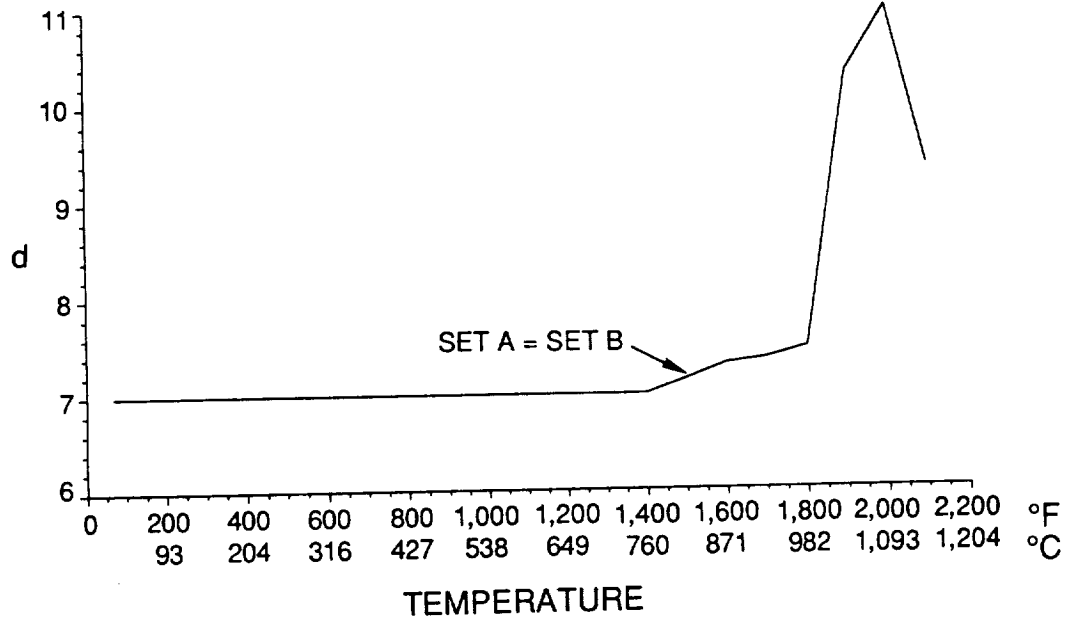
Figure 67   *PWA 1480 Cube Slip System Inelastic Strain Rate Exponent, d, Vs. Temperature*
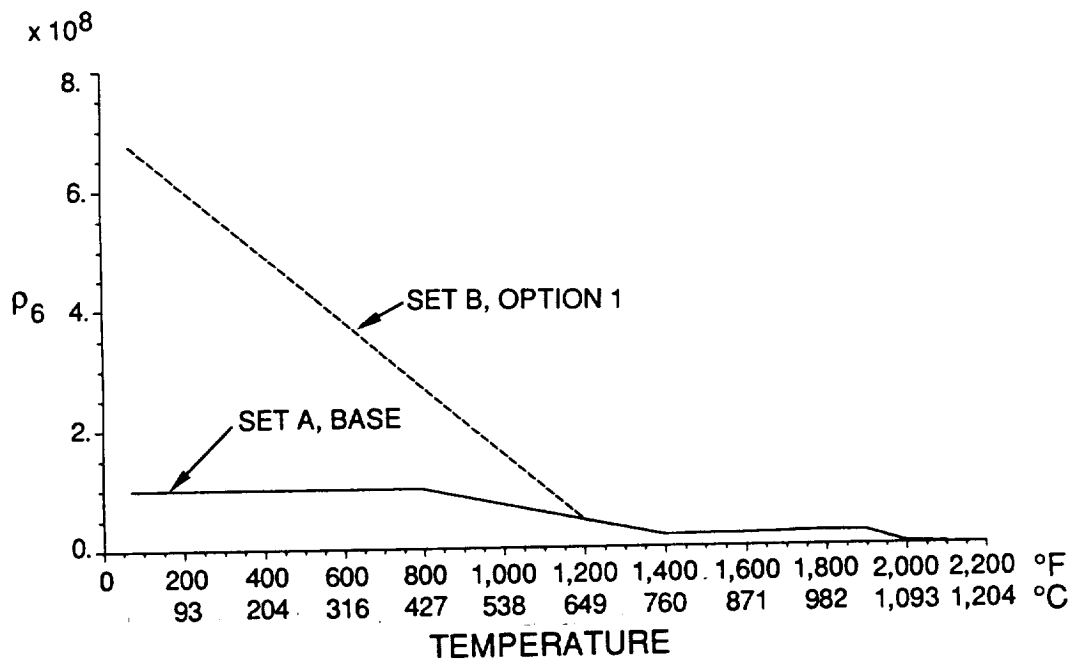
Figure 68   *PWA 1480 Cube Slip System Kinematic Hardening Constant, ρ_6, Vs. Temperature*

241
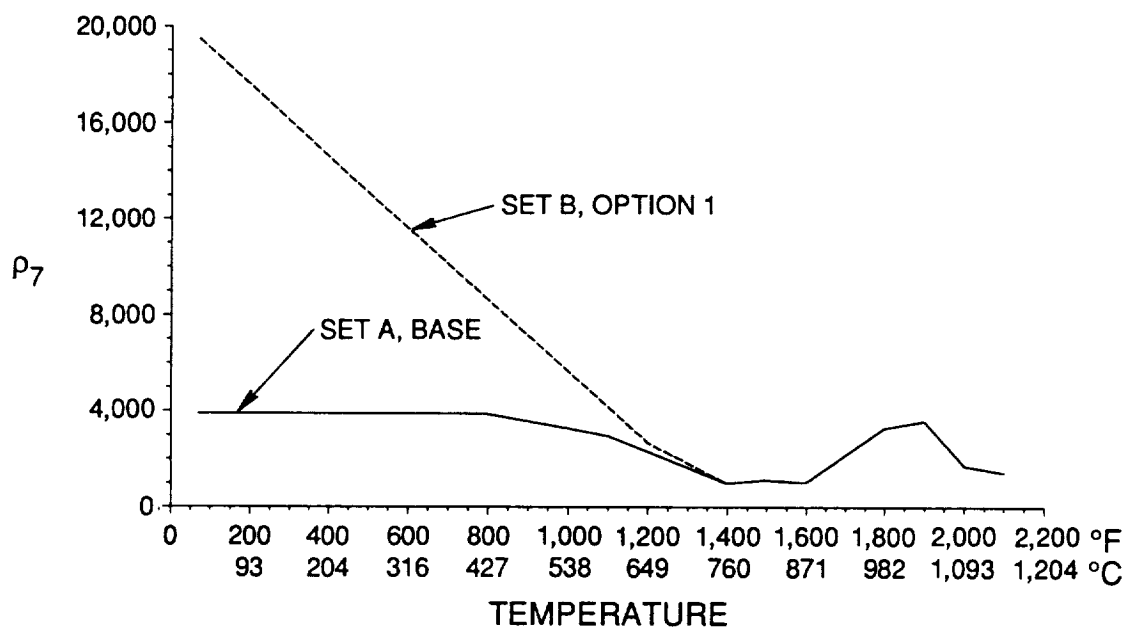
Figure 69   *PWA 1480 Cube Slip System Dynamic Equilibrium Stress Recovery Constant, ρ_7, Vs. Temperature*
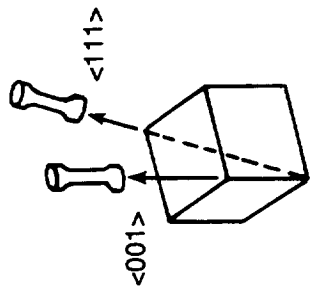
1600°F STEADY STATE CYCLIC HYSTERESIS LOOPS
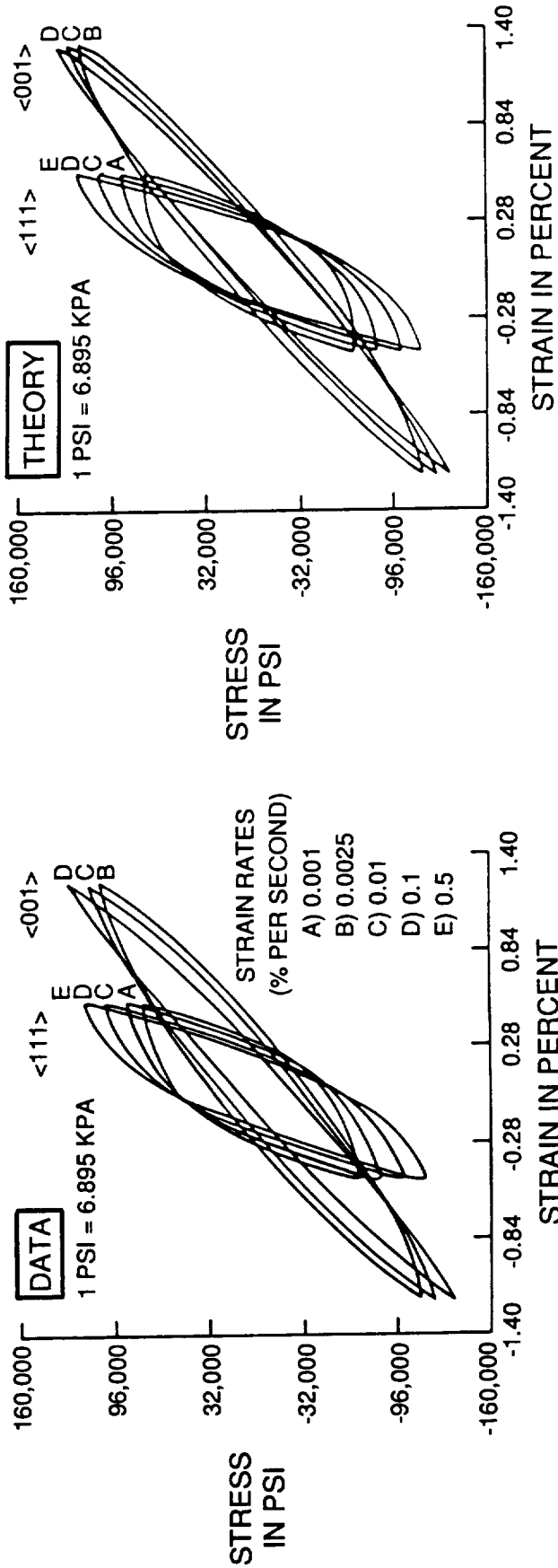
Figure 70   *Single Crystal Constitutive Model Based On Crystallographic Slip Theory Captures the Observed Orientation and Rate Dependent Deformation Behavior*

GLOBAL STIFFNESS MATRIX, K_{ij}, CHANGES DURING EACH INCREMENT IF TEMPERATURE CHANGES

$$K_{ij} \, \Delta U_i = \Delta P_i^* + \Delta P_i + \Delta R_i$$

$$\left\{ \sum \int_{VOL} B_{ik}^T D_{kl} B_{lj} \, dV \right\} \Delta U_i = \sum \int_{VOL} B_{ij}^T (\Delta G_j + \delta_j \, \alpha \, \Delta T) \, dV + \Delta P_i + \Delta R_i$$

ELASTIC CONSTANTS
AT CURRENT TEMPERATURE

THERMAL STRESS

APPLIED LOAD

INELASTIC STRESS INCREMENT

RESIDUAL LOADS FROM PREVIOUS INCREMENT

REFERENCE STIFFNESS ALGORITHM INCORPORATES STIFFNESS CHANGE IN LOAD VECTOR

$$\left\{ \sum \int_{VOL} B_{ik}^T D_{kl}^0 B_{lj} \, dV \right\} \Delta U_i = \sum \int_{VOL} B_{ij}^T (\Delta G_j^* + \delta_j \, \alpha \, \Delta T) \, dV + \Delta P_i + \Delta R_i$$

CONSTANT

$$\Delta G_j^* = \Delta G_j + (D_{jq}^0 - D_{jq}) \, \Delta \varepsilon_q^{TOT}$$

CHANGE IN STIFFNESS DUE TO TEMPERATURE

(FOR AN ISOTHERMAL INCREMENT)
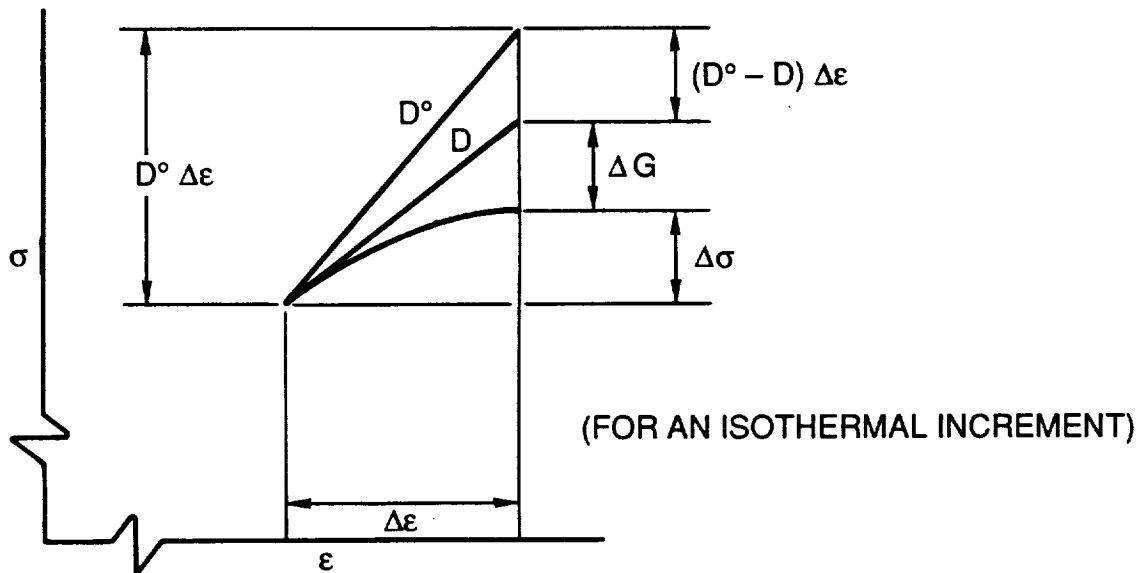
Figure 71   *Reference Stiffness Algorithm*

244

$$\Delta t_{eff} = F_1 \, \Delta t_{real} + F_2 \, b$$

$$b = \frac{\sqrt{2/3 \, \Delta e^*}}{\text{REFERENCE STRAIN RATE}}$$

$$\sqrt{2/3 \, \Delta e^*} = \text{SUBINCREMENT EFFECTIVE STRAIN}$$
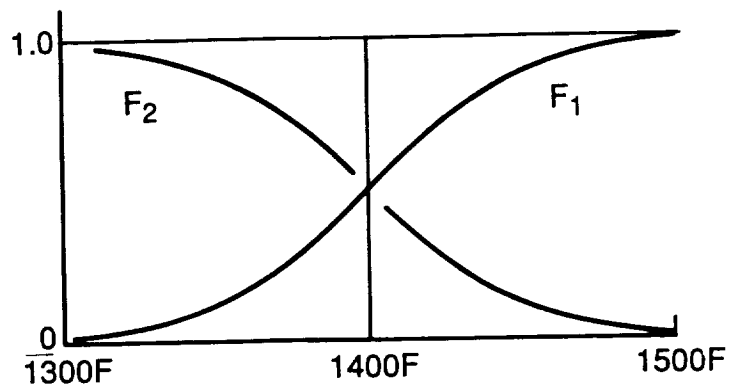
Figure 72   *Constitutive Model Is Rate Independent for T < 1300F*
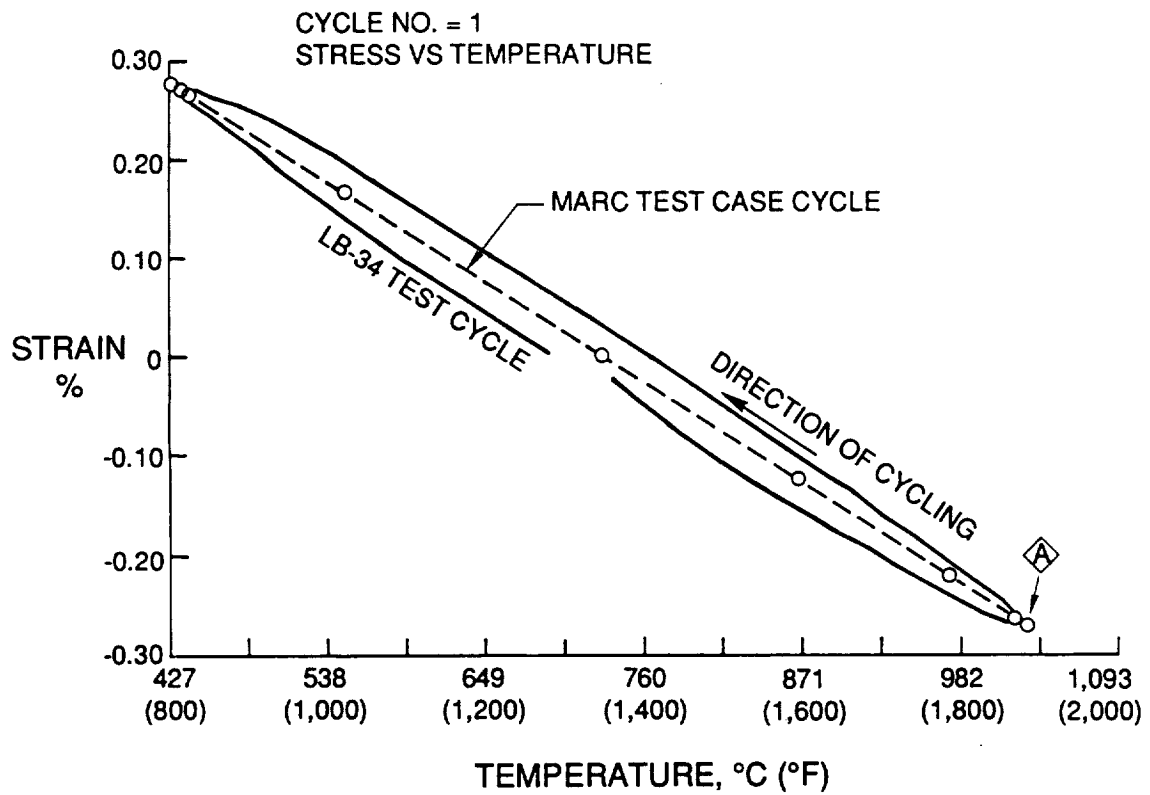
Figure 73   *Strain Vs. Temperature Waveforms of LB–34 Compared to the One Used In the Test Case*

246

CYCLE NO. = 1
STRESS VS MECHANICAL STRAIN
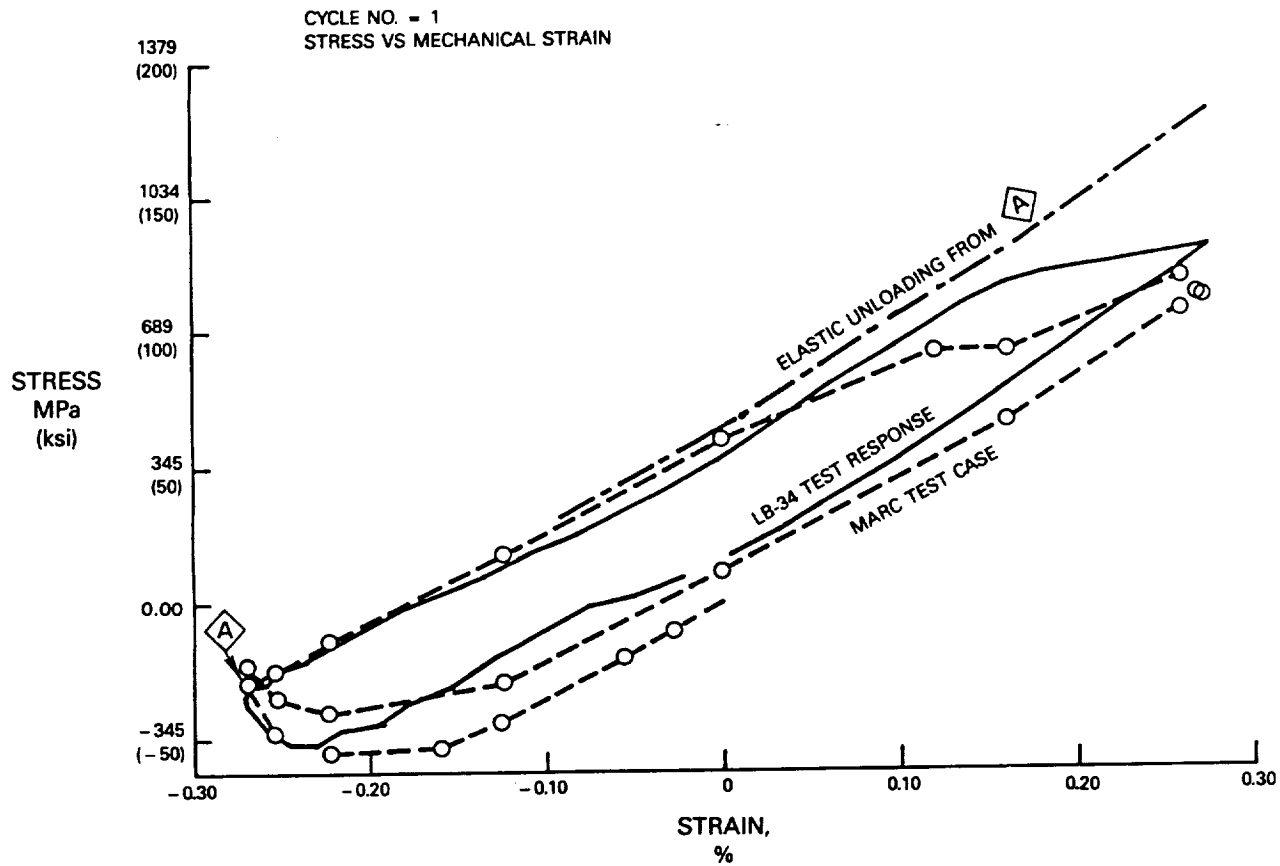
Figure 74   *Predicted Vs. Actual Behavior of Specimen LB–34*

$$\dot{\varepsilon}_p = f\left(\frac{\sigma - \omega}{K}\right)$$

COLD

COLD

$(\sigma - \omega)$

$(\sigma - \omega)$

ELASTIC

ELASTIC

ω

ω

HOT

HOT

$$\dot{\omega} = \rho_1\,\dot{\varepsilon}_p - \rho_2|\dot{\varepsilon}_p|\omega \qquad \dot{\omega} = \rho_1\,\dot{\varepsilon}_p - \rho_2|\dot{\varepsilon}_p|\omega + c\dot{T}\left(\frac{\rho_1}{\rho_2}\,\frac{\dot{\varepsilon}_p}{|\dot{\varepsilon}_p|} - \omega\right)$$

WITHOUT TEMPERATURE
RATE TERM

WITH TEMPERATURE
RATE TERM
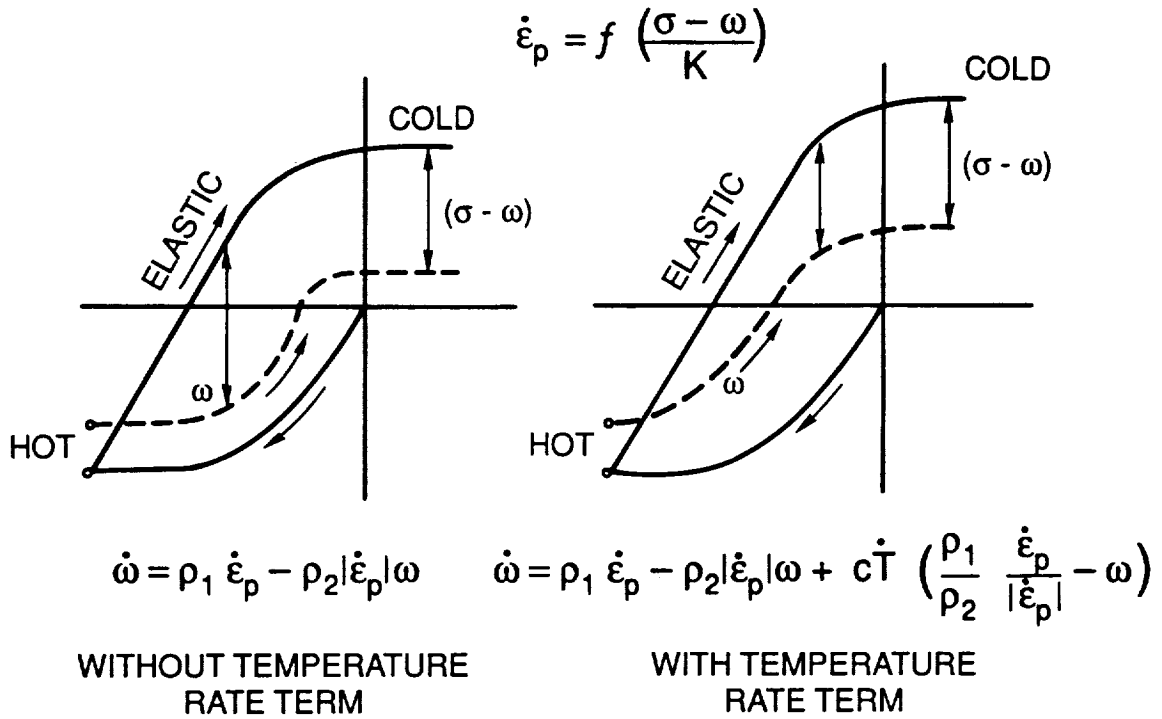
Figure 75   Evolution of Back Stress Modified to Reduce Overstress During Non-Isothermal Elastic
Unloading
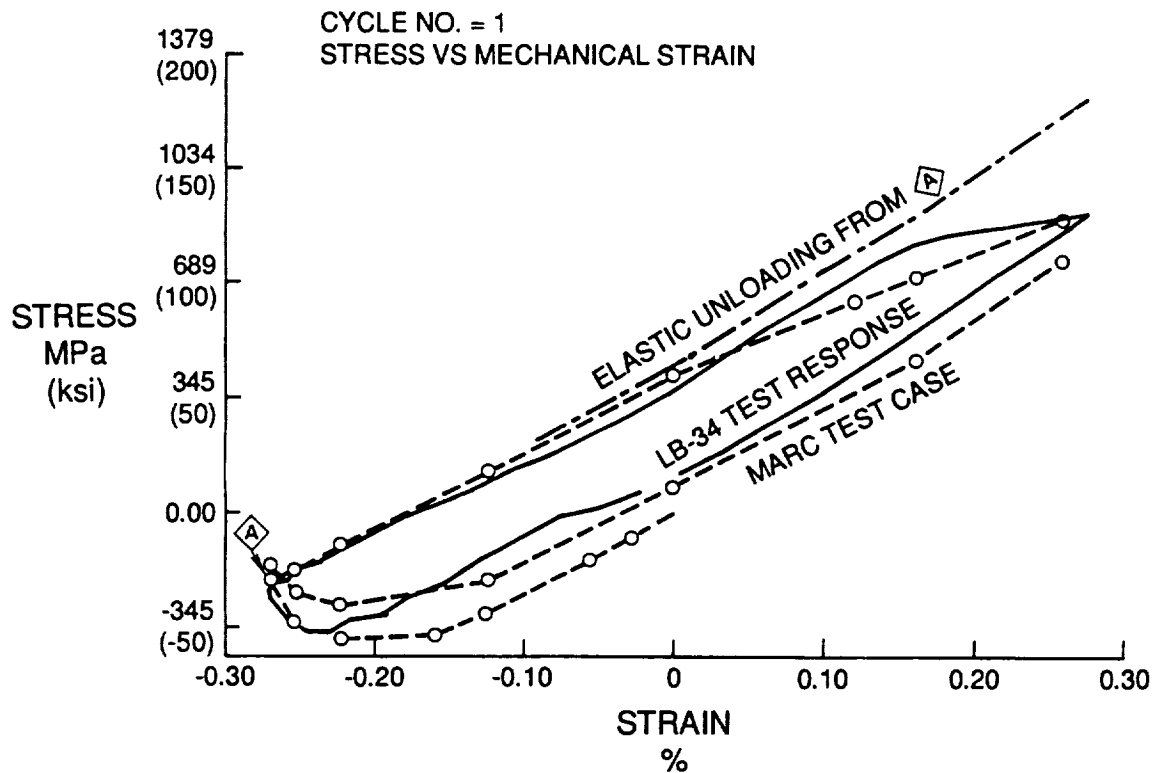
Figure 76   Predicted Vs. Actual Behavior of Specimen LB-34 With Temperature Rate Terms In-
cluded In the Back Stress Evolution Equations

248
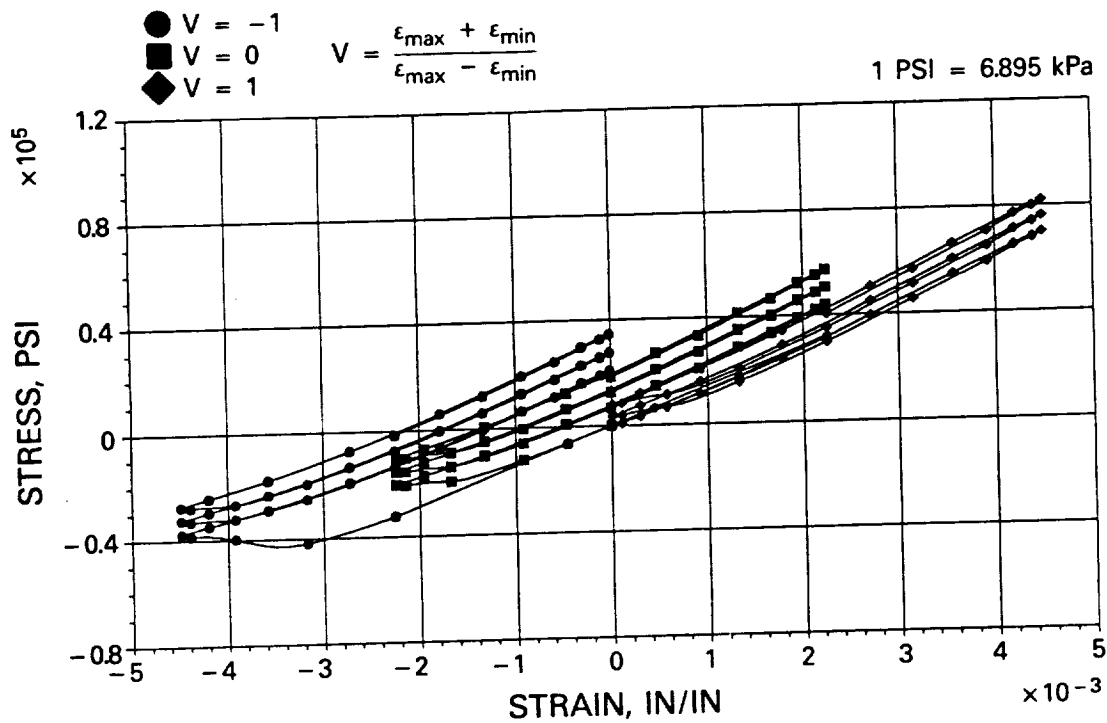
Figure 77 *PWA 1480 Constitutive Model Prediction of <001> PWA 1480 Undergoing Out-of-Phase TMF Cycling at Three Different Mean Strains – Predictions were made without equilibrium stress temperature rate terms.*
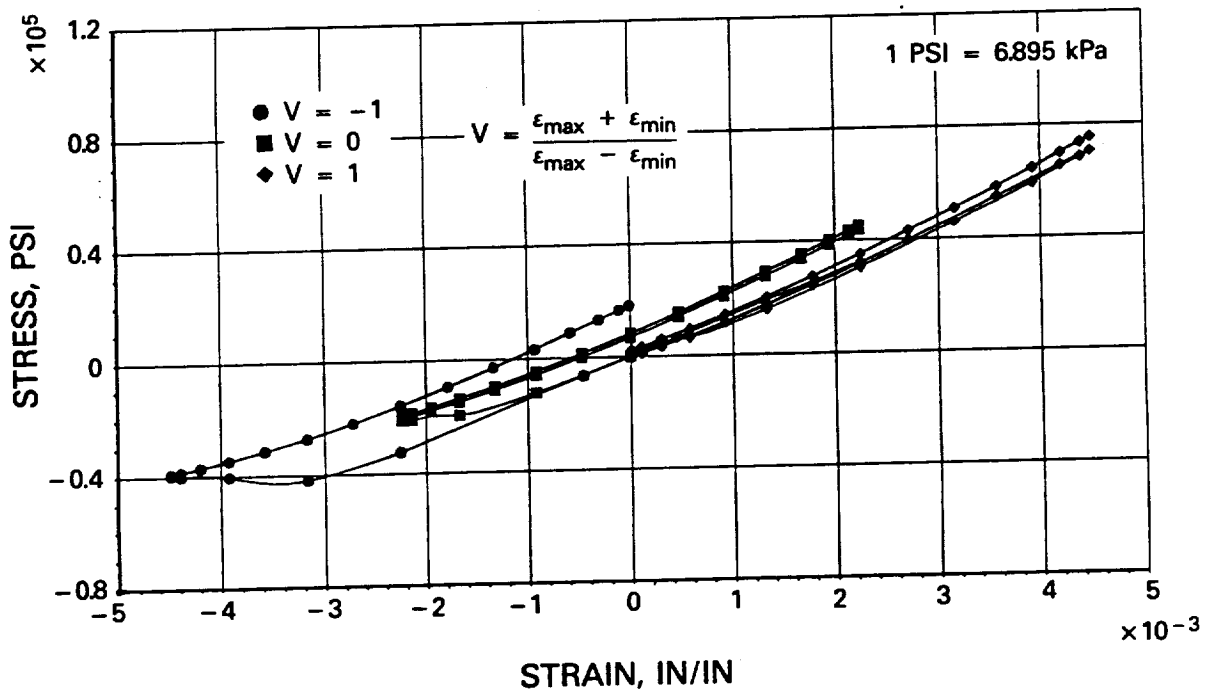
Figure 78 *PWA 1480 Constitutive Model Prediction of <001> PWA 1480 Undergoing Out-of-Phase TMF Cycling at Three Different Mean Strains – Predictions were made with the equilibrium stress temperature rate terms.*
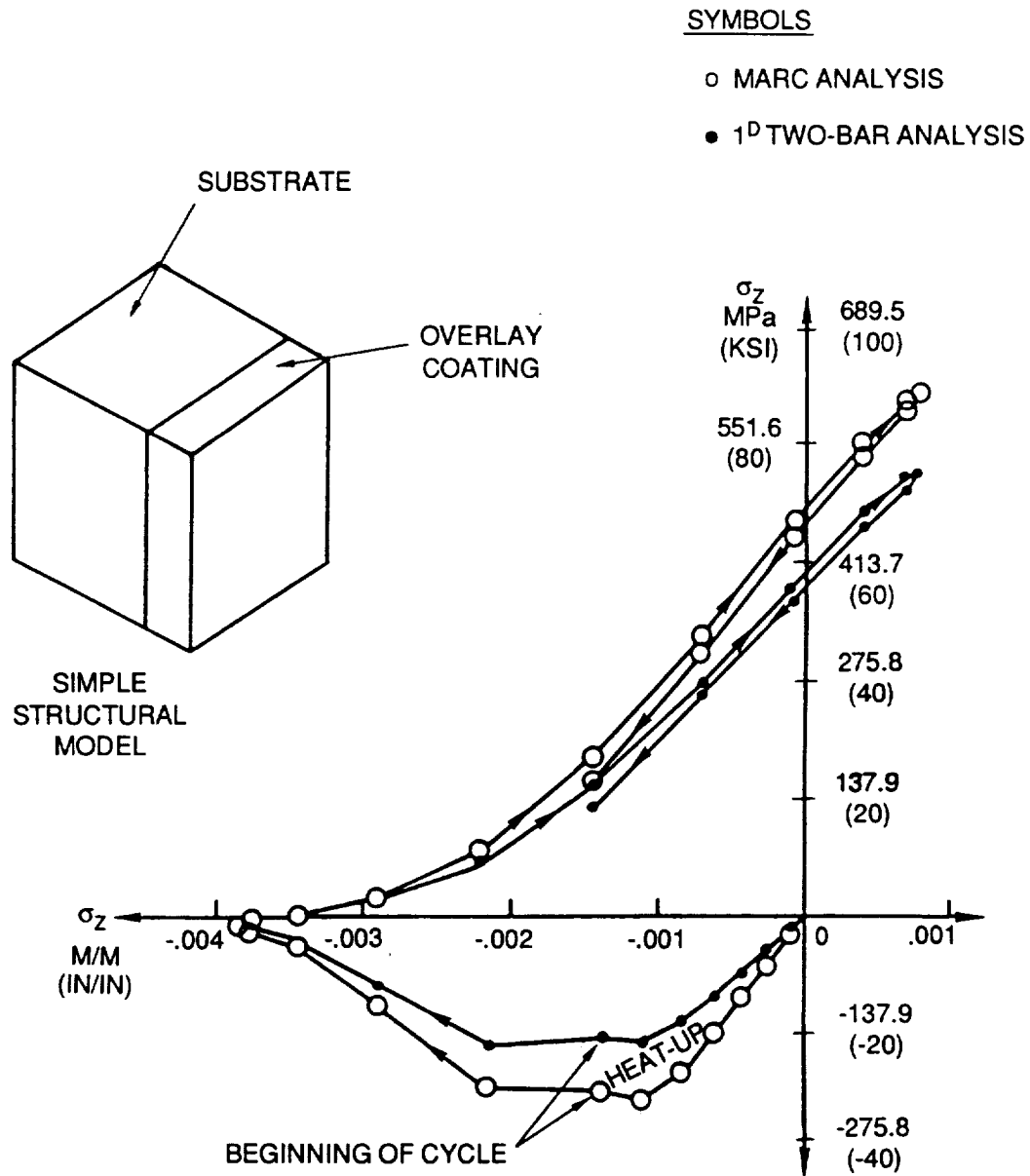
Figure 79   *Predicted PWA 286 Coating Response to 427–1038°C (800–1900°F) ±0.15 percent, 1 cpm, Out-of-Phase Uniaxial TMF Test. A hypothetical material with elastic moduli equivalent to <001> PWA 1480 was assumed for the substrate.*
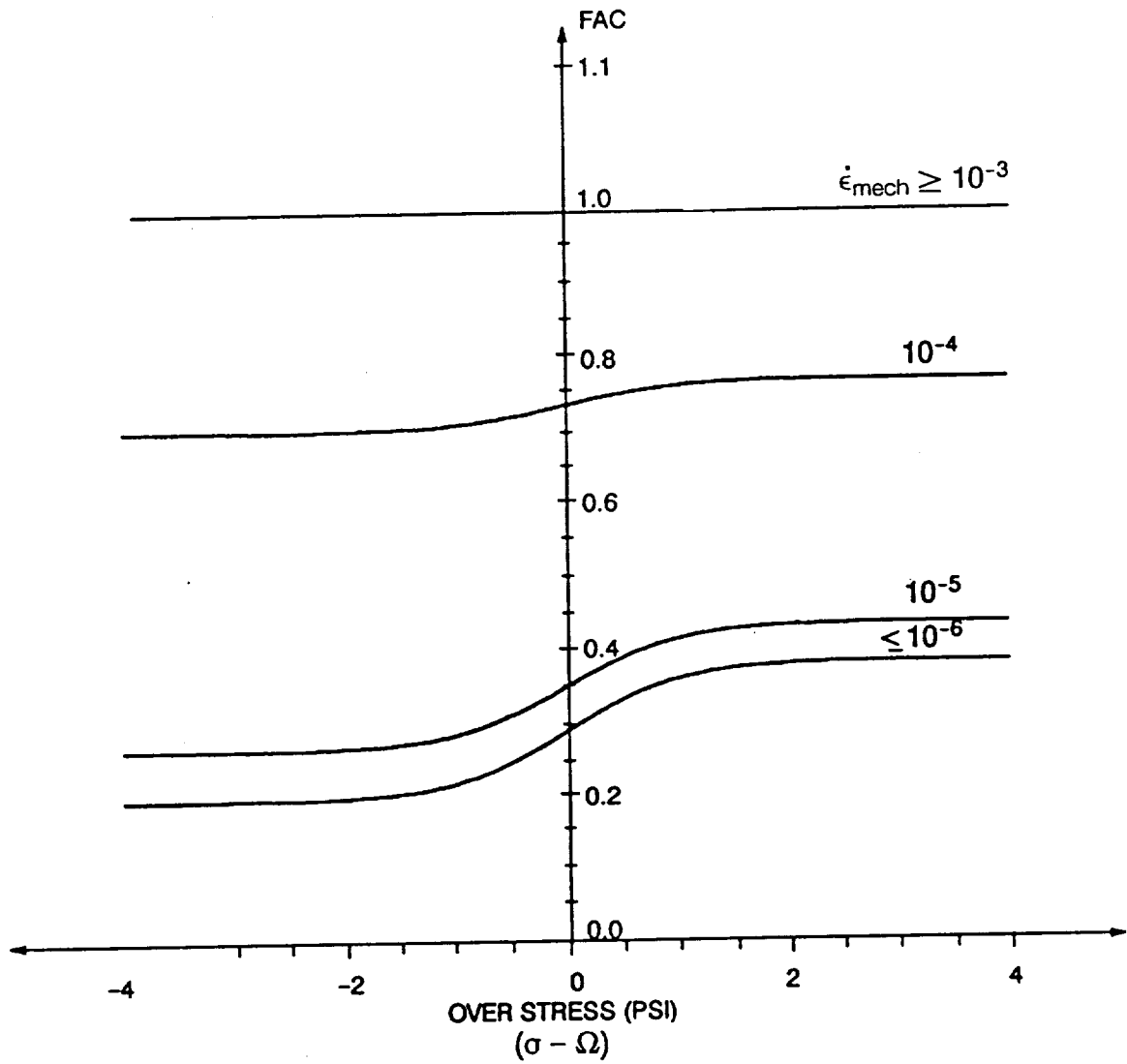
Figure 80   *Hold Time Function, Fac. For Compression Holds Fac = 0.19 and for Tension Holds
Fac = 0.38*
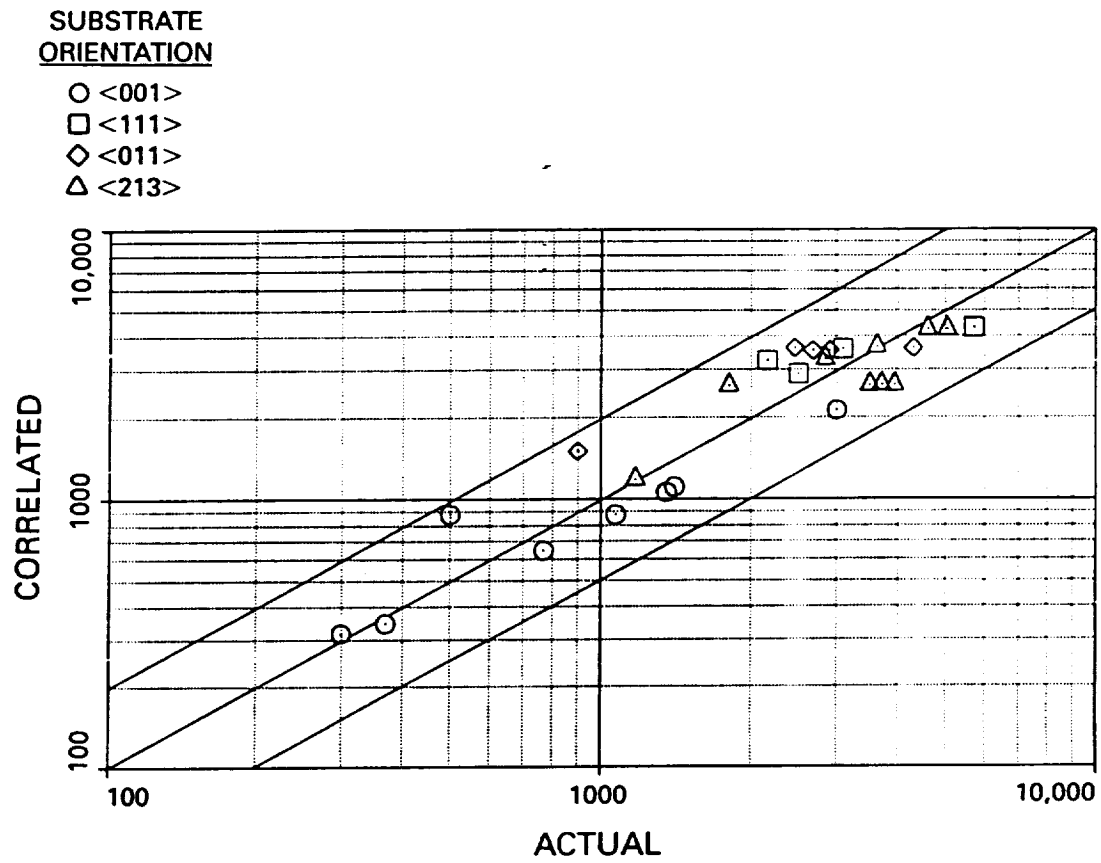
Figure 81   *PWA 286 Overlay Coating TMF Life Model Correlation*
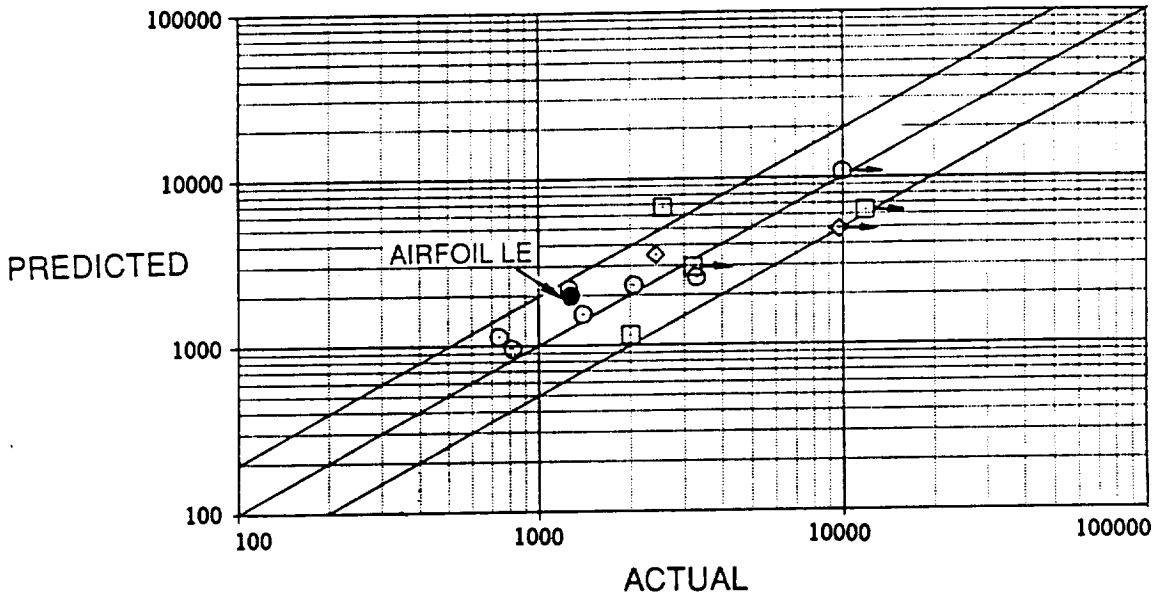
Figure 82   *PWA 286 Overlay Coating TMF Life Model Prediction of the Verification Data Set*
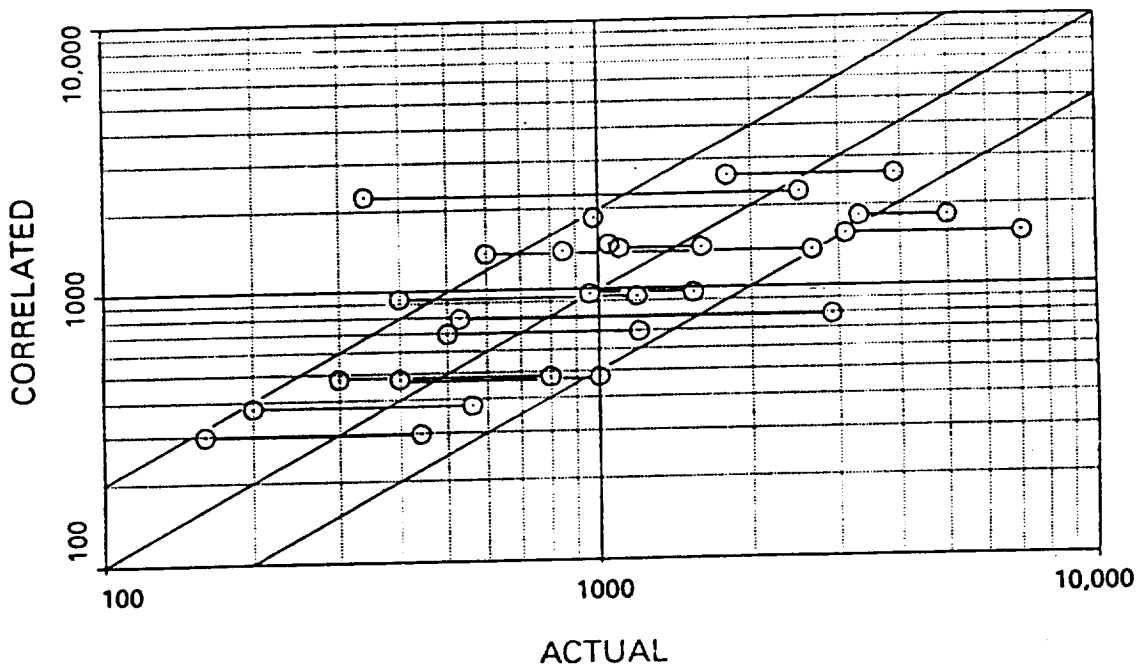
Figure 83   *PWA 1480 TMF Life Model Correlation*

CRYSTALLOGRAPHIC
ORIENTATION

O <001>
□ <111>
◇ <011>
△ <213>
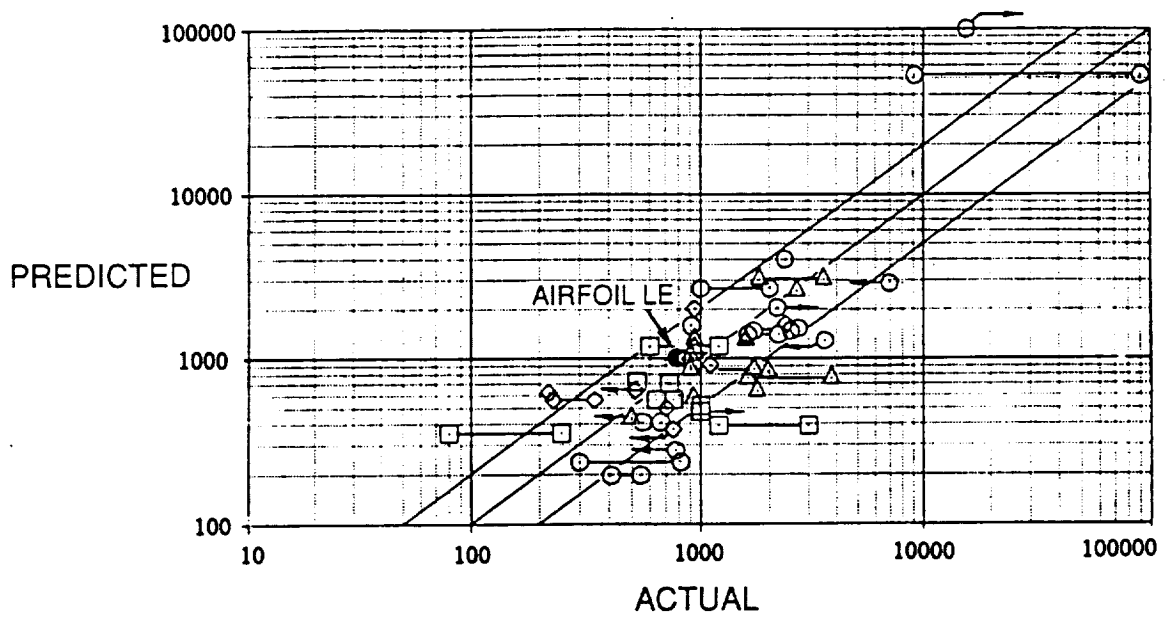
Figure 84   PWA 1480 TMF Life Model Prediction of the Verification Data Set

254

```
                    ┌─────────────────────┐
                    │  Critical Airfoil   │
                    │  Surface Location   │            Description
                    │   ϵᵢⱼ, T vs. Time   │
                    └─────────────────────┘

                    ┌─────────────────────┐      Contains Summary of cyclic
                    │     Input File      │      conditions and history
                    └─────────────────────┘

Generate Abbrev
┌──────────────┐    ┌─────────────────────┐      Generates ϵᵢⱼ, T increments
│  New Input   │◄───│     GENERATE        │      suitable for nonlinear analysis
│    File      │    └─────────────────────┘      and the simplified structural model
└──────────────┘                                 mesh and boundary conditions
Input Data           Generate │ Output
┌──────────────┐    ┌──────────────┐
│  Input Plot  │◄───│   PLINPUT    │◄──────
│    File      │    └──────────────┘
└──────────────┘
                    ┌──────────────┐
                    │   HYPELA     │───►  ┌─────────────────┐   Conducts simplified nonlinear
                    └──────────────┘      │     STRESS      │   structural analysis of multi-layered
Stress Output                            └─────────────────┘   structures
┌──────────────┐
│ σ,ϵ Output File │◄──
└──────────────┘         Strsdump │ Output
Output Data
┌──────────────┐    ┌──────────────┐
│  Output Plot │◄───│   PLOUTPUT   │◄──────
│    File      │    └──────────────┘
└──────────────┘
                    ┌─────────────────────┐      Post-processes simplified structural
                    │       POST          │      analysis results to obtain required
                    └─────────────────────┘      parameters for life prediction
                      Post │ Output
Life Output
┌──────────────┐    ┌─────────────────────┐
│Life Prediction│◄──│       LIFE          │      Calculates cyclic life
│ Output File   │   └─────────────────────┘
└──────────────┘
```

Figure 85   *A Typical LAYER Program Fatigue Life Analysis Flowchart Showing the Input and Output Files Created*
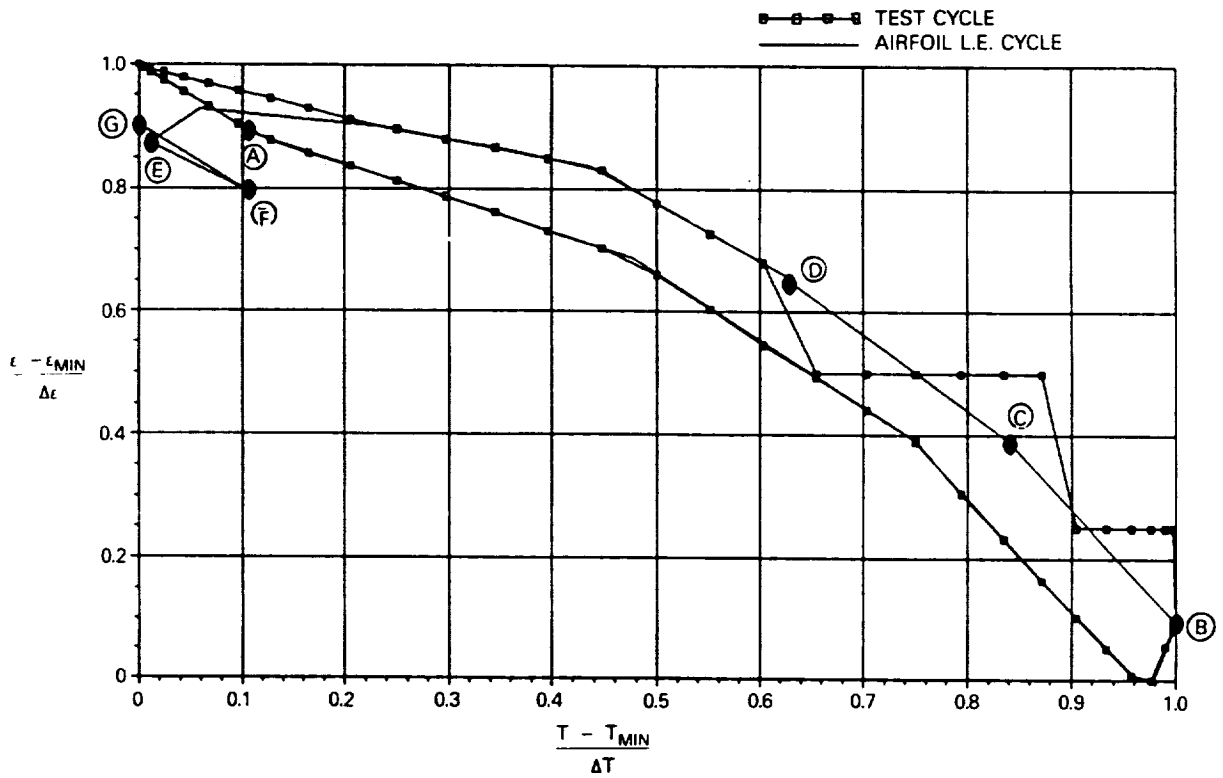
Figure 86   *Normalized Strain Vs. Normalized Temperature Comparison of Airfoil Leading Edge and Verification Test Cycles. See Table 15 for Description of Points A through G.*
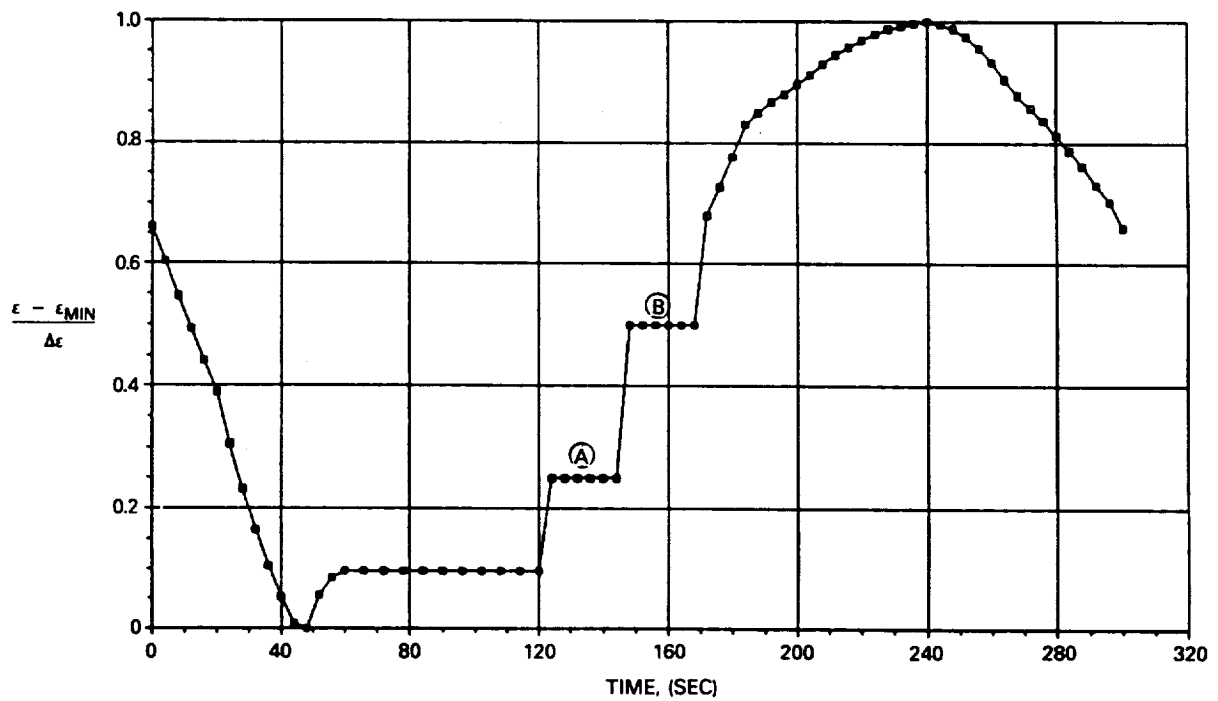
Figure 87   *Normalized Strain Vs. Time for Verification Test. Strain holds labelled A and B are designed to simulate climb and cruise holds.*

256
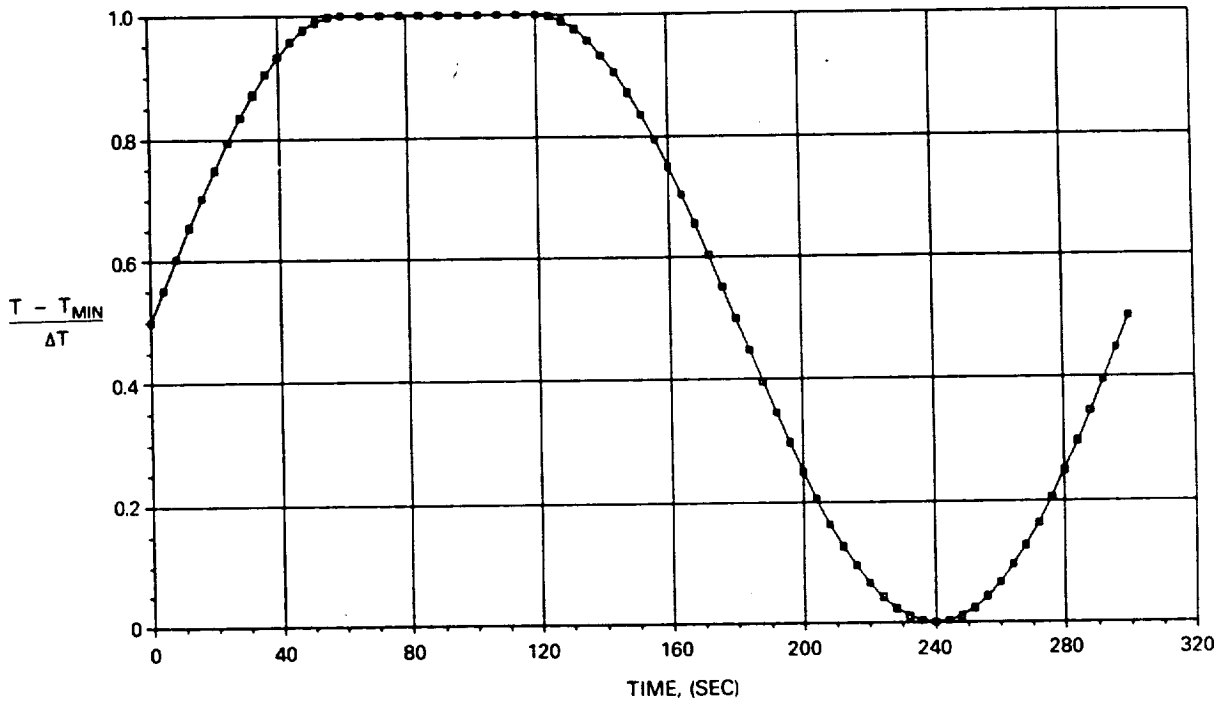
Figure 88 *Normalized Temperature Vs. Time for Verification Test. Hold at maximum temperature is designed to simulate steady state takeoff.*
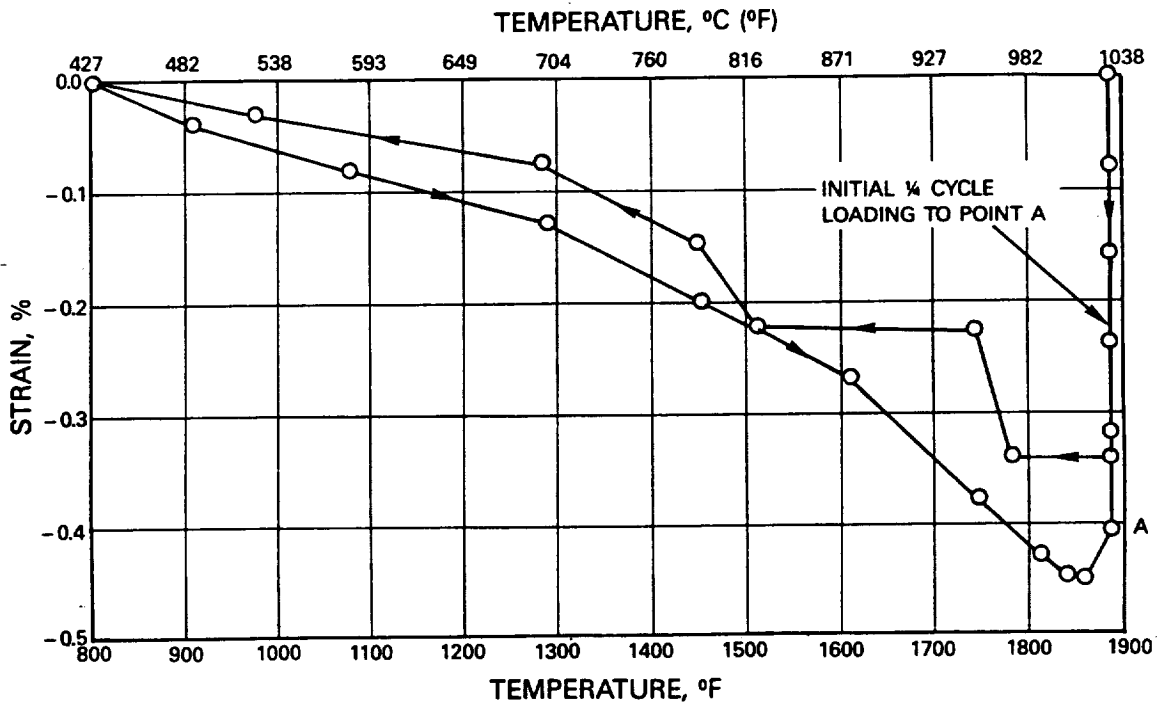
Figure 89 *Experimental Strain–Temperature History for Verification TMF Test of Specimen JB–135. $T_{max} = 1029°C$ (1885°F).*
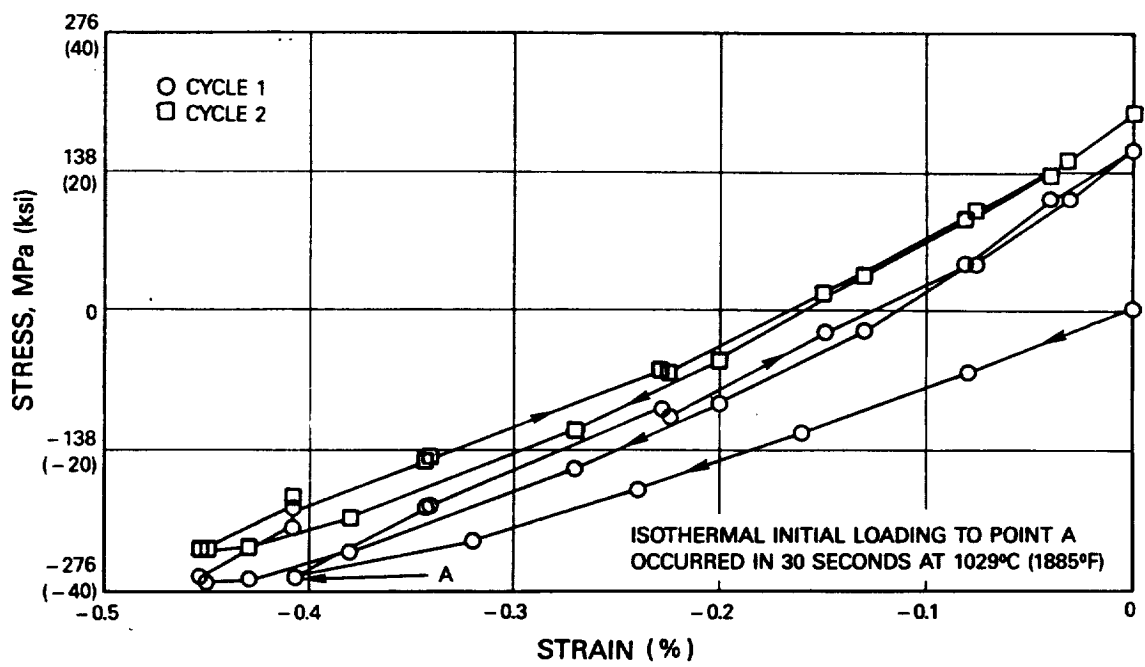
Figure 90   *Initial Hysteresis Loops for Specimen JB-135*

258

(A)
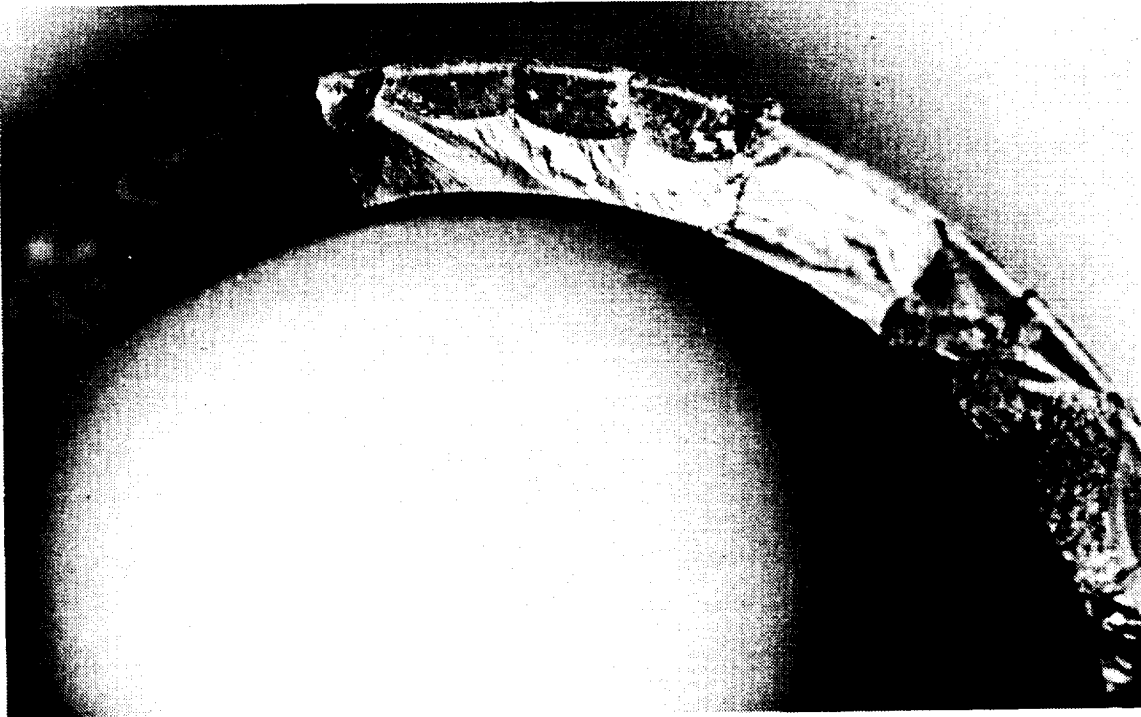
(B)

Figure 91   Fracture Surface Appearance of Verification TMF Test Specimen JB–135 After Testing At
427–1038°C (800–1900°F), 0 to –0.45%, Using the Airfoil Cycle Defined In Figures
86–88 for 5059 Cycles. (A) Appearance of major fatigue crack region and (B) Typical
appearance of secondary fatigue cracks.

A) TENSILE AND CREEP TEST SPECIMEN (M26)

10.65 cm
(4.192 in)

3.80 cm
(1.495 in)

1.27 cm
(0.50 in)

0.64 cm
(0.252 in)
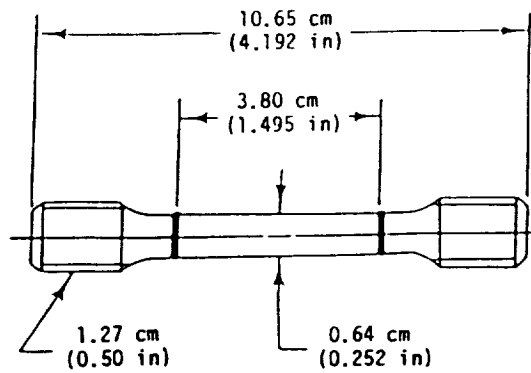
B) CYCLIC CONSTITUTIVE TEST SPECIMEN (LED 41784)

8.89 cm
(3.50 in)

6.35 cm
(2.50 in)

2.79 cm
(1.10 in)

1.02 cm
(0.40 in)

0.76 cm
(0.30 in)

1.27 cm
(0.50 in)
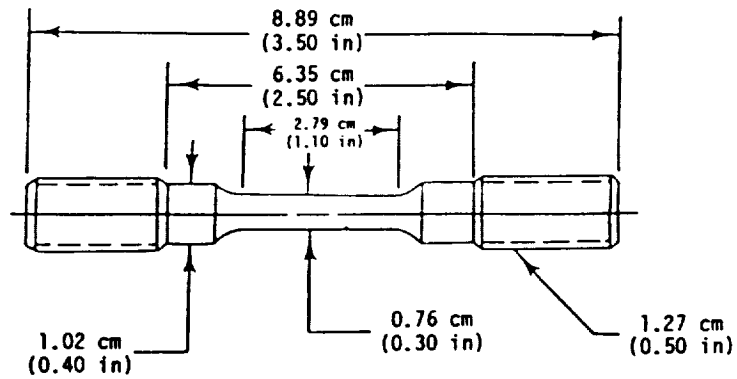
Figure 92   *Specimen Designs for Alloy 185 Single Crystal Property Tests*
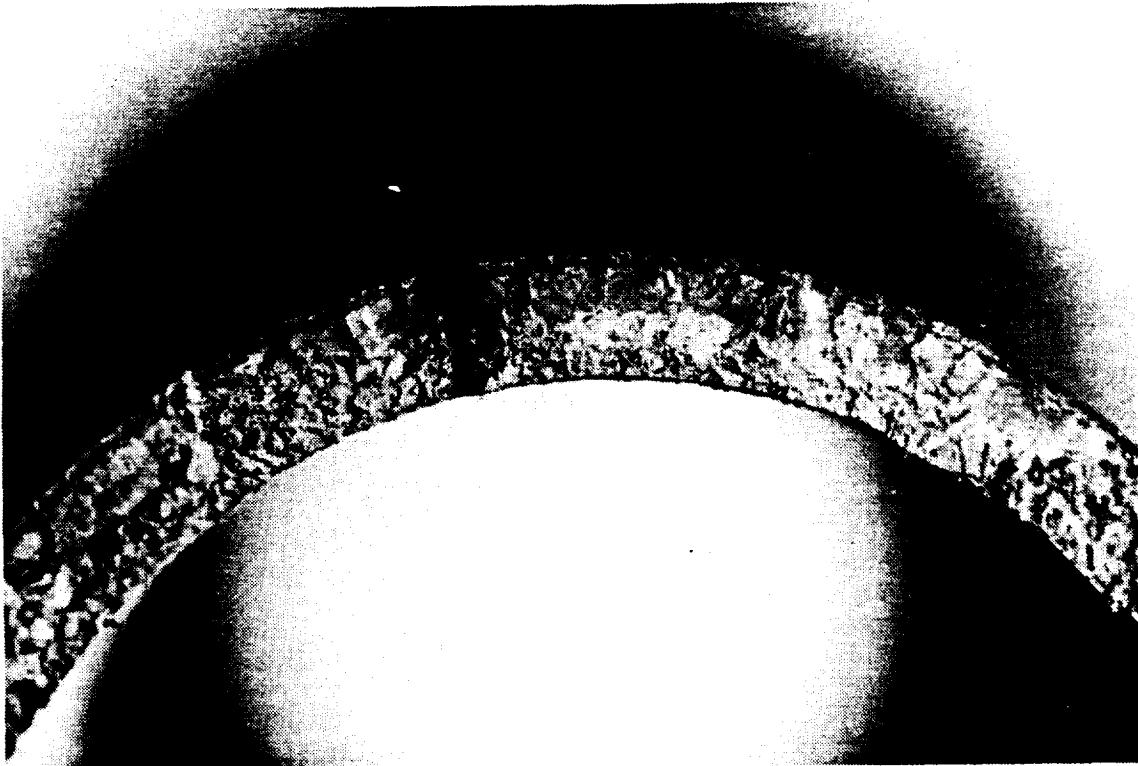
Figure 93   Typical Fracture Surface Features of PWA 286 Coated Alloy 185 Subjected to
428-1038°C (800-1900°F) Out-of-Phase TMF Testing
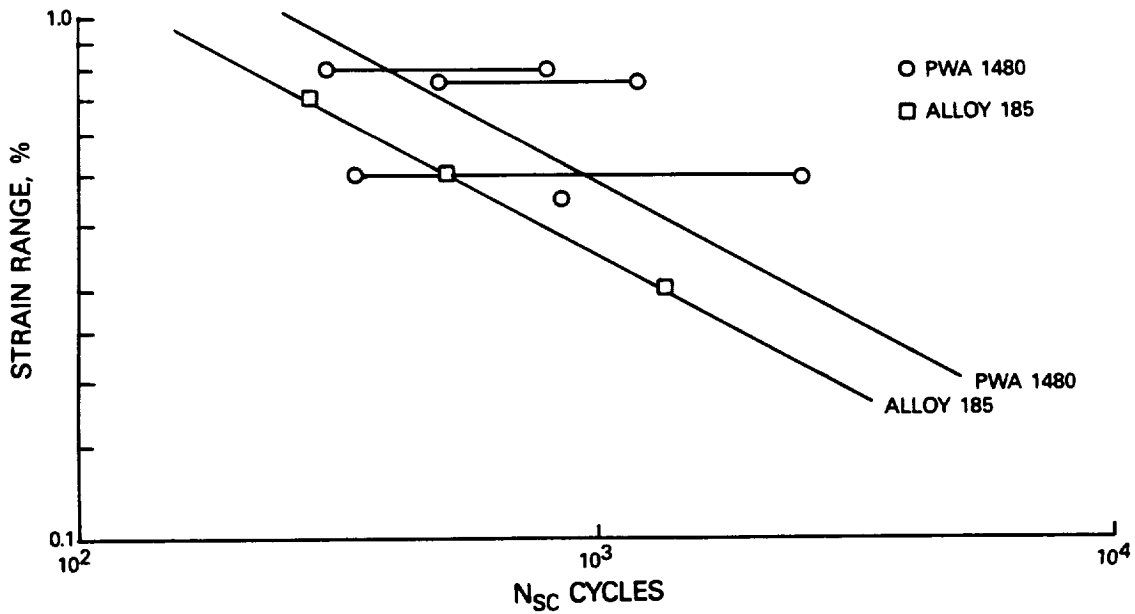
Figure 94   Comparison of PWA 1480 and Alloy 185 Overlay Coated 427-1038°C (800-1900°F)
Out-of-Phase TMF Tests

261
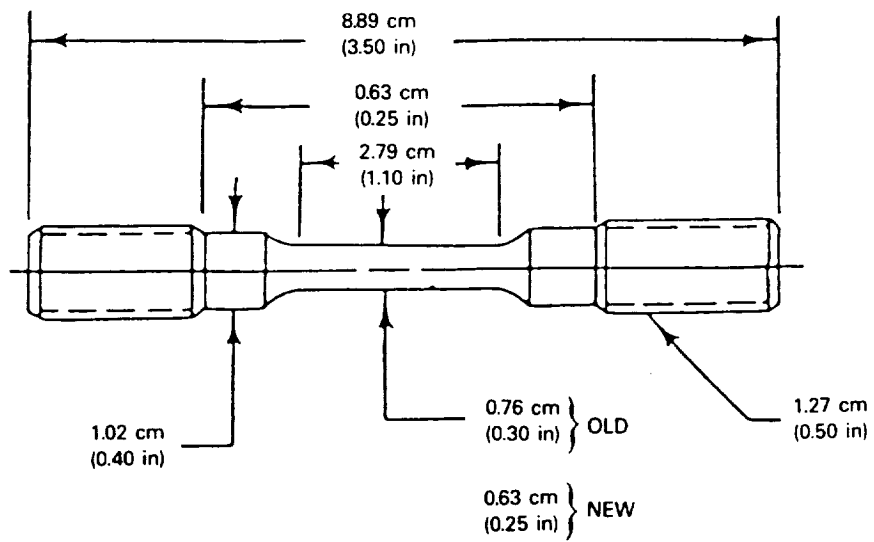
Figure 95   *Smooth, Uniaxial Specimen, LED 41784*

262
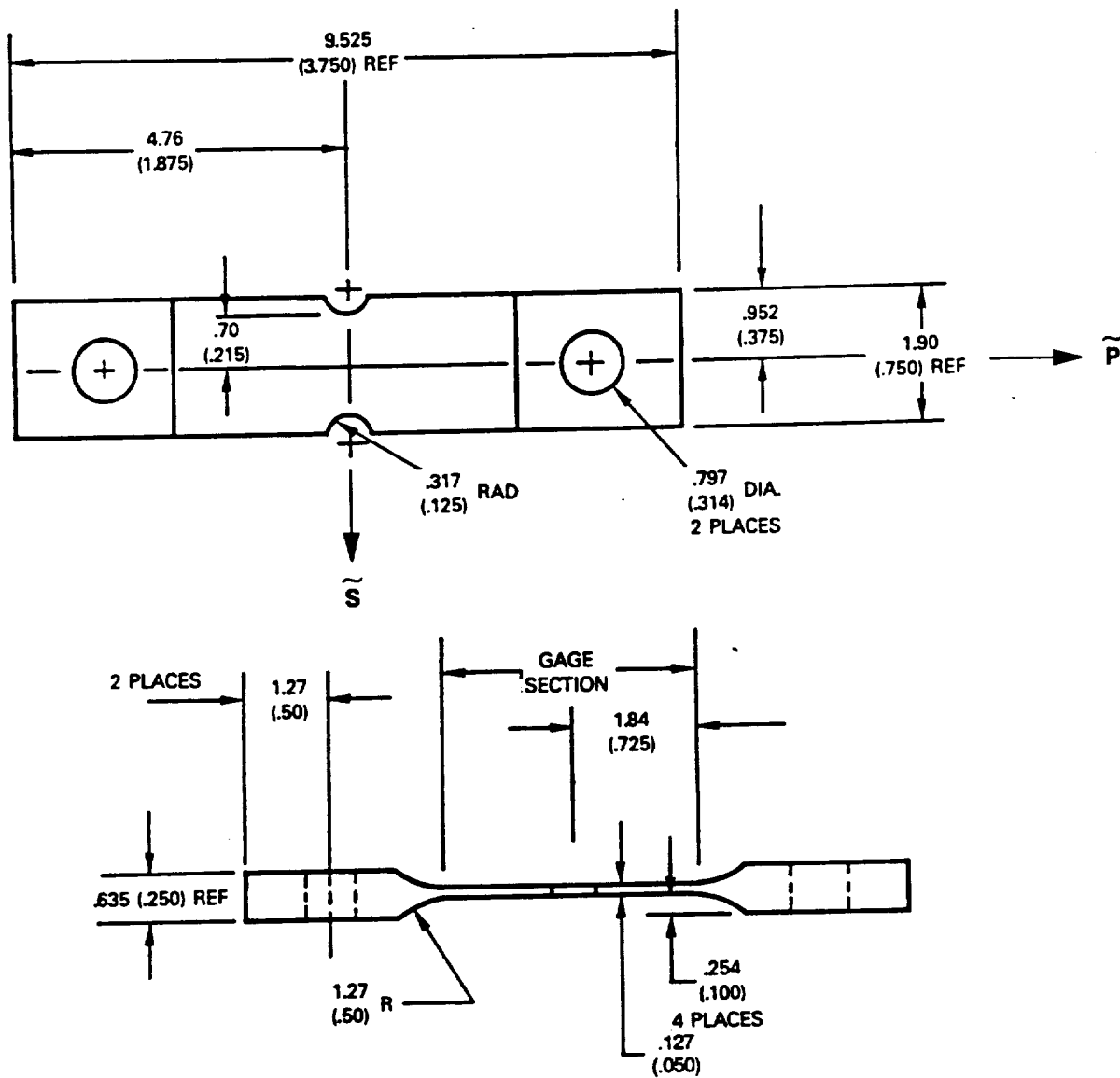
Figure 96   *Thin Mild Notched Fatigue Specimen Geometry – cm (in.)*
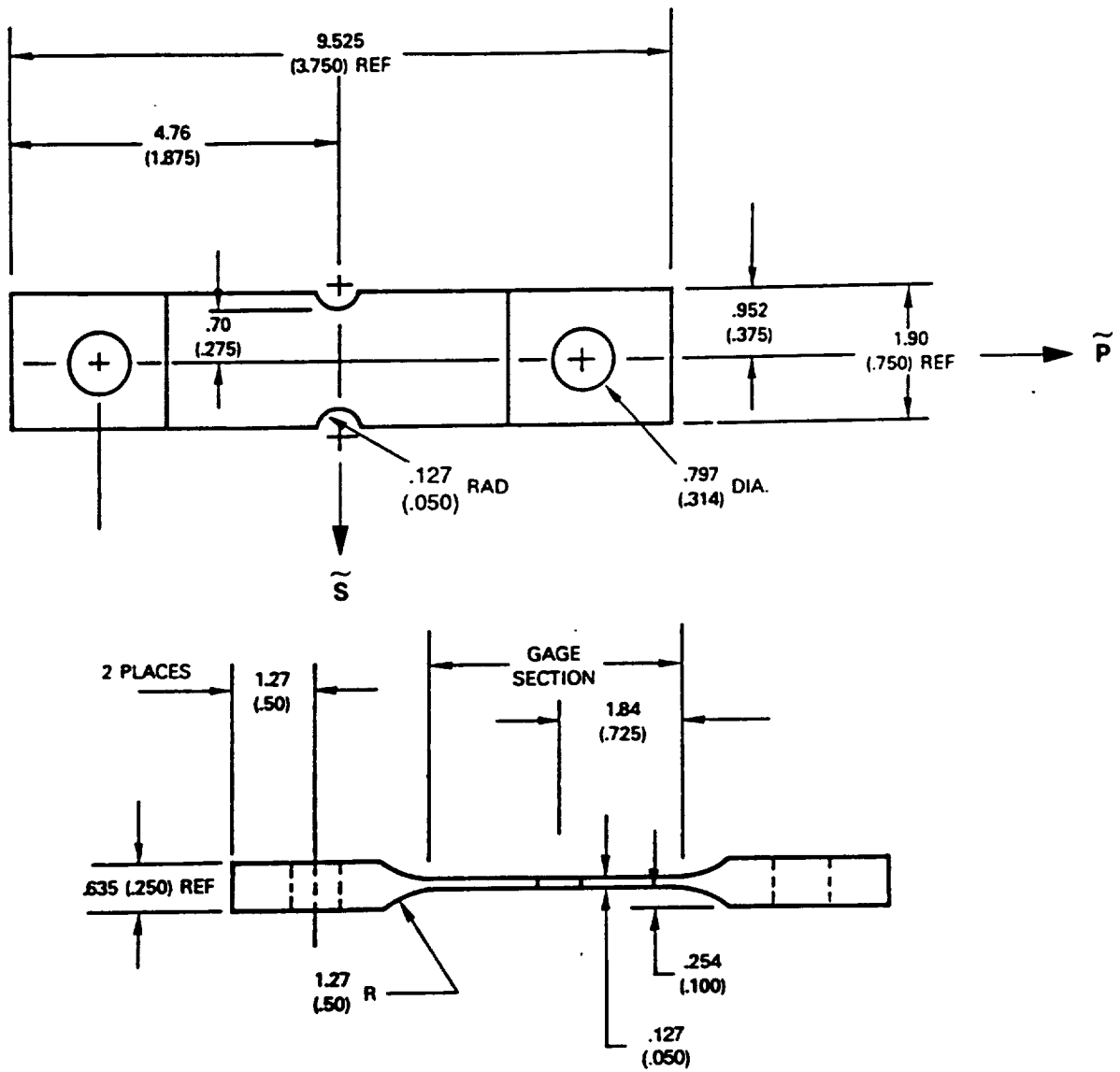
Figure 97   Thin Sharp Notched Fatigue Specimen Geometry – cm (in.)
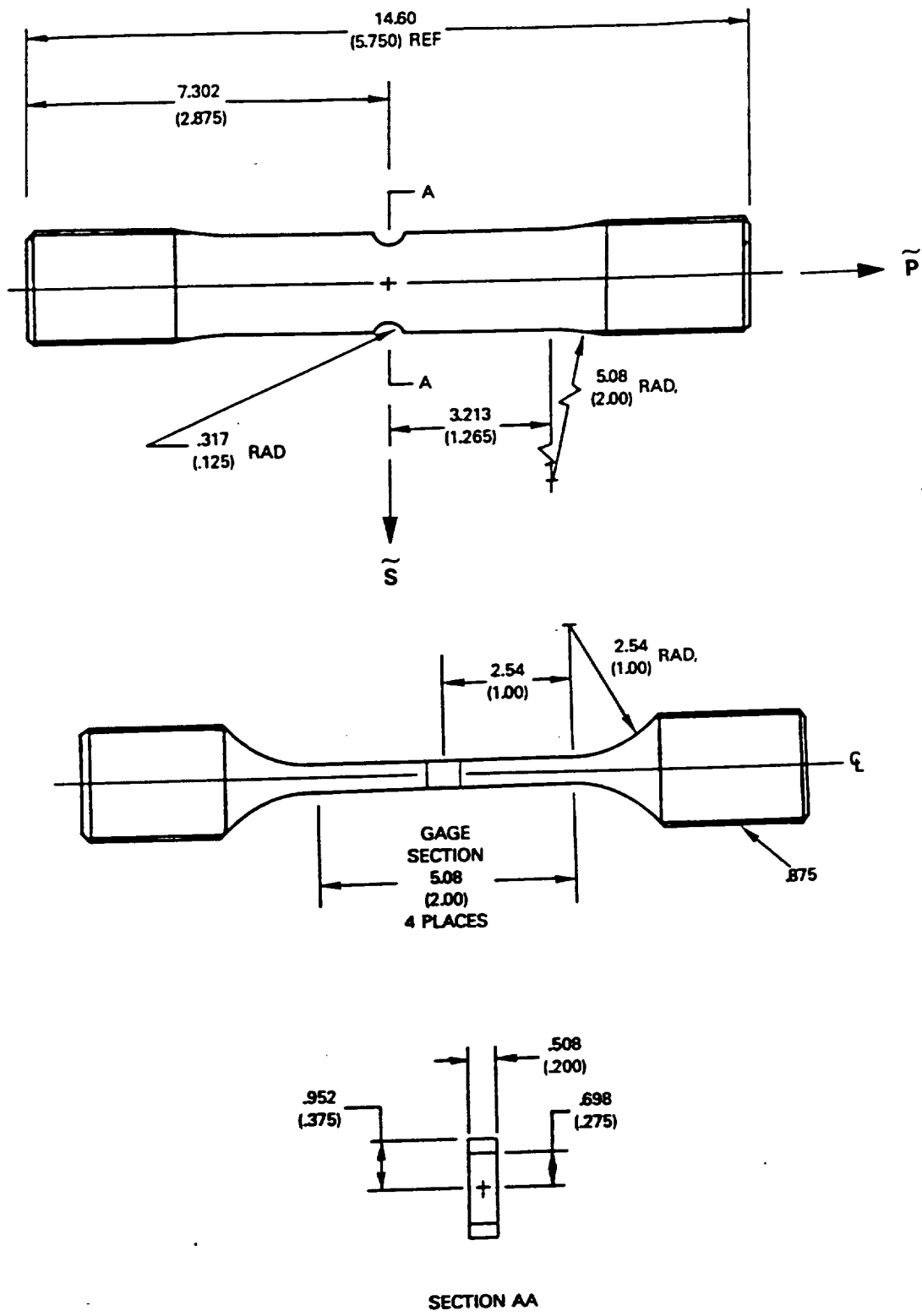
Figure 98   *Thick Mild Notched Fatigue Specimen Geometry – cm (in.)*

265
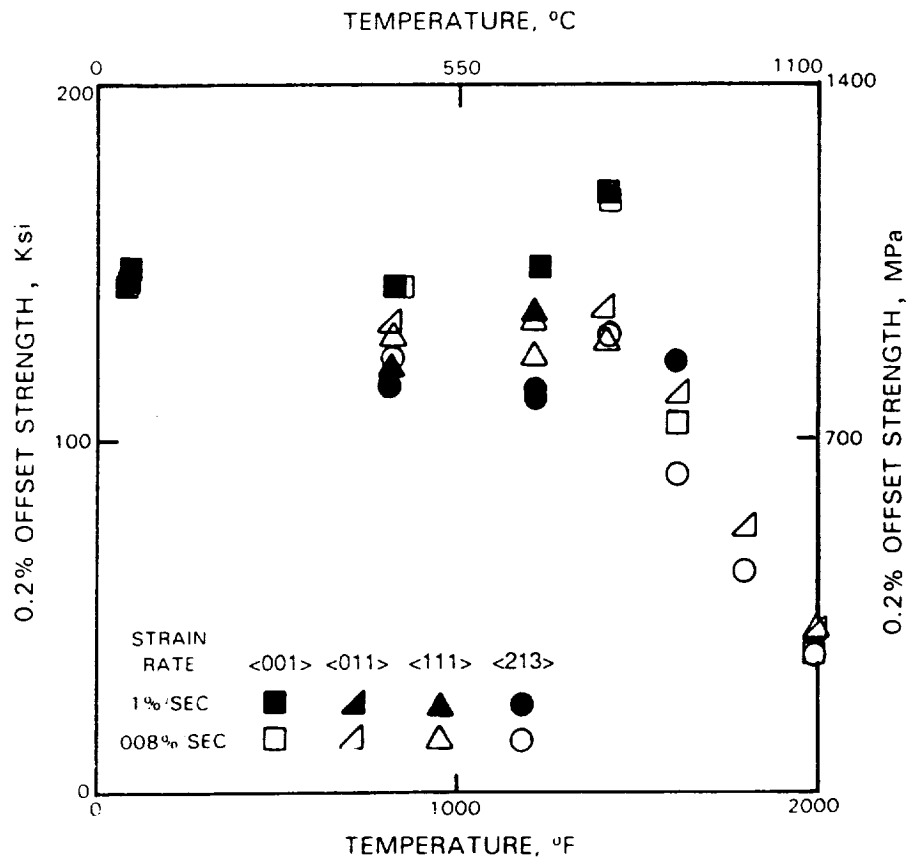
Figure 99   *PWA 1480 0.2% Yield Strength Vs. Temperature*
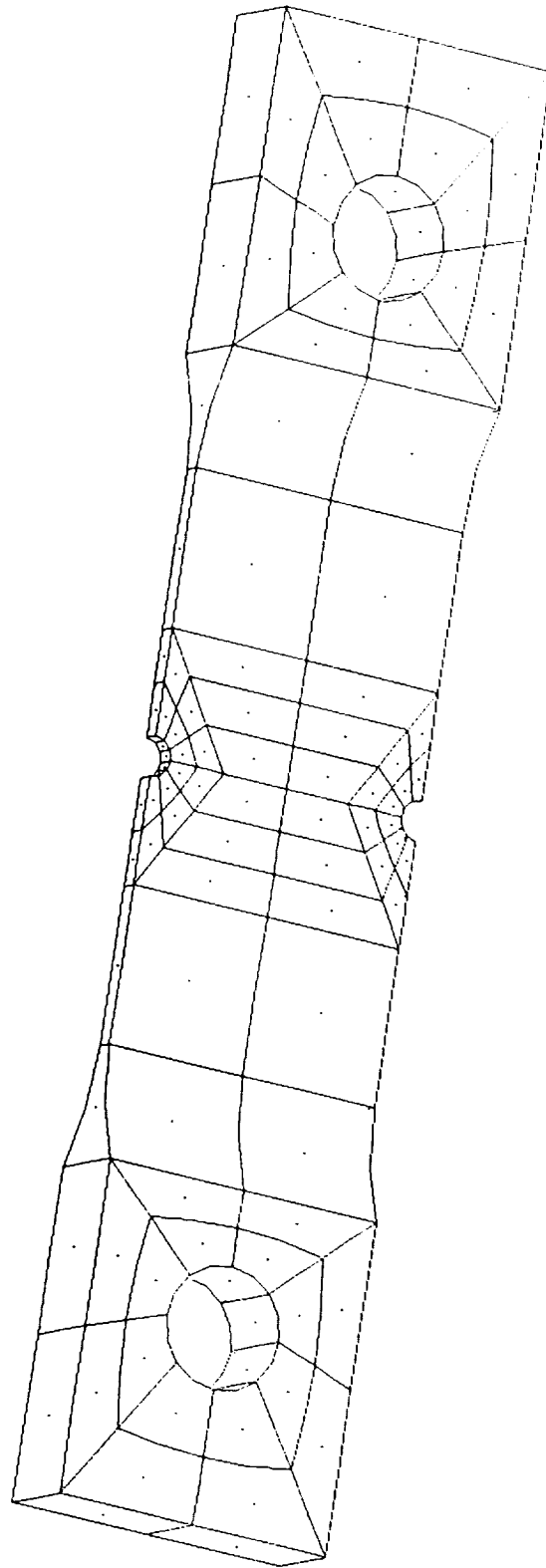
Figure 100   *Boundary Element Mesh*
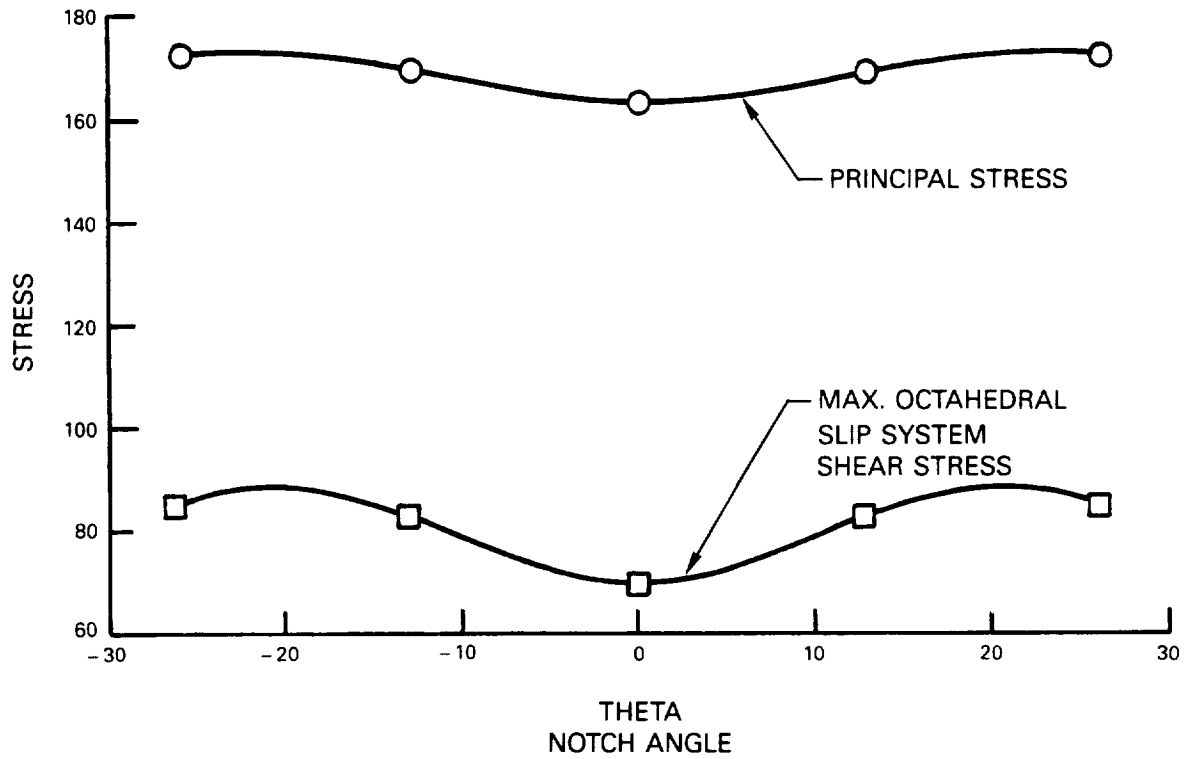
Figure 101   *Stress Variation In the Thin Sharp Notch Specimen for 689 MPa (100 Ksi) Nominal Stress*
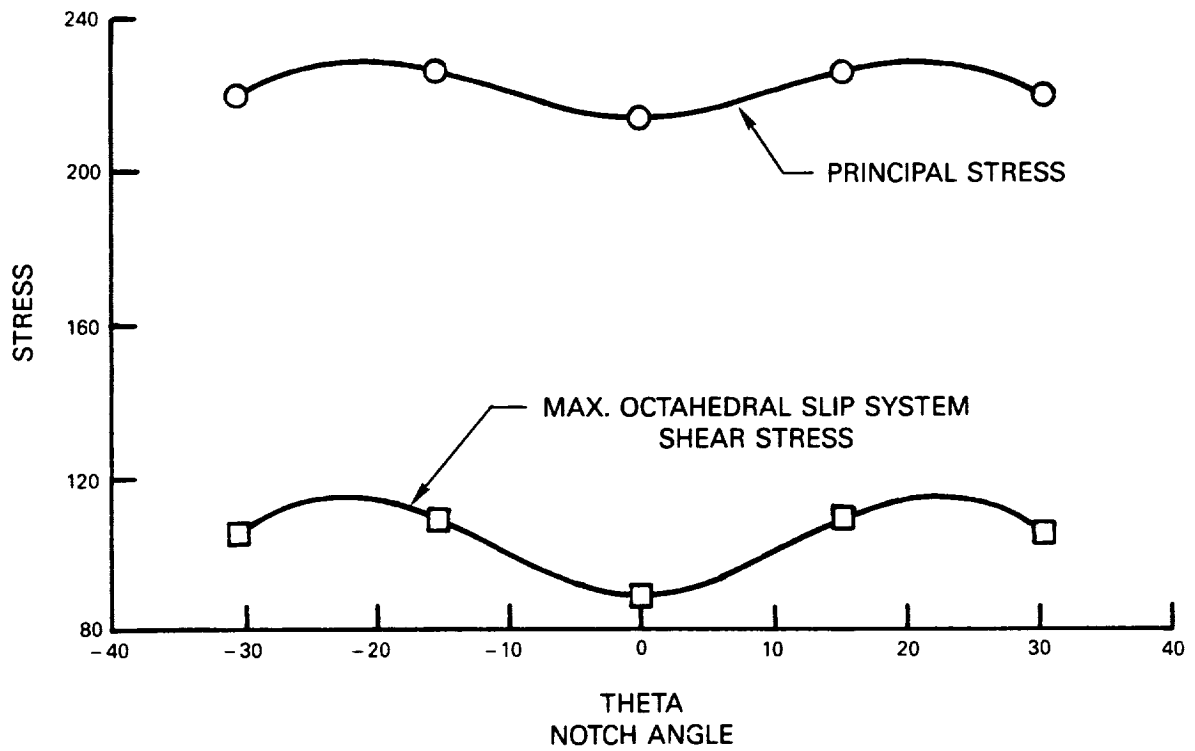
Figure 102   *Stress Variation In the Thin Mild Notch Specimen for 689 MPa (100) Ksi Nominal Stress*

268
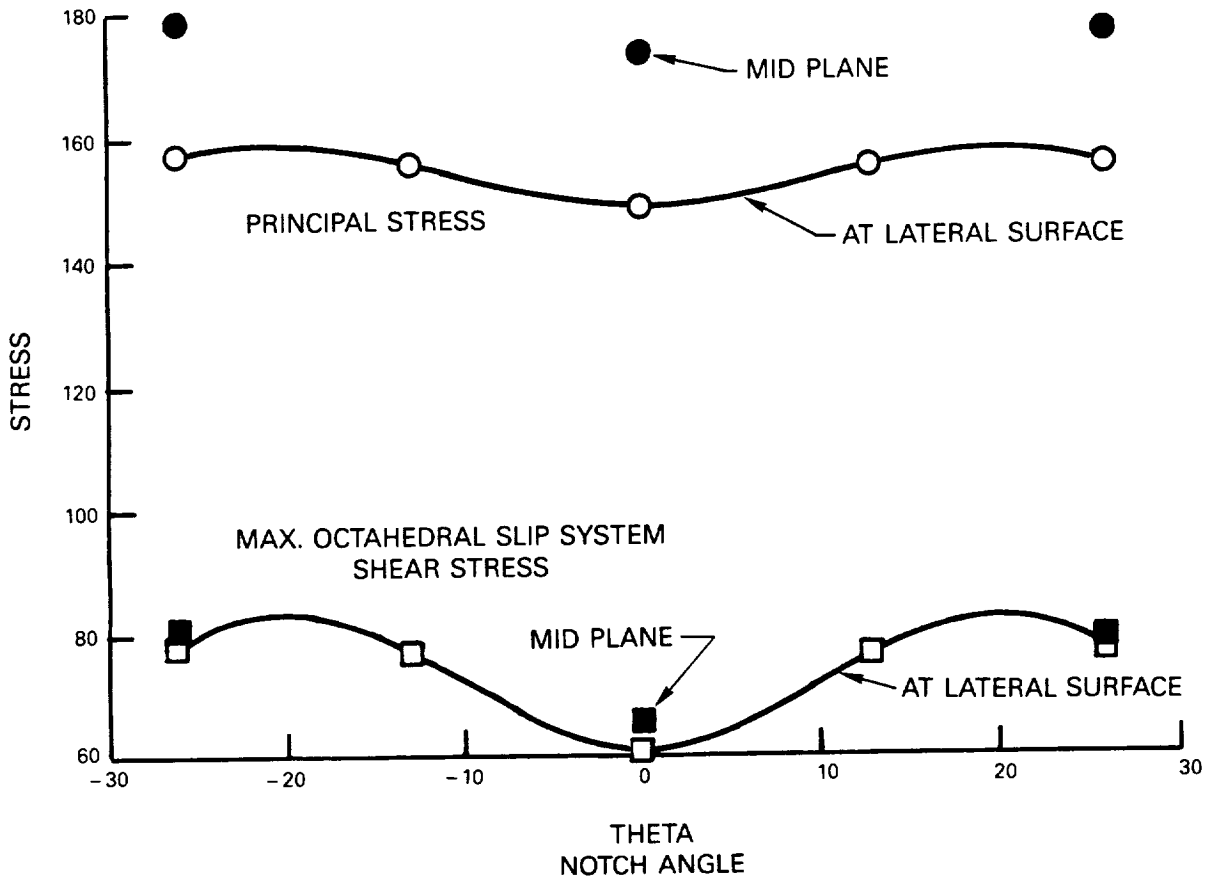
Figure 103   Stress Variation In the Thick Mild Notch Specimen for 689 MPa (100 Ksi) Nominal Stress

• THIN, MILD NOTCHED SPECIMEN; TM3487
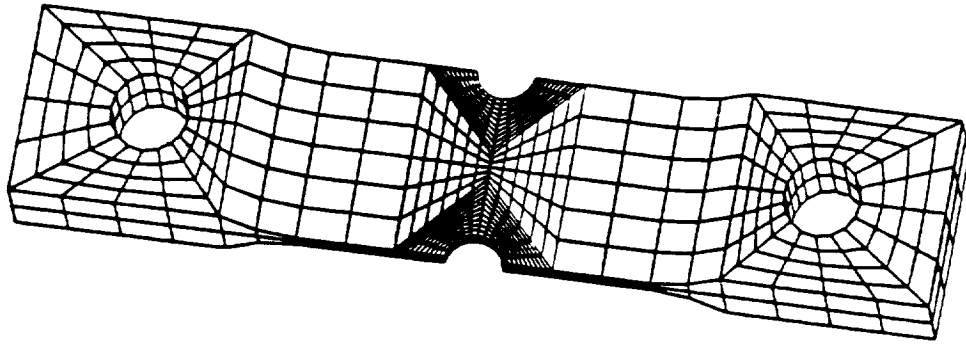
• THIN, SHARP NOTCHED SPECIMEN; TM3387
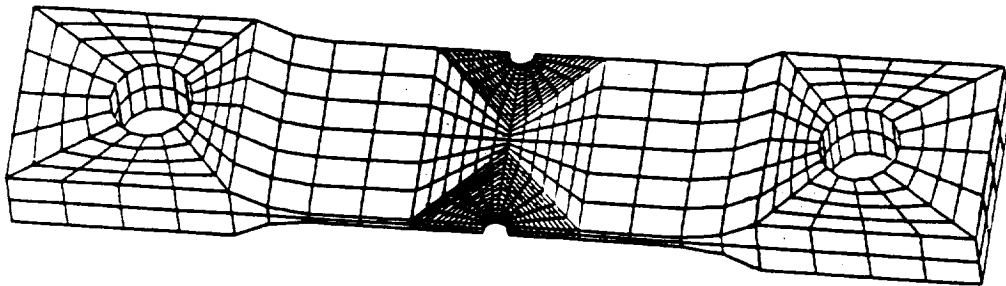
• THICK, MILD NOTCHED SPECIMEN; LED3587
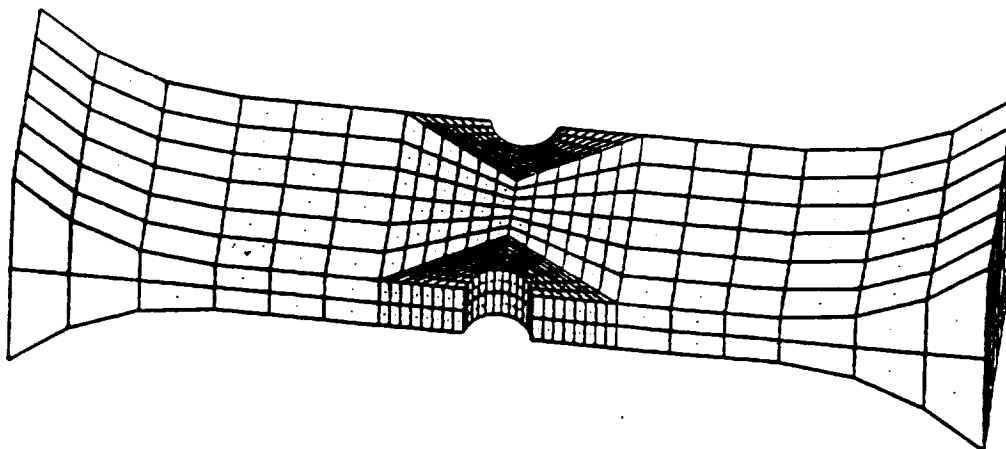
Figure 104   *MARC Finite Element Meshes*

270
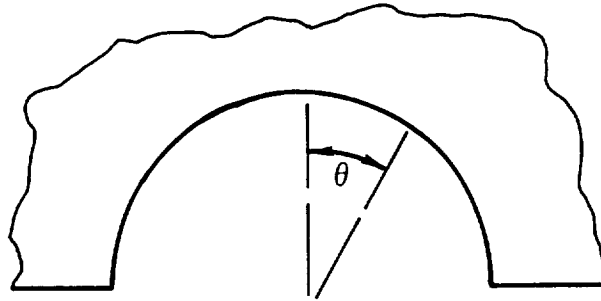
PRINCIPAL STRESSES	ORIENTATION PRIMARY	SECONDARY	TM3387 THIN, SHARP NOTCHED		TM3487 THIN, MILD NOTCHED		LED3587 THICK, MILD NOTCHED	
			Kt	θ	Kt	θ	Kt	θ
	(001)	(100)	2.48	0°	1.82	26°	2.08	26°
	(001)	(210)	2.37	0°	1.79	26°	1.98	26°
	(011)	(01-1)	3.20	0°	2.58	0°	2.90	0°
	(011)	($\sqrt{21}$-1)	3.04	0°	2.48	0°	2.44	0°
	(111)	(01-1)	2.95	0°	2.46	0°	2.54	0°
	(213)	(5-41)	2.85	5°	2.45	0°	2.27	3°

SLIP SYSTEM SHEAR STRESSES ON MOST HIGHLY STRESSED OCTAHEDRAL SLIP SYSTEM	ORIENTATION PRIMARY	SECONDARY	TM3387 THIN, SHARP NOTCHED		TM3487 THIN, MILD NOTCHED		LED3587 THICK, MILD NOTCHED	
			Kt	θ	Kt	θ	Kt	θ
	(001)	(100)	1.06	23	0.87	21	0.87	21
	(001)	(210)	1.06	23	0.87	22	0.83	22
	(011)	(01-1)	1.12	0	0.98	0	0.92	0
	(011)	($\sqrt{21}$-1)	1.02	0	0.90	0	0.88	13
	(111)	(01-1)	0.81	16	0.84	10	0.73	13
	(213)	(5-41)	0.96	5	0.90	5	0.90	3

Figure 105   *MARC Finite Element Stress Analysis Results*
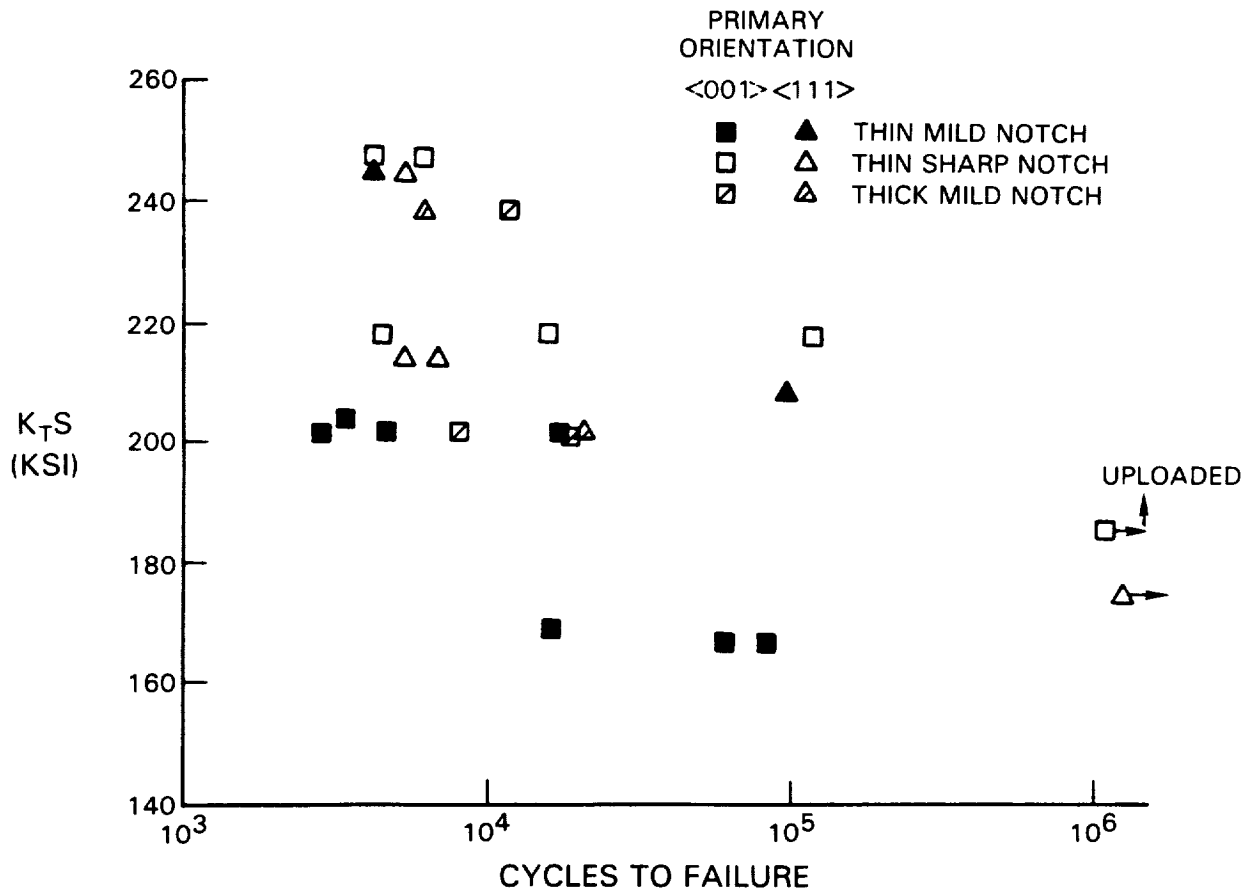
Figure 106   *649°C (1200°F) Notched LCF Un–HIP'd PWA 1480 Life Results*
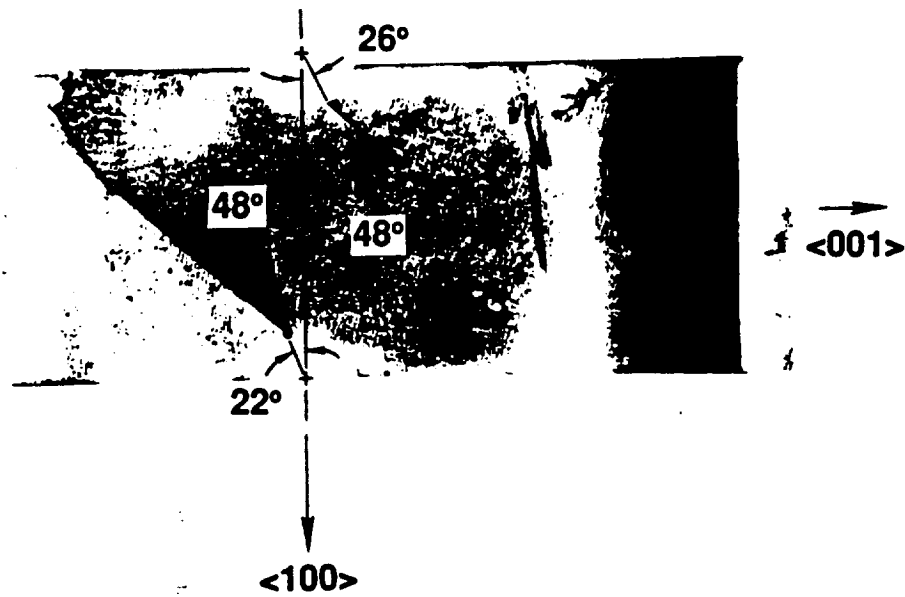
Figure 107 *Representative PWA 1480 Low Cycle Fatigue Crack Initiation Location and Crack Path*
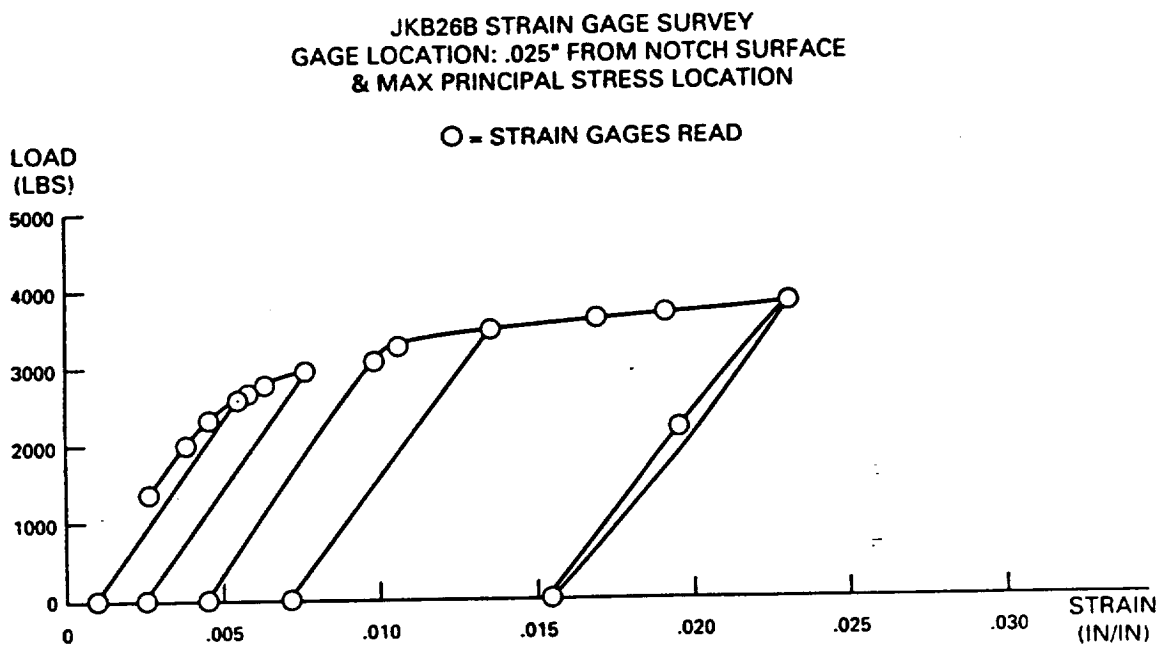
Figure 108 *Loading History for Strain Gage Survey On Specimen JKB26B*

273
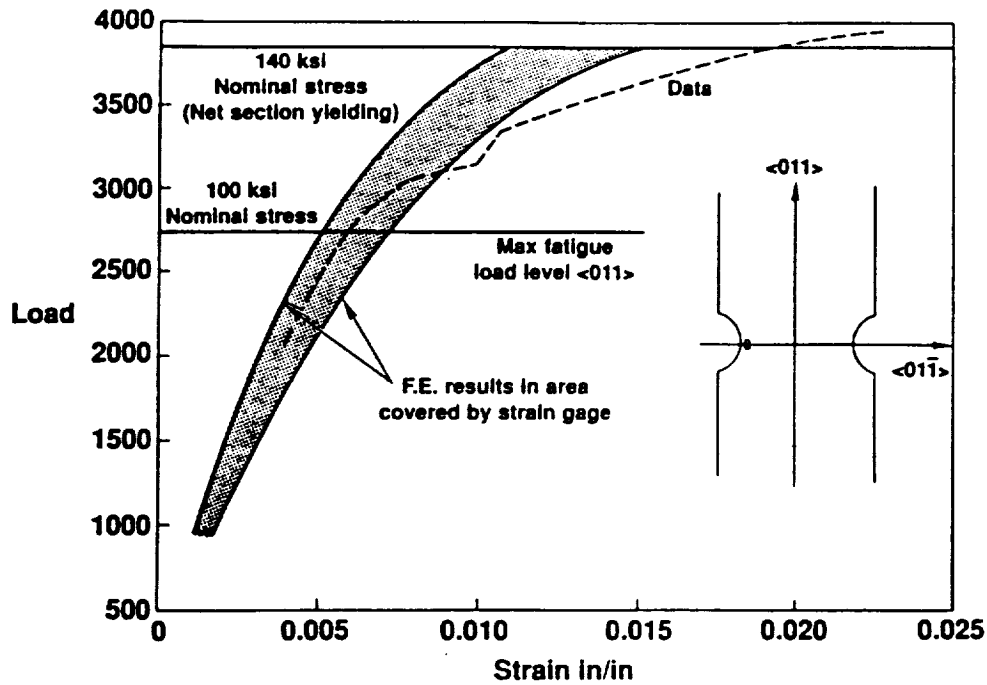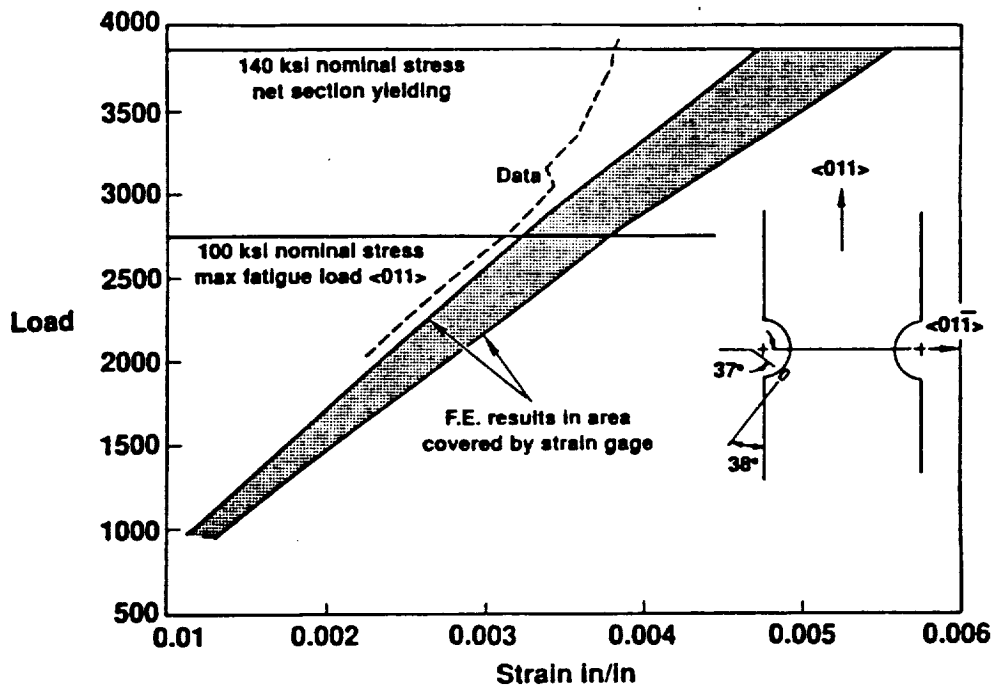
Figure 109   *(a) Comparison of Measured and Predicted at a Point. Strains on the lateral face of the specimen near the base of the notch in a thin, mild notched specimen with <011> <01-1> orientation. (b) Comparison of Measured and Predicted at a Point. Strains on the lateral face of the specimen, 37 degrees from the bottom of the notch in a thin, mild notched specimen with <011> <01-1> orientation.*

C-4
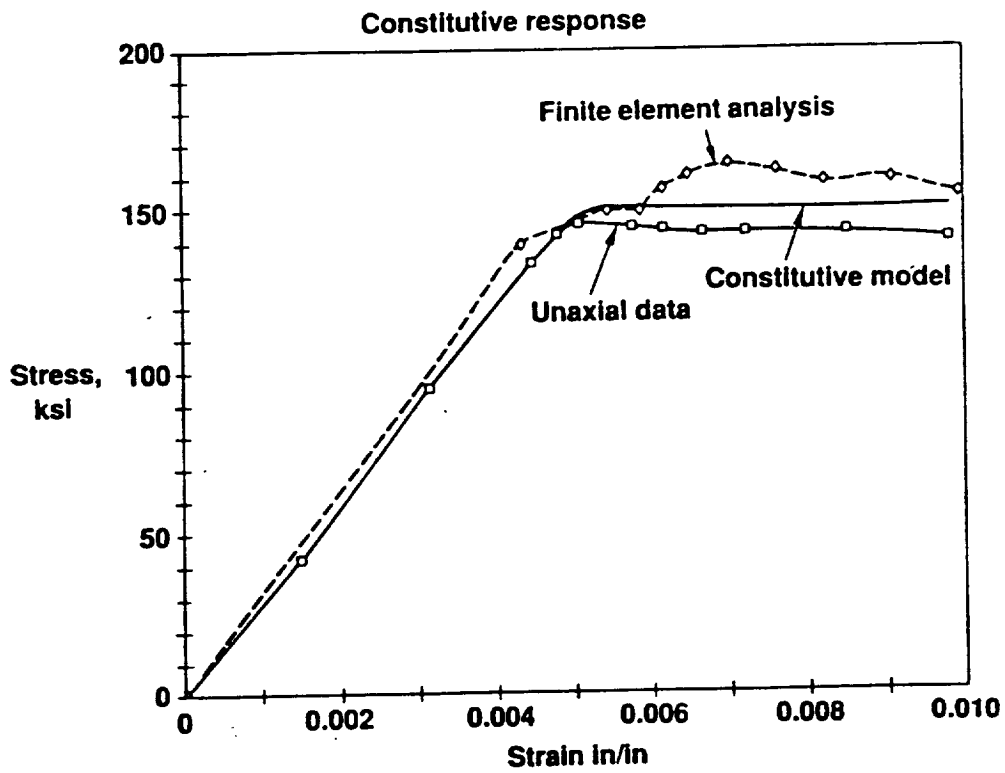
Figure 110   *Comparison of the Predicted and Actual Stress Strain Response of An <011> Tensile Bar and the Predicted Response of An Element In the Notch of a Thin, Mild Notched Specimen With <001> <01-1> Orientation*

275
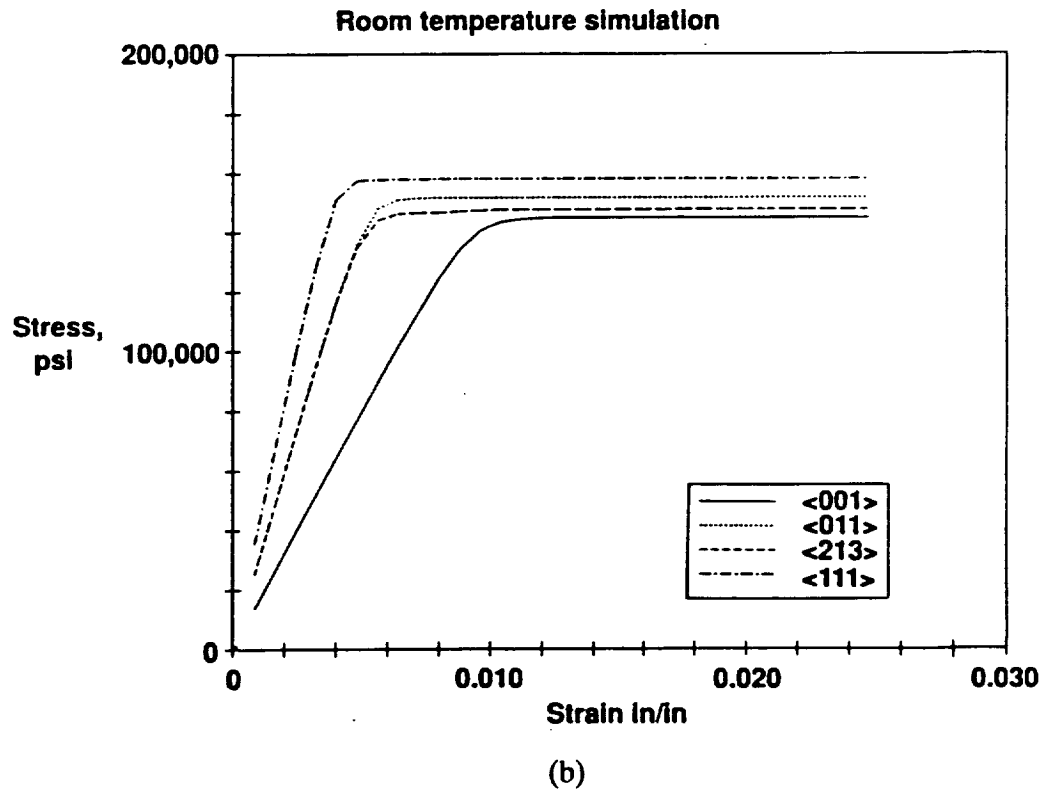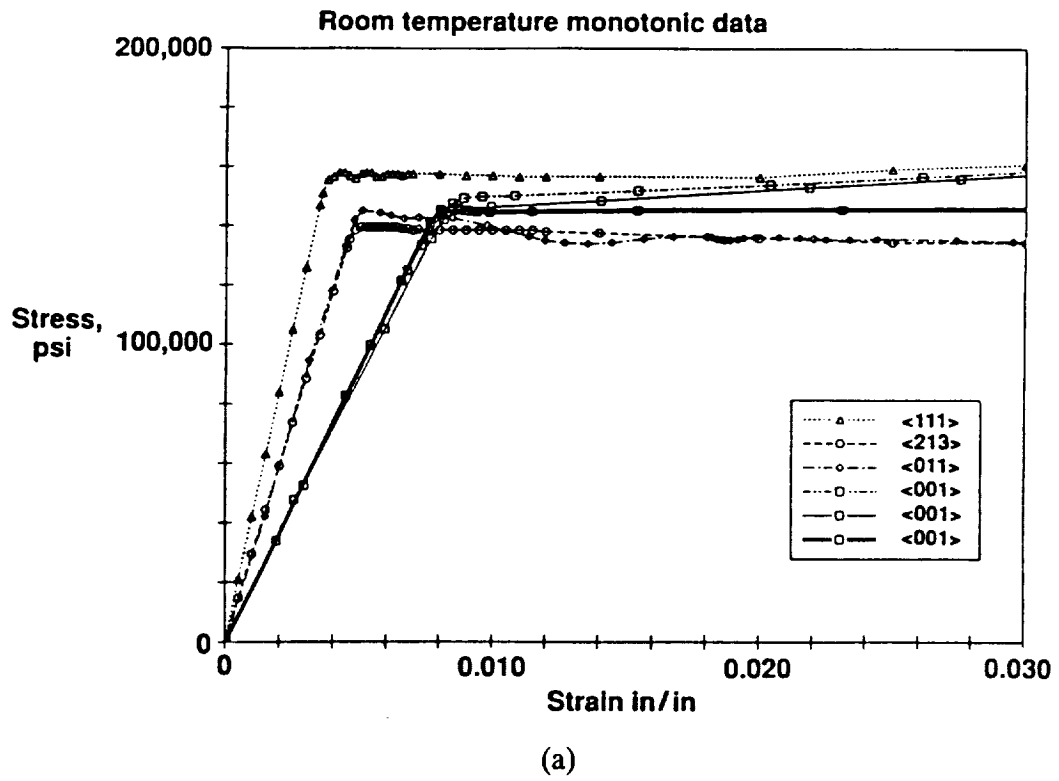
Figure 111   *(a) Room Temperature Monotonic Stress Strain Data for Uniaxial Specimens of Different Crystallographic Orientations (b) Room Temperature Stress Strain Response of Uniaxial Bars As Predicted by the Constitutive Model*
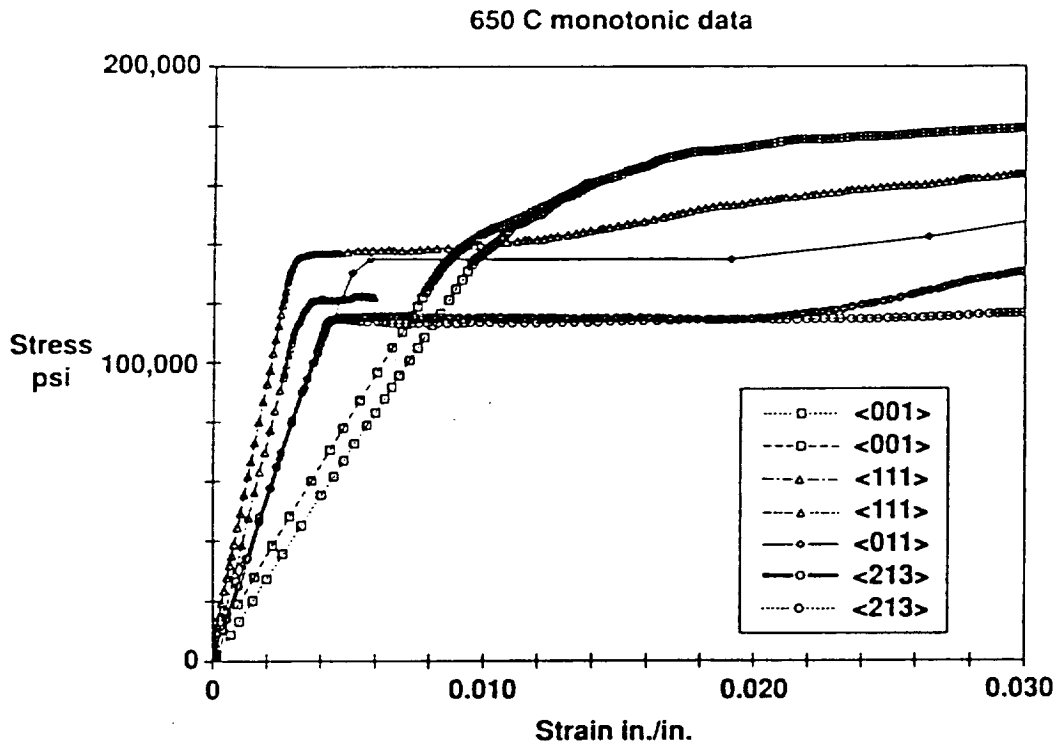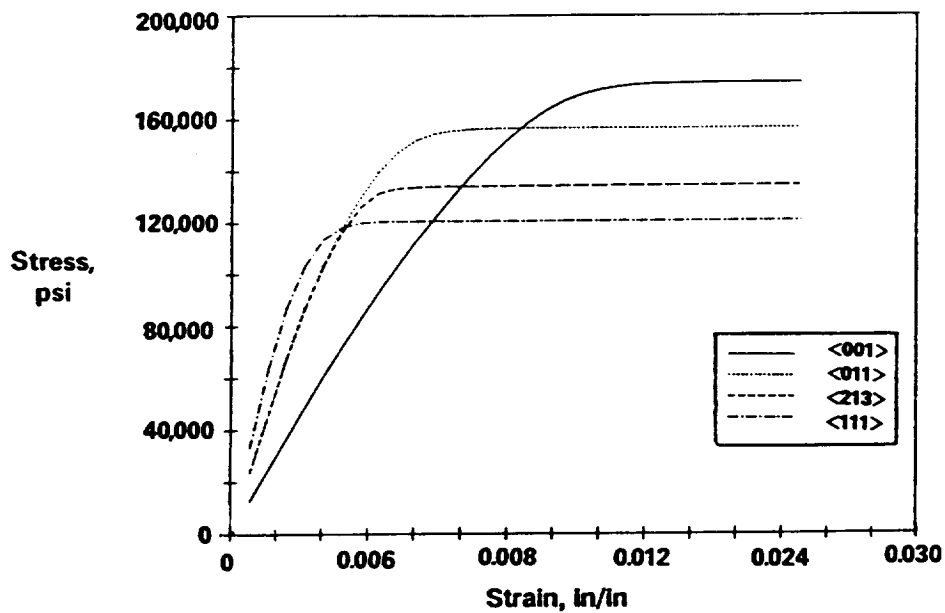
Figure 112   *(a) Monotonic Stress Strain Response at 650°C (b) Predicted PWA 1480 Monotonic Tensile Response at 650°C (1200°F)*

$$P = P_o \left(\frac{S}{S_o} \right)^2$$
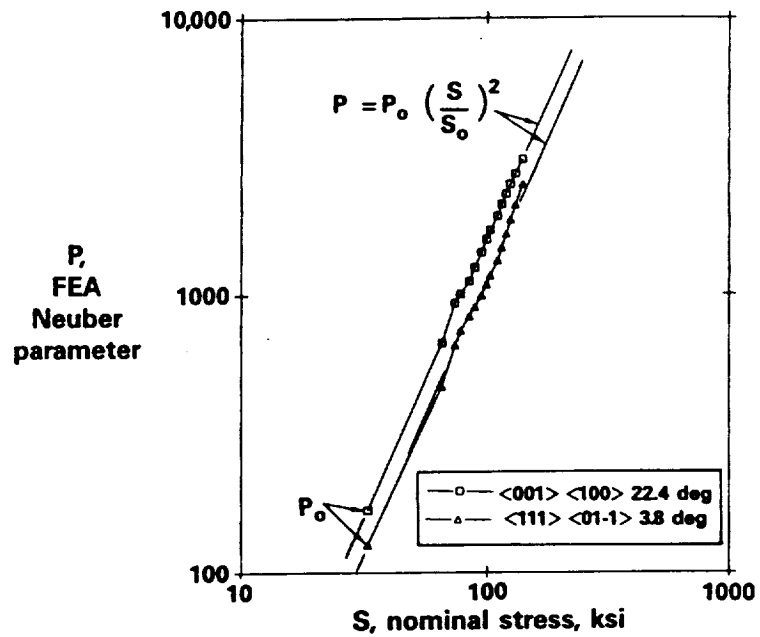
Figure 113   *Neuber Parameter Determined From Nonlinear Finite Element Analyses*
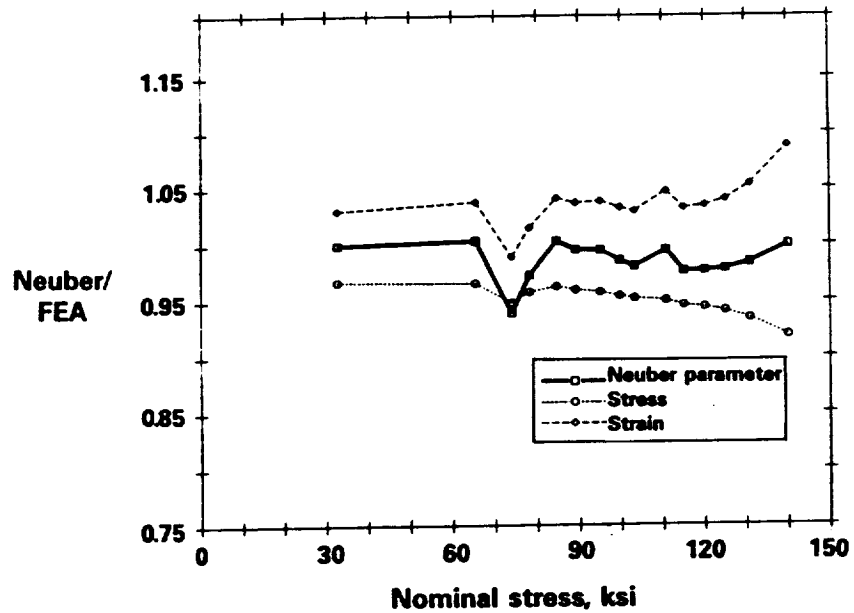
Figure 114   *Error In Neuber Calculations for <001> <100> Mild Notch Specimen at* θ = 3.77°
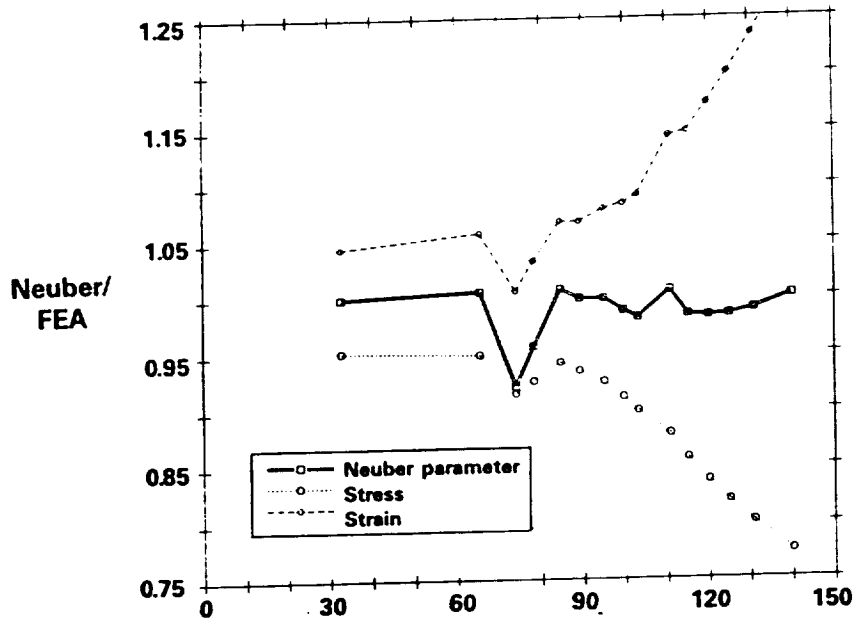
Figure 115   *Error In Neuber Calculations for <001> <100> Mild Notch Specimen at* θ *= 22.38°*
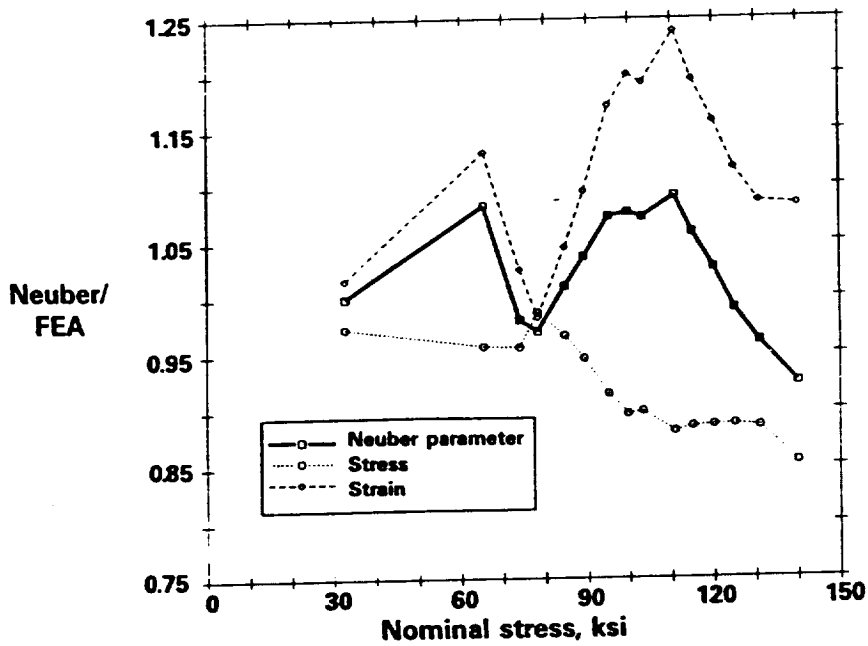
Figure 116   *Error In Neuber Calculations for <111> <01-1> Mild Notch Specimen at* θ *= 3.77°*
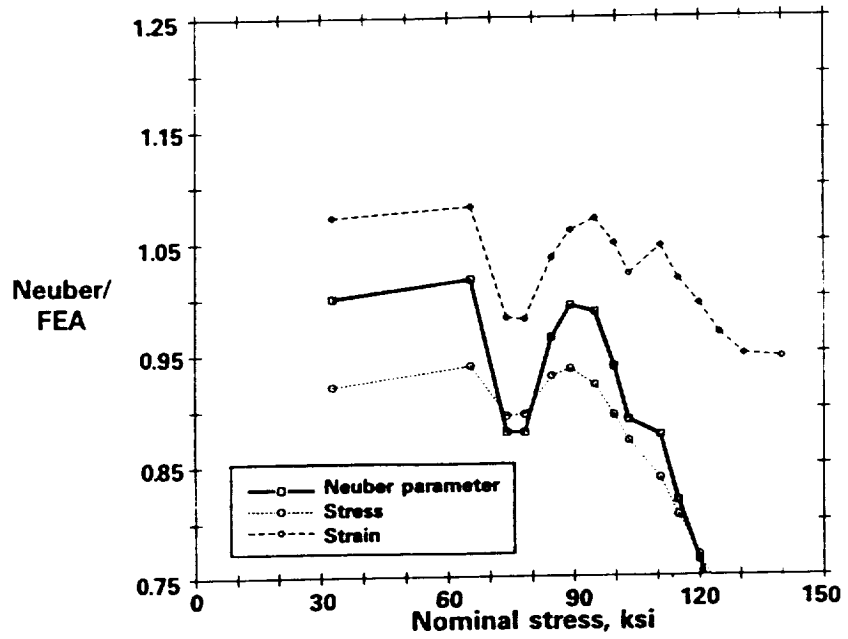
Figure 117   *Error In Neuber Calculations for < 111 > < 01–1 > Mild Notch Specimen at θ = 22.38°*
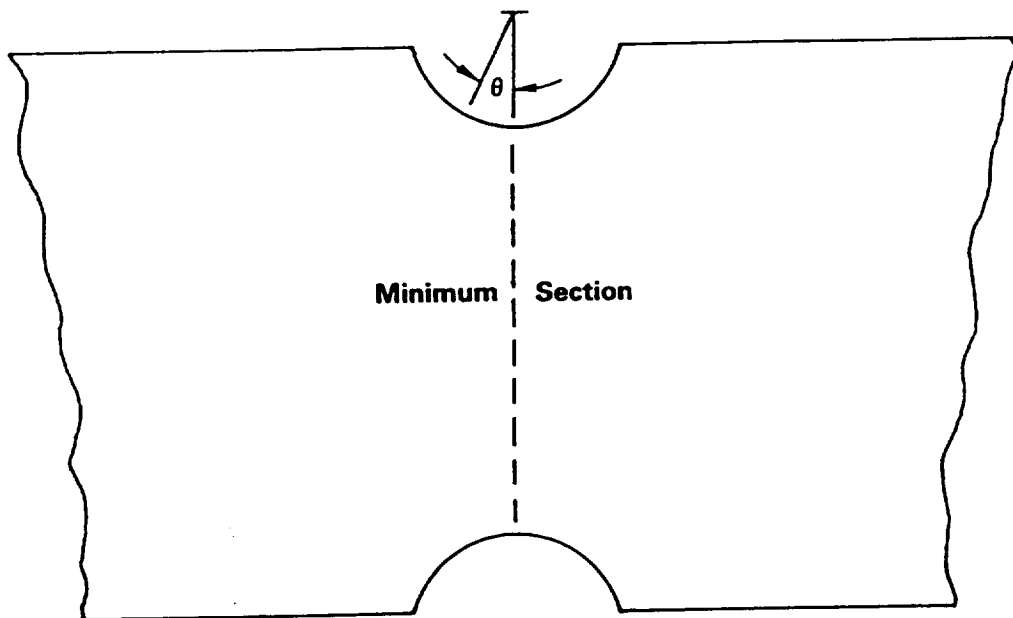
Figure 118   *A Location In the Notch Is Defined by the Angle θ, Measured From the Minimum Section*
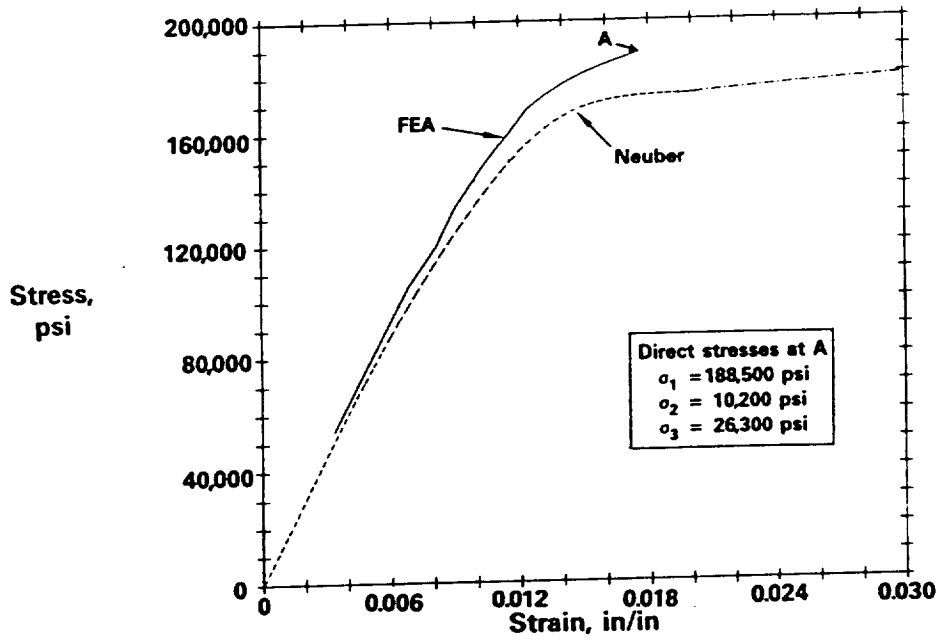
Figure 119   *Stress–Strain Response In a <001> <100> Mild Notch Specimen at* θ = 3.77°
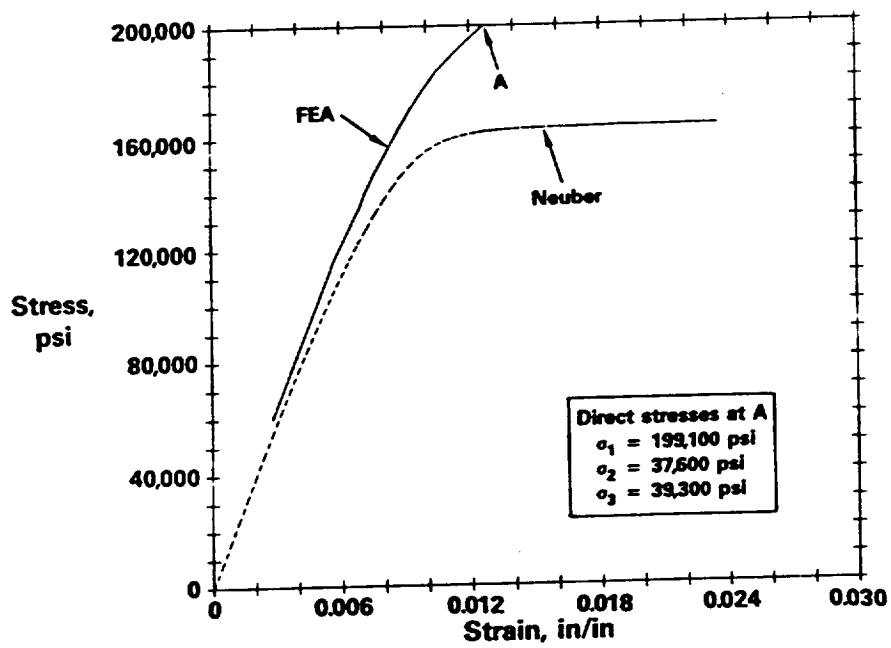
Figure 120   *Stress–Strain Response In a <001> <100> Mild Notch Specimen at* θ = 22.38°
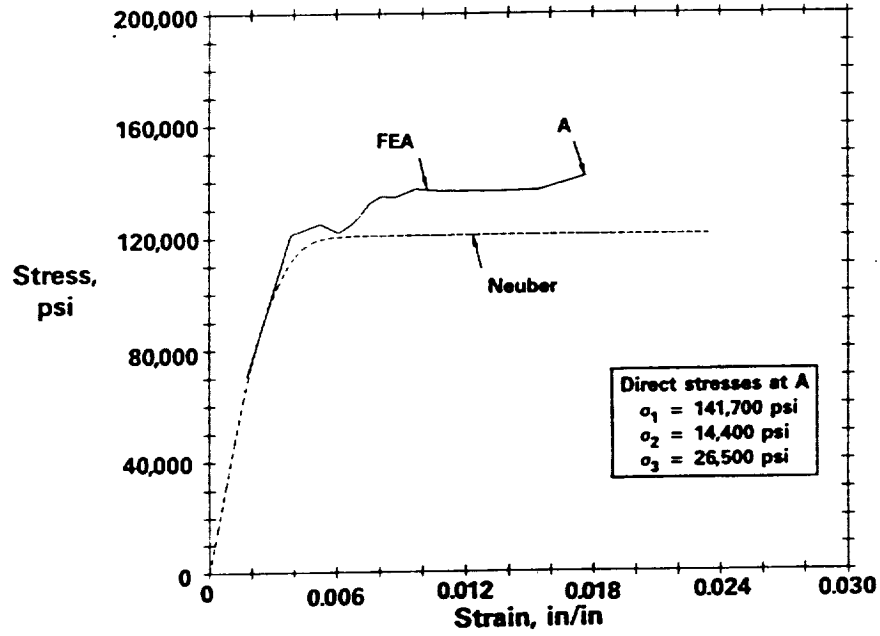
Figure 121   *Stress-Strain Response In a <111> <01-1> Mild Notch Specimen at* θ = 3.77°
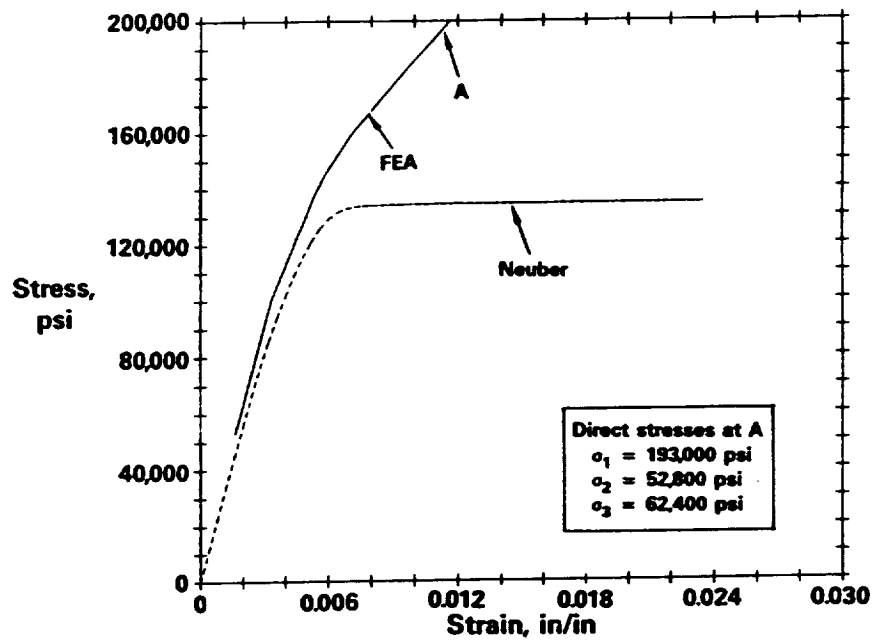
Figure 122   *Stress-Strain Response In a <111> <01-1> Mild Notch Specimens at* θ = 22.38°

282

Thin mild notch specimen <001> <100> θ = 22.38
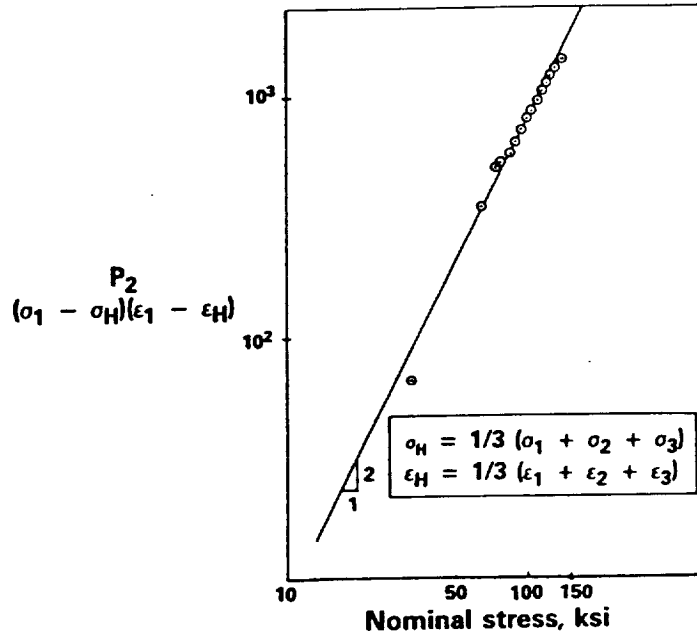
Figure 123   A Modified Neuber Parameter Based On Deviatoric Quantities
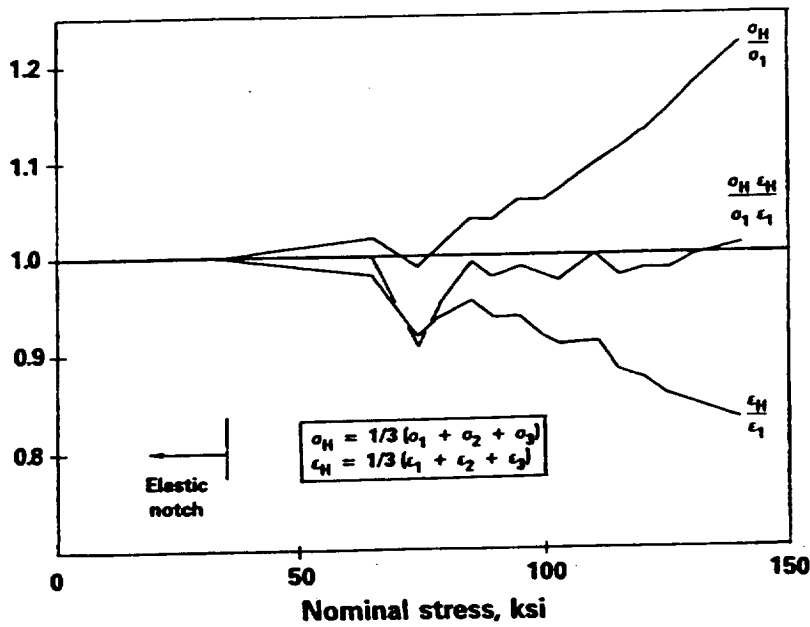
Figure 124   Evolution of Multiaxiality In a <001> <100> Mild Notched Specimen In the Model
Anisotropic Material. Results are shown at a location 22.4 degrees from the minimum
section.

283

Figure 125   1200° F Smooth and Mild Notched Data Correlation Using Slip System Shear Stress
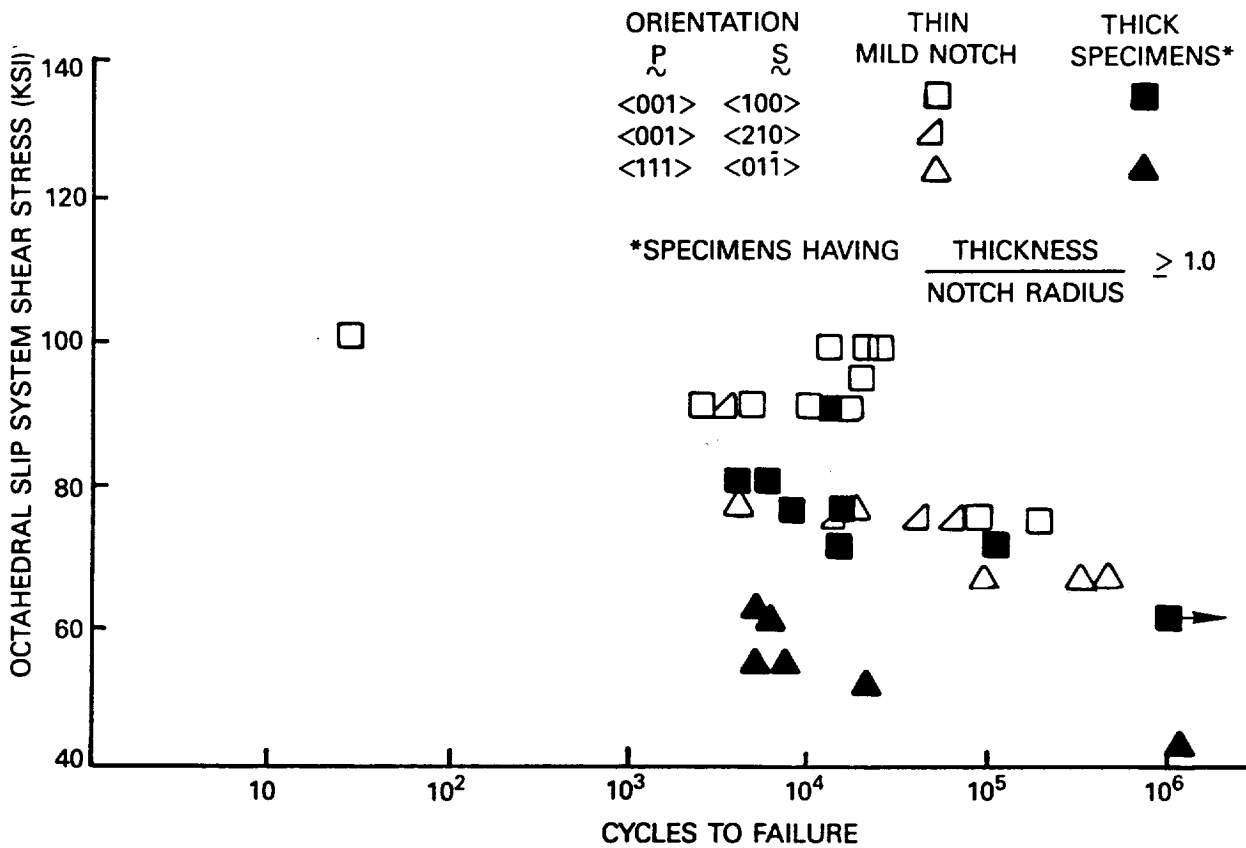
Figure 126   *1200°F Notched Specimen Correlation Using Slip System Shear Stress*

Figure 127

P~	Smooth	Notched	S~
$\langle 001 \rangle$	□	■	$\langle 100 \rangle$
$\langle 001 \rangle$		♦	$\langle 210 \rangle$
$\langle 111 \rangle$	△	▲	$\langle 01\bar{1} \rangle$
$\langle 213 \rangle$	○		
R =	$\dfrac{\varepsilon_{min}}{\varepsilon_{max}}$	$\dfrac{\sigma_{min}}{\sigma_{max}}$	

$\triangle$ R = - 0.5

R = 0.2 $\triangle$

Mean trend line

R = 0.2

R = - 1.0

R = 0.5

Unless otherwise shown, R = 0

R = 0.5

Stress range, ksi — Cycles to failure
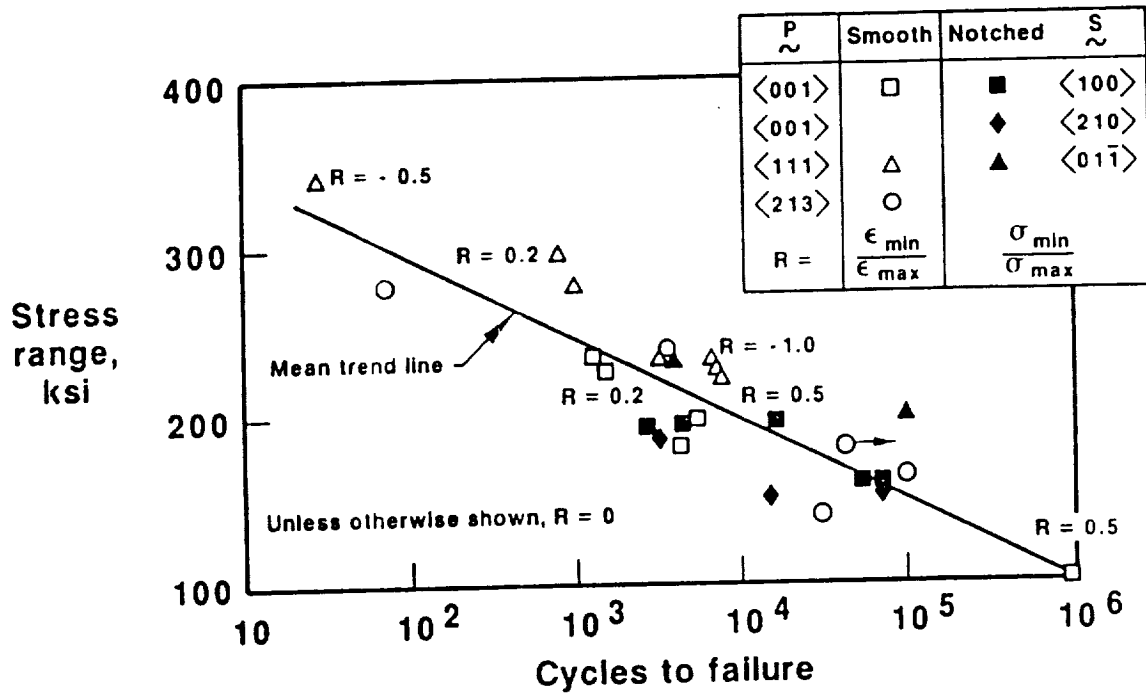
Figure 127   *1200°F PWA 1480 Fatigue Uniaxial and Mild Notched Specimens*

Figure 128

P~	Smooth	Notched	S~
$\langle 001 \rangle$	□	□	$\langle 100 \rangle$
$\langle 001 \rangle$		◇	$\langle 210 \rangle$
$\langle 111 \rangle$	△	△	$\langle 01\bar{1} \rangle$
$\langle 213 \rangle$	○		

Solid symbols indicate specimens having $\dfrac{\text{thickness}}{\text{notch radius}} \geq 1.0$

Mean trend line for smooth strain controlled and thin mild notched specimens

Stress range, ksi — Cycles to failure
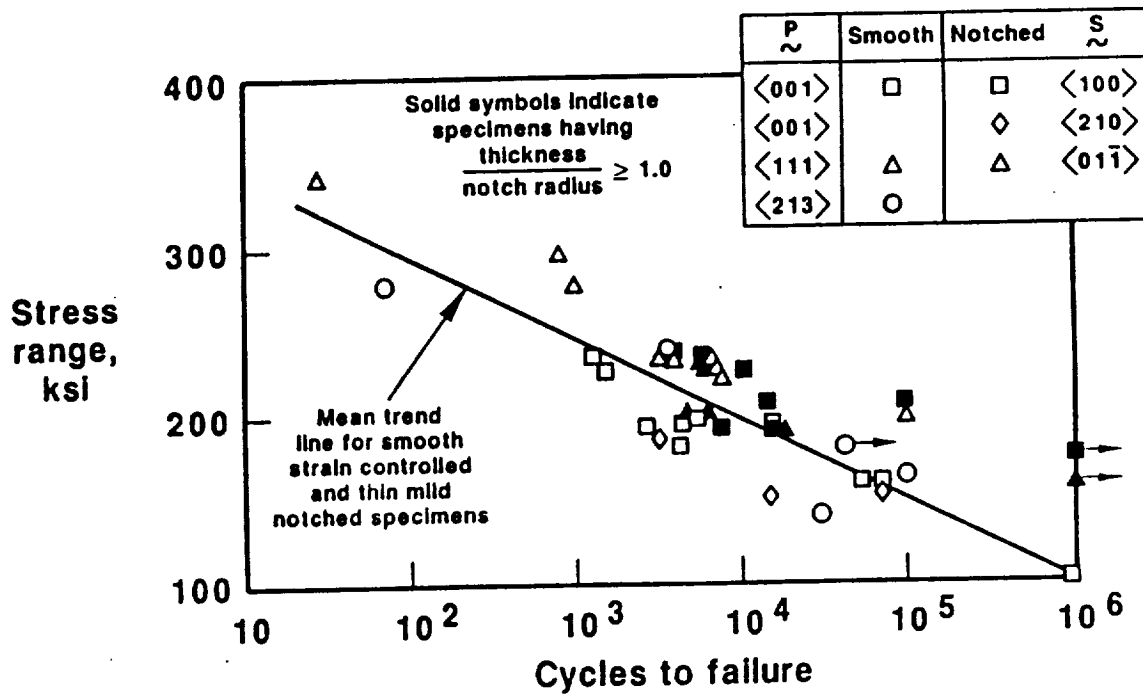
Figure 128   *1200°F PWA 1480 Fatigue, Effect of Specimen Thickness*
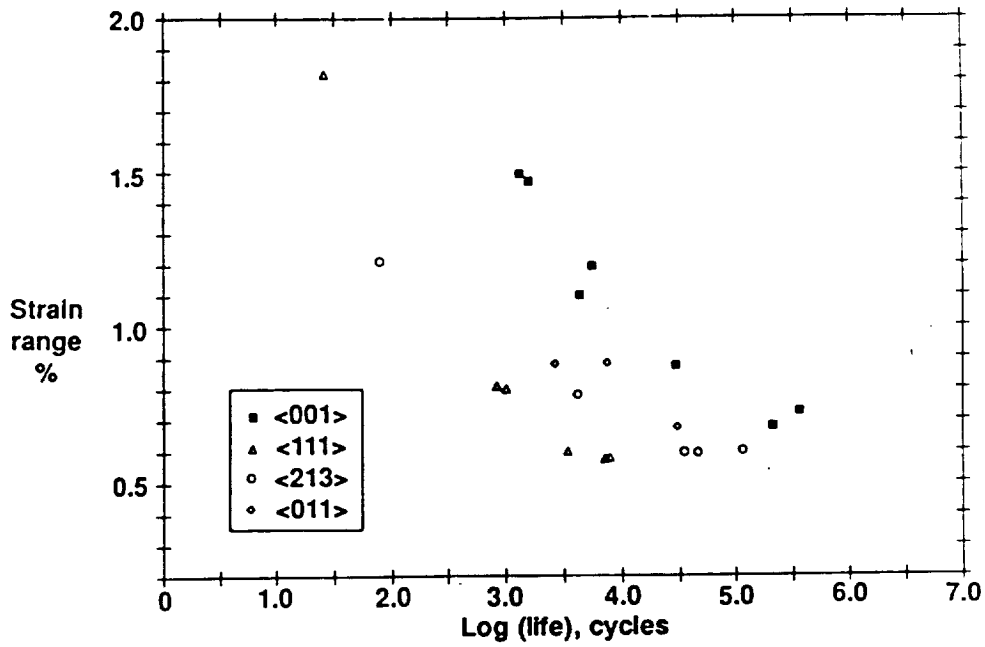
Figure 129   Strain Range Vs. Separation Life for 650°C Strain Controlled Smooth Specimens
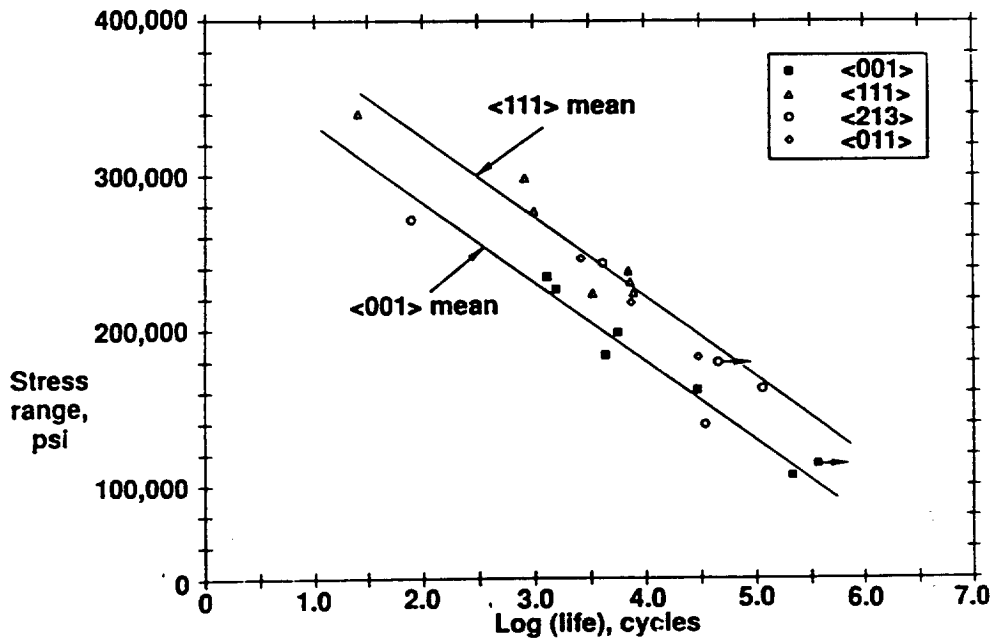
Figure 130   Stress Range Vs. Separation Life for 650°C Strain Controlled Smooth Specimens

287
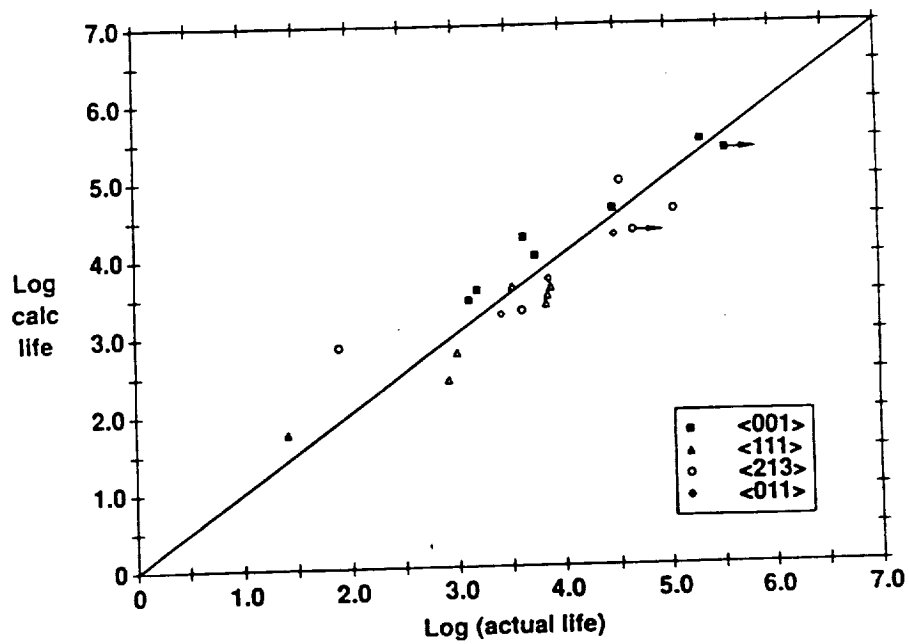
Figure 131   Smooth Fatigue Specimen Calculated Lives Vs. Actual Lives Based On Stress Range
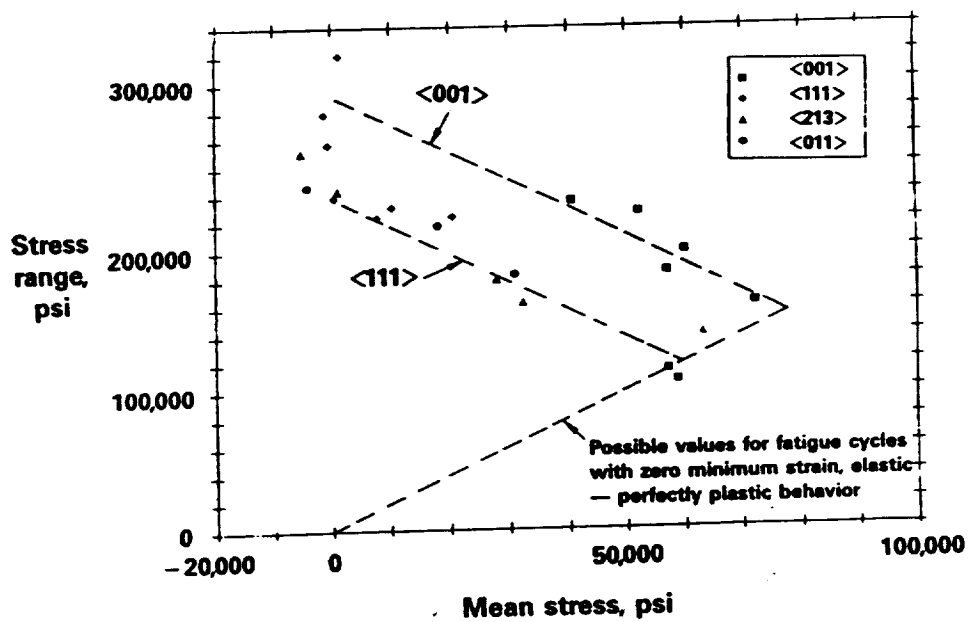
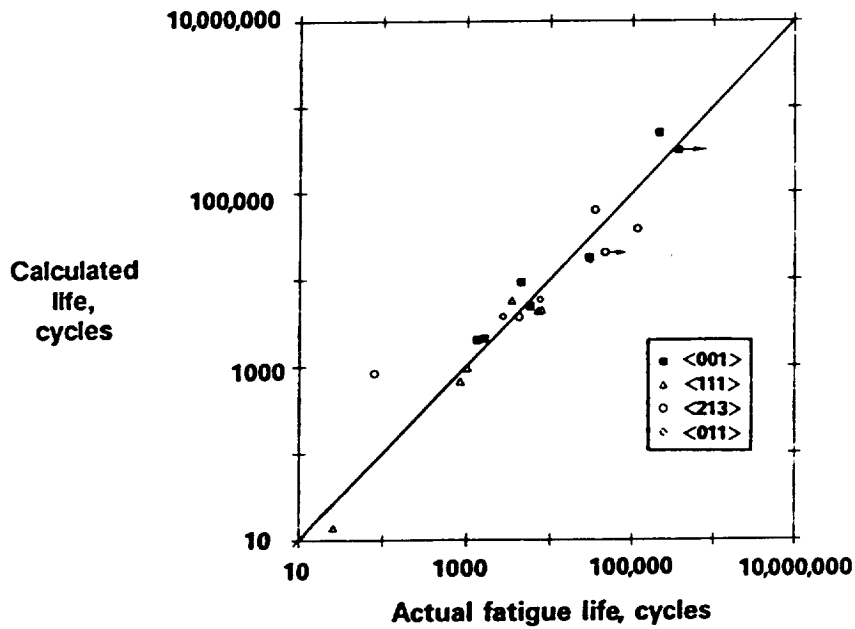*Figure 132*   *Stress Range Vs. Mean Stress of Strain Controlled Smooth Specimens*

288

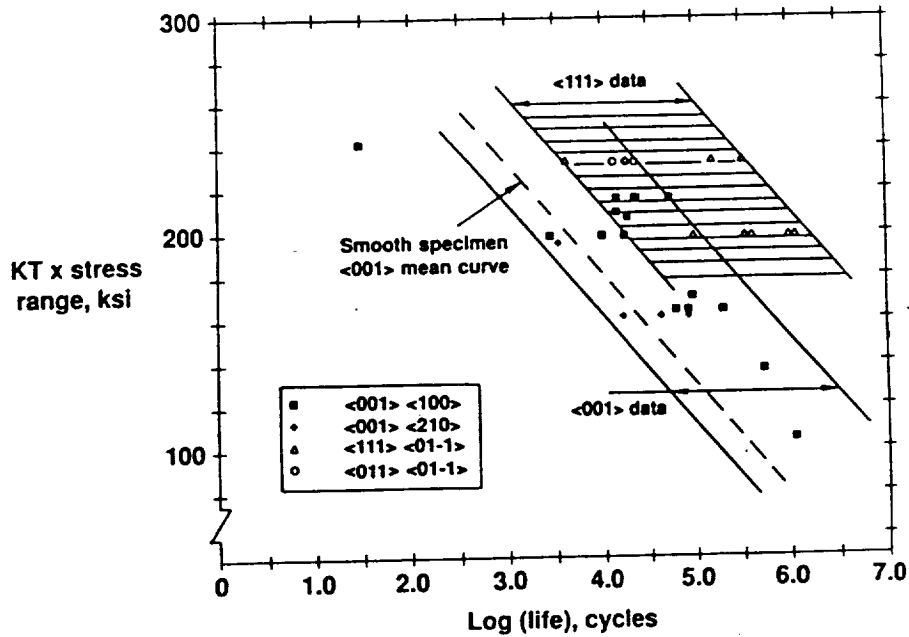*Figure 133*   *Calculated Vs. Actual Separation Lives for Smooth Specimens*

Figure 134   *Concentrated Elastic Stress Range Vs. Fatigue Life for Thin, Mild Notched PWA 1480 Specimens Having Several Orientations*
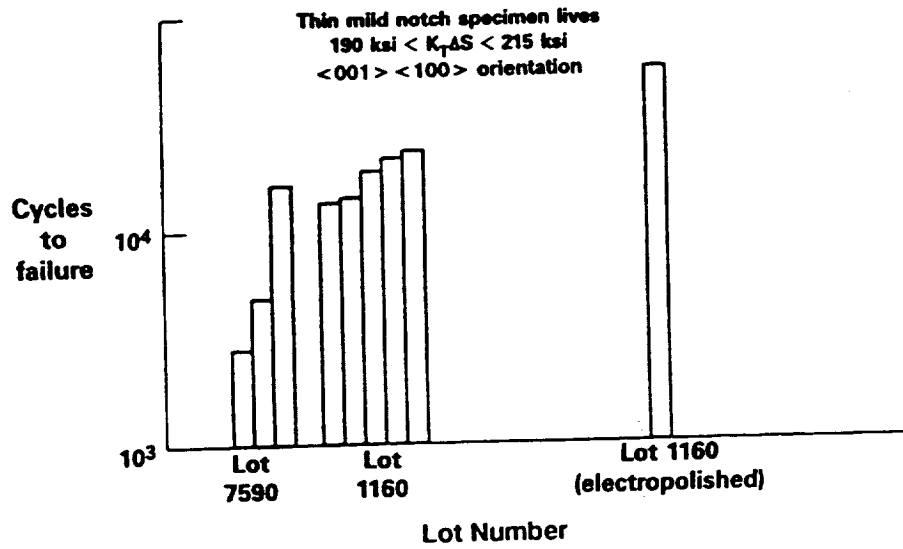
Figure 135   Lot Variation In < 001 > < 100 > Specimens
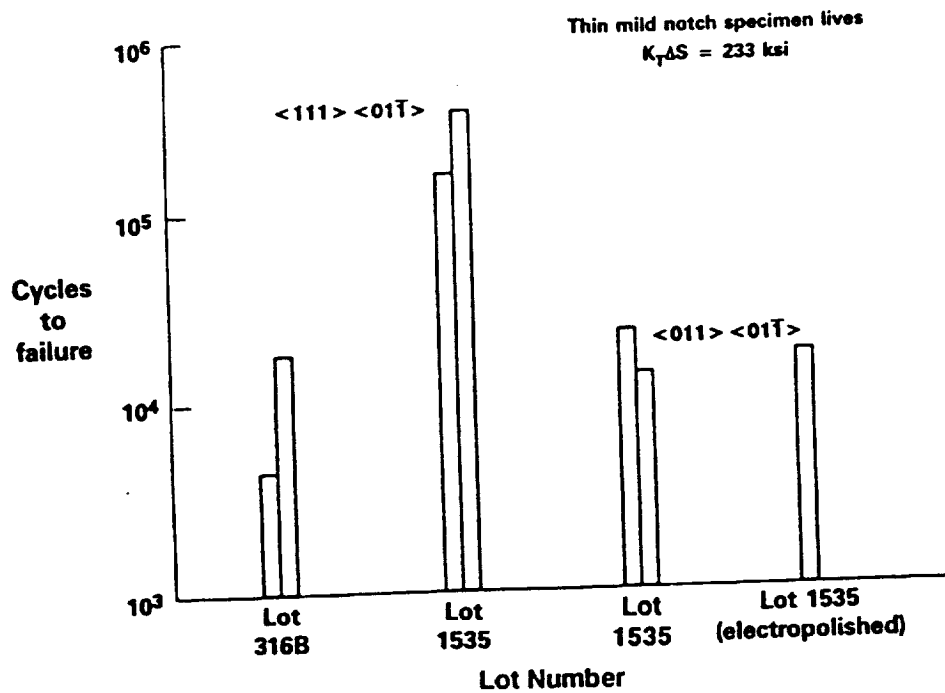
Figure 136   Lot Variation In Off Axis Specimens
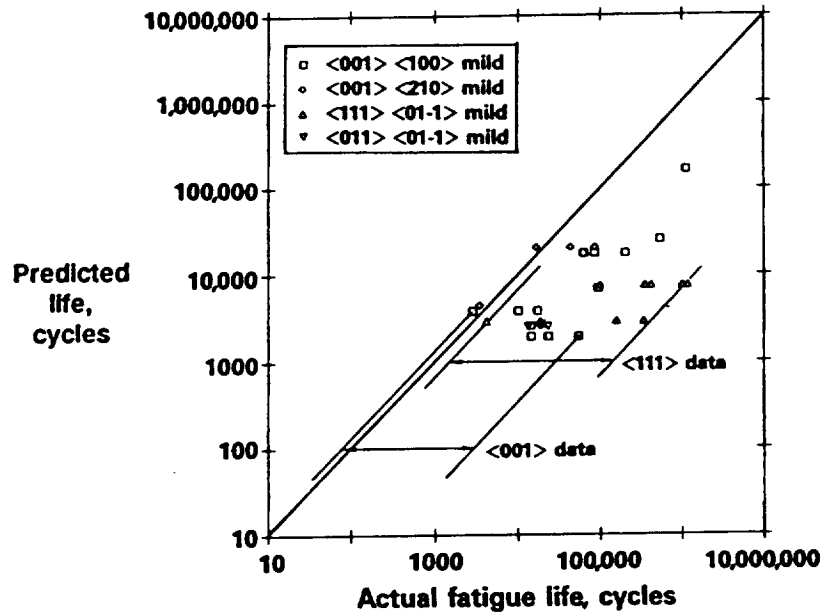
Figure 137   *Predicted Vs. Actual Fatigue Lives of Thin Mild Notched Specimens Using the Smooth Specimen Fatigue Life Model*
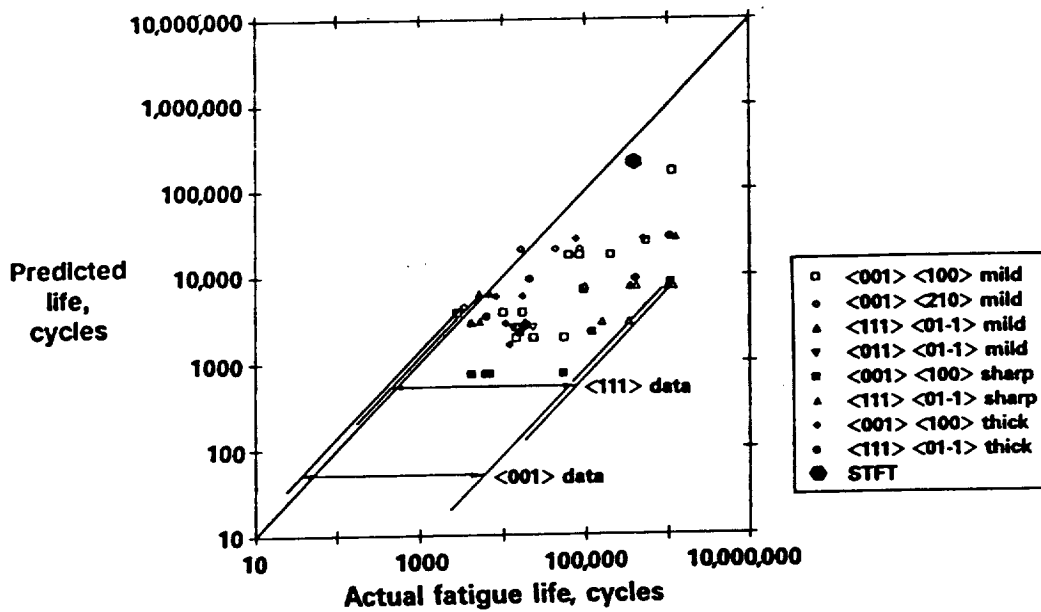

Figure 138   *Predicted Vs. Actual Fatigue Lives of Notched Specimens Using the Smooth Specimen Fatigue Life Model*
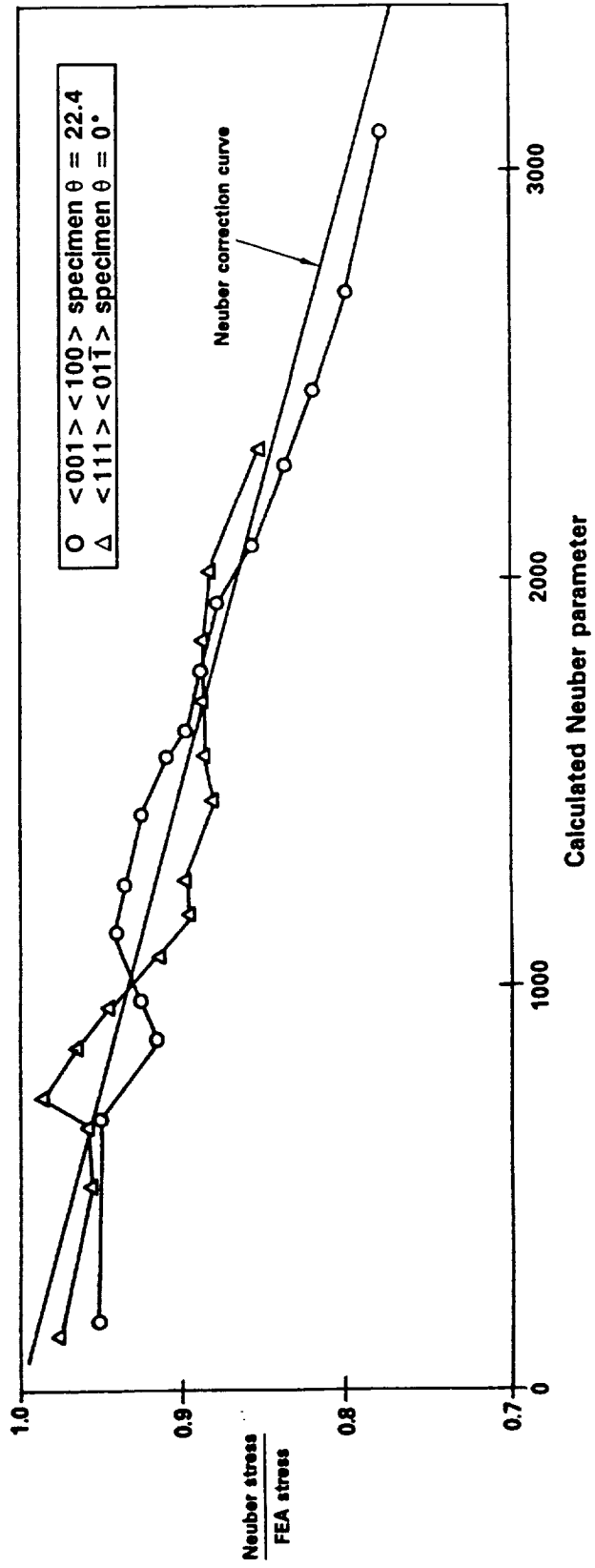
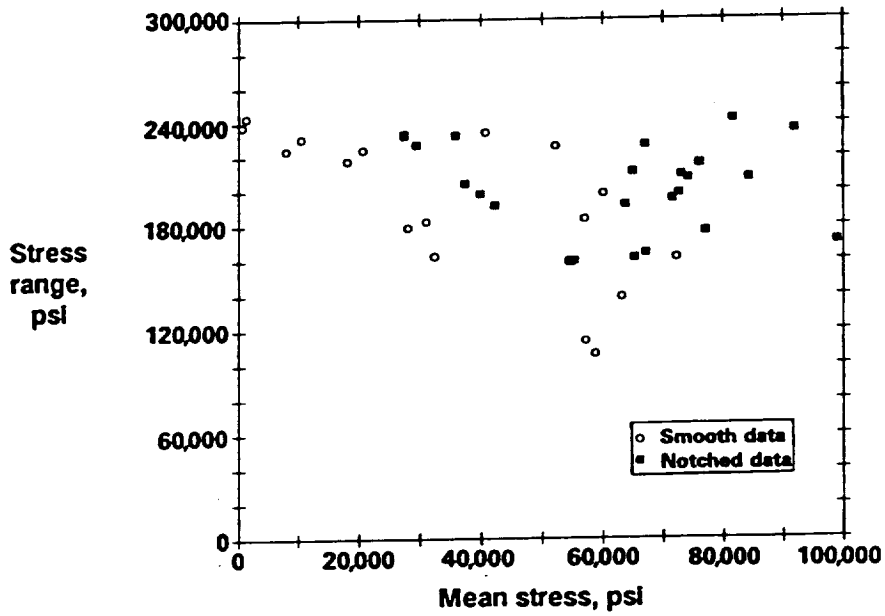Figure 139   Neuber Correction Curve Derived From a Nonlinear Finite Element Analysis

292

Figure 140   *Stress Range Vs. Mean Stress for Smooth and Notched Specimens*
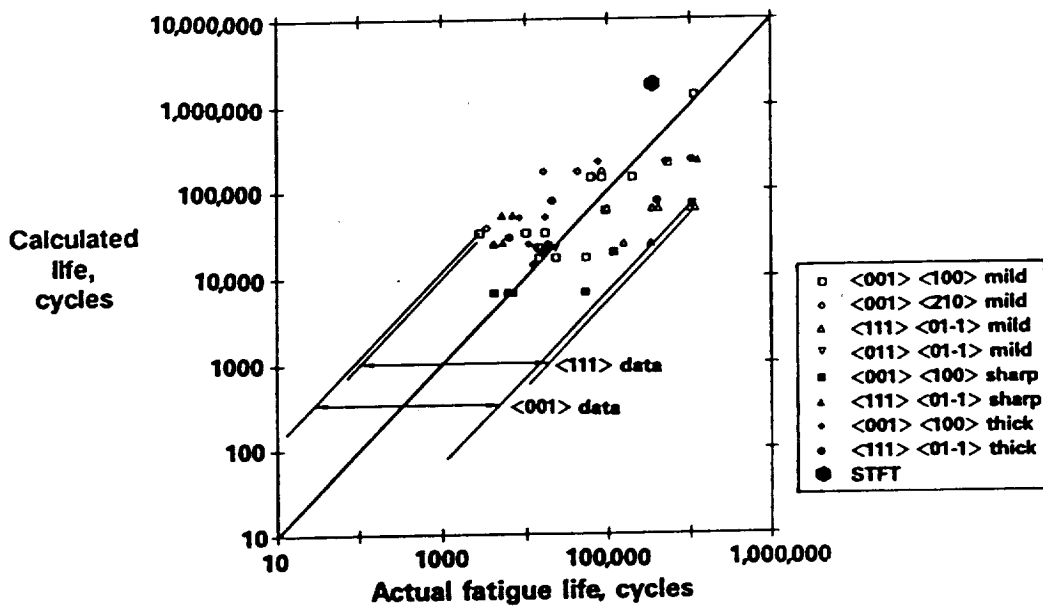

Figure 141   *Calculated Vs. Actual Notched Specimen Fatigue Lives Using Stress Range, Mean Stress Model Fit to the Notched Specimen Fatigue Data*
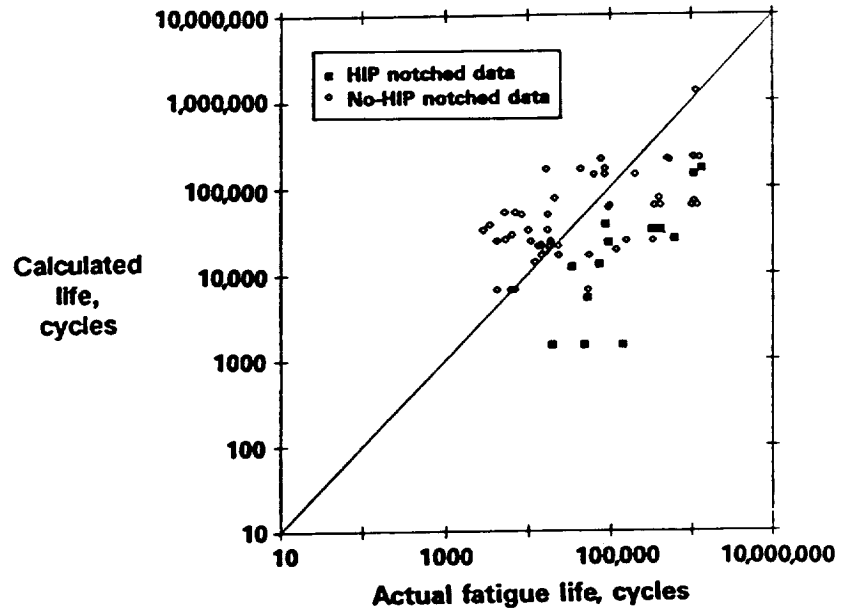
Figure 142   *Notched Fatigue Life Benefit Due to Micropore Elimination by Hot Isostatic Pressing (HIP)*
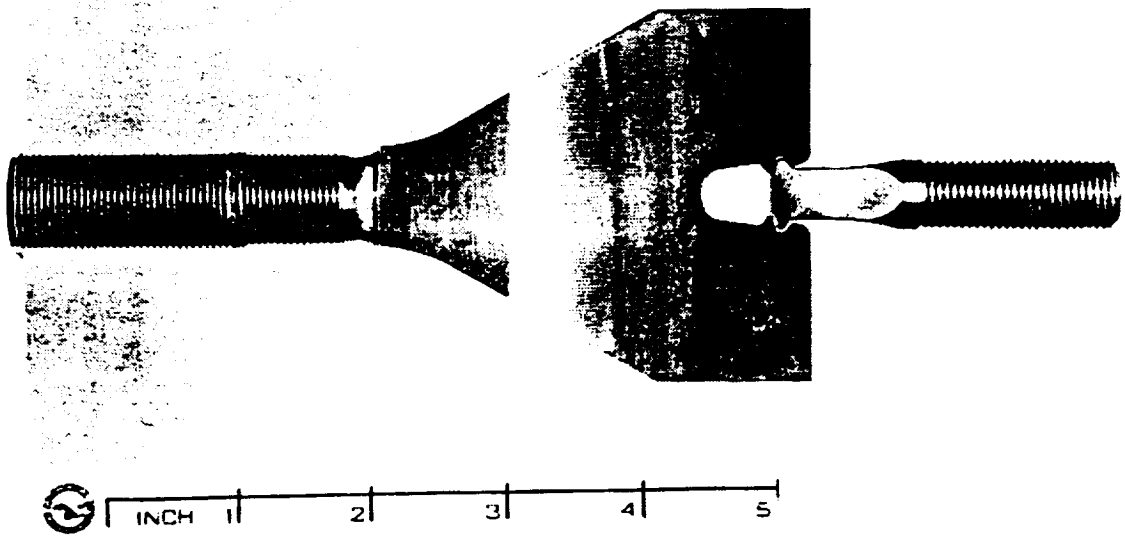

Figure 143   *A Single Tooth Firtree (STFT) Specimen In a Broach Block Fixture*

294

National Aeronautics and Space Administration

Report Documentation Page

1. Report No. NASA CR-189223	2. Government Accession No.	3. Recipient's Catalog No.
4. Title and Subtitle Life Prediction and Constitutive Models for Engine Hot Section Anisotropic Materials Program		5. Report Date September 1992
		6. Performing Organization Code 590-21-11
7. Author(s) D. M. Nissley, T. G. Meyer and K. P. Walker		8. Performing Organization Report No. PWA-5968-102
		10. Work Unit No.
9. Performance Organization Name and Address UTC-Pratt & Whitney 400 Main Street East Hartford, Connecticut 06108		11. Contract or Grant No. NAS3-23939
		13. Type of Report and Period Covered Final Report
12. Sponsoring Agency Name and Address NASA-Lewis Research Center 21000 Brookpark Road Cleveland, Ohio 44135		14. Sponsoring Agency Code

15. Supplementary Notes
Program Manager: Dr. M. A. McGaw NASA-Lewis Research Center

16. Abstract

This report presents a summary of results from a 7 year program designed to develop generic constitutive and life prediction approaches and models for nickel-based single crystal gas turbine airfoils. The program was composed of a base program and an optional program. The base program addressed the high temperature coated single crystal regime above the airfoil root platform. The optional program investigated the low temperature uncoated single crystal regime below the airfoil root platform including the notched conditions of the airfoil attachment.

Both base and option programs involved experimental and analytical efforts. Results from uniaxial constitutive and fatigue life experiments of coated and uncoated PWA 1480 single crystal material formed the basis for the analytical modeling effort. Four single crystal primary orientations were used in the experiments: <001>, <011>, <111>, and <213>. Specific secondary orientations were also selected for the notched experiments in the optional program. Constitutive models for an overlay coating and PWA 1480 single crystal materials were developed based on isothermal hysteresis loop data and verified using thermomechanical (TMF) hysteresis loop data. A fatigue life approach and life models were developed for TMF crack initiation of coated PWA 1480. A life model was developed for smooth and notched fatigue in the option program. Finally, computer software incorporating the overlay coating and PWA 1480 constitutive and life models was developed.

17. Key Words (Suggested by Author(s)) Life Prediction Constitutive Models Single Crystal Alloys Anisotropic Materials Gas Turbine Engine Airfoils		18. Distribution Statement General Release	
19. Security Classif. (of this report) Unclassified	20. Security Classif. (of this page) Unclassified	21. No. of pages 312	22. Price A14

NASA FORM 1626 OCT 86